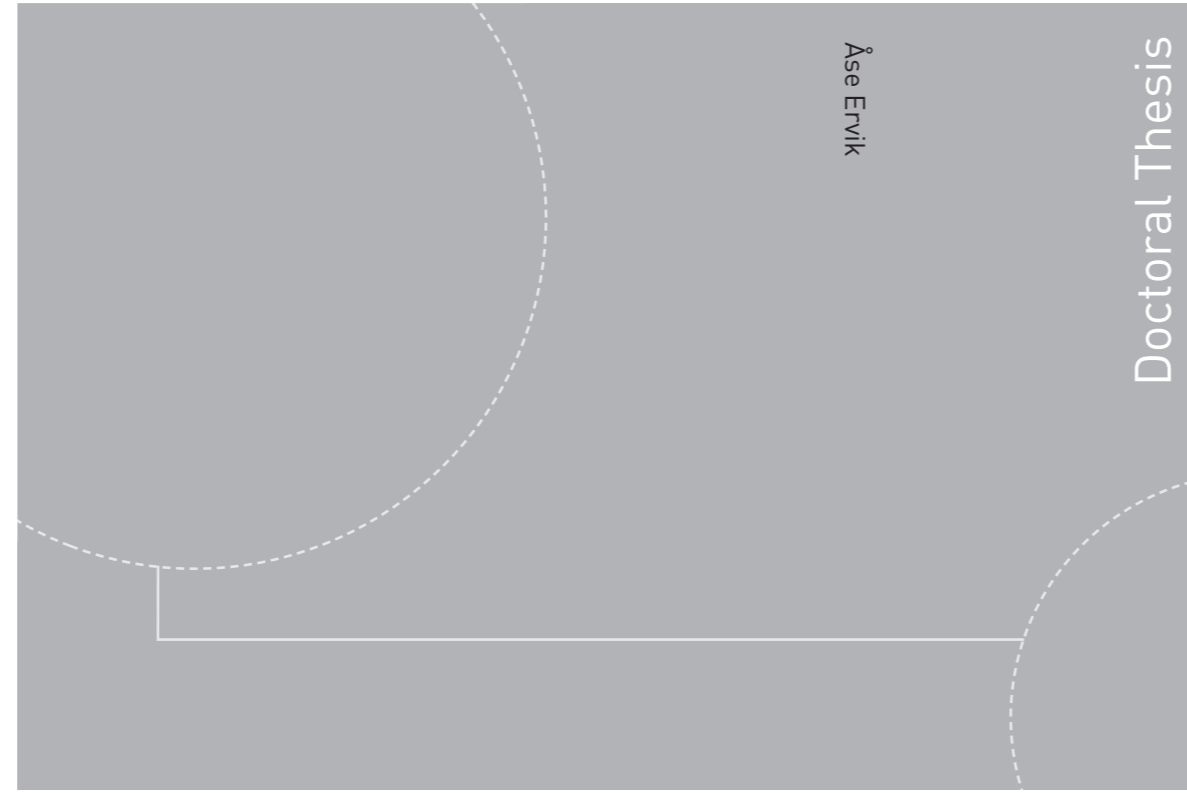


ISBN 978-82-326-3980-9 (printed version)
ISBN 978-82-326-3981-6 (electronic version)
ISSN 1503-8181



Doctoral theses at NTNU, 2019:192

Åse Ervik

**Experimental and numerical studies
related to failure of first-year ice
ridges against fixed vertically sided
structures**

Åse Ervik

Experimental and numerical studies related to failure of first-year ice ridges against fixed vertically sided structures

Thesis for the degree of Philosophiae Doctor

Trondheim, June 2019

Norwegian University of Science and Technology
Faculty of Engineering
Department of Civil and Environmental Engineering



Norwegian University of
Science and Technology

NTNU

Norwegian University of Science and Technology

Thesis for the degree of Philosophiae Doctor

Faculty of Engineering

Department of Civil and Environmental Engineering

© Åse Ervik

ISBN 978-82-326-3980-9 (printed version)

ISBN 978-82-326-3981-6 (electronic version)

ISSN 1503-8181

Doctoral theses at NTNU, 2019:192



Printed by Skipnes Kommunikasjon as

To all those who made this thesis possible: from beloved family, through wonderful friends to dear colleagues. And to you, of course, that care enough to read this.

Abstract

This thesis encompasses three main research topics including, 1) field investigations of the seasonal development in ridge structure and strength, 2) identification and classification of full-scale high force ice ridge-structure interactions and 3) numerical studies of parameters of ductile consolidated ice-structure interactions. The highest identified global forces in the full-scale ice ridge-structure interactions were caused by simultaneous failure of the consolidated layer in spring when the consolidated layer thickness was at the seasonal maximum.

The first topic is the development in thermo-mechanical properties in decaying Arctic ice ridges. In the transition from the main phase to the decay phase both the air and water temperatures exceed the freezing point and the ice ridge is thus heated from both the air and water surface. Measurements were performed on four ridges during the N-ICE2015 expedition in the Arctic Ocean in May and June. The results showed that the consolidated layer continued to grow, although being heated, as long as the temperature inside the consolidated layer was low enough that it could consume both the heat flux from the air and the latent heat released from the growth of ice. Simultaneously, the oceanic heat flux melted the bottom of the rubble, and as a result, both the rubble thickness and the macroporosity decreased towards zero in the decay phase. In the main phase, both the drilling resistance and the uniaxial compressive strength varied with depth, whereas in the decay phase the drilling resistance was low throughout the ridges. The uniaxial compressive strength remained constant after the ice had reached an isothermal state of approximately -1.8°C , although the brine volume increased.

The second research topic in this thesis is the identification of high global forces and classification of interaction modes in ice ridge interactions. Available data from the Norströmsgrund lighthouse was used in this analysis. The highest global forces measured at the Norströmsgrund lighthouse in the winters of 1999/2000-2002/2003, occurred in spring (March/April) when both the consolidated layer thickness and the transportation of ice was at maximum. Among all ice interactions with Norströmsgrund lighthouse, first-year ice ridges gave the highest global forces and the overall maximum measured global force was ~ 6 MN, but because of instrumentation limitations, the entire global forces were under-predicted. The type of high global force ice-ridge interaction mode was classified based on the signatures in force and the response time series as well as video records. The classified ice-ridge interactions included:

- 1) limit-force stalling,
- 2) limit-stress ductile failure and
- 3) limit-stress brittle failure.

All of these interaction modes potentially gave a high global force, and high global forces occurred when ice failed simultaneously across the lighthouse circumference or the ice ridge was stalled against the lighthouse. Frequency-lock-in vibrations and intermittent crushing was not identified for the high force ridge events. Due to the limited vertical extent of the load panels, the high forces were mostly caused by the consolidated layer.

The third and final research topic in this thesis is numerical studies of parameters in ductile consolidated ice interactions with fixed vertically sided structures. The highest quasi-static forces at the Norströmsgrund lighthouse were caused by the consolidated layer in ice-ridge stalling and ductile events. These events occurred without structural vibrations and thus the purpose of the numerical model is therefore not to simulate frequency lock-in vibrations. The model is applied in conjunction with two level factorial design of experiments to identify the statistical significance of material properties to the global ductile ice force transmitted to a structure. The model is an elastic-plastic finite element model, with an isotropic pressure dependent yield function and a non-associated flow rule. The model is applied in simulations of ductile ice failures at two vertically sided structures, a flat indenter in the JOIA experiment and the cylindrical Norströmsgrund lighthouse, to evaluate the effect of the structure shape on the stress-state in the ice. The model was further used to show that the stress state and thus effective pressure was affected by aspect ratio and strength heterogeneities. Low aspect ratios and flat prismatic indenters caused higher lateral ice stresses and thus higher effective pressures than high aspect ratios and cylindrical indenters.

Preface

This thesis is submitted to the Norwegian University of Science and Technology (NTNU) for partial fulfillment of the requirements for the degree of philosophiae doctor.

This doctoral work was performed at the Department of Civil and Environmental Engineering, NTNU, Trondheim and the Department of Arctic Technology of the University Centre in Svalbard, UNIS, with Professor Knut V. Høyland as the main supervisor and with co-supervisors Professor Gustav Grimstad, Professor Aleksey Marchenko, Dr. Torodd S. Nord and Dr. Aleksey Shestov.

This thesis was financed by the Research Council of Norway through NTNU's Research Centre for *Sustainable Arctic Marine and Coastal Technology* (SAMCoT CRI) and the partners of SAMCoT.

Declaration of authorship

This thesis contains a total of 6 papers (Appendices 1-6). Four papers have been submitted to journals; three have been published, and one is under review. Two papers have been published in conference proceedings.

Paper 1 Ervik, Å., Høyland, K.V., Shestov, A. and Nord, T.S., 2018. On the decay of first-year ice ridges: Measurements and evolution of rubble macroporosity, ridge drilling resistance and consolidated layer strength. *Cold Regions Science and Technology*, 151: 196-207, <https://doi.org/10.1016/j.coldregions.2018.03.024>.

The first author was responsible for planning and performing the experimental work, analysing the obtained data and writing the manuscript. The co-authors helped perform the experimental work and writing the manuscript.

Paper 2 Shestov, A., Høyland, K. and Ervik, Å., 2018. Decay phase thermodynamics of ice ridges in the Arctic Ocean. *Cold Regions Science and Technology*, <https://doi.org/10.1016/j.coldregions.2018.04.005>.

The first author was responsible for the thermodynamic calculations and the main results presented in the paper. The co-authors helped perform the experimental work and writing the manuscript.

Paper 3 Ervik, Å., 2015. Full scale actions from first year ridge interactions with fixed structures. *Proceedings of the 23rd International Conference on Port and Ocean Engineering under Arctic Conditions (POAC)*, Trondheim, Norway, Paper no. 129.

The first author was responsible for the entire work of this paper.

Paper 4 Ervik, Å., Nord, T.S., Høyland, K. V., Samardzija, Li, H.. Ice-ridge interactions with the Norströmsgrund lighthouse: global forces and interaction modes. *Cold Regions Science and Technology*, 158: 195-220
<https://doi.org/10.1016/j.coldregions.2018.08.020>.

The first author was responsible for analyzing the data and writing the manuscript. Co-authors helped with their relevant knowledge, developing tools for data analysis and recommendations and constructive criticism that improved the quality of this paper.

Paper 5 Ervik, Å., Høyland, K.V, Grimstad, G., Nord, T.S. A Continuum Model of Large Deformation Continuous Ductile Ice Crushing. Proceedings of the 24th International Conference on Port and Ocean Engineering under Arctic Conditions (POAC), Busan, Korea, Paper no. 104.

The first author was responsible for running simulations, analyzing results and writing the manuscript. Co-authors contributed with recommendations and constructive criticism that improved the quality of this paper.

Paper 6 Ervik, Å., Høyland, K.V, Kim, E. and Nord, T.S. On FEM ductile ice-structure simulations: the significance of material properties, aspect ratio, structure shape and ice strength heterogeneities. Submitted to Cold Regions Science and Technology, under revision.

The first author was responsible for running simulations, analyzing results and writing the manuscript. Co-authors contributed with data, analysis, recommendations and constructive criticism that improved the quality of this paper.

Acknowledgements

I have many to thank for their involvement in this thesis, and fortunately no constraints on the length. The present work forms part of the Centre for Research-based Innovation, *Sustainable Arctic Marine and Coastal Technology* SAMCoT. The Centre is funded by the Research Council of Norway (grant no. 203471/O30) and the partners of SAMCoT, I am grateful for this support.

The first person I would like to thank is my main supervisor, Professor Knut V. Høyland. You have always been available for discussions and have given me freedom to pursue my research interests. You also helped reveal interesting and important conclusions from inextricable data. I thank my co-supervisor Dr. Torodd S. Nord, for your experience, excellent advice and your good humor. Torodd you helped identifying important engineering applications of my work. I thank my co-supervisor Dr. Aleksey Shestov, for the collaboration. Your office door has always been open to me, and your equipment has been available and working. I would like to thank my co-supervisor Professor Aleksey Marchenko. You have given me the opportunity to participate in a variety of experiments in the field and in the laboratory. I thank also my co-supervisor Professor Gustav Grimstad, for your knowledge and discussions.

I am very grateful to the collaboration with associated professor Ekaterina Kim, Dr. Sergey Kulyakhtin and Anna Pustogvar, thank you for sharing your experience and knowledge with me. I would also like to thank the leader of our research Centre, Professor Sveinung Løset. Thanks to you, your energy and contacts, resources have always been available. I also thank you for your constructive comments during preparations for the defense of this thesis. I am grateful to our Centre coordinator, Maria Azucena Gutierrez Gonzalez, thank you for listening, giving me opportunities to convey my research and for being a good advisor and supporter to me and all of the other PhD candidates in this Centre.

I also appreciated the collaboration with the Norwegian Polar Institute, in particular Dr. Sebastian Gerland and Dr. Mads Granskog, thank you for inviting me on board the research vessel Lance during the Norwegian young sea ice expedition 2015 (N-ICE2015). Special thanks are extended to Annu Oikkonen, you provided excellent assistance and a positive mood on board. I also thank the logistics department at UNIS for helping with preparations and packing for field work.

I consider myself privileged to be part of the sea ice group in Multiconsult, with Dr. Arnor Jensen, Dr. Basile Bonnemaire, Dr. Edmond Hansen, Dr. Nicolas Serre, Trine Lundamo

and Dr. Tim Fristedt. Thank you for your interest, knowledge, straight talking and the economic support.

Special thanks to my dear colleagues and friends, apart from those mentioned above you are: Runa A. Skarbø, Lars Einar Stieng, Martina Salomon, Helene Seyr, Julie Lepage, Dr. Gordon Stewart, Dr. Andrei Tsarau, Dr. Ersegun Deniz Gedikli, Dr. Wenjun Lu, Marnix van den Berg, Hongtao Li, Evgenii Salganik, Ilja Samardzija, Weichi Wang, Ankit Aggarwal, Dr. Tu Ying, Dr. Arun M. Kamath, David Wrangborg, Dr. Wolfgang Kempel, Dr. Anton Kulyakhtin, Sanja Forsstöm, Juni Vaardal-Lunde, Juliane Borge, Andreas Ommundsen, Leiv Aspelund, Martin Arntsen, Dr. Arnt Fredriksen, Øyvind Nilsen, Dr. Jan Potac, Bård Harald Worum and Dr. Abushet Simanesev –what a wonderful mix of people. Thank you for all the discussions, the good (and the bad) humor, you made this journey less lonely.

Last, but decidedly not least, I want to thank my friends and family for your support, interest and encouragement during this time. To my friends, especially Hege, Kaja, Kristine, Marianne and Sigrid. I am very grateful for the effort that you spent to reduce the deterioration of my social presence. Also for reminding me that there is so much more to life than work and studies. To my brothers Åsmund and Daniel, I am grateful for your honest comments and feedback, your interest and for providing me with plenty of backbone. To my parents, thank you for believing in me and for motivating me when I felt I was not able to do this. I also thank Johan Arnt, for distracting me, for taking me on adventures and for his love. I also thank him for keep choosing me as his partner even at times when I was stressed and crazy about deadlines or writing this thesis, I am sorry. To Tøtta, we made most of this journey together, and you literally pulled me forward. Thank you for all the walks, your unconditional love, you were so much more than “just a dog”, and I miss you so much.

Contents

Abstract..... **i**

Preface..... **iii**

Declaration of authorship **v**

Acknowledgements **vii**

Contents **ix**

Notations **xiii**

Abbreviations **xiv**

Chapter 1 **1**

Introduction..... **1**

 1.1 *Background and motivation* *1*

 1.2 *Research approach* *4*

 1.3 *Objectives and scope* *4*

 1.4 *Thesis structure* *5*

Chapter 2 **7**

Seasonal development in ridge structure and strength **7**

 2.1 *Background* *7*

 2.2 *Method* *8*

 2.3 *Results and discussion* *9*

 2.3.1 *Overview* *9*

 2.3.2 *Seasonal development in consolidated layer thickness and rubble macroporosity* *10*

 2.3.3 *Seasonal development in ice ridge strength and drilling resistance* ... *12*

 2.4 *Conclusions and recommendations* *15*

Chapter 3 **17**

Full-scale high force ridge-structure interactions..... **17**

 3.1 *Background* *17*

 3.2 *Method* *18*

 3.2.1 *The Norstömsgrund lighthouse* *18*

 3.2.2 *Event identification and signal processing* *20*

 3.3 *Results and discussion* *20*

 3.3.1 *Ice conditions and environmental data* *20*

3.3.2	Interaction modes	21
3.3.3	Global forces and probability of exceedance	29
3.4	<i>Conclusions and recommendations</i>	32
Chapter 4	33
Numerical modelling of ductile consolidated ice interactions	33
4.1	<i>Background</i>	33
4.2	<i>Material strength and models</i>	34
4.2.1	The finite element elastic-plastic stiffness matrix	34
4.3	<i>Experimental data</i>	38
4.4	<i>Methods</i>	39
4.4.1	Two level factorial design of experiments	39
4.4.2	Simulation matrix	40
4.5	<i>Results and discussion</i>	41
4.5.1	The significance of material properties	41
4.5.2	Effect of aspect ratio on the global force.....	42
4.5.3	Effect of structure shape on the global force.....	45
4.5.4	Simulated compared to measured global forces	46
4.6	<i>Conclusions and recommendations</i>	47
Chapter 5	49
Conclusions and future outlook	49
5.1	<i>Conclusions</i>	49
5.2	<i>Future outlook</i>	51
References	53
Appendix 1	59
On the decay of first-year ice ridges: Measurements and evolution of rubble macroporosity, ridge drilling resistance and consolidated layer strength	59
Appendix 2	61
Decay phase thermodynamics of ice ridges in the Arctic Ocean	61
Appendix 3	63
Full-scale actions from first-year ridge interactions with fixed structures	63
Appendix 4	65
Ice-ridge interactions with the Norströmsgrund lighthouse: global forces and interaction modes	65
Appendix 5	67

A Continuum Model of Large Deformation Continuous Ductile Ice Crushing.	67
Appendix 6.....	69
On FEM ductile ice-structure simulations: the significance of material properties, aspect ratio, structure shape and ice strength heterogeneities	69

Notations

Scalars, vectors and matrices

x, y, z	Scalar variables
$\mathbf{x}, \mathbf{y}, \mathbf{z}$	Vector variables
$\mathbf{X}, \mathbf{Y}, \mathbf{Z}$	Matrix variables
\mathbf{I}	Identity matrix

Fixed symbols

T, T_f, T_{air}	Ice temperature, freezing point, air temperature
S_i	Ice salinity
h_i	Level ice thickness
h_c	Consolidated layer thickness
h_k	Ice ridge keel thickness
$h_{ru}=h_k - h_c$	Ice rubble thickness
ρ_i, ρ_w	Ice density, water density
$\mathbf{D}, \mathbf{D}^{ep}$	Elastic- and elastoplastic stiffness matrix
E	Elastic modulus
ν	Poisson's ratio
σ	Stress
$\hat{\sigma} = \hat{\sigma}_1 \geq \hat{\sigma}_2 \geq \hat{\sigma}_3$	Principal stress
$\varepsilon, \varepsilon^e, \varepsilon^p, \varepsilon_{eq}^p$	Strain, elastic strain, plastic strain and equivalent plastic strain, respectively
$\hat{\varepsilon} = \hat{\varepsilon}_1 \geq \hat{\varepsilon}_2 \geq \hat{\varepsilon}_3$	Principal strains
σ_t	Uniaxial tensile strength of the ice
σ_c	Uniaxial compressive strength of the ice
σ_b	Biaxial compressive strength of the ice
τ	Shear strength of the ice
F	Yield function
Q	Flow potential
ψ	Dilatancy angle
$d\lambda$	Plastic multiplier
I_1	First stress invariant
J_2	Second deviatoric stress invariant
$P=I_1/3$	Hydrostatic pressure
P^{eff}	Effective pressure
F_{global}	Global force

σ_{Acc}	Standard deviation of acceleration
σ_{Fdyn}	Standard deviation of dynamic force

Abbreviations

CEL	Coupled Eulerian Lagrangian
DOE	Design of experiments
EM	Electromagnetic ground conductivity geophysical instrument
FDD	Freezing degree days
FEM	Finite element method
FMI	Finnish Meteorological Institute
FYR	First-year ice ridge
HSE	Health, safety and environment
JOIA	Japan Ocean Industries Association
LOLEIF	Low level ice forces
MYR	Multi-year ice ridge
MWL	Mean water level
N-ICE2015	The Norwegian young sea ice expedition
NPI	Norwegian Polar Institute
OFAT	One-factor-at-a-time
SYR	Second-year ice ridge
STRICE	Structures in ice
STD	Standard deviation
SMHI	Swedish Meteorological Institute
ULS	Upward locking sonar

Chapter 1

Introduction

The highest free-floating ridge we know of was 12.8 m above the sea level. The deepest keel observed extended some 47 m below sea level. – Weeks et al. (1971)

1.1 Background and motivation

Natural resources and adventure have drawn people to the harsh environment of the polar regions for centuries, from early explorers and whalers to oil and gas companies. The transport and exploitation of natural resources in the Arctic and the sub-Arctic has led to increased demand for infrastructure that can withstand the harsh environment. Presently, various types of bottom-founded structures are designed for ice-infested waters, including lighthouses, wind turbine foundations, quay structures, mono-pod platforms, multi-legged platforms, caisson-retained islands and bridges. In the absence of old ice features, first-year ice ridges establish the quasi-static design loads for structures in ice-infested waters. Sea ice ridges (ridges in short) are common morphological features in any ice covered water and have a key role in the sea ice mass budget. Ridges form due to deformations in an ice pack, by either shearing or pressure. In average, from 1990-2011, ridges contributed to 66% of the mean ice thickness of Arctic Sea ice in the Fram Strait (Hansen et al., 2014). Thus, ridges are both common morphological ice features and they establish high global forces on structures. This thesis focuses on high global force ridge interactions with vertically sided structures.

A ridge develops during its life, a life that can span for one year, a first-year ridge (FYR), to several years, a multi-year ridge (MYR). The ridge consists of a sail above and a keel below the water surface. The first-year ridge keel consists of a consolidated and an unconsolidated layer (ice rubble), and the structure of a FYR is displayed in Figure 1. Macroporosity is a common property used to describe the internal structure of an ice feature. Macroporosity is defined as the ratio of non-sea ice volume (air or snow voids in the sail and water voids in the keel) to the total ice feature volume (Høyland, 2002). A first-year ridge that survives a summer melt transforms into a second-year ridge (SYR), and a SYR is fully consolidated (with zero macroporosity) and with low salinity. The process of transforming a FYR into a SYR affects the ridge structure including the thickness of the consolidated layer, the macroporosity as well as the strength of the ridge. The development in ridge properties is not well understood, especially the evolution during spring and summer. The development in these properties affects the modes which a ridge interacts with a structure and the global forces the ridge transmits. In high global force ridge interactions with vertically sided structures, the thickness and resistance from the consolidated layer are especially important.

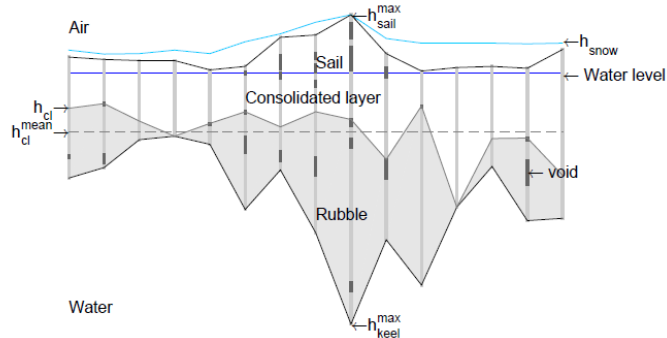


Figure 1. Ice ridge cross-section. The light blue line is the snow cover, the dark blue line is the water surface, and the black lines are ridge boundaries. The vertical lines are drill holes, the light gray shading is ice, and the dark gray sections of the vertical lines represent voids (Ervik et al., 2018).

In 2015, the Norwegian Polar Institute (NPI) led the Norwegian young sea ice expedition (N-ICE2015), which was a multidisciplinary expedition extending from January 11 until June 23. During this expedition, the research vessel RV Lance was frozen into the drifting sea ice in the Arctic Ocean. I was lucky to take part in the expedition in three weeks in May/June and my colleague Dr. Aleksey Shestov took part in the following three weeks in the end of June. We studied the development of the consolidated layer, in terms of its structure and strength, in drifting Arctic ice ridges during spring and early summer.

Properties of ridges in spring and summer are important because the global ice movement often accelerates in spring. Several extreme ridge events also occurred in spring, including the failure of the Swedish Björnklack lighthouse (Engelbrektson, 1987b), the extreme ice loading events on the Confederation Bridge (Brown et al., 2010; Shrestha and Brown, 2018) and high global force events at Norströmsgrund lighthouse (Poirier, 2014). Blenkarn (1970) notes, with reference to ice forces measured at platforms in Cook Inlet, Alaska, that “*if anything, it would appear that the largest ice forces correspond to somewhat warmer ice ...*”. Among those events, high forces at Cook Inlet platforms and at Baltic lighthouses were caused by ductile interactions (Blenkarn, 1970; Engelbrektson, 1987b; Ervik et al., 2018b; Neill, 1976). Presently several oil and gas fields are explored in the southwestern Barents Sea (Hasle et al., 2009). Properties of ice entering the southwestern Barents Sea will probably resemble Arctic ice properties measured in spring and summer.

In 1941 the first five Swedish lighthouses were built to offer safe navigation and transportation between the Öland island and the city of Kalmar on mainland Sweden (Frost, 1941). The following years until 1990, 59 caisson lighthouses were built along the Swedish coastline, and since 1971 year around navigation was maintained in the Gulf of Bothnia. Among the Swedish lighthouses, three suffered from failure due to ice actions.

Engelbrekton (1987b), provides a detailed description of the extreme overloading event of the cylindrically shaped Björnklack lighthouse in 1985 on April 4. The event was considered a 10,000-year event. In the overloading event, the lighthouse slid 17 m and tilted 12° due the movement of a 10 km wide ice sheet. The ice that caused the failure of the Björnklack on April 4 was deformed ice with thickness 1.4-1.5 m and the calculated effective pressure from the ice was 2.6 MPa (Engelbrekton, 1987b). The Swedish lighthouses were unmanned and to save costs a certain level of risk was accepted. During the Low Level Ice Forces project (LOLEIF) and Structures in Ice project (STRICE) (winters 1999/2000-2002/2003), ice forces were measured at the Norströmsgrund lighthouse located in the Gulf of Bothnia (N65°6.6' E22° 19.3'), 60 km southeast of Luleå in Sweden. The lighthouse was instrumented to measure ice forces at MWL, structural responses (accelerations and tilt), ice thickness, meteorological data and videos. A detailed description of the instrumentation is available in Bjerås (2006), Haas (2000), Jochmann and Schwarz (2000). Because ice forces were measured with load panels extending approximately 1.6 m below the MWL, the global force in ridge interactions was mostly caused by the consolidated layer.

Although deformed ice and ridges establish some of the most severe ice conditions, they are among the least understood types of ice-structure interactions and are not described in standards, such as the ISO19906 (2018). For ridge-structure interactions, very little has been reported on the signatures in force and response, and before studies presented in this thesis only Bjerås (2006), Brown et al. (2010) and Poirier (2014) had presented time series of force signatures in ridge interactions and identified ridge failure modes. However, the identified signatures in forces and responses have never previously been systematically associated with the type of ridge-structure interaction mode. The LOLEIF and STRICE data, measured at Norströmsgrund lighthouse, offered a unique possibility to both investigate the global force levels in ice ridge interactions and to classify different types of high force interaction modes. High global force ridge events were chosen for this study because they govern quasi-static design loads.

The data collected at the Norströmsgrund lighthouse is among the most detailed full-scale data that currently exists. However, the behaviour of the ice cannot be extractable from the experimental data. That means, it is not possible to solve the inverse problem of determining the behaviour and deformations of the ice from the forces measured in the experiment. A numerical model is a supplement to full-scale experiments where both the forces on the lighthouse and the behaviour of the ice can be studied. In numerical models, the ice properties and boundary conditions can be controlled and thus effects of aspect ratio, structural shape and strength heterogeneities can be studied. The model can also be used, in conjunction with a statistical framework, to evaluate the effect of varying ice properties, in addition to estimating forces missed by the limited instrumentation. The global forces measured at the Norströmsgrund lighthouse in ridge interactions were

mostly caused by the consolidated layer in the ridges, due to the limited vertical extent of the load panels. Generally, forces measured from ice rubble in full-scale ridge interactions are absent. Therefore, the applied numerical model aims at simulating the consolidated layer in ice ridge interactions. Furthermore, at the Norströmsgrund lighthouse the highest global forces occurred when the ice failed simultaneously across the lighthouse circumference. At other structures such as; the Cook Inlet platforms, Baltic lighthouses and in the medium-scale indentation tests in the JOIA experiment, maximum quasi-static forces occurred during ductile ice-interactions (Blenkarn, 1970; Engelbrekton, 1987b; Ervik et al., 2018b; Neill, 1976; Sodhi and Haehnel, 2003; Sodhi et al., 1998). As part of this thesis, ductile consolidated ice interactions will be studied numerically with an elastic-plastic Finite Element Model (FEM).

1.2 Research approach

The research was conducted by obtaining and analysing field measurements of ice ridge properties, analysing existing full-scale measurements of ice ridge-structure interactions, combining numerical modelling with statistical methods and understanding of the underlying physical processes.

1.3 Objectives and scope

The main objectives of this thesis are to study the seasonal development in first-year ridge properties, identify high global force ridge interactions with the fixed vertical sided Norströmsgrund lighthouse and studying numerically parameters of ice ridge-structure interactions. High global forces at the Norströmsgrund lighthouse were mostly caused by the consolidated layer in ridges, and the interactions were quasi-static. Therefore, ice-induced vibrations are considered outside the scope of this thesis. Ice rubble forces were not quantified in measurements at the Norströmsgrund lighthouse and the ice rubble was therefore not considered in the numerical simulations. The rubble forces were considered less significant compared to the forces from the consolidated layer at the Norströmsgrund lighthouse.

The scope of the work is the following:

- Measure the seasonal development in consolidated layer thickness, consolidated layer strength and rubble macroporosity in drifting ridges in the Arctic Ocean in spring 2015.
- Establish the magnitude of global forces in previously measured ridge interactions with the Norströmsgrund lighthouse and study how the seasonal development in ridge properties affects high global force ridge events.
- Classify high force ridge-structure interaction modes from measurements of force and response time series at the Norströmsgrund lighthouse.
- Review and use existing material models in combination with measured material properties to simulate high global force interactions between consolidated ice and vertically sided fixed structures.

- Determine the statistical significance of ice property variations in the applied material model and evaluate how this is related to the seasonal variation in ice properties.
- Use the numerical model to study the ice stress state in consolidated ice-structure interactions and evaluate the effect of aspect ratio, structure shape and heterogeneities on the global force.

1.4 Thesis structure

This thesis encompasses a collection of papers, provided in Appendices 1-6. Following the introduction (Chapter 1), three chapters provides a summary of each of the three research topics treated in this thesis. The first research topic includes field measurements of the development in the thickness and strength of the consolidated layer as well as the rubble macroporosity in Arctic ridges (in Chapter 2). In the second research topic, full-scale high force ridge interactions at the Norströmsgrund lighthouse are identified and classified (in Chapter 3). The third research topic is numerical modelling of ductile consolidated ice interactions with fixed vertically sided structures (in Chapter 4).

The development in measured ridge properties described in Chapter 2 is related to the occurrence of high global forces and interaction modes identified in Chapter 3. The identified high force interaction modes in Chapter 3 are simulated in Chapter 4. Because rubble forces are not quantified in interactions presented in Chapter 3, the rubble is excluded from simulations in Chapter 4. The rubble forces were also considered less significant compared to the forces from the consolidated layer. The structure of this thesis is illustrated in Figure 2.

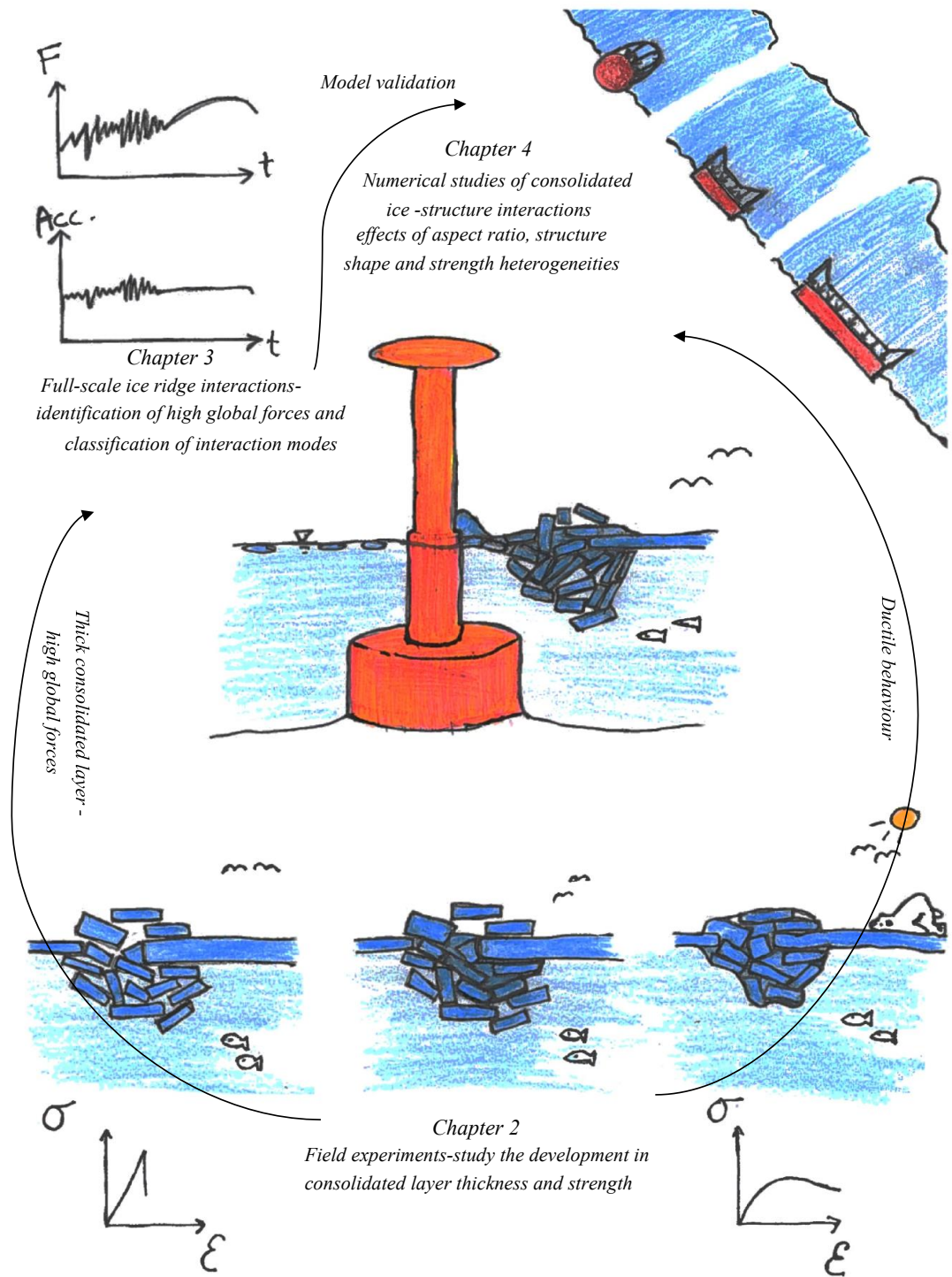


Figure 2. Illustration of the objective-related activities of the doctoral study, including the connections between these activities.

Chapter 2

Seasonal development in ridge structure and strength

Most analyses produce the apparently self-evident result that forces are greatest – other things being equal – when ice strength is greatest; yet it seems to be well-known that icebreakers have the greatest difficulty with apparently weak, easily deformable ice.
- (Neill, 1976)

This chapter summarizes analyses and results from experimental data collected from ridges drifting in the Arctic Ocean in 2015. Experimental studies of the seasonal development in rubble macroporosity, consolidated layer thickness and strength are presented in the full length paper (Appendix 1). Thermodynamics and consolidation of decaying ridges are presented in the full length paper (Appendix 2).

2.1 Background

A first-year ridge lifespan, from formation to breakup or transition into a second-year ridge, can be divided into the following phases: 1) the ‘initial’ phase, 2) the ‘main’ phase, and 3) the ‘decay’ phase (Høyland and Liferov, 2005). In the initial phase, the ridge is formed, and cold ice blocks are submerged, which results in strong, local thermal gradients between cold ice pieces and warm water pockets. The initially low temperature of the ice increases due in part to the freeze bond formation as well as seawater energy transfer (oceanic heat flux). The energy transfer from the seawater, which is the oceanic heat flux, is stronger near the bottom surface of the ice rubble. Because of this difference in the oceanic heat flux, the temperatures in the lower rubble increase and approach the seawater freezing point (T_f) faster. If the seawater is at T_f , the isothermal conditions gradually spread upward through the keel, and because the air is colder than T_f , an assumed linear temperature profile will slowly spread downward simultaneously. The end of the initial phase is defined as the moment when the ice rubble becomes isothermal. The main phase begins, and the break point between the linear temperature profile above the isothermal rubble defines the consolidated layer thickness, as shown by Høyland (2002). The freezing front in the consolidated layer insulates the underlying ice rubble (unconsolidated layer) from the cold air. Therefore, there is a continuous rubble degradation process (heating) leading toward transformation into a second-year ridge or melting/disintegration. Finally, the decay phase begins when the air temperature stabilizes around or above 0°C; thus, the ridge is heated from the air surface and from the bottom. Toward the end of the decay phase, the first-year ridge either disintegrates and melts completely or transforms into a second-year ridge.

Although the air temperature exceeds 0°C, in the decay phase, the snow may insulate the consolidated layer, which allows further consolidation (i.e. new ice growth). Simultaneously, keel melting is accelerated during this phase, and the rubble temperature and water temperature both increase toward 0°C, which causes strong oceanic heat fluxes. These processes are not well understood, but even under isothermal conditions, the rubble continues to consolidate while being heated during the transformation of macroporosity to microporosity (Shestov and Marchenko, 2016b). In addition, the freshwater supply (either from melted snow or changing salinity of the underlying water) may be a key factor contributing to further consolidation (Shestov and Marchenko, 2016a).

The consolidation process affects both the internal structure (macroporosity) and strength of a ridge, and these properties are essential for estimating design ridge loads. Most previous ridge studies were conducted over just a few days' time, and only Leppäranta et al. (1995) studied the full history of a Baltic ridge, from formation to break up. Most sea ice compressive strength measurements were obtained in laboratories using ice temperatures colder than -10°C (Poplin and Wang, 1994; Schulson and Duval, 2009; Sinha, 1984; Timco and Frederking, 1990; Timco and Weeks, 2010). However, decaying saline ice has temperatures of around -1.8°C. Strength measurements of decaying Arctic and subarctic first-year ice were presented by Johnston (2006), Moslet (2007) and Johnston (2017).

This part of the thesis presents the seasonal development in consolidated layer thickness, rubble macroporosity, ridge drilling resistance and consolidated layer uniaxial compressive strength measured in four ridges (R1, R2, R3 and R4). Ridges R1-R4 were measured on two ice drift stations (floes) in the Arctic Ocean in May and June during the Norwegian young sea ice expedition (N-ICE2015).

2.2 Method

N-ICE2015 was a multidisciplinary expedition extending from January 11 to June 23, 2015 and led by the Norwegian Polar Institute (NPI). The expedition base took place on the research vessel RV Lance, which was frozen into and drifted with the young sea ice in the Arctic Ocean. Two researchers from the Centre *Sustainable Arctic Marine and Coastal Technology* (SAMCoT) were invited to study ridges on Floe 3 (May 21st to June 9th) and on Floe 4 (June 9th to June 23rd). Figure 3 shows the ice floe drift trajectories.

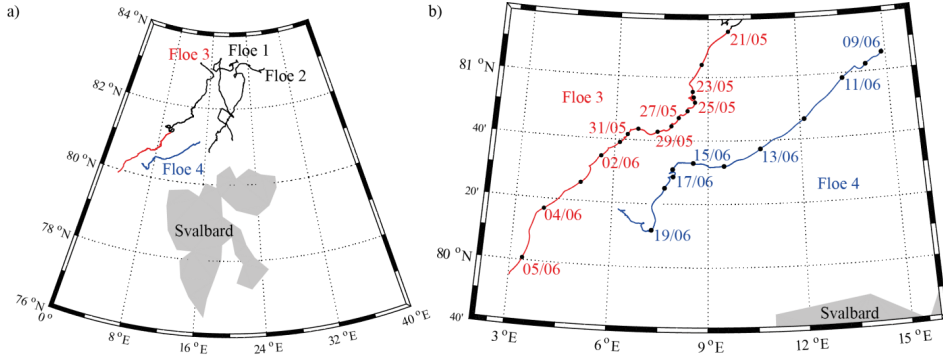


Figure 3. a) Drift trajectories of all four floes visited during the N-ICE2015 expedition and b) drift trajectories of Floe 3 and Floe 4 when ice ridge work was conducted. The distance to the ice edge on Floe 3 was approximately 200 km on April 26 and 40 km on June 5, and on Floe 4, the distance was approximately 70 km on June 9 and 15 km on June 17, 2015 (Oikkonen et al., 2017).

The ridges investigated were equipped with thermistor strings (ridge R1 and R4), morphology mapped by mechanical drilling, and cored for physical property (temperature, density and salinity) measurement. Uniaxial compressive strength was also measured (in field) in cores sampled from the ridges, under constant effective strain rate $\dot{\epsilon} = 10^{-3} \text{ s}^{-1}$, measured in a mobile compression machine (KOMPIS). Temperature data were used to calculate heat fluxes and study the evolution in consolidated layer thickness in R1 and the keel melting in R4. Mechanical drilling was conducted to study the evolution in ridge geometry, macroporosity and drilling resistance. For details about the experimental methods, see papers by Ervik et al. (2018a) and Shestov et al. (2018) in Appendices 1 and 2.

2.3 Results and discussion

2.3.1 Overview

Ridge R1, with maximum keel depth of 13 m and length 200 m, had formed before April 18, and the ridge was still intact when the ship left Floe 3 on June 5. Ridge R2, with maximum keel depth of 5 m and length of 500 m, formed during a storm when a refrozen lead was pushed against thicker level ice April 26 – April 30, and this ridge broke up on June 4. The formation and break up was captured by the ship radar (Haapala et al., 2017) and observed from the ship. Ridge R3, with maximum keel depth of 6 m and length of 75 m, and R4, with maximum keel depth of 9 m and length of 150 m, both formed before June 8.

The transition from the main phase to the decay phase occurred at the beginning of June (Figure 4), when air temperatures stabilizes around 0°C and ridges were thus heated from both the air and water surfaces. The oceanic heat flux changed during the transition from

the main phase to the decay phase. In Floe 3, which was measured towards the end of the main phase, the oceanic heat flux was in the range of 10-15 W/m², whereas on floe 4, which was measured in the decay phase, the oceanic heat flux was 20-400 W/m² (Peterson et al., 2017).

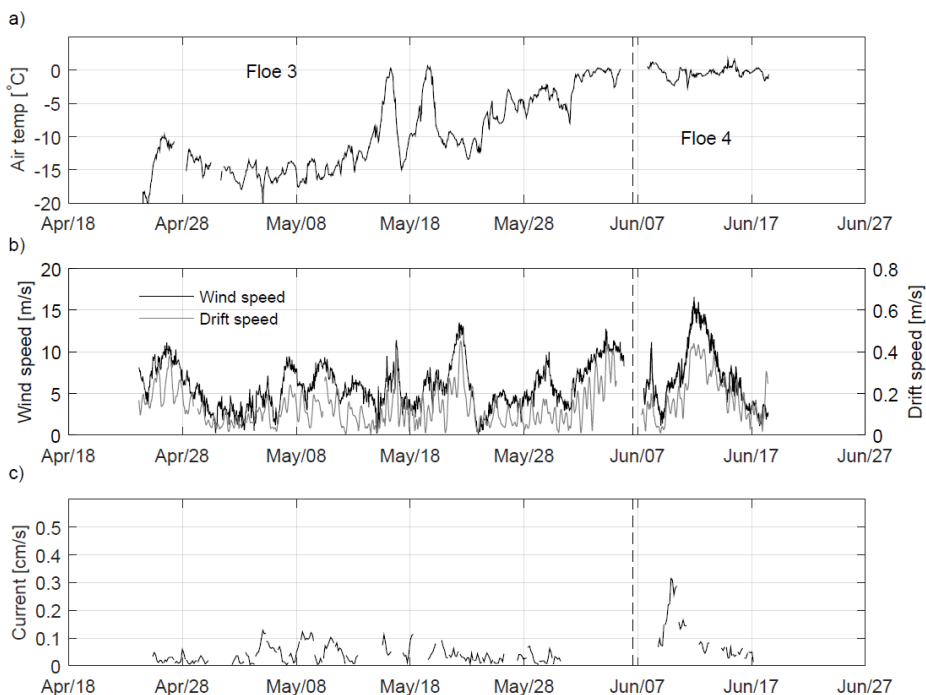


Figure 4. Hourly time series of a) air temperature b) wind and drift speeds and c) current speed. The dashed vertical line separates the data collected on Floe 3 (left side) and Floe 4 (right side).

2.3.2 Seasonal development in consolidated layer thickness and rubble macroporosity

Measurements in ridge R1-R4 showed that the consolidated layer thickness grew during the transition from the main phase to the decay phase, whereas the rubble macroporosity decreased. The rubble macroporosity in our four ridges ranged from 10% to 27% and were all measured with the same equipment. Temperature and salinity profiles in ridge R1-R4 are displayed in Figure 5.

Ridge R1 and R2, on Floe 3, were studied at the end of the main phase. In ridge R1, which was instrumented with a thermistor string, a 3-4 W/m² upwards vertical conductive heat flux through the keel was calculated, which caused cooling and growth of new ice (i.e.

0.5 m over 22 days between May 5 and May 27). The growth of the consolidated layer thickness was also estimated from repeated mechanical drilling (i.e. 0.2 m over 12 days between April 22 and June 3/4). The thickness measured by means of drilling was 2.5 ± 1.2 m (May 22) and 2.7 ± 1.4 m (June 3/4). The large standard deviation in the consolidated layer thickness estimated from drilling, was partly due to the subjective observation and partly due to the natural variation of the ice block orientation inside the consolidated layer. In ridge R2, the consolidated layer kept constant over the measurement period (i.e. 0.8 ± 0.3 m on May 24 and 0.8 ± 0.4 m on May 31). Ridges R1 and R2 were both exposed to the same meteorological-oceanic environment, but the consolidated layer thickness in R1 was greater than in R2, mainly because R1 was exposed to a larger number of freezing degree days (FDD) and formed from thicker level ice.

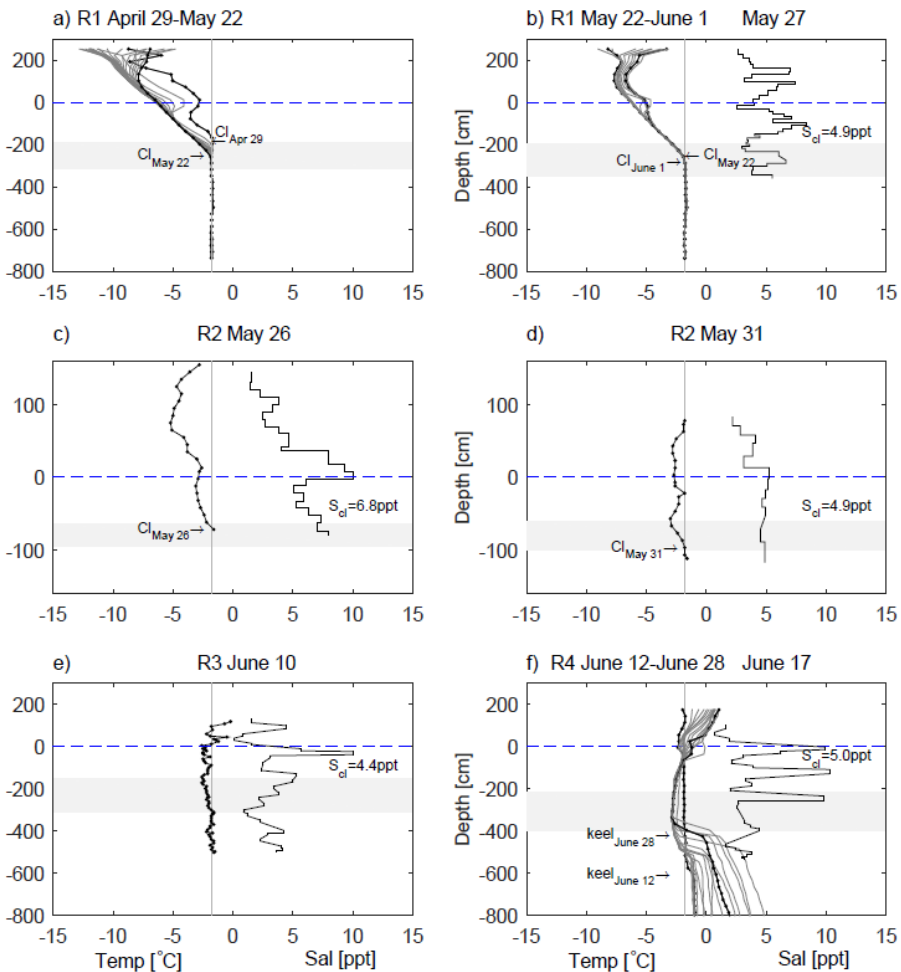


Figure 5. In situ temperature and salinity profiles.

Ridge R3 and R4, on Floe 4, were studied during the decay phase, Ridge R4 was instrumented with a thermistor string that measured temperatures over 12 days from June 12 to June 24. Over these 12 days, R4 consumed 1.83 MJ/m^2 of energy. The consolidated layer in R4 (that coincided with the keel at the position of the thermistor string) melted by approximately 1.5 m. Drilling measurements were not repeated for ridges on Floe 4, therefore consolidated layer thickness developments based on drilling were unavailable. The consolidated layer thickness in ridge R3 and R4 was $2.3 \pm 1.4 \text{ m}$ (June 10) and $3.0 \pm 1.9 \text{ m}$ (June 12), respectively.

Considerable rubble transformation occurred in R2 (rubble macroporosity decreased from 25% to 16% between May 24 and May 31), whereas little transformation occurred in R1 (macroporosity changed from 11% to 10% between May 22 and June 3/4). The different macroporosities in R1 and R2 were mainly caused by different permabilities in these ridges. The two macroporosity reducing effects explained in Shestov and Marchenko (2016a) and Shestov and Marchenko (2016b) may explain the measured macroporosity development. First, the strong non-linear specific heat capacity (Schwerdtfeger, 1962) during melting results in transformation of macro- to microporosity. This process occurs without measured temperature gradient, and in order to understand this process salinity should be measured in a future study. Second, a cyclic change in water salinity, which was caused due to the percolation of fresh meltwater would draw energy out of the rubble and contribute to further consolidation and reduction in macroporosity. Mechanical erosion, flushing, gravitational adjustments and drift-induced turbulence may also affect the ridge structure and macroporosity.

From the thermistor string in ridge R4 (Figure 5f) the rubble thickness melted completely between June 12 and June 28. Rubble macroporosity in R3 and R4 was 22% (June 10) and 27% (June 12), respectively, which were higher than those in R1 and more in line with previously reported values of 30-35% (Høyland, 2007; Leppäranta and Hakala, 1992; Leppäranta et al., 1995; Strub-Klein and Sudom, 2012).

2.3.3 Seasonal development in ice ridge strength and drilling resistance

The development in drilling resistance in R2 is displayed in Figure 6, where vertical lines represents boreholes and yellow, orange and red represents soft, medium and hard drilling resistance respectively. The gray vertical lines display voids, whereas the blue and black horizontal lines display the snow and ice surfaces, respectively. Repeated measurements of drilling hardness are places next to one another in Figure 6. In ridge R1 and R2 the drilling resistance decreased, the decrease was consistent with the temperature increase.

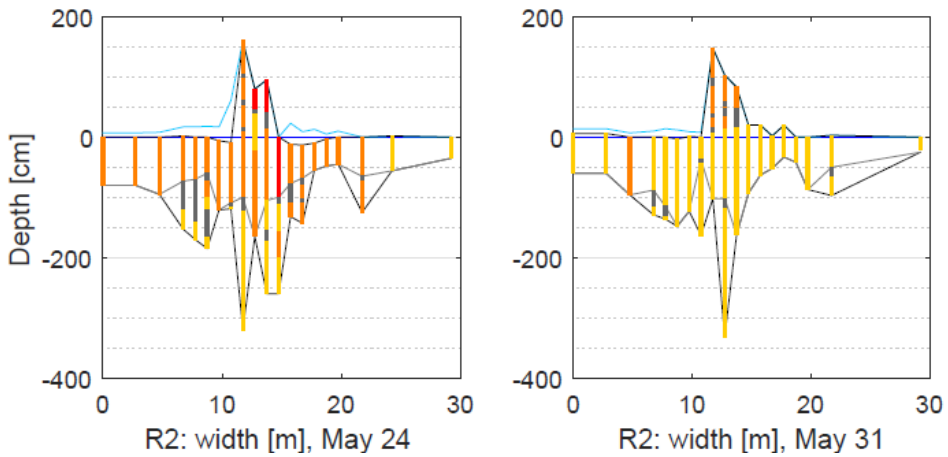


Figure 6. Cross-section drilling of ridge R2.

Small-scale uniaxial compressive field strength tests were completed in 21 samples from the sail and the consolidated layer (in R1, R2 and R3). Uniaxial compressive strength and effective modulus measured in R1 is displayed in Figure 7, where strength and effective modulus was normalized by the maximum strength measured among the ice ridge samples. The maximum uniaxial compressive strength coincided with the highest in-situ temperature measured (-6.9°C). All samples were loaded in the vertical direction of the ice sheet. Temperature and salinities were measured in separate cores, sampled a few centimeters from the core used in the strength test. In ridge R1 the temperature was obtained from thermistor string data.

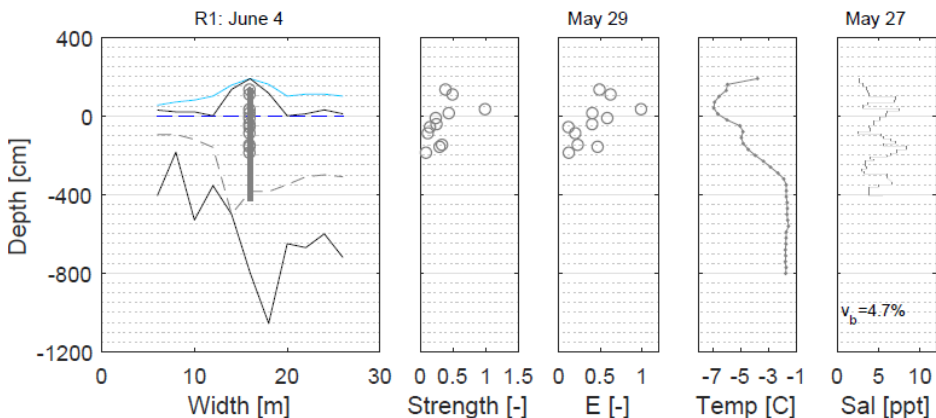


Figure 7. Vertical uniaxial compression strength, secant modulus, TS.

The average brine volumes were estimated (Cox and Weeks, 1983; Leppäranta and Manninen, 1988) under a constant density assumption of 0.881 Mg m^{-3} , which was equal to the average density measured in the R2 samples. The strength decreased until the ice temperature approached -1.8°C . For the ice samples tested on May 26 and June 13, the average temperature increased (from -5.5°C to -2.3°C) and the average brine volume increased (from 5% to 11%), whereas the average strength decreased (from $0.4 \cdot \sigma_{\text{max}}$ to $0.2 \cdot \sigma_{\text{max}}$).

The standard variation in ice strength also decreased when the ice temperature approached -1.8°C , the variation in strength is displayed in Figure 8.

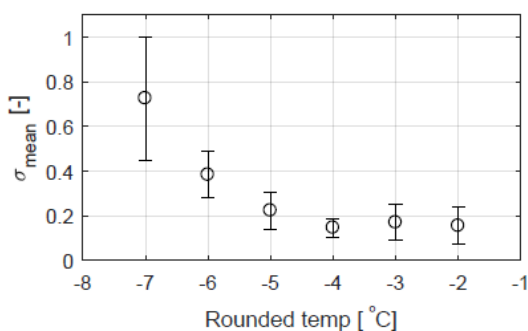


Figure 8. Mean strength with standard deviation compared to temperature rounded to the closest integer.

A similar development in borehole strength was measured by Johnston (2006), who found that the borehole strength continuously decreased until the ice became isothermal at -1.8°C . When the ice became isothermal (in July and August in the Beaufort Sea), the brine drained and was replaced by air; thus, additional radiation increased the gas pocket volumes and increased the microporosity. The increase in gas volume and microporosity was visually observed in the ice cores. Johnston (2006), further suggests that when the microporosity reaches 15-20%, the strength changes very little with increasing microporosity. Moslet (2007) showed the same pattern for the horizontal level ice uniaxial compressive strength, which is similar to the consolidated layer strength. Høyland (2007) also found uniaxial compressive strength values to level out for microporosity values above 15-20%.

All samples were ductile except the coldest and strongest sample that was brittle. Measurements presented in this study, Moslet (2007) and Johnston (2006) indicated that the decaying ice was ductile, and the strength was less dependent on brine volume (microporosity) than the strength in cold and brittle ice.

2.4 Conclusions and recommendations

Four first year ice ridges were studied in the transition from the main phase to the decay phase. The changes in consolidated layer thickness, consolidated layer strength, drilling resistance and rubble macroporosity were investigated. Based on temperature profiles in conjunction with mechanical drilling:

- The consolidated layer continued growing although being heated as long as the temperature inside the consolidated layer was low enough to consume the latent heat and the heat flux from the air.

The repeated drilling measurements showed that:

- The rubble macroporosity in the decaying saline first-year ridges decreased and reached a minimum measured rubble macroporosity of 10%. Probably the rubble macroporosity in saline ridges continuously decreases during the first year and the process accelerates during the decay phase.

A decrease in drilling resistance was observed when the in situ ice temperature increased. The ice drilling resistance varied with depth in the ridges during the main phase, whereas the drilling resistance was low through all ridge depths during the ridge decay phase. Furthermore, the decreasing trend of drilling resistance and measured uniaxial compressive strengths of the sail and consolidated layer were all in agreement.

- After the ice reached an isothermal state of approximately -1.8°C , the brine volume increased, whereas the ice strength remained almost constant.

Measuring strength in decaying ice is difficult, and more data are required to fully understand how the strength in decaying ice is affected by brine volume, especially to rule out equipment limitations.

- To understand the processes inside the rubble that occur without measured temperature gradients, salinities should be continuously measured in future investigations.

Furthermore, the currently used technique for obtaining the macroporosity is uncertain due to factors such as drill chips filling the boreholes, drill auger jams, bending of drill augers and subjective observations made by the drill operator.

- To eliminate uncertainties in measurements of macroporosity and consolidated layer thickness, more advanced measurement techniques should be explored.

How the development in consolidated layer thickness and strength affects the modes which a ridge fail and the global force the ridge transmits are studied in the following (Chapter 3). The statistical significance of ice strength is studied in Chapter 4.

Chapter 3

Full-scale high force ridge-structure interactions

The difference between cold and warm ice is clearly evident in the character of the resulting sound. Upon failure, warm ice will cause a low, muffled, steady rumble, while hard, cold ice produces a sharper, louder sound with a greater degree of randomness. - (Blenkarn, 1970)

This chapter summarizes analyses of high global force ice ridge-structure interactions measured at previously instrumented fixed structures. An overview of full-scale ridge interactions with the Molikpaq drilling platform, the Confederation Bridge piers and the Norströmsgrund lighthouse is presented in the full length paper (Appendix 3). Details on identification and classification of high global force ridge interactions with the Norströmsgrund lighthouse are presented in the full length paper (Appendix 4).

3.1 Background

The best documented full-scale fixed structures instrumented to measure forces from drifting ice (and ice ridges) include the Molikpaq drilling platform (Frederking et al., 1999; Wright and Timco, 2001), two of the Confederation Bridge piers (Brown et al., 2010; Shrestha and Brown, 2018) and the Norströmsgrund lighthouse (Poirier, 2014; Sudom and Frederking, 2014). The Molikpaq was located in the Arctic Beaufort Sea in the winters of 1984/1985 and 1985/1986 (Timco et al., 2000) The Confederation Bridge crosses the Northumberland Strait in Canada, whereas the Norströmsgrund lighthouse is located in the Gulf of Bothnia. Other instrumented structures includes Cook Inlet platforms (Blenkarn, 1970; Neill, 1976), the Baltic Kemi-1 lighthouse (Brown and Määttänen, 2009), and a few caisson structures located in the Beaufort Sea (Timco and Johnston, 2003).

The Molikpaq platform was 90 m wide at MWL and nearly vertical (with 8° inclination to the vertical) and the instrumentation included load panels, strain gauges and video footage. Because of the large width of the platform, direct failures of ice ridges onto the full width of the platform were never reported (Wright and Timco, 2001). The limit ridge building length was estimated to approximately 10 km for failure of a typical ridge across the full platform width, see Appendix 3 (Ervik, 2015). Due to the structure width, ice ridge forces at the Molikpaq were often limited by the driving or pack-ice driving forces (Wright and Timco, 2001).

The Confederation Bridge is a 13 km long bridge with conically shaped piers 14.2 m in diameter, (with 38° inclination from the vertical) with 250 m spacing. Two of the bridge piers were instrumented in 1997 with tiltmeters, an upward looking sonar and video footage (Brown and Määttä, 2009; Brown et al., 2010). Data are still being collected at the Confederation Bridge piers. Analysis have shown that during ice ridge interactions, the ice rubble does not contribute significantly to the global force and was over-estimated during the design of the bridge piers (Brown et al., 2010). Furthermore, based on 20 years of monitoring of the Confederation Bridge, the two highest peak force events were one extreme simultaneous ice ridge failure event (6.74 MN) and one ridge stalling event (>10 MN).

The Norströmsgrund lighthouse is cylindrically shaped, with diameter 7.2 m at MWL. The lighthouse was instrumented in the winters of 1999/2000-2002/2003 with load panels, tiltmeters, an upward looking sonar, an EM-antenna and video footage. Ice ridge interactions with the Norströmsgrund lighthouse were not systematically documented prior to the work presented in this thesis.

Time series of forces and responses are crucial when observations of processes at the ice-structure interface are attributed to the different modes of ice-structure interactions, e.g., ductile or brittle failure. The signatures of these different interaction modes when level ice interacts with a structure are well-established (Jordaan, 2001; Sodhi and Haehnel, 2003). Interaction mode classification was important to narrow the scope of experimental campaigns and the development of phenomenological models in the “ice-induced vibrations” community. For ice-ridge interactions, very little has been reported on the signatures in force and response, and only Bjerkås (2006), Brown et al. (2010), Ervik (2015) and Poirier (2014) have presented time series of force signatures in ridge interactions and identified ridge failure modes. However, the identified signatures in forces and responses have never been systematically associated with the type of ice ridge-structure interaction mode.

High global force ridge events were chosen in the study because they are likely to establish events that will govern the quasi-static ultimate limit state design and the high global force ridge events are required when probabilistic design methods are applied. The data collected at the Norströmsgrund lighthouse was applied in this study.

3.2 Method

3.2.1 The Norströmsgrund lighthouse

During the LOLEIF and STRICE projects (winters 1999/2000-2002/2003), ice forces were measured at the Norströmsgrund lighthouse located in the Gulf of Bothnia (N65°6.6' E22° 19.3'), 60 km southeast of Luleå in Sweden. Since 1971, year-around

navigation has been maintained in the Gulf of Bothnia, and ice-breaking activities have increased the movability of the ice in the area around the Norströmsgrund lighthouse (Engelbrektson, 1987a). The ice drift is wind-driven and predominantly along the coast in the southwesterly and northeasterly directions (Engelbrektson, 1987a). Typical level-ice conditions are 40-60 cm, but the thickness of rafted ice may exceed 1 m, and ridges are frequent. The Norströmsgrund lighthouse is a gravity-based concrete structure (displayed in Figure 9) with a diameter of 7.2 m at mean water level (MWL) and 23 m at the underwater caisson at +7.5 m elevation from the seabed (Bjerkås and Nord, 2016). The estimated MWL was + 14.5 m elevation from the seabed (Jochmann and Schwarz, 2000). The lighthouse was instrumented to measure ice forces at MWL, structural responses (accelerations and tilt), ice thickness, meteorological data and videos. A detailed description of the instrumentation is available in Bjerkås (2006), Haas (2000) and Jochmann and Schwarz (2000).

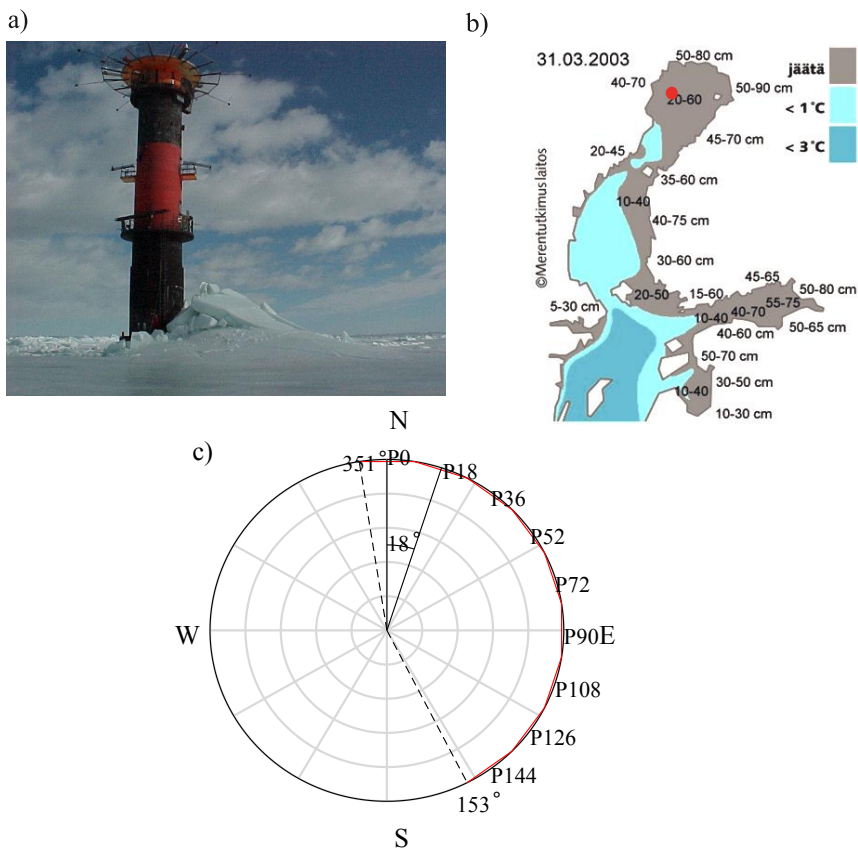


Figure 9. The Norströmsgrund lighthouse (Photo: Basile Bonnemaire, 2003 March 27); b) the Gulf of Bothnia with the position of the lighthouse marked with a red dot and ice-covered areas shaded in gray, the light blue and dark blue areas represents water at temperatures colder than +1°C and +3°C respectively (2003 March 31, FMI); c) load panel orientation.

3.2.2 Event identification and signal processing

All data files recorded during LOLEIF and STRICE were considered in this study. A program in MATLAB 2017a (The MathWorks, Inc., Natick, Massachusetts, United States) was developed to search through all data files and filter out data files based on requirements (e.g., ranges in ice thickness, acceleration and/or global panel force). The individual data file records contained time series of various length, sampling frequency and interaction modes. First, data files with a global force in excess of 3MN was filtered out. Then the ridge events were selected manually, based on a combination of global force, acceleration, ice thickness and video footage, to capture different interaction modes in which the maximum global force exceeded 3 MN. The 3 MN global force limit was applied to obtain a manageable amount of high global force data files for detailed analysis, the limit was approximately 50% of the maximum global force (~6 MN). Unfortunately, a quantifiable criteria to define event time intervals was not found, due to different sampling frequencies between measurements within the same data file (ice thickness, drift speed, global force/acceleration were sampled with different frequencies).

To classify the type of ice interaction mode, both force-time series and acceleration-time series were investigated qualitatively, similar to that described by Sodhi and Haehnel (2003) for level ice and adopted by ISO19906 (2018). Additionally, the dynamic forces was quantified. To quantify the dynamic global force (σ_{Fdyn}), the time series was filtered with a Butterworth high-pass filter with a cutoff frequency of 0.3 Hz. The cutoff frequency was chosen such that it both removed as much as practically possible of the slow-varying drift in the global force signals, and that the filter worked for a range of sampling frequencies. For the acceleration-time series, the standard deviation (σ_{Acc}) was calculated.

For more details about the methods applied, see Appendix 4 Ervik et al., 2018b.

3.3 Results and discussion

3.3.1 Ice conditions and environmental data

The ice conditions for the winters of 1999/2000-2002/2003 were mild or average winters based on seasonal FDDs, seasonal FDDs for winters of 1952/1953-2014/2015 are displayed in Figure 10a, where the horizontal dashed line displays the average seasonal FDD over the time period. Figure 10b displays the seasonal development in FDD for the winters of 1999/2000-2002/2003, where dates with high force events are displayed with circles.

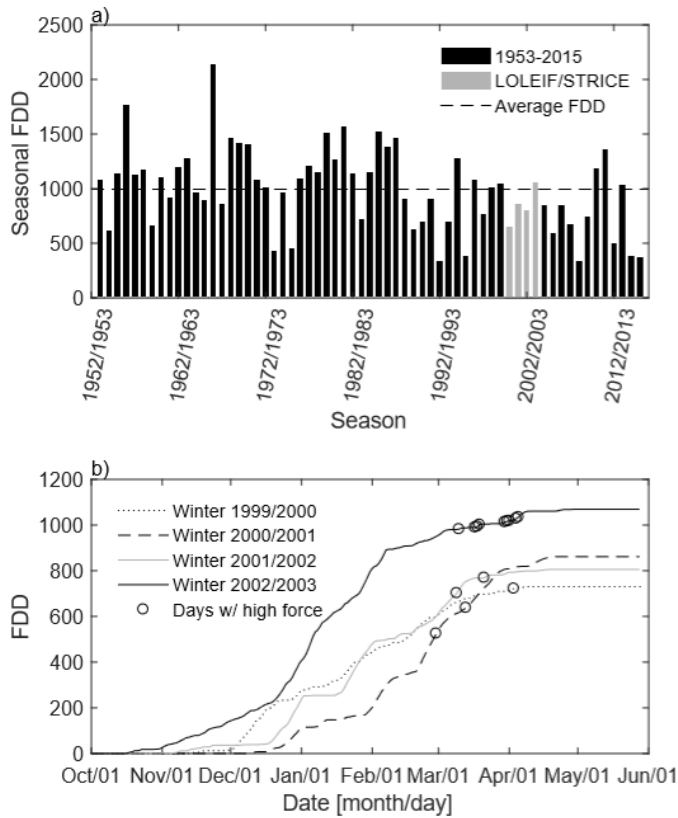


Figure 10. FDDs measured at the Rödkallen meteorological station located 23.6 km north-northeast of the Norströmsgrund lighthouse. a) Seasonal FDDs from winter 1952/1953 to 2014/2015 and b) time development in FDD for winters 1999/2000-2002/2003, where circles display days with high global force ridge events.

3.3.2 Interaction modes

During LOLEIF and STRICE, ice interacted with the Norströmsgrund lighthouse on 162 days, where 519 data files were recorded. In total, 35 ridge events with a maximum global force above 3 MN were identified, and the following three ice-ridge interaction modes were identified:

- Limit-force stalling (stalling in short);
- Limit-stress ductile failure (ductile in short); and
- Limit-stress brittle failure (brittle in short).

No intermittent or frequency lock-in ice ridge events were identified among the high global force events. The interaction modes including some measured quantities are summarized in Table 1, time series of measured quantities in a stalling -, ductile- and brittle event is displayed in Figure 11, Figure 12 and Figure 13, respectively. Figure 11- Figure 14a) time series of the global force (black line) including a seven-second average (red line) and accelerations measured at +16.5 m (light gray line) and + 37.1 m elevation (dark gray line); b) at left, the average panel force, including a blue arrow marking the wind direction; at right, the panel force distribution at the time of maximum global force, including a red arrow marking the ice-drift direction; c) time series of EM (black line) and laser (gray line) ice thickness; d) at left, the average segment force; at right, the segment force at the time of maximum global force. The water level is marked with red arrows and the text WL; e) time series of ice speed from image processing and a table with ice speed for the logbook and met-ocean data; f) time series of panel forces.

Table 1. Summary of the parameters identified for the different interaction modes.

Interaction Mode	Unit	Stalling	Ductile	Brittle
σ_{Acc}	m/s^2	0.007	0.008	0.02-0.11
σ_{Fdyn}	kN	3-14	8-27	83-203
Ice drift speed	m/s	~0	0.005-0.02	0.1-0.4
Mean air temperature	°C	-1.2	+0.8	-6.6
Mean wind speed	m/s	10.7	7.6	10.1

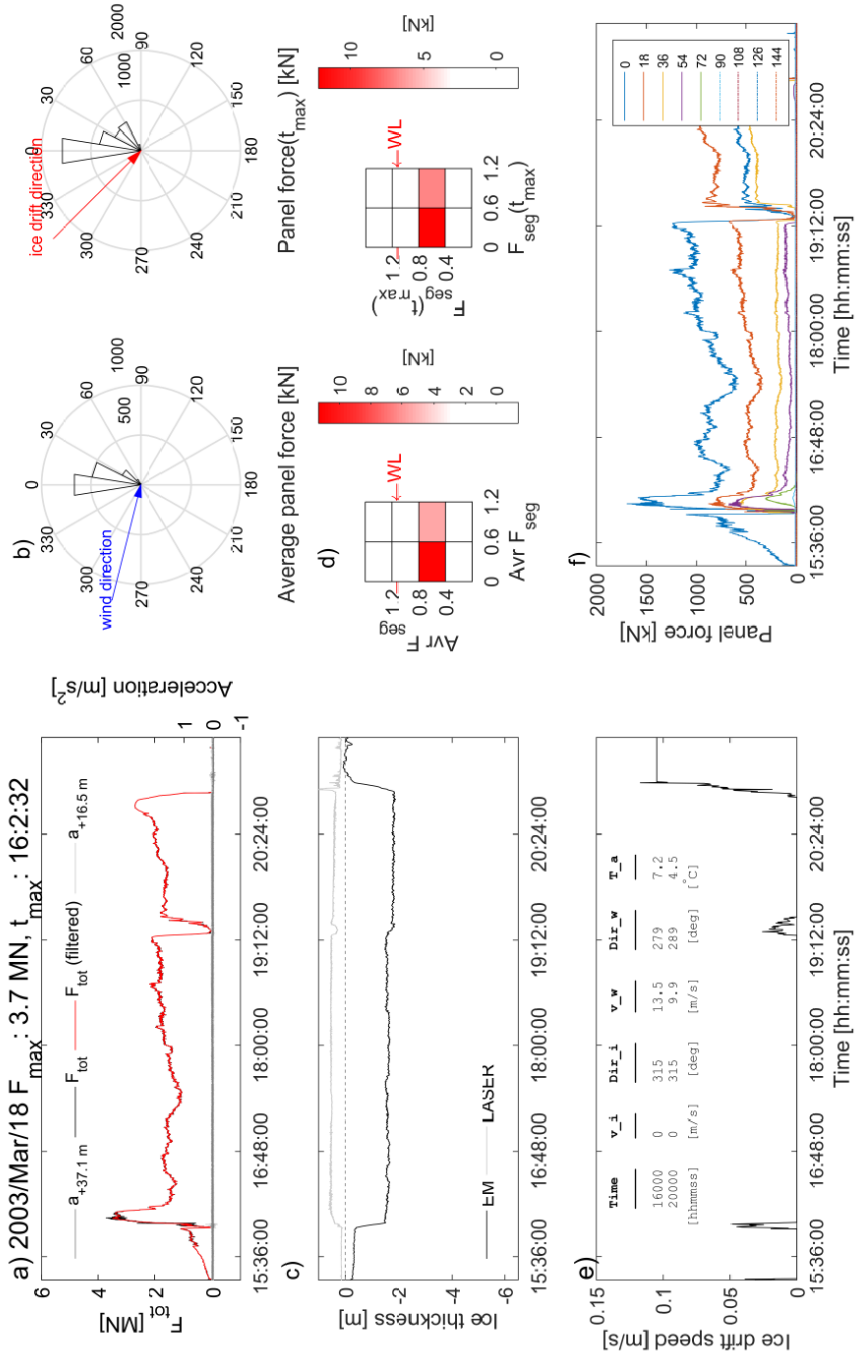


Figure 11. Time series data of a stalling event.

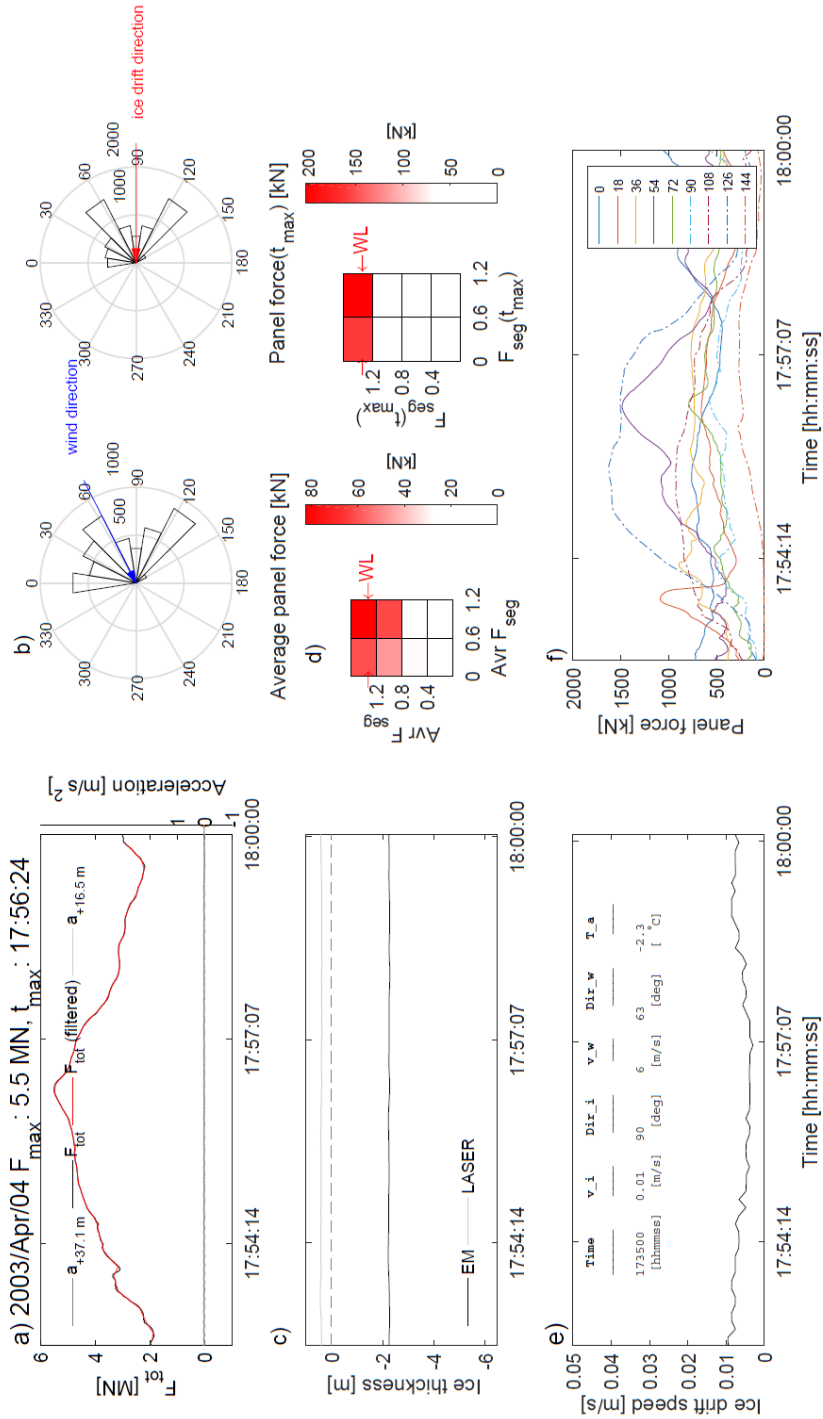


Figure 12. Time series data of a ductile event.

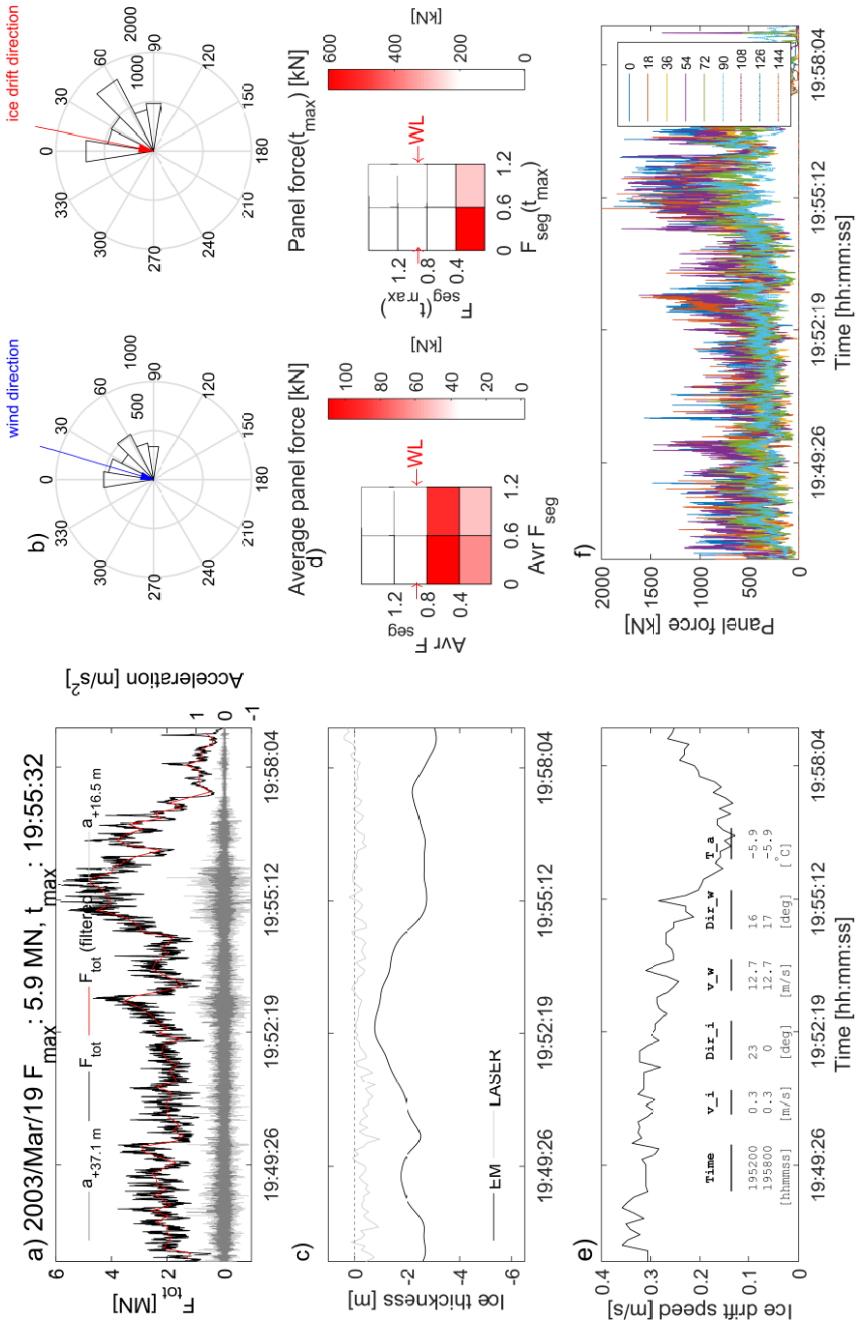


Figure 13. Time series data of a brittle event.

3.3.2.1 Limit force stalling

The dynamic force had low amplitudes during all stalling events, with $\sigma_{F_{dyn}}$ in the range 3-14 kN. The acceleration measured at +16.5 m elevation with a sampling frequency of 10 Hz was low ($\sigma_{Acc} = 0.007 \text{ m/s}^2$). The ice speed was equal to zero most of the time duration in stalling events, and the duration of these events was between 5 minutes and 6 hours. The peak global force measured during stalling events was recorded either just before the ice sheet started moving or the moment the ice sheet came to a halt. However, for the second type of stalling events (where the global force peaked the moment the ice sheet came to a halt) the force development was not always captured by the load panels because the ice sheet rotated such that the ice interacted with parts of the lighthouse not instrumented. During stalling events, the ice sheet could be stalled against the lighthouse for several hours attaining a high global force. The stalled events ended when either the ice-drift direction changed, allowing the thick ice feature to avoid the lighthouse, or a global failure occurred, e.g., cracks and splitting.

The accuracy of the ice-drift measurements was insufficient to quantify ice speeds on the order of mms^{-1} at which ice creeps (Michel and Toussaint, 1977; Sodhi and Haehnel, 2003). Among the identified high-force events, the ice interacted with the lighthouse only in stalling events from the southeast to the northwest 157.4° - 315° outside the load panel coverage (351° - 153°). In the event in Figure 9a (2003 March 26-27), a large ice ridge came to a halt and was grounded on the underwater caisson ($\sim 7 \text{ m}$ below MWL) (Bjerkås et al., 2003). Because the ice interacted with the south-southwest interface of the lighthouse (with no load panels), the event was not identified as a high-force event. The tilts measured at +22.8 m were compared between the maximum global force event (6 MN), and the grounding event on 2003 March 26-27 (Figure 9a), and the absolute maximum values were, respectively, 1.33 mrad, and 1.41 mrad. Because the events occurred within approximately one week in 2003, it is assumed that the measurement signal drift was negligible, and therefore it is likely that the stalled event on March 26-27 was also a high-force event, perhaps with global force higher than 6 MN. On the Confederation Bridge, considering all ice events with global force $> 3 \text{ MN}$, almost 55% of high global forces were measured in limit force stalling events, and the overall highest global force $> 10 \text{ MN}$ was a stalling event (Shrestha and Brown, 2018).

3.3.2.2 Limit stress ductile failure

The dynamic force had low amplitudes during all ductile events, with $\sigma_{F_{dyn}}$ in range 8-27 kN. The acceleration measured at +16.5 m elevation with a sampling frequency of 10 Hz was ($\sigma_{Acc} = 0.008 \text{ m/s}^2$), approximately the same as the acceleration for stalling events. The ice speed was 0.005-0.02 m/s, lower than for the brittle events, and the duration of these events was between 5 minutes and 2 hours. The wind velocity under these conditions was 7-8 m/s, the mean air temperature was $+0.8^\circ\text{C}$ (minimum of -2.7°C and maximum of $+4.4^\circ\text{C}$), and the ice drift was from 72° or 90° .

Level-ice ductile failure occurs at low indentation speeds, and the force signature gradually increases, reaches a peak value and decreases to a steady state value of approximately 50% of the peak force without structural vibrations (Michel and Toussaint, 1977; Sodhi and Haehnel, 2003). This classification agrees with the classification identified for ridge interactions, with the exception of the steady state force. The force signature for the ductile ridge interaction (identified in this paper) increased, attained a peak and decreased but never reached a steady state value, perhaps because of heterogeneities in the ice ridge, variations in ice drift speed or the formation of cracks. During ductile events, both the dynamic force ($\sigma_{F_{dyn}}$ 8-27 kN) and structural acceleration ($\sigma_{Acc} \sim 0.008 \text{ m/s}^2$) were low, and the interactions were thus quasi-static. The type of ice-ridge interaction was related to ice speed, where interactions with low ice speed (0.005-0.02 m/s) were ductile, whereas interactions with high ice speed (0.1-0.4 m/s) were brittle.

3.3.2.3 Limit stress brittle failure

During brittle events, the signature of the force-time series was dynamic ($\sigma_{F_{dyn}}$ 83-203 kN). The structure acceleration was larger than the structure acceleration for both ductile and stalling events, and the standard deviation of the acceleration ranged from 0.02 to 0.11 m/s^2 . The ice speed was 0.1-0.4 m/s, higher than for any other interaction mode. The ice drift was mostly from 23°, but a few events were from 0°, 45°, and 90°, and one from 180°. The duration of these events was from 1 minute to 1 hour. The wind speed was 7-14 m/s and the mean air temperature was -6.6°C (minimum of -14.4°C and maximum of -0.8°C).

During level-ice brittle failures, the interaction force attains a steady state mean value with random variations above and below the average force level (Sodhi and Haehnel, 2003). This classification of the force signature is qualitatively different from the classification presently identified for ice ridge-structure interactions. The force-time series appeared non-stationary for ridged ice (Figure 13), whereas stationary for rafted and level ice (Figure 14). There was generally a larger spread in measured quantities for brittle-ridge events than level- or rafted-ice events, noting that there was also a greater number of high-force ridge events than level- or rafted-ice events.

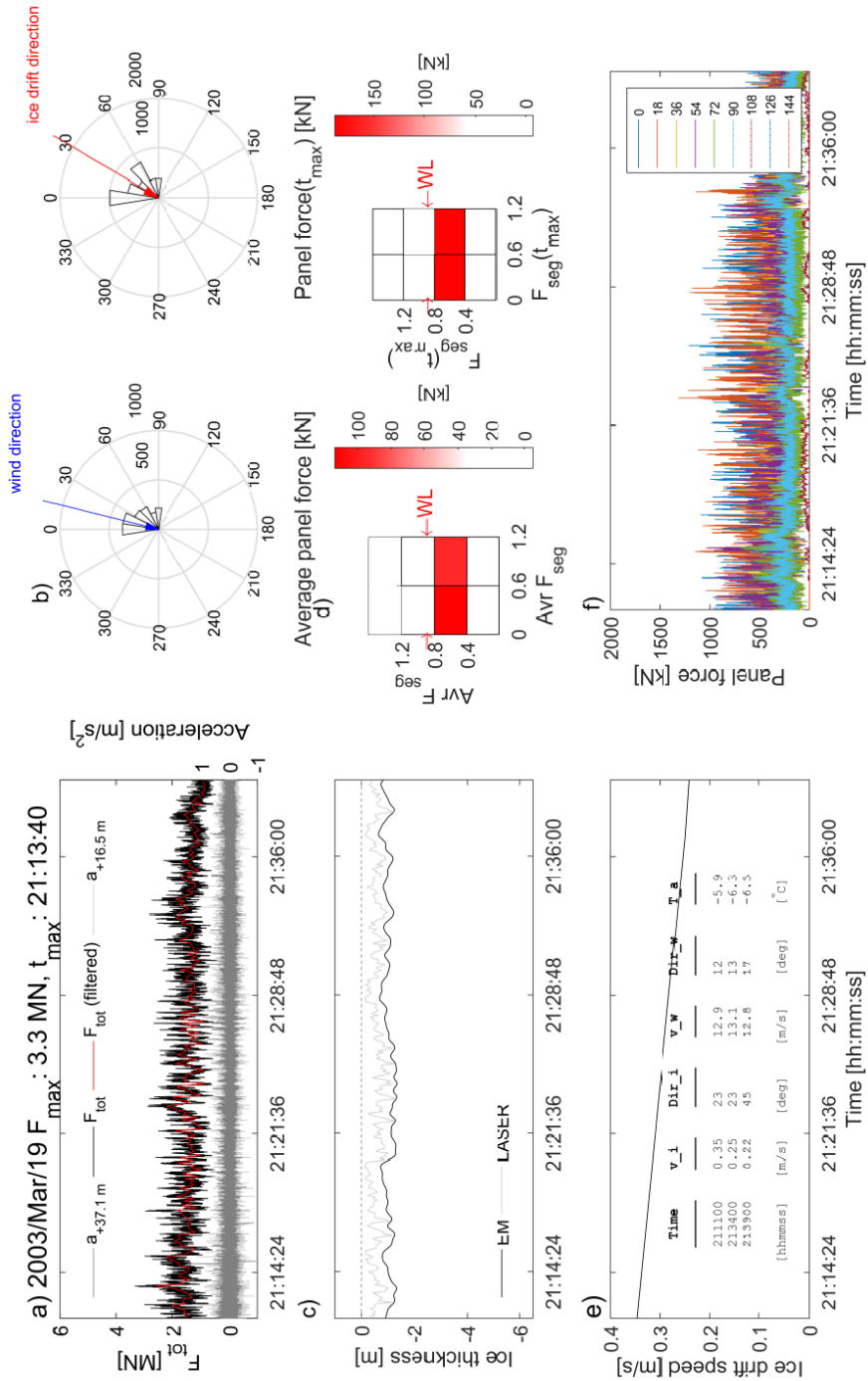


Figure 14. time series data for rafted ice brittle event.

3.3.3 Global forces and probability of exceedance

All the 35 identified high global force ridge events occurred in March and April and among the 35 events, 77% occurred in winter of 2002/2003. This may have several reasons, and probably a combination of the high number of FDD in winter of 2002/2003 compared to the winters of 1999/2000-2001/2002, the increased ice transportation in spring and the thickness of the consolidated layer. In spring, the thickness of the consolidated layer is at maximum, as shown in the previous chapter. The frequency (in per cent) of both high ice concentration (>90%) and ice ridges in the Bay of Bothnia were typically at maximum in March and April based on data from 1965-1985 (Engelbrektson, 1987a). In 2003 February 14, a global crack formed north in the Bay of Bothnia resulting in a global movement of the Baltic ice sheet of approximately 15 km until March 31 displayed in Figure 15. Assuming ice drift from the north only (and no rafting or ridge formation), Bjerckås et al. (2012) found that the daily drift past Norströmsgrund was approximately 300-350 m. However, the ice drift between February 14 and March 31 changed directions several times, such that the ice drift past Norströmsgrund was probably considerably higher and from both a northerly and southerly direction.

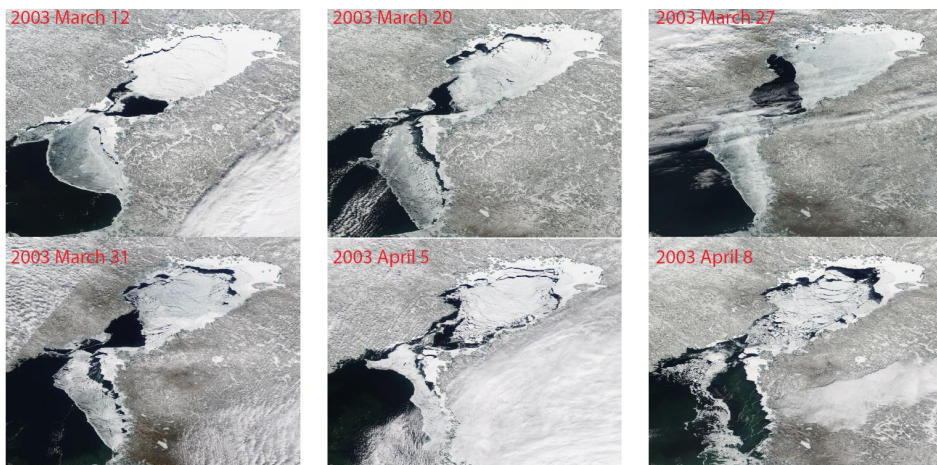


Figure 15. The ice movement in the Bay of Bothnia between 2003 March 12 and April 8. <https://worldview.earthdata.nasa.gov/> (2018)

The largest global forces were caused by the ice ridges with the largest EM ice thickness, but the global pressure decreased with increasing ice thickness and was independent of ice speed (Figure 16). Note that the maximum panel vertical length was 1.6 m, the water level varied and thus forces from thicker ice might be missed.

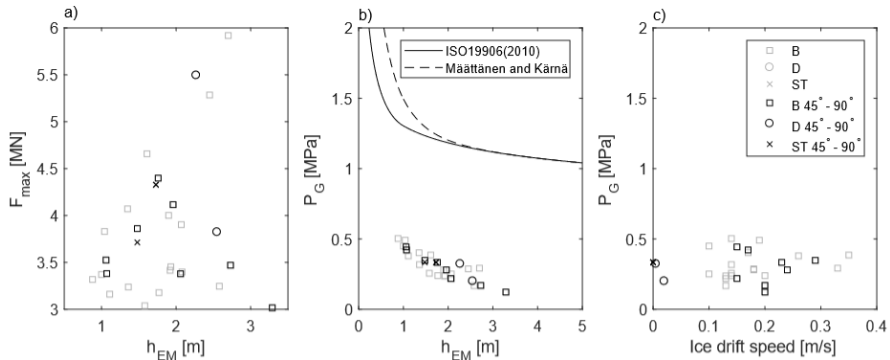


Figure 16. Global force and pressure compared to EM ice thickness and drift speed. a) Maximum force compared to ice thickness, b) global pressure compared to ice thickness, and c) global pressure compared to ice speed. B=brittle, D=ductile and ST=stalling event, 45°-90° represents events with ice drift from north to northeast.

In 7 of the 35 identified events, the ice drift was from a direction only partly covered with load panels. For these events, panel forces were mirrored with respect to the ice-drift direction on fictive load panels at the ice-structure interface. In cases where the ice came from a direction with no panel coverage (in Figure 17 b-d), the force on the panel closest to the ice-drift direction was extrapolated to the ice-drift direction and mirrored accordingly. With this technique, the maximum global force was estimated as ~9 MN for the stalling event in Figure 11. Panel force distributions are displayed in Figure 17a-g, where the black and gray panel forces represent measurements and mirroring estimates, respectively, and the blue arrows display ice-drift directions. Furthermore, two of the load panels (36° and 108°) had problems with water filling and freezing inside, and thus force components may have been missing (Kärmä and Yan, 2009).

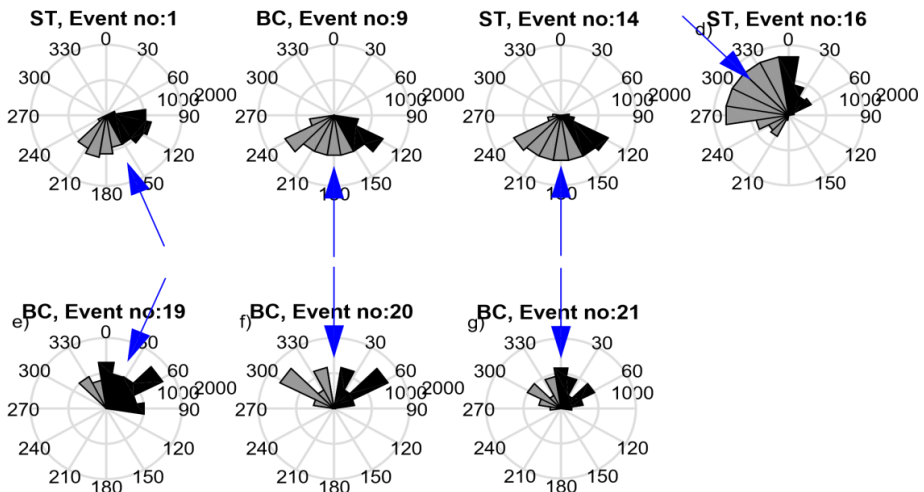


Figure 17. Force distribution with the mirroring technique. The blue arrows mark the direction of the ice drift. The black panel forces show the measurements on actual load panels, and the gray panel forces are estimated on fictive panels. ST=stalled, B=brittle events.

The probability of exceedance is displayed in Figure 18 ($i/(n+1)$), where i is the rank of the global force and n is the number of events). Figure 18 a) displays 42 identified events (including 7 level and rafted ice events) with a global panel force above 3 MN. In Figure 18b, the global force was recalculated for the 7 events displayed in Figure 17, and one can see that the maximum force increased to 9.4 MN. The global forces measured at the vertically sided lighthouse were significantly higher than those measured at the conical piers of the Confederation Bridge, with similar structural width and ice conditions. For the Confederation Bridge, the force level with a probability of exceedance of 0.1 was approximately 2 MN based on twenty years of measurements (Shrestha and Brown, 2018) compared to approximately 4.5 MN from four years of measurements at the Norströmsgrund lighthouse (Figure 18a). The number of events recorded at the Confederation Bridge was approximately 16,000/9,000 on the two piers.

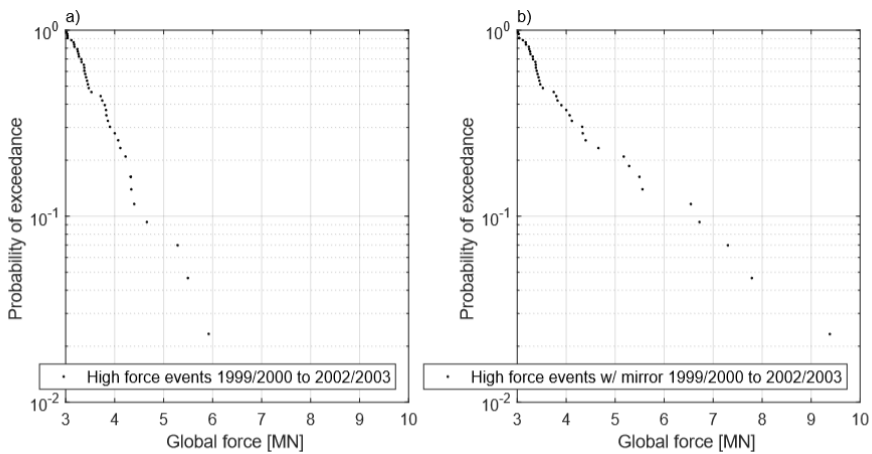


Figure 18. Probability of exceedance for events above 3 MN from four years of measurements: a) global force from instrumented panels; b) global force including fictive panel forces.

3.4 Conclusions and recommendations

All data files from LOLEIF and STRICE were analysed, and 35 ridge events with a global panel force above 3 MN were identified. In addition to 35 ridge events, 7 level and rafted ice events were identified with a global panel force above 3 MN, where ice ridge events governed the highest global forces. For the identified ridge events, the type of interaction mode was classified based on the signatures in the force and response time series as well as footage of the ice failure. The following conclusions were drawn:

- Three types of ice-ridge interaction modes were identified ordered by increasing ice speed: 1) limit-force stalling events, 2) limit-stress ductile events, and 3) limit-stress brittle events. All of these interaction modes potentially gave a high global force and were associated with high forces occurring simultaneously across the lighthouse.
- Frequency-lock in and intermittent crushing was not observed during high force ridge events.
- The overall maximum global force was ~6 MN, but because of instrumentation limitations, the global forces were under-predicted.
- 77% of the high force ridge events occurred in the winter of 2002/2003, with the highest seasonal FDD compared to the winters 1999/2000-2001/2002.
- All high force events occurred in spring (March and April) when the ice transportation and consolidated layer thickness was at seasonal maximum, despite the strength of the ice decreasing compared to the winter (cf. Chapter 2).

At the Norströmsgrund lighthouse, ice rubble forces were not measured due to the limited load panel coverage. For future instrumentation of similar full-scale structures capable of also measuring rubble forces, the following is suggested:

- Necessary instrumentation includes accelerometers and inclinometers or strain gauges. For accurate tilt and acceleration measurements, instruments need repeated zeroing and calibration. The sampling frequency should be constant for all measurements and sufficient to capture dynamic modes of interaction.

Acceleration and tilt or strain measurements, when repeatedly calibrated, are sufficient to determine both global forces and responses and to classify the type of interaction mode. Load panels are expensive, have limited coverage, only measure normal forces, and can break.

Because of the limited vertical extent of the load panels the rubble forces were probably not measured at the Norströmsgrund lighthouse. The highest global forces were measured in simultaneous failure of the consolidated layer with high contact areas. The high force ridge events were quasi-static, and ice-induced vibrations were absent. In Chapter 4 a plasticity based model is used to simultaneous failure of consolidated ice and to study the significance of parameters in the ice-structure interactions.

Chapter 4

Numerical modelling of ductile consolidated ice interactions

Essentially, all models are wrong, but some are useful. - (Box and Draper, 1987)

This chapter summarizes numerical simulations of ductile consolidated ice interactions with fixed structures. An isotropic, pressure dependent material model is applied in simulations of a medium-scale ductile ice-structure interactions presented in the full-length paper (Appendix 5). The same material model is applied in simulations of ductile ice interactions with the Norströmsgrund lighthouse and the medium-scale JOIA experiment, where effects of parameters in the ice-structure interactions are presented in the full-length paper (Appendix 6).

4.1 Background

At the Norströmsgrund lighthouse, the highest quasi-static global forces were measured during simultaneous failures in ice-ridge interactions (Ervik et al., 2018b). In the medium-scale indentation tests under the sponsorship of the Japan Ocean Industries Association (JOIA) (Saeki et al., 1997; Sodhi et al., 1998), the highest global forces occurred during ductile interactions. These events occurred without any significant structural vibrations, so the purpose of the proposed model is to predict quasi-static design forces in cases for which the dynamic response of the structure is not of interest.

Because of limited instrumentation at the Norströmsgrund lighthouse, the peak global forces were underestimated (Ervik et al., 2018b). A numerical model is a supplement to field experiments where both global and local forces as well as responses can be studied, without issues related to instrumentation. In numerical models, the ice properties and boundary conditions can be controlled and thus effects of aspect ratio, structural shape and strength heterogeneities can be studied.

At the Norströmsgrund lighthouse, the measured global forces were most probably caused by the consolidated layer in ice ridges (Ervik et al., 2018b). The consolidated layer consists of solid ice, and the structure and strength of the consolidated layer is typically more isotropic than level ice (Høyland, 2007). Furthermore, in the JOIA data the level ice was composed of an almost even layer of granular snow-ice and columnar sea ice which was more isotropic than columnar level ice (Ushikoshi et al., 2001). These observations support the use of an isotropic model.

In addition to the Norströmsgrund lighthouse and the JOIA experiment, a medium-scale indentation experiment in the Van Mijen Fjord on Svalbard, was modelled. The Van Mijen Fjord experiment was level ice indentation with a cylindrical indenter. The purpose of modelling this experiment, was to compare the measurements at the Norströmsgrund lighthouse to this simple medium-scale indentation experiment. Unfortunately, the stiffness of the ice-structure system was too soft to keep a constant ice indentation speed, because the ice sheet was towed against the indenter with a series of chains and wires. The system setup made it difficult to separate the ice response from the system response, for details see Appendix 5 Ervik et al., 2017.

The two main classes of existing numerical models are continuum and discrete models. Discrete element models (DEM) have been applied in simulations of interactions between rigid ice fragments, handled by contact models (Hopkins, 1992). DEM is used in simulations including discontinuities such as in interactions between discrete ice blocks in ice rubble (Polojärvi and Tuhkuri, 2009). DEM has also been applied to study the formation and deformation of ice rubble and rubble piles (Tuhkuri and Polojärvi, 2018). The contact force laws used in DEM are relatively simple, however they often include parameters without any physical interpretation. Contrarily, continuum finite element models (FEM) are formulated based on the constitutive behaviour of the material. In simulations where discontinuities are absent, such as during ductile ice deformation, FEM is preferred to DEM. In this part of the thesis ductile deformations are simulated with an elastic-plastic FEM and the simulation results are used to study effects of aspect ratio, structure shape and strength heterogeneities.

4.2 Material strength and models

4.2.1 The finite element elastic-plastic stiffness matrix

The required mathematical relationships between stress and strain (constitutive equations) necessary to obtain the elastic-plastic stiffness matrix are presented in the following. All equations are expressed in matrix notation. Eq. (1) presents the strain decomposition equation.

$$d\boldsymbol{\varepsilon} = d\boldsymbol{\varepsilon}^e + d\boldsymbol{\varepsilon}^p, \quad (1)$$

where $d\boldsymbol{\varepsilon}$, $d\boldsymbol{\varepsilon}^e$ and $d\boldsymbol{\varepsilon}^p$ denotes the 6×1 vector of the total, elastic and plastic strain, respectively. Eq.(2) is Hooke's law.

$$d\boldsymbol{\sigma} = \mathbf{D}d\boldsymbol{\varepsilon}^e, \quad (2)$$

where $\boldsymbol{\sigma}$ denotes the 6×1 stress vector and \mathbf{D} denotes the 6×6 elastic stiffness matrix, which is expressed through the elastic modulus E and the Poisson's ratio ν for an isotropic linearly elastic material. Eq. (3) is the plastic flow rule.

$$d\boldsymbol{\varepsilon}^p = d\lambda \frac{\partial Q}{\partial \boldsymbol{\sigma}}, \quad (3)$$

where $d\lambda$ denotes the plastic multiplier and Q denotes the plastic flow potential (hereafter flow potential). Eq. (4) expresses the development of the yield function called the hardening rule.

$$d\mathbf{\kappa} = d\lambda \mathbf{h}(\boldsymbol{\sigma}, \boldsymbol{\kappa}, \lambda), \quad (4)$$

where $\boldsymbol{\kappa}$ denotes a set of state variables either scalar or vector and $\mathbf{h}(\boldsymbol{\sigma}, \boldsymbol{\kappa}, \lambda)$ expressed the evolution of the yield function. The elastic limit (yield criteria F) is expressed in Eq. (5).

$$\begin{aligned} F < 0, \quad d\boldsymbol{\varepsilon}^p = 0 \\ F = 0, \quad d\boldsymbol{\varepsilon}^p > 0 \end{aligned} \quad (5)$$

The final equation required to obtain the plastic multiplier and the stiffness matrix, is called the consistency condition, which comes from the condition than $F=0$ during plastic deformation. Eq. (6) expresses the consistency condition.

$$\left\{ \frac{\partial F}{\partial \boldsymbol{\sigma}} \right\}^T d\boldsymbol{\sigma} - A d\lambda = 0, \quad (6)$$

where A denotes the plastic resistance number expressed in Eq. (7).

$$A = - \left\{ \frac{\partial F}{\partial \boldsymbol{\kappa}} \right\}^T \frac{d\boldsymbol{\kappa}}{d\lambda} = - \left\{ \frac{\partial F}{\partial \boldsymbol{\kappa}} \right\}^T \mathbf{h}(\boldsymbol{\sigma}, \boldsymbol{\kappa}) \quad (7)$$

By combining Eqs. (1-7), the plastic multiplier is expressed in Eq. (8).

$$d\lambda = \frac{\left\{ \frac{\partial F}{\partial \boldsymbol{\sigma}} \right\}^T \mathbf{D}}{A + \left\{ \frac{\partial F}{\partial \boldsymbol{\sigma}} \right\}^T \mathbf{D} \frac{\partial Q}{\partial \boldsymbol{\sigma}}} d\boldsymbol{\varepsilon} \quad (8)$$

Finally, by combining Eq. (1), (2), (3) and (8) the stiffness matrix is expressed in Eq. (9).

$$\mathbf{D}^{ep} = \mathbf{D} - \frac{\mathbf{D} \left\{ \frac{\partial Q}{\partial \boldsymbol{\sigma}} \right\} \left\{ \frac{\partial F}{\partial \boldsymbol{\sigma}} \right\}^T \mathbf{D}}{A + \left\{ \frac{\partial F}{\partial \boldsymbol{\sigma}} \right\}^T \mathbf{D} \left\{ \frac{\partial Q}{\partial \boldsymbol{\sigma}} \right\}}, \quad (9)$$

where \mathbf{D}^{ep} denotes the elastoplastic stiffness matrix. If the material is perfectly plastic, F is independent of $\boldsymbol{\kappa}$ and $A=0$, and if the material follows the normality condition (typical for metals) the flow rule is associated, and $F=Q$.

4.2.1.1 Yield surface

The constitutive model is essential in a FEM, and particularly the yield function. Triaxial compressive strength measurements (displayed in Figure 19) show that the deviatoric ice strength is pressure dependent (Gagnon and Gammon, 1995; Jones, 1982; Riska and Frederking, 1987; Rist and Murrell, 1994). The strength displayed in Figure 19 was tested at strain rate 10^{-3} s^{-1} and the ice texture was granular/discontinuous columnar (polycrystalline, iceberg and multi-year sea ice). Several pressure dependent ice yield

functions exists, a selection of the most frequently used yield functions is presented in Table 2.

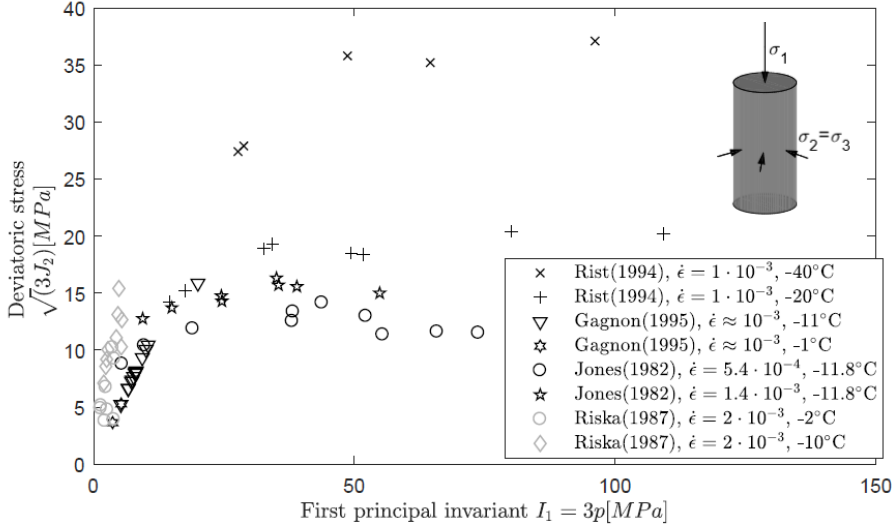


Figure 19. Multi-axial compression data, strain rate $\sim 10^{-3} \text{ s}^{-1}$. The references (Rist and Murrell, 1994), (Riska and Frederking, 1987) and (Gagnon and Gammon, 1995) was shorted to Rist (1994), Riska(1987) and Gagnon (1995), respectively. The Jones (1982) data was obtained by digitalization of images.

In this thesis, the pressure dependent yield function presented by Lubliner et al. (1989) is applied, available in ABAQUS 6.13, which is similar to the Pariseau (1968) yield function, but is extended to also fit the tensile strength, and is given in Eq. (10).

$$F(\boldsymbol{\sigma}) = \frac{1}{1-\alpha} \left(\sqrt{3J_2} - \alpha \cdot I_1 + \beta \cdot \langle -\hat{\sigma}_{\min} \rangle \right) - \sigma_c \quad (10)$$

, where $\alpha = \frac{\sigma_{b0} - \sigma_{c0}}{2\sigma_{b0} - \sigma_{c0}}$, $\beta = \frac{\sigma_c}{\sigma_t} \cdot (1-\alpha) - (1+\alpha)$ and the operator $\langle -\hat{\sigma}_{\min} \rangle$ is defined as

$\langle -\hat{\sigma}_{\min} \rangle = \frac{1}{2} (\hat{\sigma}_{\min} - \text{abs}(\hat{\sigma}_{\min}))$, which is non-zero in the tensile part of the yield function only.

Table 2. Yield functions including the number of required strength parameters and a sketch of the yield function, $\sqrt{3J_2}$ compared to I_1 .

Yield function:	Strength parameters	Sketch of the yield function
Von Mises: $F(J_2) = \sqrt{3 \cdot J_2} - \sigma_c$	Anisotropic: - Isotropic: 1	
Extended von Mises, (Pariseau, 1968): $F(\boldsymbol{\sigma}) = a_1(\sigma_{11} - \sigma_{22})^2 + a_2(\sigma_{11} - \sigma_{33})^2 + a_3(\sigma_{22} - \sigma_{33})^2 + a_4\sigma_{12}^2 + a_5\sigma_{23}^2 + a_6\sigma_{13}^2 + a_7\sigma_{11} + a_8\sigma_{22} + a_9\sigma_{33} - 1$	Anisotropic: 9 Isotropic: 2	
Extended von Mises, Smith (1974): $F(\boldsymbol{\sigma}) = A(\sigma_{11} - \sigma_{22})^2 + B(\sigma_{11} - \sigma_{33})^2 + U(\sigma_{22} - \sigma_{33})^2 + H\sigma_{12}^2 + K\sigma_{23}^2 + L\sigma_{13}^2 - (M\sigma_{11} + N\sigma_{22} + P\sigma_{33}) - (R\sigma_{11} + S\sigma_{22} + V\sigma_{33})^2 - 1$	Anisotropic: 12 Isotropic: 3	
Teardrop model, Nadreau and Michel (1986): $F(\boldsymbol{\sigma}) = a_{10}(\sigma_{11} - \sigma_{33})^2 + a_{11}(\sigma_{33} - \sigma_{11})^2 + a_{12}(\sigma_{11} - \sigma_{22})^2 + a_{13}\sigma_{12}^2 + a_{14}\sigma_{23}^2 + a_{15}\sigma_{13}^2 + a_{16}\sigma_{11} + a_{17}\sigma_{22} + a_{18}\sigma_{33} + (a_{19}\sigma_{11} + a_{20}\sigma_{22} + a_{21}\sigma_{33})^2 + (a_{22}\sigma_{11} + a_{23}\sigma_{22} + a_{24}\sigma_{33})^3 - 1$	Anisotropic: 15 Isotropic: 3	
Tsai-Wu model (failure function not yield function): $F(J_2, I_1) = \chi I_1^3 + \xi I_1^2 + \zeta I_1 + \omega J_2 - 1$	Anisotropic: 27 Isotropic: 3	
Extended von Mises, Lubliner et al. (1979): $F(\boldsymbol{\sigma}) = \frac{1}{1-\alpha} \left(\sqrt{3J_2} - \alpha \cdot I_1 + \beta \cdot \langle -\hat{\sigma}_{\min} \rangle \right) - \sigma_c$	Anisotropic: - Isotropic: 3	

4.2.1.2 Flow rule

In addition to the yield function, the flow potential is also required to formulate the elastic-plastic stiffness matrix. Pressure dependent materials such as rock/soil/concrete dilate i.e. they disobey the normality condition. According to the normality condition, the plastic flow is normal to the yield surface, and the flow potential is associated i.e. identical to the yield function. Measurements presenting dilatancy (volumetric expansion) or generally triaxial strain measurements in ice are rare, however Dorris (1991) presents

both stress and strain measured in multiyear Arctic sea ice, and showed that ice dilates, where the dilatancy increased with increasing strain rate and decreasing pressure (I_1). The dilatancy is described via a parameter called the dilatancy angle. For rocks and concrete, the dilatancy angle (ψ) is typically in the range 10° to 20° at low to moderate pressure (I_1) (Alejano and Alonso, 2005; Vakili, 2016; Vermeer, 1998).

The significance of dilatancy is studied though the non-associated flow rule with flow potential given in Eq. (11) that is expressed though the dilatancy angle ψ , available in ABAQUS 6.13. The dilatancy angle is varied in the range (10° - 20°), and the significance is quantified by means of two-level factorial design of experiments (in Section 4.4.1).

$$Q(\sigma) = \sqrt{(\sigma_1 \tan \psi)^2 + 3J_2} - \frac{I_1}{3} \tan \psi \quad (11)$$

4.3 Experimental data

4.3.1.1 The medium-scale JOIA data

The ice in JOIA experiment was first-year level sea ice (the mean salinity in 1998 was 5.5‰ from 139 samples) with ice thickness of approximately 0.2-0.4 m and the ice crystal structure was a mixture of granular and columnar (Ushikoshi et al., 2001). A stiff vertically sided flat indenter was pushed against the level ice at constant indentation speed. The indenter was instrumented with load cells, displacement transducers, an accelerometer and an inclinometer, for details about the instrumentation see papers presented by Sodhi et al. (1998), Saeki et al. (1997) and Sakai et al. (1998).

The events considered were measured in 1998 and 1999, where the indenter width and height was equal to 1.5/0.6 m and 0.4 m respectively, the indentation speed was constant equal to 0.0003 ms^{-1} , for which the type of ice failure mode was ductile deformation (Sodhi et al., 1998). In addition to global and local forces, ice properties were measured including; density, salinity, uniaxial compressive strength (averaged for each day) and tensile splitting strength was occasionally measured (Kamio et al., 2000; Matsushita et al., 1999). Material properties are summaries in Table 3.

4.3.1.2 The full-scale Norströmsgrund lighthouse data

See Appendix 4 or Section 3.2.1 in this thesis for details about the Norströmsgrund lighthouse and instrumentation, some additional information about the considered data, is provided here. The maximum level ice thickness in 2003, estimated from the number of freezing degree days (FDD), was 0.71 m (Li et al., 2016). Strub-Klein and Sudom (2012), found that in the Baltic Sea the maximum ratio of the consolidated layer to level ice thickness was 1.84. Accordingly, assuming that the level ice thickness was 0.71 m, the maximum consolidated layer thickness was estimated to 1.3 m. This is considered a conservative estimate. Ice thickness was measured with an EM antenna at the

Norströmsgrund lighthouse, however for ice ridges, the EM antenna underestimated the maximum keel depth and overestimated the consolidated layer thickness (Ervik et al., 2018b; Haas, 2017). The maximum global force measured at the Norströmsgrund lighthouse was ~6 MN measured during simultaneous failure, but due to limited load panel coverage the global force might have reached ~9 MN during a stalling event, see Appendix 4 (Ervik et al., 2018b). Material properties are summaries in Table 3.

Table 3. Measured ice properties in the JOIA experiment in both 1998 and 1999, in the Van Mijen Fjord experiment and at the Norströmsgrund lighthouse. In the JOIA experiment ice properties (except tensile strength) were measured daily, in the van Mijen Fjord ice properties were measured for each test, whereas at Norströmsgrund lighthouse ice properties were measured 2003 March 20. σ_c measured at $T=-3^\circ\text{C}$, and $\dot{\epsilon}=10^{-3}\text{s}^{-1}$, except at Norströmsgrund, where at $T=-1^\circ\text{C}$, and $\dot{\epsilon}=0.5\cdot 10^{-3}\text{s}^{-1}$.

Parameter	Unit	JOIA		Norströmsgrund
		1998	1999	2003
ρ_i	kg/m^3	857	849	894
S_i	‰	6.1	2.6	0.7
h_i	m	0.254	0.357	1.3
T	$^\circ\text{C}$	-2.1	-	-0.5
T_{air}	$^\circ\text{C}$	-	-4.8	-6.7
E	GPa	-	-	4.8
ν	-	-	-	-
σ_c	MPa	1.04 (0.27-1.4)	1.6 (0.57-3.27)	3.2 (2.0-5.0)
σ_t	MPa	$0.16 \cdot \sigma_c$	$0.16 \cdot \sigma_c$	0.59-2.23
Structure width	m	1.5	0.6	7.2
Peak F_{global}	MN	0.34	0.36	6/9

4.4 Methods

4.4.1 Two level factorial design of experiments

Two level factorial design of experiments (2^k DOE) is a statistical tool used to determine the statistical significance of factors in an experiment (here numerical model). In 2^k DOE, a given set of factors (here material properties) are varied in combination to investigate how the different factors and combination of factors affect an output response (here the peak global force). Each factor is given two levels one “low” and one “high” level. The combination of the “low” and “high” values for the different factors produces 2^k number of experiments, where k is the number of factors. The benefit of 2^k factorial compared to one-factor-at-a-time (OFAT) DOE, is that the 2^k factorial DOE considers the interaction between the different factors. Interactions between factors are very common, and if they occur, the OFAT produces poor results (Montgomery, 2013).

Presently, where factors represent material properties and experiments represent simulations, six elastic-plastic material properties are considered, provided in Table 4. The simulation setup consists of a rigid indenter and deformable ice where the global force on the rigid indenter is the output, for details see Appendix 6.

Table 4. Factors in 2^k factorial DOE, low and high value for each factor.

Parameter	Unit	Factor	Low	High
σ_c	MPa	A	1	10
σ_t / σ_c	-	B	0.05	0.15
σ_b / σ_c	-	C	1.2	2
E	GPa	D	1	10
ν	-	E	0.2	0.4
ψ	°	F	10	20

The effect of each factor on the output response is calculated. The effects are t-statistics that test the null hypothesis that the effect is zero. Positive effects increase the response (peak global force) when the settings change from the low value of the factor to the high value. Negative effects decrease the response (peak global force) when they change from the low value of the factor to the high value of the factor. The effects that are not significant are normally distributed, with mean zero and variance (STD^2), whereas significant effects will have nonzero means. (Montgomery, 2013).

The statistical software Minitab 18.1 (Minitab Inc., State College, Pennsylvania, United States) was used to make the setup and to analyze the results.

4.4.2 Simulation matrix

The simulation matrix including important ice properties for a selection of the JOIA and the Norströmsgrund lighthouse simulations are provided in Table 5. For details about the simulation setup, and additional simulations, see Appendix 6.

Table 5. Simulation matrix. *mean value (minimum- maximum)

Simulation identity	σ_t	σ_b/σ_c	σ_c	h_i	Indenter/lighthouse width/diameter
Unit	MPa	-	MPa	m	m
JOIA98L	0.16 σ_c	1.1	1.04	0.25	1.5
JOIA99L	0.16 σ_c	1.1	2.6	0.36	0.6
JOIA99H	0.16 σ_c	1.1	1.6(0.57-3.27)*	0.36	0.6
JOIA99VM	1.6	-	1.6	0.36	0.6
NSGL	0.59	1.1	2.0	1.30	7.2

4.5 Results and discussion

4.5.1 The significance of material properties

The normal probability plot displayed in Figure 20 shows which factors and combination of factors that are statically significant. Significant factors include A, B, AB, F, C, AF, ABC, BC, AC, AD, where factor names are provided in Table 4 and in Figure 20. Effects further from 0 on the x-axis have greater magnitude and are more statistically significant. The three most statistically significant factors and combination of factors were the uniaxial compressive strength (A), the ratio of the uniaxial compressive/tensile strength (B) and the combination AB. Among the main factors, the poissons ratio (E) and elastic modulus (D) were not significant to the global force, whereas the combination of the uniaxial compressive strength and the elastic modulus (AD) was the least significant effect (among the significant effects).

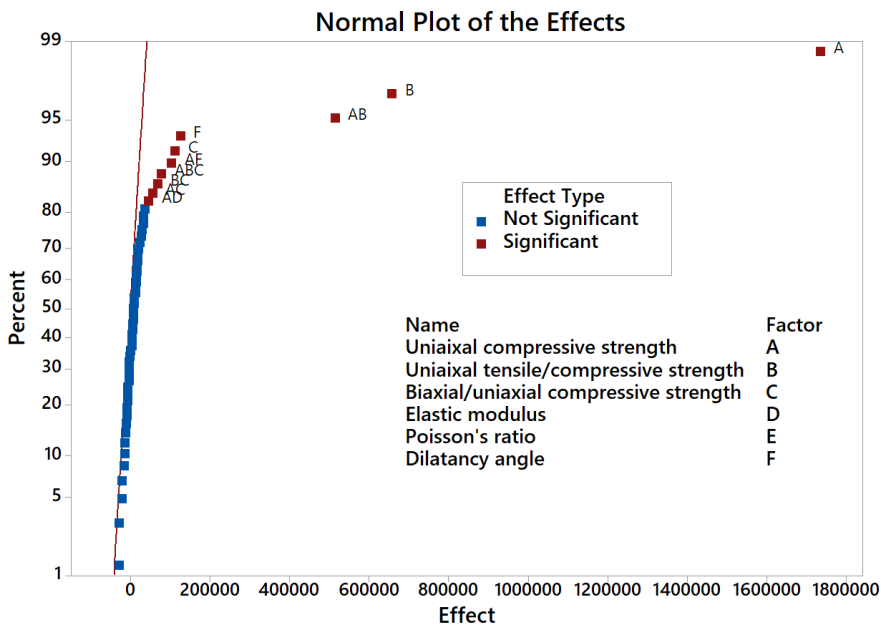


Figure 20. Normal plot of the effects, the red line shows the effects that are normally distributed with zero mean and variance (STD^2).

Among the strength properties the uniaxial properties were most significant. On one hand, this is beneficial because uniaxial strengths are among the ice properties that are typically measured in field experiments. On the other hand, uniaxial strengths vary significantly in naturally grown sea ice. The variation in uniaxial compressive strength depends on at least ice temperature and strain rate. The uniaxial compressive strength measured in decaying ice presented in Chapter 2 showed that the strength was almost constant when

the ice temperature exceeded approximately -3°C or when microporosity reached 15-20%, whereas for colder ice the strength varied more.

The dilatancy angle, which is the ratio between the volumetric and deviatoric strain was also significant to the global force. Few measurements report strains, and thus little is known about the dilatancy in ice. It is suggested that the dilatancy should be studied further and that it probably is a function of both temperature, confinement and strain rate as also suggested by Dorris (1991). It is expect that the ice dilates more under low degree of confinement, because cracks can form and open freely, whereas under high confinements crack formation and frictional sliding is suppressed.

4.5.2 Effect of aspect ratio on the global force

Results of peak global forces (F_{global}) and effective pressures (P^{eff}) in the simulation setup in Table 5 are presented in Table 6. The stress state was studied in nodes at the ice/structure contact in nodes displayed in Figure 21.

Table 6. Simulation results, including measured results(labeled data).

Results	Peak F_{global}	P^{eff}	h_i	Indenter width
Unit	MN	MPa	m	m
JOIA98L	0.46	1.20	0.25	1.5
JOIA98H	0.38	0.98		
Data 98	0.34 (0.17-0.49)	0.97 (0.60-1.54)	0.25 (0.18-0.29)	1.5
JOIA99L	0.56	2.59	0.36	0.6
Data 99	0.36(0.28-0.39)	1.67(1.38-1.81)	0.36 (0.34-0.37)	0.6
NSGL	25	2.67	1.3	7.2
NSGH	11	1.18	1.3	7.2
Data NSG	~6(9)	-	-	7.2

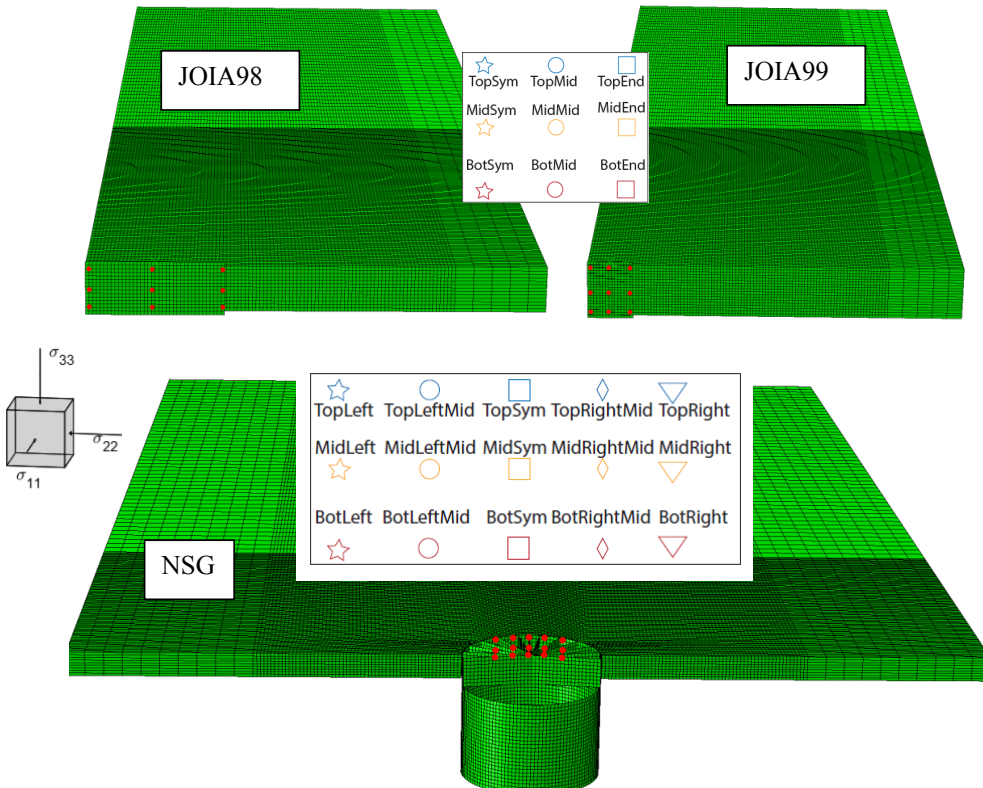


Figure 21. Nodes in the ice, used to study the ice stress state, top left: JOIA98L, top right: JOIA99L and bottom: NSGL, Red dots display nodes where stresses were studied and the nodal labels and symbol

The aspect ratio in the JOIA98L and JOIA99L simulation was 5.9 and 1.7, respectively. An additional simulation was ran with the JOIA98L material model and the JOIA99L aspect ratio. To visualize how the aspect ratio affects the ice stress states, the deviatoric stress is compared to the first principal stress invariant in Figure 22 (nodes displayed in Figure 21). In addition to the nodal stresses the plastic limits of the von Mises and Lubliner yield functions are displayed. When the aspect ratio decreased from 5.9 to 1.7, with all else being equal, the lateral stress increased as well as $\sqrt{3J_2}$, I_1 and thus the effective pressure. The effective pressure increased from 1.2 MPa to 1.6 MPa, when the aspect ratio decreased from 5.9 to 1.7.

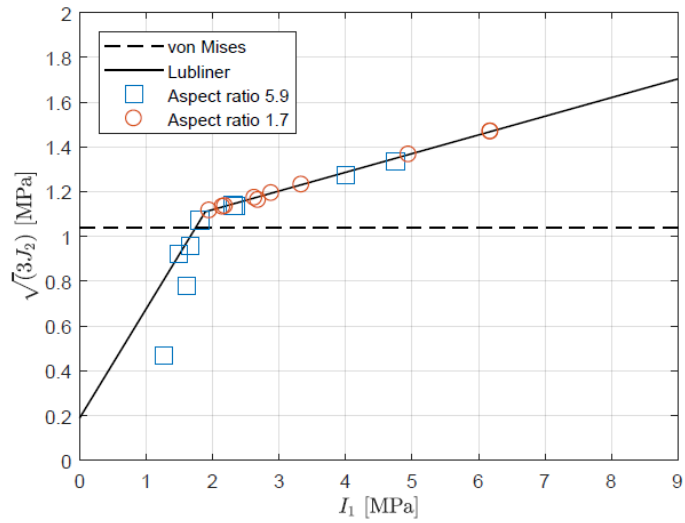


Figure 22. Aspect ratio effect. von Mises and Lubliner display the plastic limits in the respective material models.

In ISO19906 (2018) the effective pressure is a function of both ice thickness and aspect ratio, whereas the effective pressure equation in API-RP-2N (1995) is independent of both ice thickness and aspect ratio. Määttänen and Kärnä (2011) suggested a modification of ISO19906 (2010) because it was proven unsafe for narrow structures with small aspect ratios. In Figure 23 effective pressure is compared to aspect ratio in simulations, measurements and standards. The effective pressure simulated with the Lubliner model captures the aspect ratio effect observed in the JOIA data.

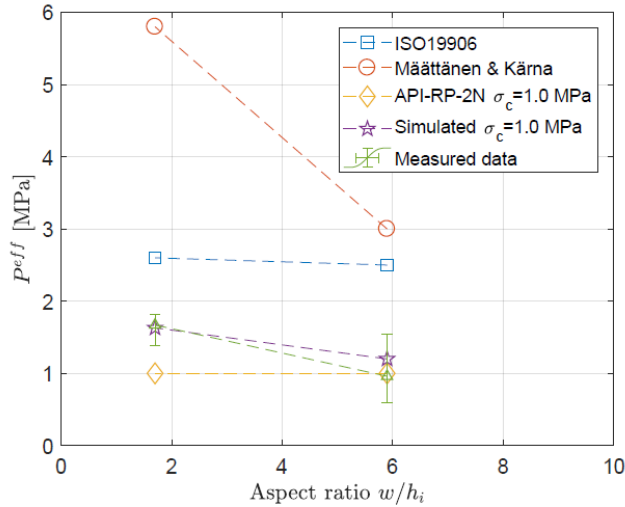


Figure 23. Aspect ratio and codes. The markers display effective pressure and aspect ratio for JOIA98 (aspect ratio 5.9) and JOIA99 (aspect ratio 1.7) simulation setup.

4.5.3 Effect of structure shape on the global force

The structure shape in contact with the ice influences the lateral stress in the ice. With the cylindrical indenter, in the NSGL simulation, the highest stress in the ice was observed on the symmetry line on the ice/structure contact (□ in Figure 24). Contrary, on the flat indenter the highest stress was observed in the ice in contact with the indenter edge. Tactile sensor data confirm that the pressure was higher on the indenter edges than elsewhere (Sodhi et al., 1998). If the flat indenter (in the JOIA simulations) was replaced with a cylindrical indenter of equal width, the effective pressure would decrease. This is consistent with the observations made by Korzhavin (1962) and adopted by the API-RP-2N (1995). The effect of structural shape is not included in the ISO19906 (2018).

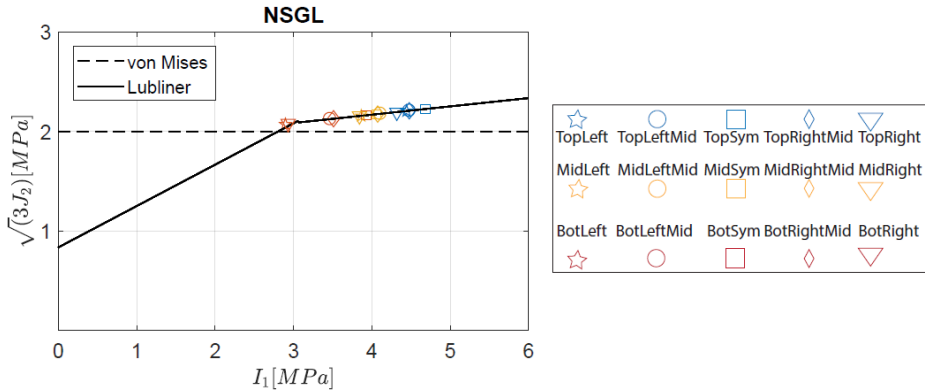


Figure 24. Deviatoric stress vs. fist principal invariant, the markers indicate stresses in nodes from the NSGL simulation.

4.5.4 Simulated compared to measured global forces

In the JOIA simulations the global forces (0.38-0.46 MN) were similar to the measured forces (0.17-0.49 MN). Ice interactions with the flat and stiff indenter in the JOIA experiment are considered worst cases in terms of the global force. The intact ice cover and indenter stiffness ensured that the ice failed simultaneously across the full contact area and the ice was grown in a stable environment such that the ice was more homogenous than at the Norströmsgrund lighthouse.

At the Norströmsgrund lighthouse the simulated global forces (11-25 MN) were higher than the measured global forces (6-9 MN). The measured ice interactions at the Norströmsgrund lighthouse are not considered worst cases, in terms of the global force. The ice field was broken, measurements were conducted in mild/average winters (based on FDD), the instrumentation was insufficient to measure the total global force and the ice was probably more heterogeneous compared to the JOIA experiment. The simulations are considered worst cases, in terms of the global force, because the ice is perfectly level, the total global force is obtained and the ice sheet is not broken.

4.6 Conclusions and recommendations

In this part of the thesis, an elastic-plastic finite element model was applied in simulations of ductile failure of solid ice measured in the JOIA experiment, and at the Norströmsgrund lighthouse. A non-associated flow rule was included in the applied model in order to study whether the dilatancy in ice was significant to the global force in ductile ice-structure interactions. Statistical significance of ice properties in the material model was identified by means of two-level factorial design of experiments. The stress state in the ice was used to explain how the effective pressure was affected by aspect ratio and structure shape. The following conclusions were made:

- Simulations show that the most statistically significant properties were the strength properties and thereafter the dilatancy angle.
- The pressure dependent model predicted an aspect ratio effect due to changes in the lateral stresses.
- The pressure dependent model predicted higher effective pressure with the prismatic indenter than the cylindrical indenter because of increased lateral stresses on the edge of the prismatic indenter.
- The strength in ice is pressure dependent and therefore the pressure independent von Mises yield function should be avoided.
- Lower uncertainty may be expected when predicting global forces in decaying warm ice, because the range in strengths are lower compared to that in colder ice as shown in Appendix 2 and Chapter 2.

The focus in this thesis has mainly been on the consolidated layer in quasi-static ridge interactions. Full-scale data of ridge interactions including force measurements from the unconsolidated rubble should be measured in the future in order to develop and verify a numerical model including both the consolidated and the unconsolidated layer. However, in the simulated interactions of ice-ridge interactions at the Norströmsgrund lighthouse the rubble forces were considered less significant compared to the consolidated layer forces.

Chapter 5

Conclusions and future outlook

Computers are great tools, but they need to be applied to the physical world. – Tony Fadell

5.1 Conclusions

The presence of ice ridges is a potential threat to structures located in ice infested waters. Ice ridges caused the highest global forces at the Norströmsgrund lighthouse during its instrumentation in the winters 1999/2000-2002/2003. The global ridge forces measured at the Norströmsgrund lighthouse, were most probably caused by the consolidated layer in the ridges. Measurements of four Arctic ridges during the N-ICE2015 expedition, revealed that the consolidated layer continued to grow as long as the temperature inside the consolidated layer was low enough that it could absorb both the heat flux from the air and the latent heat released from growth of ice. It continued to grow while the level ice melted, so that the ratio between consolidated layer thickness and level ice thickness exceeded the commonly used maximum value of 2. Simultaneously, there was a continuous degradation process inside the rubble that resulted in a continuous decrease in the rubble macroporosity. Melting of the rubble insulated the consolidated layer from the underlying water. Due to this, the consolidated layer thickness is at its maximum in spring. This coincides with the occurrence of high global force events at the Norströmsgrund lighthouse, and also at other structures such as the Confederation Bridge and Cook Inlet platforms. Despite cold ice being stronger than warm ice, some of the most severe ice loading events have occurred in spring when the ice is relatively warm. It should be noted, that temperature affects both ice strength and ice failure mode.

The type of interaction mode seems to govern ice forces. Different types of ice ridge interaction modes were classified based on the measured signatures in force and responses at the Norströmsgrund lighthouse. The identified high global force ridge interaction modes were 1) stalling 2) ductile failure and 3) brittle failure. All these interaction modes potentially caused a high global force, as long as the failure occurred simultaneously across the lighthouse circumference. The ridge interaction modes were generally different from level ice interactions in that the global force was non-stationary with a large slow-varying mean. Unfortunately, the instrumentation of the lighthouse was limited and therefore the global forces were underestimated and the rubble forces were not quantified. It was also difficult to extract general trends from the data due to the large number of variables and uncertainties in naturally grown and broken ice. A numerical model was applied to study general trends and parameter variations, where ice properties and boundary conditions were controlled.

An elastic plastic FEM was used to model the consolidated layer failure at the Norströmsgrund lighthouse, in addition to level ice indentation with a flat indenter in the JOIA experiment. Ductile interactions were modelled, because the highest forces on the Norströmsgrund lighthouse were caused by simultaneous failure, where dynamic forces were low compared to the slow varying mean force. Ductile interactions also caused the highest forces in the JOIA experiment. Ice strength data were used to demonstrate ice strength pressure dependency which disregarded the use of the Von Mises yield function in modelling of ice failure. The elastic-plastic ice model included a pressure dependent isotropic yield function and a non-associated flow rule. The significance of material properties to the global force was quantified by two level factorial design of experiments, where the strength properties were most statistically significant. Because of the significance of strength, and because ice strength is sensitive to temperature, in-field strength values should be measured and used in the numerical model. Furthermore, simulation were used to study how aspect ratio and structure shape affected the ice stress state. Simulations revealed that low aspect ratios and flat prismatic indenters caused higher lateral ice stresses and thus higher effective pressures than high aspect ratios and cylindrical indenters. Simulations helped improved the understanding of what caused previously observed effects of aspect ratio and structural shape.

To summarize the following main conclusions were made:

- The consolidated layer continuous to grow as long as the temperature inside is low enough to consume the heat transferred to the consolidated layer, whereas the rubble macroporosity continuously decreases during the lifetime of a first-year ridge.
- At the Norströmsgrund lighthouse, the highest global forces were caused by failure of ridges in spring, where the ridge either failed simultaneously across the lighthouse circumference or was stalled against the lighthouse.
- Three types of high force ridge interaction modes were identified at the Norströmsgrund lighthouse; 1) stalling 2) ductile failure and 3) brittle failure, arranged by increasing ice drift velocity.
- High force ridge interactions were generally different from level ice interactions in that the global force was non-stationary with a large slow varying mean.
- Ice strength is pressure dependent and strength properties are most statistically significant to the global force. Because of the significance of strength, and because ice strength is sensitive to temperature, in-field strength values should be used in the numerical model.
- The FE-model predicts an aspect ratio effect similar to ISO19906. This is caused by different stress-states inside the ice.

The results from the work summarized above has improved the understanding of ice ridge-structure interactions. It has shown that ice ridge interactions are different to level ice interactions and therefore not described in standards, such as ISO19906 (2018). The ISO19906 (2018) should contain separate information about ice ridge interactions as well as effects of structure shape. It should also be acknowledge that both the rubble macroporosity and the ratio of the consolidated layer/ level ice thickness evolve during the life of a first-year ice ridge. The macroporosity continuously decreases, whereas the ratio of the consolidated layer/ level ice thickness increases.

5.2 Future outlook

Answering a question often raises several new ones. During studies presented in this thesis, many such unanswered questions were raised. The ice rubble was unfortunately difficult to study in terms of its structure and strength. It was also difficult to quantifying ice rubble forces in full-scale ice ridge-structure interactions. Furthermore, the currently used technique for obtaining ridge geometry and macroporosity is uncertain due to factors such as, drill chips filling the boreholes, jamming of drill augers, bending of drill augers and especially the subjective observations made by the drill operator. To eliminate these uncertainties, more advanced measurement techniques should be explored, e.g. multibeam sonar mapping or multi-frequency electromagnetic sensor scanning. Furthermore, in order to understand the thermodynamic consolidation in isothermal rubble, the temporal and spatial variation in ice rubble salinity should be measured in a future investigation. In order to measure full-scale global forces from the rubble, necessary instrumentation include accelerometers and inclinometers or strain gauges in addition to load panels. For accurate tilt and acceleration measurements, instruments need repeated zeroing and calibration.

In terms of modelling, the consolidated layer and the ice rubble should be combined in a future study. However, this requires data in order to verify the numerical model, data that is currently unavailable. Due to the size of ice ridges, model-scale experiments are preferred over full-scale experiments. However, it is presently unclear how to scale ridges in terms of consolidation time and temperature.

This study has mainly focused on global forces in ice ridge interactions. The structure response in ice ridge-structure interactions should also be investigated. It is unclear whether frequency lock-in vibrations are less likely to occur during ridge-structure interactions because the ice rubble damps the structural vibrations.

In 2006, Timco and Croasdale (2006) , asked a number of ice experts to predict the global force from an ice ridge interacting with a fixed vertically sided structure. The predicted ice ridge force varied by a factor of five, which illustrates the level of uncertainty.

Research is continuously needed to reduce this uncertainty and to improve standards, to ensure safe and sustainable Arctic design.

References

- Alejano, L.R. and Alonso, E., 2005. Considerations of the dilatancy angle in rocks and rock masses. *International Journal of Rock Mechanics and Mining Sciences*, 42(4): 481-507.
- API-RP-2N, 1995. Recommended Practice for Planning, Designing and Constructing Structures and Pipelines for Arctic Conditions American Petroleum Institute, Exploration and Production Department.
- Bjerkås, M., 2006. Ice action on offshore structures, NTNU.
- Bjerkås, M., Bonnemaire, B., Sodhi, D.S., Gerisch, S. and Jochmann, P., 2003. STRICE report: Extended observations of ice-structure interactions at the lighthouse Norströmsgrund winter 2003. Report N. D-3.1.
- Bjerkås, M., Lønøy, C. and Gürtner, A., 2012. Seasonal Variations In the Occurrence of Ice Induced Vibration of a Bottom Fixed Structure, The Twenty-second International Offshore and Polar Engineering Conference. International Society of Offshore and Polar Engineers, Rhodes, Greece.
- Bjerkås, M. and Nord, T.S., 2016. Ice action on Swedish lighthouses revisited, Proceedings of the 23rd IAHR International Symposium on Ice, Ann Arbor, Michigan USA.
- Blenkarn, K.A., 1970. Measurements and Analysis of Ice Forces on Cook Inlet Structures. Proceedings of the second annual conference on Offshore Technology Conference, Houston, Texas.
- Box, G.E.P. and Draper, N.R., 1987. Empirical model-building and response surfaces. Empirical model-building and response surfaces. John Wiley & Sons, Oxford, England, xiv, 669-xiv, 669 pp.
- Brown, T.G. and Määttänen, M., 2009. Comparison of Kemi-I and Confederation Bridge cone ice load measurement results. *Cold Regions Science and Technology*, 55(1): 3-13.
- Brown, T.G., Tibbo, J.S., Tripathi, D., Obert, K. and Shrestha, N., 2010. Extreme ice load events on the Confederation Bridge. *Cold Regions Science and Technology*, 60(1): 1-14.
- Cox, G.F.N. and Weeks, W.F., 1983. Equations for Determining the Gas and Brine Volumes in Sea-Ice Samples. *Journal of Glaciology*, 29(102): 306-316.
- Dorris, J.F., 1991. A Plasticity Model for the Crushing of Ice. IUTAM-IAHR Symposium St. John's Newfoundland, Canada, Springer-Verlag Berlin Heidelberg.
- Engelbrektson, A., 1987a. Analysis of field observations from Norströmsgrund lighthouse during the period 1979–1985. A. Study project ice forces against offshore structures. VBB Project M7334. Report, No 2. Jan 15. VBB; 1987.
- Engelbrektson, A., 1987b. Evaluation of Extreme Ice Forces on a Lighthouse in the Botnian Bay, A study of the Björnklack overloading event April 1985. Report No. 1, National Administration of Shipping and Navigation, Sweden, University of Luleå.
- Ervik, Å., 2015. Full scale actions from first-year ridge interactions with fixed structures, Proceedings of the 23rd International Conference on Port and Ocean Engineering under Arctic Conditions Trondheim, Norway, pp. 129-140.

- Ervik, Å., Høyland, K.V., Grimstad, G. and Nord, T.S., 2017. A Continuum Model of Large Deformation Continuous Ductile Ice Crushing. Proceedings of the 24th International Conference on Port and Ocean Engineering under Arctic Conditions (POAC), Busan, Korea, Paper no. 104.
- Ervik, Å., Høyland, K.V., Shestov, A. and Nord, T.S., 2018a. On the decay of first-year ice ridges: Measurements and evolution of rubble macroporosity, ridge drilling resistance and consolidated layer strength, <https://doi.org/10.1016/j.coldregions.2018.03.024>. Cold Regions Science and Technology, 151: 196-207.
- Ervik, Å., Nord, T.S., Høyland, K.V., Samardzija, I. and Hongtao, L., 2018b. Ice-ridge interactions with the Norströmsgrund lighthouse: global forces and interaction modes. Cold Regions Science and Technology, <https://doi.org/10.1016/j.coldregions.2018.08.020>.
- Frederking, R., Timco, G.W. and Wright, B.D., 1999. Ice pressure distribution from first-year sea ice features interacting with the Molikpaq in the Beaufort Sea. Proceedings 9th International Offshore and Polar Engineering Conference ISOPE '99, Brest, France, vol. II (1999), pp. 541-548.
- Frost, R.V., 1941. Construction of five bottom-founded lighthouses by the deep water channel in Kalmarsund (Translated from Swedish), Uppförandet av fem bottenfasta fyror vid djuprännan i Kalmarsund, Lecture note for the Swedish union of concrete, 21st of February 1941, pp. 40.
- Gagnon, R.E. and Gammon, P.H., 1995. Triaxial experiments on iceberg and glacier ice. Journal of Glaciology, 41(139): 528-540.
- Haapala, J., Oikkonen, A., Gierisch, A., Itkin, P., Nicolaus, M., Spreen, G., Wang, C., Karvonen, J. and Lensu, M., 2017. N-ICE2015 Ship Radar Images. In: N.P. Institute (Editor), doi:10.21334/npolar.2017.6441ca81.
- Haas, C., 2000. LOLEIF report: EM ice thickness measurements at the lighthouse Norströmsgrund, Luleå, Sweden, within the LOLEIF project. Part 1: system installation, modelling and calibration.
- Haas, C., 2017. EM thickness and the consolidated layer, personal communication
- Hansen, E., Ekeberg, O.C., Gerland, S., Pavlova, O., Spreen, G. and Tschudi, M., 2014. Variability in categories of Arctic sea ice in Fram Strait. Journal of Geophysical Research-Oceans, 119(10): 7175-7189.
- Hasle, J.R., Kjellén, U. and Haugerud, O., 2009. Decision on oil and gas exploration in an Arctic area: Case study from the Norwegian Barents Sea. Safety Science, 47(6): 832-842.
- Høyland, K.V., 2002. Consolidation of first-year sea ice ridges. Journal of Geophysical Research: Oceans, 107(C6): 15-1-15-16.
- Høyland, K.V., 2007. Morphology and small-scale strength of ridges in the North-western Barents Sea. Cold Regions Science and Technology, 48(3): 169-187.
- Høyland, K.V. and Liferov, P., 2005. On the initial phase of consolidation. Cold Regions Science and Technology, 41(1): 49-59.
- ISO19906, 2018. Petroleum and natural gas industries - Arctic offshore structures. International Standardization organization, Geneva, Switzerland.
- Jochmann, P. and Schwarz, J., 2000. LOLEIF-report: Ice Force Measurements at Lighthouse Norströmsgrund - Winter 1999. Rep no 5.

- Johnston, M., 2006. A comparison of physical properties and strength of daying first-year ice in the Arctic and sub-Arctic. *Annals of Glaciology* 44: 13.
- Johnston, M.E., 2017. Seasonal changes in the properties of first-year, second-year and multi-year ice. *Cold Regions Science and Technology*, 141: 36-53.
- Jones, J.S., 1982. The Confined Compressive Strength of Polycrystalline Ice. *Journal of Glaciology*, 28(98): 171-178.
- Kamio, Z., Takawaki, T., Matsushita, H., Takeuchi, T., Sakai, M., Terashima, T., Akagawa, S., Nakazawa, N. and Saeki, H., 2000. Medium Scale Field Indentation Tests: Physical Characteristics of First-Year Sea Ice at Nototo Lagoon, Hokkaido. *Proceedings of the Tenth (2000) International Offshore and Polar Engineering Conference, Seattle, USA, May 28-June 2.*
- Korzhasin, K.N., 1962. Action of Ice on Engineering Structures (English title) IZDATEL 'STVO SIBIRSKOGO OTDELESIYA AKADEMII HAUK SSSR, Publishing House of Siberian Branch of USSR Academy of Sciences, 202p.
- Kärnä, T. and Yan, Q., 2009. Analysis of the size effect in ice crushing- edition 2, Technical Report No. RTEU50-IR-6/2005, VTT.
- Leppäranta, M. and Hakala, R., 1992. The structure and strength of first-year ice ridges in the Baltic Sea. *Cold Regions Science and Technology*, 20(3): 295-311.
- Leppäranta, M., Lensu, M., Kosloff, P. and Veitch, B., 1995. The Life Story of a 1st-Year Sea-Ice Ridge. *Cold Regions Science and Technology*, 23(3): 279-290.
- Leppäranta, M. and Manninen, T., 1988. The brine and gas content of sea ice with attention to low salinities and high temperatures, Helsinki, Finland, Finnish Institute of Marine Research, 15pp. (Finnish Institute of Marine Research Internal Report, 1988-2).
- Li, H., Bjerckås, M., Høyland, K.V. and Nord, T.S., 2016. Panel loads and weather conditions at Norstrømsgrund lighthouse 2000-2003, *Proceedings of the 23rd IAHR international Symposium on Ice, Ann Arbor, Michigan USA.*
- Lubliner, J., Oliver, J., Oller, S. and Oñate, E., 1989. A plastic-damage model for concrete. *International Journal of Solids and Structures*, 25(3): 299-326.
- Matsushita, H., Takawaki, T., Tuboi, T., Takeuchi, T., Sakai, M., Terashima, T. and Saeki, H., 1999. Medium Scale Field Indentation Tests: Strength Characteristics of the Ice Sheet (First-Year Sea Ice), *The Ninth International Offshore and Polar Engineering Conference. International Society of Offshore and Polar Engineers, Brest, France.*
- Michel, B. and Toussaint, N., 1977. Mechanisms and Theory of Indentation of Ice Plates. *Journal of Glaciology*, 19(81): 285-300.
- Montgomery, D.C., 2013. *Design and Analysis of Experiments (8th Edition)*. John Wiley & Sons. Online version available at: <https://app.knovel.com/hotlink/pdf/id:kt011B0NGM/design-analysis-experiments/strategy-experimentation>. John Wiley & Sons.
- Moslet, P.O., 2007. Field testing of uniaxial compression strength of columnar sea ice. *Cold Regions Science and Technology*, 48(1): 1-14.
- Määttänen, M. and Kärnä, T., 2011. ISO 19906 ice crushing load design extension for narrow structures, *Proceeding of the 21st International Conference on Port and Ocean Engineering under Arctic Conditions, Montreal, Canada.*
- Nadreau, J.-P. and Michel, B., 1986. Yield and failure envelope for ice under multiaxial compressive stresses. *Cold Regions Science and Technology*, 13(1): 75-82.

- Neill, C.R., 1976. Dynamic ice forces on piers and piles. An assessment of design guidelines in the light of recent research. *Canadian Journal of Civil Engineering*, 3(2): 305-341.
- Oikkonen, A., Haapala, J., Lensu, M., Karvonen, J. and Itkin, P., 2017. Small-scale sea ice deformation during N-ICE2015: From compact pack ice to marginal ice zone. *Journal of Geophysical Research: Oceans*(122): 5105-5120, doi:10.1002/2016JC012387.
- Pariseau, W.G., 1968. Plasticity theory for anisotropic rocks and soils. In K.E. Gray (ed.), *Proc. Tenth Symp. on Rocks Mechanics*, pp. 267-295.
- Peterson, K.A., Fer, I., McPhee, M.G. and Randelhoff, A., 2017. Turbulent Heat and Momentum Fluxes in the Upper Ocean Under Arctic Sea Ice. *Journal of Geophysical Research: Oceans*(122): 1439-1456, doi:10.1002/2016JC012283.
- Poirier, L., 2014. Detailed ice ridge loading events on Norströmsgrund lighthouse, International Conference and Exhibition of Performance of Ships and Structures on Ice (ICETECH), Banff, Alberta.
- Poplin, J.P. and Wang, A.T., 1994. Mechanical properties of rafted annual sea ice. *Cold Regions Science and Technology*, 23(1): 41-67.
- Riska, K. and Frederking, R., 1987. Ice load penetration modelling, *Proceedings of the Port and Ocean Under Arctic Conditions Conference Fairbanks, Alaska, USA*, pp. 317-327.
- Rist, M.A. and Murrell, S.A.F., 1994. Ice triaxial deformation and fracture. *Journal of Glaciology*, 40(135): 305-318.
- Saeki, H., Hiyayama, K.-i., Kawasaki, T., Akagawa, S., Kato, K., Kamesaki, K., Saka, K. and Kurakawa, A., 1997. JOIA Project of Study on Ice Load *Proceedings of the Seventh (1997) International Offshore and Polar Engineering Conference*, Honolulu, USA, May 25-30, 1997.
- Sakai, M., Aoshima, M. and Saeki, H., 1998. Measurements of Ice Sheet Strain Area During Ice/Vertical Sided Structure Interactions Using Strain Gages In Field Indentation Tests, *The Eighth International Offshore and Polar Engineering Conference. International Society of Offshore and Polar Engineers, Montreal, Canada*.
- Schulson, E.M. and Duval, P., 2009. *Creep and Fracture in Ice* Cambridge University Press.
- Schwerdtfeger, P., 1962. The thermal properties of sea ice *Journal of Glaciology*: 789-807.
- Shestov, A., Høyland, K. and Ervik, Å., 2018. Decay phase thermodynamics of ice ridges in the Arctic Ocean. *Cold Regions Science and Technology*, 152: 23-34.
- Shestov, A.S. and Marchenko, A.V., 2016a. The consolidation of saline ice blocks in water of varying freezing points: Laboratory experiments and computer simulations. *Cold Regions Science and Technology*, 122: 71-79.
- Shestov, A.S. and Marchenko, A.V., 2016b. Thermodynamic consolidation of ice ridge keels in water at varying freezing points. *Cold Regions Science and Technology*, 121: 1-10.
- Shrestha, N. and Brown, T.G., 2018. 20 years of monitoring of ice action on the Confederation Bridge piers. *Cold Regions Science and Technology*, 151: 208-236.

- Sinha, N.K., 1984. Uniaxial compressive strength of first-year and multi-year sea ice. *Canadian Journal of Civil Engineering*, 11(1): 82-91.
- Sodhi, D.S. and Haehnel, R.S., 2003. Crushing Ice Forces on Structures. *Journal of Cold Regions Engineering*, 17(4).
- Sodhi, D.S., Takeuchi, T., Nakazawa, N., Akagawa, S. and Saeki, H., 1998. Medium-scale indentation tests on sea ice at various speeds. *Cold Regions Science and Technology*, 28(3): 161-182.
- Strub-Klein, L. and Sudom, D., 2012. A comprehensive analysis of the morphology of first-year sea ice ridges. *Cold Regions Science and Technology*, 82: 94-109.
- Sudom, D. and Frederking, R., 2014. First-year ice ridge loads on Norstrømsgrund lighthouse in 2002 and 2003, International Conference and Exhibition on Performance of Ships and Structures in Ice (ICETECH), Banff, Alberta, Canada.
- Timco, G.W. and Croasdale, K.R., 2006. How well can we predict ice loads, Proceedings 18th International Symposium on Ice, IAHR'06, Sapporo, Japan, pp. pp167-174.
- Timco, G.W., Croasdale, K.R. and Wright, B., 2000. An overview of First-Year Ice Ridges, Canadian Hydraulics Centre.
- Timco, G.W. and Frederking, R., 1990. Compressive strength of sea ice sheets. *Cold Regions Science and Technology*(17): 227-240.
- Timco, G.W. and Johnston, M., 2003. Ice loads on the caisson structures in the Canadian Beaufort Sea. *Cold Regions Science and Technology*(38): 185-209.
- Timco, G.W. and Weeks, W.F., 2010. A review of the engineering properties of sea ice. *Cold Regions Science and Technology*, 60(2): 107-129.
- Ushikoshi, J., Kamio, Z., Matsushita, H., Sakai, M., Takeuchi, T., Terashima, T., Akagawa, S., Nakazawa, N. and Saeki, H., 2001. Summary of Five Years' Field Test On Mechanical Properties, The Eleventh International Offshore and Polar Engineering Conference. International Society of Offshore and Polar Engineers, Stavanger, Norway.
- Vakili, A., 2016. An improved unified constitutive model for rock material and guidelines for its application in numerical modelling. *Computers and Geotechnics*, 80: 261-282.
- Vermeer, P.A., 1998. Non-Associated Plasticity for Soils, Concrete and Rock. In: H.J. Herrmann, J.P. Hovi and S. Luding (Editors), *Physics of Dry Granular Media*. Springer Netherlands, Dordrecht, pp. 163-196.
- Weeks, W.F., Kovacs, A. and D., H.W., 1971. Pressure ridge characteristics in the Arctic coastal environment Port and Ocean Engineering under Arctic Conditions Technical University of Norway.
- Wright, B.D. and Timco, G.W., 2001. First-year ridge interaction with the Molikpaq in the Beaufort Sea. *Cold Regions Science and Technology*, 32(1): 27-44.

Appendix 1

On the decay of first-year ice ridges: Measurements and evolution of rubble macroporosity, ridge drilling resistance and consolidated layer strength

This appendix includes the paper published in the journal Cold Regions Science and Technology (see below).

- Ervik, Å., Høyland, K.V., Shestov, A. and Nord, T.S., 2018. On the decay of first-year ice ridges: Measurements and evolution of rubble macroporosity, ridge drilling resistance and consolidated layer strength. Cold Regions Science and Technology, 151: 196-207, <https://doi.org/10.1016/j.coldregions.2018.03.024>.



Contents lists available at ScienceDirect

Cold Regions Science and Technology

journal homepage: www.elsevier.com/locate/coldregions

On the decay of first-year ice ridges: Measurements and evolution of rubble macroporosity, ridge drilling resistance and consolidated layer strength

Åse Ervik^{a,b,*}, Knut V. Høyland^a, Aleksey Shestov^{a,b}, Torodd S. Nord^{a,b}^a Sustainable Arctic Marine and Coastal Technology (SAMCoT), Centre for Research-based Innovation (CRI), Norwegian University of Science and Technology, Trondheim, Norway^b The University Centre in Svalbard (UNIS), Longyearbyen, Spitsbergen, Svalbard and Jan Mayen

ARTICLE INFO

Keywords:

Field measurements
 Properties of decaying ice ridges
 Rubble macroporosity
 Drilling resistance
 Uniaxial compressive strength

ABSTRACT

In this study, four first-year ice ridges (R1, R2, R3 and R4) were measured during the transition from the “main” phase to the “decay” phase. The measurements were conducted on two ice floes in the Arctic Ocean northwest of Svalbard during May and June 2015. Ice ridge R1 was approximately 13 m thick and 200 m long, R2 was 5 m thick and 500 m long, R3 was 6 m thick and 75 m long, and R4 was 9 m thick and 150 m long. The objective of this study was to investigate the rubble macroporosity evolution, ridge drilling resistance and consolidated layer small-scale strength in the decaying ridges. The ice rubble macroporosity and ridge drilling resistance values were obtained through mechanical drilling. The drilling resistance was measured by the drill operator, which was defined as hard, medium or soft. The small-scale strength was measured in the field via uniaxial compression with a nominal strain rate of 10^{-3} s^{-1} . The rubble macroporosities in R1, R2, R3 and R4 ranged from 10% to 27%, and the temporal macroporosity variation was the result of seasonal developments. The rubble macroporosity in R2 decreased from 25% (27 days old) to 16% (34 days old, 4 days before breakup). In R1, which was larger, colder and older than R2, the rubble macroporosity remained constant (11%–10%) over a ten-day period. Because ridges R3 (22% rubble macroporosity) and R4 (27% rubble macroporosity) were only mapped once, no temporal development was measured. We suggest that the ice rubble macroporosity in saline, first-year ridges continuously decreases over time and that this decrease accelerates during the decay phase. Furthermore, both the consolidated layer uniaxial compressive strength (measured in R1, R2 and R3) and the ridge drilling resistance (measured in R1, R2, R3 and R4) decreased during the transition from the main phase to the decay phase, due to an increase in ice temperatures. After the ridges reached an isothermal state, the drilling resistance and strength remained constant, and the brine volume (microporosity) increased. The ice cores collected from the decaying ice exhibited ductile failure modes when subjected to uniaxial compression.

1. Introduction

The extent of Arctic sea ice is declining (Mahoney et al., 2008; Xia et al., 2014) as it becomes thinner (Kwok and Rothrock, 2009) and younger (Maslanik et al., 2011). The drastic decrease in old sea ice allows greater shipping accessibility through the Arctic Northeast Passage and transportation to Arctic communities (Lei et al., 2015). Sea ice ridges (ridges, hereafter) form due to shearing and/or pressure in an ice pack. Ridges consist of a sail above and a keel below the water. First-year keels consist of consolidated and unconsolidated parts (ice rubble). Ridges are common features in all ice-covered waters and play key roles in the sea ice mass budget. On average, from 1990 to 2011, ridges comprised 66% of the Arctic Sea ice mean thickness in the Fram Strait

(Hansen et al., 2014). First-year ridges are considered in Arctic and subarctic marine structural design (CAN/CSA-S471-92, R2001, 2001; ISO/FDIS/19906, 2010; SNI P2.01.07-85, 1987). Design ice loads depend on ridge size, geometry, macroporosity and strength, as well as other parameters. These parameters evolve as a ridge consolidates and melts over its lifetime. A ridge exposed to warm air and water temperature (strong oceanic heat fluxes) as well as wave action will transform and may ultimately melt. For a ridge exposed to warm water, the oceanic heat flux may rapidly increase from a few W/m^2 (for water at the freezing point) to several hundred W/m^2 , which accelerates the melting process. In some temperate areas, such as the southwestern Barents Sea, ice is rare but may still occur. The measurements obtained in this study suggest that a ridge in the southwestern Barents Sea is

* Corresponding author at: Sustainable Arctic Marine and Coastal Technology (SAMCoT), Centre for Research-based Innovation (CRI), Norwegian University of Science and Technology, Trondheim, Norway.

E-mail address: ase.ervik@ntnu.no (Å. Ervik).

<https://doi.org/10.1016/j.coldregions.2018.03.024>

Received 24 January 2017; Received in revised form 23 March 2018; Accepted 27 March 2018

Available online 30 March 2018

0165-232X/ © 2018 Elsevier B.V. All rights reserved.

likely a large, decaying first-year ridge. Therefore, understanding decaying first-year ridge evolutionary properties is important.

The consolidation process affects both the internal structure (macroporosity) and strength of a ridge, and these properties are essential for estimating design ridge loads. Most previous ridge studies were conducted over just a few days' time, and only Leppäranta et al. (1995) studied the full history of a Baltic ridge, from formation to break up.

Most sea ice compressive strength measurements were obtained in laboratories using ice temperatures colder than -10°C (Poplin and Wang, 1994; Schulson and Duval, 2009; Sinha, 1984; Timco and Frederking, 1990; Timco and Weeks, 2010). However, decaying saline ice has temperatures of around -1.8°C . Strength measurements of decaying Arctic and subarctic first-year ice were presented by Johnston (2006, 2017).

In this study, we present the rubble macroporosity evolution, ridge drilling resistance and uniaxial compressive strength in the consolidated layers of four ridges (R1, R2, R3 and R4), which were measured on two ice drift stations (floes) in the Arctic Ocean (Floe 3 and Floe 4) in May and June during the Norwegian young sea ice expedition (N-ICE2015). An overview of the N-ICE2015 expedition has been presented by Granskog et al. (2016). Ridges R1 and R2, with maximum ice thicknesses of approximately 13 m and 5 m, respectively, were imbedded in ice Floe 3, which was several kilometers in size. Ridge R2 was formed from ice in a refrozen lead. Ridges R3 and R4, with maximum ice thicknesses of approximately 6 m and 9 m, respectively, were imbedded in Floe 4. Floe 4 was smaller than Floe 3 and closer to the ice edge.

These data provide novel insights into how the rubble macroporosity and consolidated layer strength of Arctic first-year ridges evolve during the late spring and early summer. In a companion study by Shestov et al. (2018), temperature data and thermodynamic processes are analyzed, and the consolidated layer growth in R1 and keel melting in R4 are estimated.

2. Review of macroporosity and strength

In this section, the different first-year ridge phases are described, and then, reviews of macroporosity and consolidated layer strength are given.

2.1. First-year ice ridge phases

A first-year ridge lifespan, from formation to breakup or transition into a second-year ridge, can be divided into the following phases: 1) the “initial” phase, 2) the “main” phase, and 3) the “decay” phase (Høyland and Liferov, 2005). In the initial phase, the ridge is formed, and cold ice blocks are submerged, which results in strong, local thermal gradients between cold ice pieces and warm water pockets. The initially low temperature of the ice increases due in part to the freeze bond formation as well as seawater energy transfer (oceanic heat flux). The energy transfer from the seawater, which is the oceanic heat flux, is stronger near the bottom surface of the ice rubble. Because of this difference in the oceanic heat flux, the temperatures in the lower rubble increase and approach the freezing point (T_f) faster. If the seawater is at T_f , the isothermal conditions gradually spread upward through the keel, and because the air is colder than T_f , a linear temperature profile will slowly spread downward simultaneously. The end of the initial phase is defined as the moment when the ice rubble becomes isothermal. The main phase begins, and the break point between the linear temperature profile above the isothermal rubble defines the consolidated layer thickness, as shown by Høyland (2002). The freezing front in the consolidated layer insulates the underlying ice rubble (unconsolidated layer) from the cold air. Therefore, there is a continuous rubble degradation process (heating) leading toward transformation into a second-year ridge or melting/disintegration. Finally, the decay phase begins when the air temperature (T_{air}) stabilizes around or above 0°C ;

thus, the ridge is heated from the air surface as well as from the bottom. Toward the end of the decay phase, the first-year ridge either disintegrates and melts completely or transforms into a second-year ridge.

Although the air temperature exceeds 0°C , in the decay phase, the snow may insulate the consolidated layer, which allows further consolidation (i.e. new ice growth). Simultaneously, keel melting is accelerated during this phase, and the rubble temperature and water temperature both increase toward 0°C , which causes strong oceanic heat fluxes. These processes are not well understood, but even under isothermal conditions, the rubble continues to consolidate while being heated during the transformation of macroporosity to microporosity (Shestov and Marchenko, 2016b). In addition, the freshwater supply (either from melted snow or changing salinity of the underlying water) may be a key factor contributing to further consolidation (Shestov and Marchenko, 2016a). For details and discussions on thermodynamic measurements, please refer to the study by Shestov et al. (2018).

2.2. Macroporosity and ridge structure

An ice feature can be defined as the entire ridge, sail, keel or rubble. Macroporosity, which is a common property used to describe the internal structure of an ice feature, is defined as the ratio of non-sea ice volume (air or snow in the sail and water in the keel) to the total ice feature volume (Høyland, 2002). The macroporosity is normally obtained by cross-sectional drilling, which provides linear macroporosity measurements (the experimental setup is described in Section 3.2). The microporosity is defined as the gas and brine volume sum relative to the total pure ice volume. The microporosity is estimated by measuring the temperature, density and salinity of ice samples. Equations are provided in Cox and Weeks (1983) for ice temperatures colder than -2°C and in Leppäranta and Manninen (1988) for ice temperatures warmer than -2°C . For level ice with zero macroporosity, the term “total porosity” is used where we use microporosity (Cox and Weeks, 1983; Johnston, 2006; Leppäranta and Manninen, 1988; Timco and Frederking, 1990).

Many studies have presented information on ridge porosity, especially macroporosity. However, several of these studies failed to specify whether the measurements are of the keel macroporosity (η_{keel} including the consolidated layer) or the rubble macroporosity (η_{ru} , the unconsolidated part only). Additionally, few studies have described the seasonal development of macroporosity, and to our knowledge, only Leppäranta et al. (1995) described seasonal development into the decay phase. The ridge macroporosity (η_r) is a function of the sail and keel macroporosities and thicknesses. Because the volume of the sail is small, we concentrate on the keel macroporosity, which is a function of the consolidated layer thickness (h_c), rubble thickness ($h_{ru} = h_{keel} - h_c$), and rubble macroporosity (h_{keel} denotes the keel thickness). During the main phase, the consolidated layer grows; therefore, the keel macroporosity will decrease even if the rubble macroporosity is unchanged (as reported by Leppäranta et al., 1995). Many studies have reported rubble macroporosity values of 30–35% (Høyland, 2007; Leppäranta and Hakala, 1992; Leppäranta et al., 1995; Strub-Klein and Sudom, 2012). However, measured macroporosity values range from 12% (Kharitonov, 2008) and 11% (Høyland, 2007) to 45% (Høyland, 2007). Because Kharitonov and Høyland used different methods, the values may not be directly comparable, but the two ridges studied by Høyland (2007) were measured with the same method and equipment and are directly comparable. The low value (11%) was measured in an old first-year ridge, and the high value (45%) was measured in a newly formed first-year ridge, both of which were measured in mid-May. These data from other studies and our data presented in this paper suggest that the rubble macroporosity decreases from an initial value throughout the lifetime of a first-year ridge. The initial macroporosity is a function of several parameters, including the formation process and ice and snow thicknesses, which are also important. The values of these parameters result in different block sizes, and based on granular materials, the block size distribution governs the packing and macroporosity. Surkov

(2000) performed laboratory tests on ice rubble and suggested a function for the initial ice rubble macroporosity as a function of block length to thickness.

2.3. Strength of the consolidated layer

Ridge strength can be defined in several ways depending on scale, confinement and boundary conditions. The thickness and small-scale strength of the consolidated layer, as well as the ice rubble amount and rubble strength are important components of the full-scale ridge strength or resistance. In this paper, the small-scale vertical uniaxial compressive strength was measured to investigate the ice strength within both the consolidated layer and sail (experimental setup is described in Section 3.3).

The measured uniaxial compressive strength depends on the state of the material (temperature, strain rate, etc.), the type of material (grain size, gas or brine volume) and the testing equipment. Ice strength is often compared to microporosity; Timco and Frederking (1990) and Moslet (2007) developed equations for deriving uniaxial compressive strength from the microporosity. The microporosity affects small-scale strength by reducing the effective area that resists the applied load in a compression test. Thus, a sample with a high microporosity is expected to have a lower strength compared to a sample with very low microporosity, if all else being equal. The strength of ice decreases when the ice temperature increases, which occurs well before the ice decay phase begins. Johnston (2006) found that the borehole strength decreased with increasing brine volume until the ice became isothermal, a state in which the strength remained nearly constant, while the brine volume decreased. Based on visual ice core observations, Johnston argued that although the brine volume decreased, the microporosity increased because of the gas volume increase, which was due to brine drainage and solar radiation melting the ice lattice. Johnston (2006) omitted microporosity calculations in her study due to density measurement inaccuracies in the decaying ice. Measuring strength and calculating microporosity from measured ice temperatures, salinities and densities of decaying ice is particularly difficult. Due to high air temperatures ($T_{air} > 0^{\circ}\text{C}$) during the decay phase, brine drainage was enhanced during ice sampling compared to the main or initial phase when air temperatures were colder.

The failure mode of ice tested under uniaxial compression is either ductile or brittle (Schulson and Duval, 2009). A brittle failure is defined as a sharp drop in the stress-strain curve after peak stress, whereas a ductile failure is defined as a continuous decrease in the stress-strain curve after peak stress until the test is ceased.

3. Arctic Ocean expedition and measurements

3.1. Overview

N-ICE2015 was a multidisciplinary expedition extending from January 11 to June 23, 2015 and led by the Norwegian Polar Institute (NPI). The expedition occurred on the research vessel RV Lance, which was frozen into and drifted with the young sea ice in the Arctic Ocean. Two researchers from the Centre for Sustainable Arctic Marine and Coastal Technology (SAMCoT) were invited to study ridges on Floe 3 (May 21st to June 9th) and on Floe 4 (June 9th to June 23rd). Fig. 1 shows the ice floe drift trajectories and Table 1 provides an overview of the ridge work; see Table 2 in Section 4.2 for the results. Four first-year ridges were investigated: two ridges (R1 and R2) on Floe 3 and two ridges (R3 and R4) on Floe 4. Ridges R1, R2, R3 and R4 were visited 6 times (April 29–June 4), 6 times (May 24–June 3), 3 times (June 10–June 17) and twice (June 12–June 17), respectively.

Fig. 2 shows the ridge measurement sites. The flags indicate the positions of drill holes used to estimate the ridge geometry and macroporosities. A ridge tracking buoy with a 10-m long vertical thermistor string was deployed (labeled OTB in Fig. 2a and d) in the center of the

drill transect of R1 on April 29 and R4 on June 12 (see Shestov et al. (2018) for full description and analysis). Furthermore, cores used to measure temperature, salinity (in all four ridges) and small-scale strength (in R1, R2 and R3) were sampled at 0.5 m from the center of the ridge crest (labeled OTB in Fig. 2a and d).

3.2. Macroporosity and structural measurements

Macroporosities were measured in R1 on May 22 ($T_{air} - 11.1^{\circ}\text{C}$) and repeated on June 3/4 ($T_{air} - 0.2^{\circ}\text{C}$), in R2 on May 24 ($T_{air} - 7.7^{\circ}\text{C}$) and repeated on May 31 ($T_{air} - 4.3^{\circ}\text{C}$), in R3 on June 10 ($T_{air} - 1.9^{\circ}\text{C}$) and in R4 on June 12 ($T_{air} - 0.8^{\circ}\text{C}$). Cross-sectional drilling of the ridge was performed, similar to previous studies (Høyland, 2007; Leppäranta et al., 1995; Shestov, 2011; Strub-Klein et al., 2009), and the transect drill holes were perpendicular to the ridge length. The schematic in Fig. 3 shows the different ridge features (sail, consolidated layer and rubble), in which the keel includes both the consolidated layer and rubble. The vertical lines represent drill holes, the light gray shading represents ice, and the dark gray sections of the vertical lines represent voids. During drilling, one person operated a 2-stroke engine connected to a series of 5.1 cm augers, each 1 m in length. The drill operator reported the ridge drilling resistance to a second person who took notes and measured the drill drops with a measuring rod adjacent to the drill auger. The ice hardness was recorded based on the drilling resistance and graded as hard (red), medium (orange) or soft (yellow). All the drill drops were voids of non-sea ice and were used to calculate the macroporosity. In practice, mechanical drilling provides a linear macroporosity that is calculated by dividing the total void length by the total length of the ice feature (sail, rubble, keel and ridge). This calculation yields an average macroporosity, which is different from averaging the macroporosities in each drill hole. When drilling a transect across a single ridge, drill holes were spaced 1–2 m apart. Cross-sectional drilling was repeated across ridges R1 and R2 after approximately a week. The second drill transect was shifted 10–30 cm to the side from the previous drill transect. The repeated cross-section drillings were used to calculate the average ice ridge ablation rates. The turbulent heat flux was obtained from the specific heat of the seawater, which was calculated from the measured values of the water temperature and vertical oceanic current following standard methods reported in (McPhee, 2008). These measurements are presented and analyzed in (Peterson et al., 2017).

The transition from the consolidated layer to unconsolidated rubble was defined as either the transition to soft ice or by the first drop of the drill. Alternatively, the break point between the linear temperature profile above the isothermal rubble was used to define the consolidated layer thickness (h_c (T) in Table 2). The sail height was the freeboard. The keel depth was the vertical distance from the freeboard to the end of the hole, and the rubble depth was the vertical distance from the consolidated layer bottom to the end of the drill hole. The thickness and macroporosity measurements involve uncertainties, such as drill chips filling boreholes, drill augers jamming, drill augers bending and a subjective interpretation of the transition from the consolidated to unconsolidated layer. The measurement error of the keel depth was less than one decimeter, which was obtained by comparing drilling data to data from a purpose-made tape measure.

3.3. Strength, temperature and salinity measurements

The small-scale uniaxial compressive strength, temperature and salinity (TS) were measured in cores sampled from the thickest part of the ridge, which was 10–50 cm from the highest flag on the cross-sectional drilling line and is shown in Fig. 2a, b and c. First, temperature was measured with a temperature probe (accuracy 0.3°C) in holes made along the core using a hand-held drill with a spacing of 10 cm. Second, each core was divided into 10–20 cm-long ice samples, placed in sealed boxes and melted for salinity measurements using a

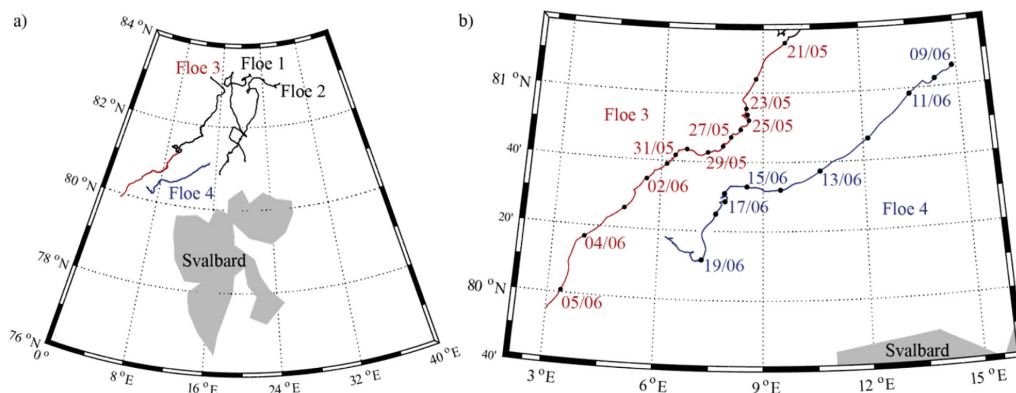


Fig. 1. a) Drift trajectories of all four floes visited during the N-ICE2015 expedition and b) drift trajectories of Floe 3 and Floe 4 when ice ridge work was conducted. The distance to the ice edge on Floe 3 was approximately 200 km on April 26 and 40 km on June 5, and on Floe 4, the distance was approximately 70 km on June 9 and 15 km on June 17 (Oikkonen et al., 2017).

conductivity sensor with an accuracy of 0.01 ppt. The small-scale strength was measured by compressing the 17.5-cm-long ice samples from the sail and consolidated layer with cross-sectional diameters of 7.2 cm in a mobile compression machine (KOMPIS). The measurements were conducted a few meters from the sampling site within 10 min of sampling on May 26 ($T_{air} - 4.2\text{ }^{\circ}\text{C}$) in R2, May 29 ($T_{air} - 4.3\text{ }^{\circ}\text{C}$) in R1 and June 13 ($T_{air} - 0.4\text{ }^{\circ}\text{C}$) in R3. A saw with two parallel blades separated by distances equivalent to the necessary sample length ensured that the sample ends were parallel and sample lengths were consistent. The nominal strain rate was 10^{-3} s^{-1} , and previous studies have published results obtained using the same machine (Høyland, 2007; Moslet, 2007; Shafrova and Høyland, 2008). Unfortunately, a thin steel bracket between the load cell and lower plate that compressed the ice sample was missing during N-ICE2015. This resulted in a small gap between the load cell and lower plate, which had to be compensated for by the combined compliance of the machine and load cell. Subsequent service and recalibration of the machine showed that the measured loads (0.3–5 kN) were consistently underestimated by approximately 2 kN.

Despite this error, we judged the relative load difference to be valid, even though the absolute values of the loads (and thus, the ice strengths) are erroneous. The machine stiffness was accounted for in the effective modulus (or secant modulus) calculation, which was described in Timco and Frederking (1984), and the machine stiffness value provided in Moslet (2007) was used.

4. Results and discussion

4.1. Overview

A total of four ridges (R1, R2, R3 and R4) on two ice floes (Floes 3 and 4) were investigated. The goal was to investigate changes in the rubble macroporosity, ridge drilling resistance, and small-scale uniaxial compressive strength of the consolidated layer. Fig. 4 shows the air temperature (2-m-level), wind speed (10-m-level) and drift speed measurements from a meteorological tower moored on each floe approximately 300–400 m away from the ship (Cohen et al., 2017;

Table 1
Overview of activities related to Floes 3 and 4. The RV Lance GPS positions and temperatures are given at 12 AM on the relevant date. See Table 2 for results.

Date	RV lance location		Activity	Feature	Temperature, °C		
	Latitude °N	Longitude °E			Air		
Floe 3	29 April	82.0676	13.4587	OTB	R1	-13.9	
	22 May	81.0621	8.7698	MAP	R1	-11.1	
	24 May	80.8935	8.5268	MAP	R2	-7.7	
	26 May	80.8219	8.3246	COMP, TS	R2	-4.2	
	27 May	80.7849	8.0394	TS	R1	-5.3	
	28 May	80.7431	7.8077	GRAD	R2	-4.8	
	29 May	80.7123	7.3613	COMP	R1	-3.7	
	31 May	80.6942	6.3963	MAP, TS	R2	-4.3	
	02 June	80.5728	5.5484	GRAD	R2	-0.5	
	03 June	80.4363	5.0313	CORE, MAP	R2/R1	-0.2	
	04 June	80.2770	3.8751			-0.3	
	Floe 4	10 June	81.0354	14.2823	MAP, TDS	R3	-1.9
		12 June	80.7629	12.0677	MAP, OTB	R4	-0.8
		13 June	80.6239	10.7006	COMP	R3	-0.4
17 June		80.4758	7.8862	MAP, TS, TS	R3	1.7	
					R4		

COMP: Small-scale compression tests.
 OTB: Oceanic Thermistor Buoy deployment.
 CORE: Sampling cores to bring back to UNIS.
 MAP: Ridge cross-sectional drilling.
 TS: Temperature and salinity profile core.
 GRAD: Ice block measurement.

Table 2

Evolution of ridge geometrical properties and temperatures. Geometrical properties were defined in Section 2.2. Each column represents one drill transect. The notation \pm indicates the standard deviation. CoV is the variation coefficient. The consolidated layer thickness (h_c) was obtained from both drilling and the break point between the linear temperature profile above the isothermal rubble (T).

Ridge	R1	R1	R2	R2	R3	R4
Date	22.05.15	03/04.06.15	24.05.15	31.05.15	10.06.15	12.06.15
Number of holes	15	11	20	19	11	5
Spacing [m]	2	2	1	1	2	4
Sail height [m]	2.5	1.9	1.3	1.5	1.3	1.8
Max keel depth [m]	10.8	10.6	3.2	3.3	4.8	7.3
Snow thickness [cm]	60 \pm 39	61 \pm 36	13 \pm 17	4 \pm 5	73 \pm 32	75 \pm 49
Ridge area [m ²]	153 ^a	141 ^a	28	20	79	101
h_c (drilling) [m]	2.5 \pm 1.2	2.7 \pm 1.4	0.8 \pm 0.3	0.8 \pm 0.4	2.3 \pm 1.4	3.0 \pm 1.9
CoV h_c [%]	49	49	39	48	60	63
h_c (T) [m]	2.6	2.8 (June 1)	0.7 (May 26)	0.9	–	–
Ridge width [m]	28 ^b	20 ^b	19.5	19.5	20 ^b	16 ^b
Ridge length [m]	200	200	500	500	75	150
Ridge macroporosity	9%	6%	12%	7%	8%	8%
Sail macroporosity	30%	17%	13%	18%	0%	0%
Keel macroporosity	6%	6%	12%	4%	8%	8%
Rubble macroporosity	11%	10%	25%	16%	22%	27%
Date	27.05.15	01.06.15	26.06.15	31.05.15	10.06.15	17.06.15
Mean sail temperature [°C]	–5.6	–5.4	–4.0	–2.4	–1.5	–0.9
Mean h_c temperature [°C]	–4.5	–3.5	–2.9	–2.3	–2.1	–1.8
Mean rubble temperature [°C]	–1.8	–1.7	–1.9	–	–1.8	–

^a For ridge R1, the area was computed based on the 11 holes that were drilled twice, equal to a cross-section length of 20 m.

^b Level ice was not found on either side of the ridge; this is the drill cross-section length.

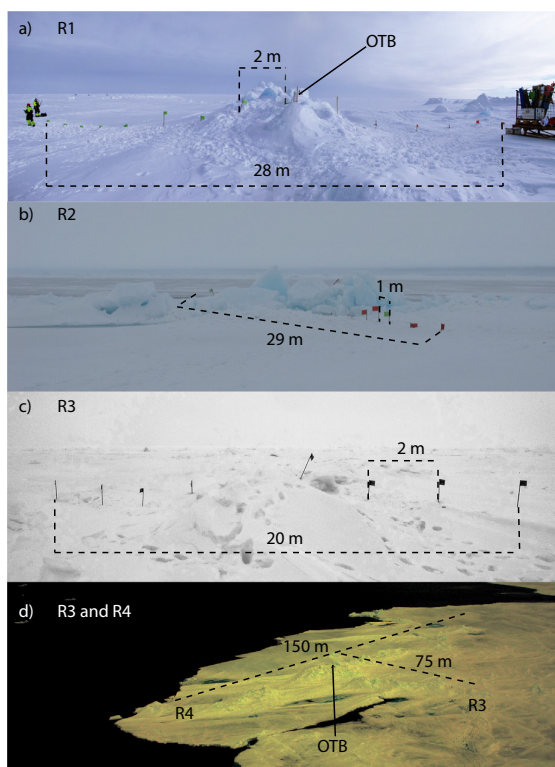


Fig. 2. Ridge measurement sites, where the flags mark the positions of drill holes: a) R1 on May 22, b) R2 on June 2, c) R3 on June 10, and d) R3 and R4 on June 23. The ridge width is displayed in a) and b), and the ridge length is displayed in c). The OTB shows the position of the thermistor chain.

Hudson et al., 2015). The ocean current at 1 m below the level ice was measured a few hundred meters away from the ship in a turbulent instrument cluster (TIC) (Peterson et al., 2017). Ridge R1 (maximum thickness of 13 m and length of 200 m) formed before April 18, and the ridge was still intact when the ship left Floe 3 on June 5. The ridge was instrumented with a thermistor string (accuracy 0.1 °C) on April 29, which logged hourly temperatures until June 1. Ridge R2 (maximum thickness of 5 m and length of 500 m) formed during a storm when a refrozen lead was pushed against the thicker level ice from April 26–April 30, and this ridge broke up on June 4. The formation and break up of R2 was captured by the ship’s radar (Haapala et al., 2017) and observed from the ship. During the storm, the peak wind speed was 14.3 m/s (Cohen et al., 2017), and the snow cover was approximately 2 cm (Rösel et al., 2016). Ridges R3 (maximum thickness of 6 m and length of 75 m) and R4 (maximum thickness of 9 m and length of 150 m) both formed before June 8.

4.2. Macroporosity and ridge structure evolution

4.2.1. Ridges R1 and R2

The macroporosities, geometries (including thicknesses), and average temperatures of the different parts of the four ridges are provided in Table 2. The transition from the main phase to the decay phase occurred at the beginning of June (Table 1 and Fig. 4a). Therefore, ridges R1 and R2 were mapped toward the end of the main phase (in May), whereas ridges R3 and R4 were measured during the decay phase (in June). Ridges R1 and R2 were mapped twice so that temporal development could be evaluated. Only ridge R2 featured level ice at the boundaries of the drill transect, which allowed the ridge cross-section width to be estimated. Level ice thickness was measured repeatedly throughout the expedition (Rösel et al., 2016). The surrounding level ice thickness on the lead from which ridge R2 formed was measured with an electromagnetic ground conductivity geophysical instrument (EM-31) along a 1-km-long transect on May 8, May 11, May 18, May 28 and June 1; the mean ice thicknesses with standard deviations on the respective days were 20 \pm 1 cm, 24 \pm 1 cm, 23 \pm 1 cm, 23 \pm 1 cm and 22 \pm 1 cm, respectively. Based on measurements from 18 drill holes on May 5, the level ice thickness on the refrozen lead was 18 \pm 4 cm, and the snow thickness was 2 \pm 0.5 cm. For ridges R1, R3 and R4, the ridge width could not be determined, even if the ice

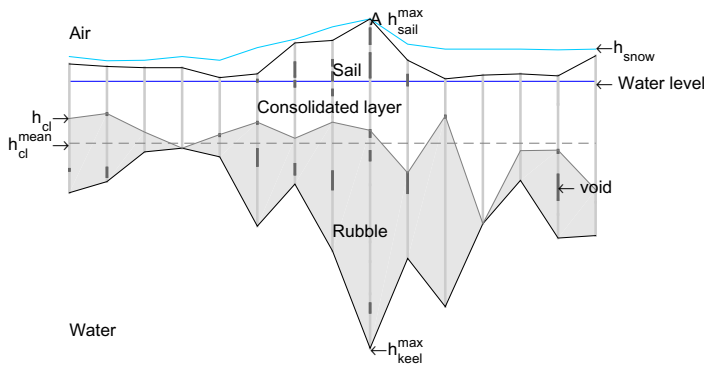


Fig. 3. Features of an ice ridge including: the ridge sail, consolidated layer and rubble. The light blue colour is snow cover, the dark blue is water surface, and the black lines are ridge boundaries. The vertical lines are drill holes, the light gray shading is ice, and the dark gray sections of the vertical lines represent voids. This figure shows R1, which was drilled on May 22. (For interpretation of the references to colour in this figure legend, the reader is referred to the web version of this article.)

appeared level on the surface adjacent to the ridge sail.

In ridge R2, the dimensions (length L , width w , thickness h_b and tilt α) of 101 ice blocks were measured in an approximately 100 m² polygon, which was centered on the drilling transect.

Table 3 provides an overview of the measured ice block dimensions, which include h_b , L , w and α of $N = 101$ ice blocks in the R2 ridge sail. Fig. 5 shows the ice-block length compared to thickness as well as the ice-block-thickness histogram. The large block thickness variations (from 5 to 65 cm) have two possible explanations. First, the level ice on the lead may have been thicker on the lead edges compared to the lead center. Second, rafting likely occurred. Hopkins et al. (1999) showed that during thin ice ridging, rafting was often observed. Bonnemaire et al. (2003) also found a large variation in ice-block thicknesses in one Barents Sea ridge (20–190 cm) and separated the variations into three block thickness groups, which were 1, 2 and 3 times the level ice thickness from which the ridge was formed. Bonnemaire suggested that the level ice rafted, broke and piled during ridging. The R2 block thicknesses (Fig. 5b) can also be divided into three groups of

Table 3

Ice block measurements for ridge R2 where h_b is the thickness, L is the length, w is the width, α is the tilt, N is the number of ice blocks, and STD is the standard deviation.

	h_b [m]	L [m]	w [m]	α [°]	L/h_b [-]	w/h_b [-]	L/w [-]	N [-]
Maximum	0.6	2.6	1.8	90	11.6	8.3	3.8	101
Average	0.17	0.59	0.38	32	4.0	2.6	1.6	101
STD	0.13	0.51	0.35	29	2.1	1.4	0.4	101

approximately 1, 2 and 3 times the level ice thickness (5–20 cm, 20–40 cm and 40–65 cm, respectively). These thicknesses indicate that the ridge was formed from level ice on the refrozen lead rafting, breaking and piling against the thicker level ice.

Ridges R1 and R2 were both exposed to the same meteorological-oceanic environment, but the consolidated layer thickness (h_c) in R1 was greater than that in R2, mainly because R1 was exposed to a larger

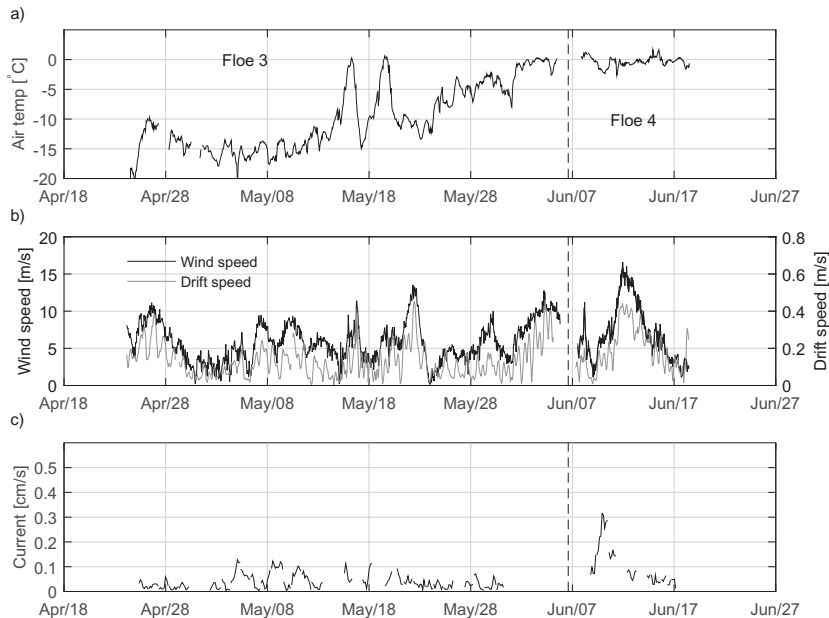


Fig. 4. Hourly time series of a) air temperature, b) wind and drift speeds and c) current speed. The dashed line separates the data collected on Floe 3 (left side) and Floe 4 (right side).

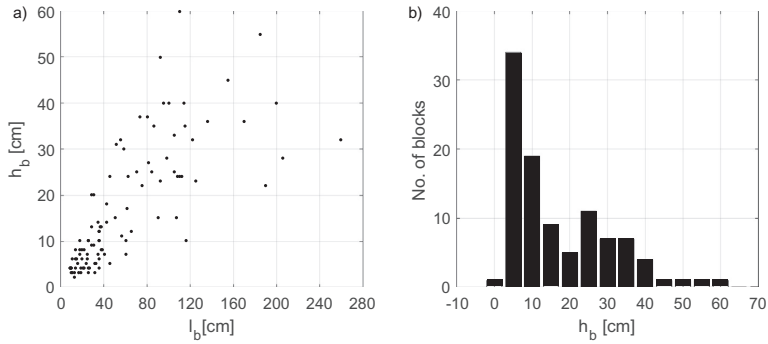


Fig. 5. Morphology of ice blocks in the R2 ridge sail. a) Ice-block thickness vs. length and b) ice-block-thickness histogram.

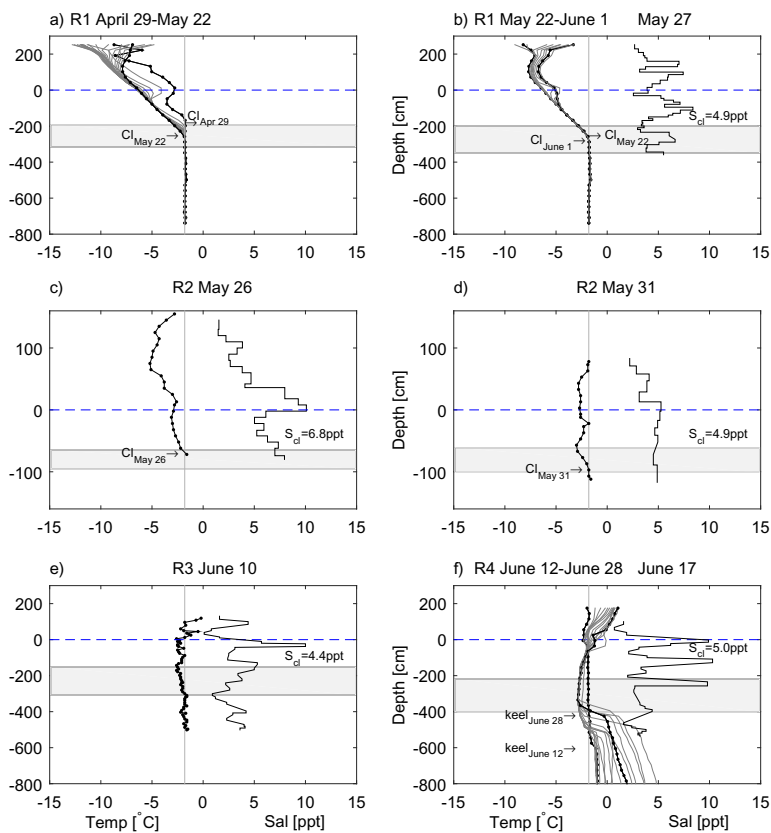


Fig. 6. In situ TS profiles. In R1 and R4, the temperature was measured in the thermistor chains, and the hourly data for each node were averaged for the entire day (dark gray lines). In R2 and R3, the temperature was measured in the ice cores (black lines). The vertical light gray line shows the approximate freezing point. The blue dashed line represents the water level. S_{cl} shows the mean salinity of the consolidated layer. The gray shading is equal to $\bar{h}_c \pm 0.5STD$, which was obtained from mechanical drilling. The temperature was measured as follows: a) R1 on April 29–May 22, b) R1 on May 22–June 1, c) R2 on May 26, d) R2 on May 31, e) R3 on June 10 and f) R4 on June 12–June 28. Salinity was measured as follows: a) no salinity measurement b) R1 on May 27, c) R2 on May 26, d) R2 on May 31, e) R3 on June 10 and f) R4 on June 17. Dates for mechanical drilling include the following: a) R1 on May 22, b) R1 on June 3/4, c) R2 on May 24, d) R2 on May 31, e) R3 on June 10, and f) R4 on June 12. (For interpretation of the references to colour in this figure legend, the reader is referred to the web version of this article.)

number of freezing degree days (FDD) and formed from thicker level ice. The mean h_c based on drilling was 2.5 m in R1 on May 22, 2.7 m in R1 on June 3/4, 0.8 m in R2 on May 24, and 0.8 m in R2 on May 31. Based on the temperature gradients (see Fig. 6), the h_c was 2.6 m in R1

on May 22, 2.8 m in R1 on June 1, 0.7 m in R2 on May 26, and 0.9 m in R2 on May 31; this finding indicates that the difference between mean h_c obtained from drilling and temperature gradients was ± 0.1 m. For ridges R1 and R2, the maximum-to-average ratio for h_c (from drilling)

was an average of 2 (1.85–2.30), and the minimum-to-average ratio was an average of 0.47 (0.35–0.56). These numbers are slightly less varied than are the corresponding values (2 and 0.38) of the four ridges measured in the Barents Sea in the spring by Høyland (2007), whereas the variation was larger than that of the corresponding values (1.61 and 0.51) measured by Timco and Burden (1997). The variation in h_c is due to both the subjective transition observation and the natural variation in the ice block orientation inside the consolidated layer. Obtaining accurate h_c measurements is difficult; however, obtaining drilling and temperature data is the only currently available technique.

Considerable rubble transformation occurred in R2 (rubble macroporosity decreased from 25% to 16% between May 24 and May 31), whereas little transformation occurred in R1 (macroporosity changed from 11% to 10% between May 22 and June 3/4). The R1 sail macroporosity decreased, which caused a decrease in the ridge macroporosity from 9% to 6%. In contrast, the decreasing ridge macroporosity in R2 (from 12% to 7%) was due to keel processes. Additionally, the sail macroporosities were derived from a relatively small number of drill holes, and therefore, the measured values are less certain.

The keel and rubble macroporosities were constant in R1 (6% and 11%–10%, respectively), whereas both the keel and rubble macroporosities decreased in R2 (from 12% to 4% and from 25% to 16%, respectively). Both Kharitonov (2008) and Høyland (2007) reported similar values. We suggest that the different ice rubble macroporosities in R1 and R2 are mainly caused by different permeabilities in these ridges. Ridge R1 was larger, colder and older, whereas R2 was a younger, smaller ridge that formed from warm ice. Ridge R1 was exposed to a longer history of heat transport from the warm ocean in comparison to R2, which resulted in a lower rubble macroporosity. The differences in driving forces, initial level ice and snow thickness also affect the initial rubble macroporosity. The Surkov (2000) model and mean ice-block length to thickness ratio in R2 ($\bar{l}/\bar{h}_b = 4.0$) give an initial macroporosity of approximately 45%, which is the same as that measured in a young, first-year ridge (Høyland, 2007). The snow cover on the refrozen lead, from which R2 was formed, was thin (approximately 2 cm); thus, we expect few snow-filled voids and a negligible effect on the initial rubble macroporosity. Ice-block and initial snow-thickness data were not collected for R1.

The melt rates were similar: 0.92 m²/day in R1 and 1.14 m²/day in R2 (both over a width of 20 m). The water temperatures increased to approximately 0.1 °C above freezing, and the turbulent oceanic flux (q_{ocean}) was in the range of 10–15 W/m² during Floe 3 (Peterson et al., 2017). Eq. (1) expresses a simple way of estimating the melt rate (dh/dt) when the oceanic flux (q_{ocean}) is known. ρ_i and l are the ice density and latent heat of formation, respectively.

$$\frac{dh}{dt} = \frac{q_{ocean}}{\rho_i \cdot l \cdot (\text{ice fraction})} \quad (1)$$

Using Eq. (1), the 10–15 W/m² oceanic heat flux would melt 0.3–0.4 cm/day of level ice with an ice fraction of 0.8, ice density ρ_i of 917 kg/m³ and a latent heat of fusion l equal to 333.4 kJ/kg. This would result in a melt rate equal to 0.07–0.11 m²/day over 20 m width, which is only approximately 10% of the observed reduction in keel depths. Along with the findings of Amundrud et al. (2006), Ekeberg (2015) and Hansen et al. (2015), this observation indicates that first-year ridge keels melt more easily than the level ice. This phenomenon may be due to (at least) two reasons: a) ridge keels penetrate deeper than level ice and have a greater exposure area, and b) first-year ridge keels are more permeable than are level ice. Additionally, a reduction in keel depth results from rubble packing as well as a corresponding reduction in rubble macroporosity and from sail melting, which causes percolating water to freeze in the interstices. Turbulent oceanic heat flux measurements for Floe 4 were in the range of 20–400 W/m² (Peterson et al., 2017). Thermodynamic calculations presented in Shestov et al. (2018)

indicate that the observed keel melt in R4 (2 m from June 12 to June 28, Fig. 6f) coincided with an oceanic heat flux equal to 298 W/m².

4.2.2. Ridges R3 and R4

Ridges R3 and R4, which were investigated during the decay phase, were only mapped once, and thus, no temporal development can be described. The R3 and R4 consolidated layer thicknesses (2.3 and 3.0 m, respectively) were similar to those of R1. The nearly isothermal data ceases to show the transition from the consolidated layer to the rubble (see Fig. 6e and f). The surface melting progressed to a point where the sail macroporosities decreased to zero, and both ridges were nearly isothermal (a portion with relatively cold temperatures remained in R3, Fig. 6e). Moreover, upon bottom melting onset, an increasing amount of ice slush was observed in the drill holes. Thus, as melting progressed, it became increasingly difficult to feel the transition between the consolidated ice and rubble during drilling, and the structural measurements in R3 and R4 were less certain. For ridges R3 and R4, the maximum-to-average ratio for h_c was an average of 1.95 (1.83–2.07), and the minimum-to-average ratio was an average of 0.3 (0.15–0.45). These numbers show larger variations than do both of the corresponding values (2 and 0.38) obtained by Høyland (2007), by Timco and Burden (1997) (1.61 and 0.51), and (2 and 0.47) in R1 and R2.

The rubble macroporosities (22% in R3 and 27% in R4) were higher than those in R1 and more in line with the previously reported values of 30–35% (Høyland, 2007; Leppäranta and Hakala, 1992; Leppäranta et al., 1995; Strub-Klein and Sudom, 2012). Furthermore, the high rubble macroporosity (compared to the ridge and keel macroporosities) of ridge R3 (22%) appear to be partly due to the small volume of rubble and a single large void (Fig. 7c) inside the rubble. By removing the hole with the single large void, the calculated rubble macroporosity is 6%, instead of 22%. To obtain the actual rubble macroporosity, the spacing between the holes should be reduced. The number of holes penetrating the rubble and the spacing between the holes, respectively, were as follows: 13 holes and 2 m in R1 (May 22), 10 holes and 2 m in R1 (June 3/4), 10 holes and 1 m in R2 (May 24), 5 holes and 1 m in R2 (May 31), 8 holes and 2 m in R3 (June 10) and 4 holes and 2 m in R4 (June 12).

The rubble macroporosities in our four studied ridges ranged from 10% to 27% and were measured using the same equipment and method. The two macroporosity reducing processes described by Shestov and Marchenko (2016a,b) may explain the measured macroporosity development. First, the strong non-linear specific heat capacity (Schwerdtfeger, 1962) during heating results in a transformation from macro to microporosity. Second, a cyclic change in the water salinity, which was caused by percolation of fresh meltwater inside the rubble cavities would draw energy out of the rubble and contribute to further consolidation and reduction in the macroporosity. This process occurs without measured temperature gradients, and thus, to understand macroporosity reducing processes, the salinity inside the rubble cavities should be continuously measured in a future experiment. Mechanical erosion, flushing, gravitational adjustments and drift-induced turbulence may also affect the ridge structure and macroporosity.

4.3. Evolution of drilling resistance and strength in relation to physical properties

4.3.1. Drilling resistance

The drilling resistance was greater in cold ice ($T < -1.8$ °C) than that in warm ice ($T \approx -1.8$ °C). The ice was soft throughout ridges R3 (Fig. 7e) and R4 (Fig. 7f) on June 10 and 12, respectively, when both ridges were nearly isothermal (a small region of relatively cold temperatures remained in R3) (cf. Fig. 6e and f). Drilling hardness was measured in R1 on May 22 and June 3/4, in R2 on May 24 and May 31, in R3 on June 10, and in R4 on June 12. Repeated measurements of drilling hardness (next to one another in Fig. 7a–d) were used to quantify the transition from main phase to decay phase. For ridges R1 and R2, the drilling resistance of the sail and consolidated layer

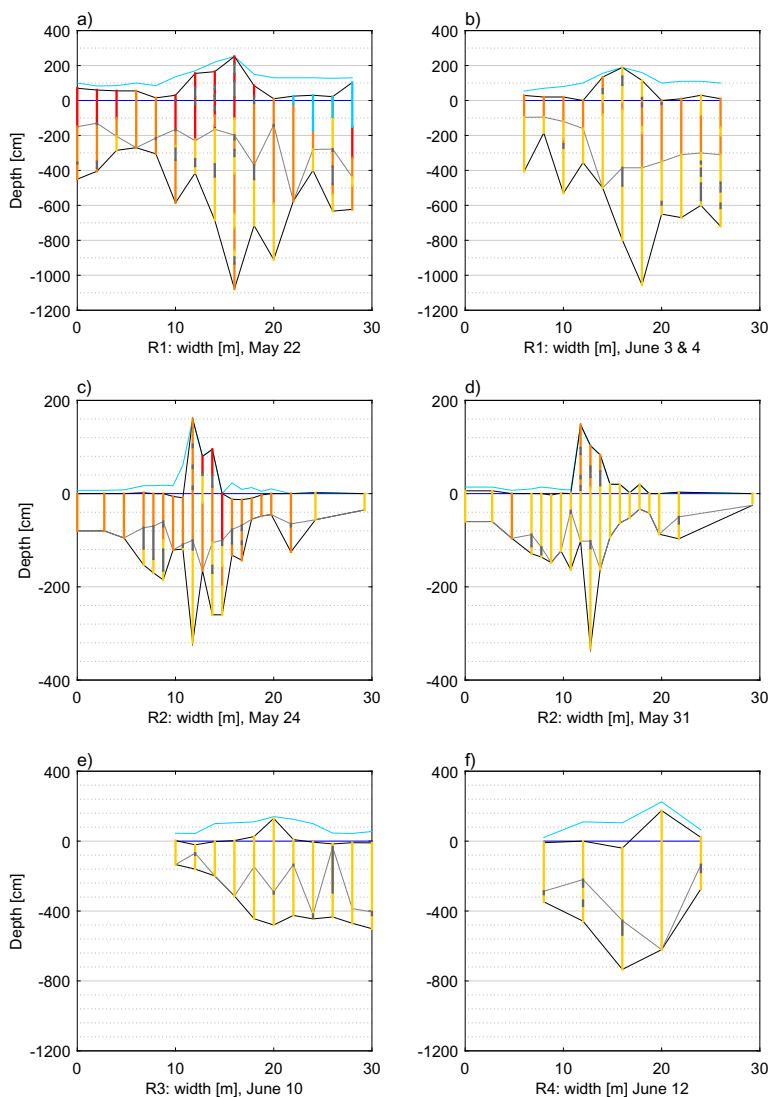


Fig. 7. Cross-sectional drilling of ridges. The light blue line is the snow thickness, the dark blue line is water freeboard, and the black lines are ridge boundaries. The thick vertical lines represent the drill holes: red is hard ice, orange is medium-hard ice, yellow is soft ice, light blue is snow ice, and dark gray represents voids. a) R1 drilled on May 22, b) R1 drilled on June 3 and 4, c) R2 drilled on May 24, d) R2 drilled on May 31, e) R3 drilled on June 10, and f) R4 drilled on June 12. Note that ridge R2 (c, d) is plotted at half the scale of R1 (a, b) and R3 (e, f). (For interpretation of the references to colour in this figure legend, the reader is referred to the web version of this article.)

decreased between measurements. The drilling resistance decrease was consistent with the ice temperature increase.

4.3.2. Small-scale strength

Small-scale uniaxial compressive strength field tests were completed for 21 samples in both the sail and consolidated layer. Consistent with the drilling resistance, the small-scale compressive strength measured in R1, R2 and R3 decreased when the in situ ice temperatures increased. Because of the measurement error described in Section 3.3, the strength and effective modulus were normalized by the maximum stress, which was measured among all ridge samples (σ_{max}). The strength values ranged from $0.06 \cdot \sigma_{max}$ to $1 \cdot \sigma_{max}$, and the ice temperatures ranged from $-1.8\text{ }^{\circ}\text{C}$ to $-6.9\text{ }^{\circ}\text{C}$. Fig. 8 shows the uniaxial compressive strength, effective modulus, ice TS of ice sample vertical profiles from the sail and consolidated layer. A horizontal or vertical sample refers to the cylindrical sample height orientation. The load was consistently applied along the cylindrical sample height. Ice TS (Fig. 8) were measured in a

separate ice core, which was sampled a few centimeters from the core used in the strength test. For ridge R1, the ice temperature was obtained using the OTB 908-20. The coldest ice temperature ($-6.9\text{ }^{\circ}\text{C}$) was measured in the R1 consolidated layer, which also yielded the highest measured strength value σ_{max} . Fig. 9 displays the mean strength and standard deviation compared to temperature rounded to the closest integer. The salinity obtained from the compressed samples were expected to under-predict the actual sample salinities due to brine drainage (Poplin and Wang, 1994). Therefore, we used separate cores to obtain the salinities and temperature. The brine volumes and strengths were averaged across the sail thickness and consolidated layer to present the overall change in strength with increasing ice temperatures.

The average brine volumes were estimated (Cox and Weeks, 1983; Leppäranta and Manninen, 1988) under a constant density assumption of 0.881 Mg m^{-3} , which was equal to the average density measured in the R2 samples. The average brine volume was 4.7% for R1 (salinity and temperature were measured on May 27 and May 29, respectively),

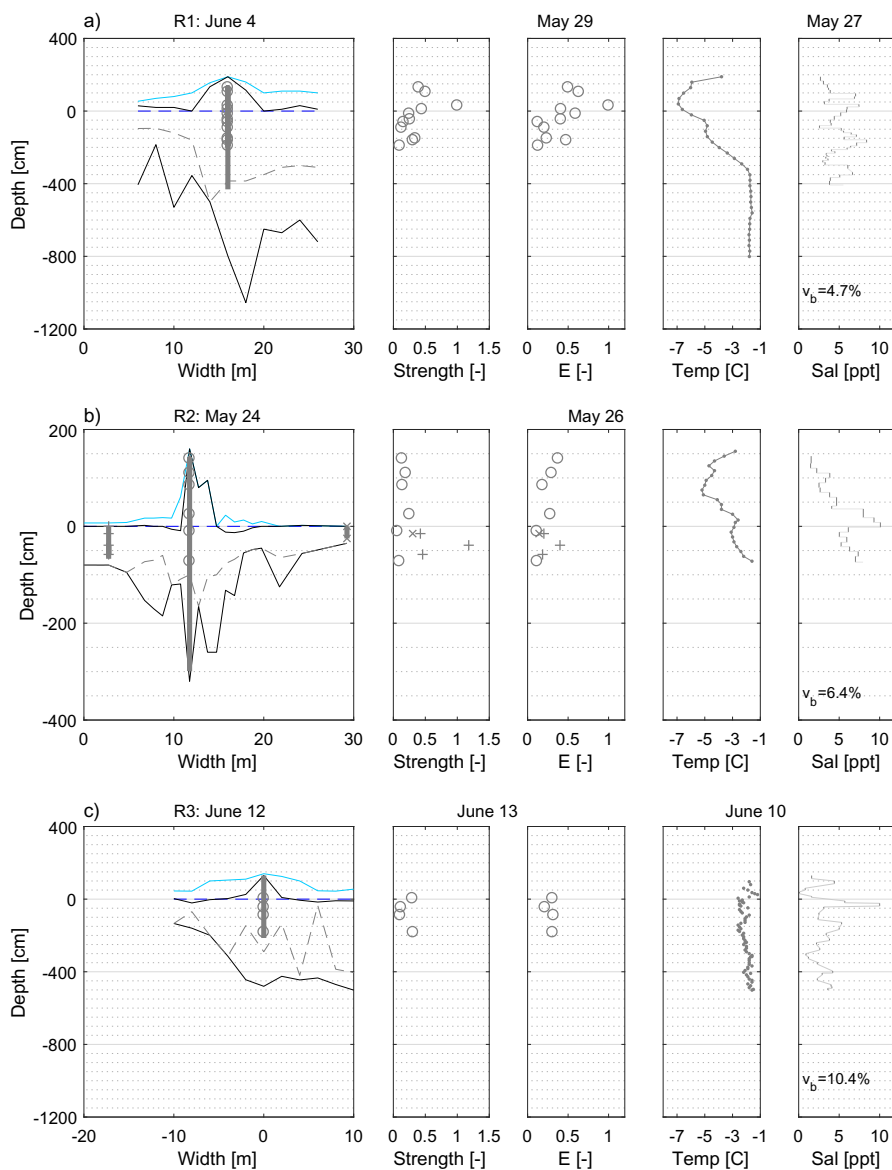


Fig. 8. Vertical uniaxial compression strength, secant modulus, TS. The dark gray points display temperature measurements. In a), the temperature is taken from the thermistor string (on May 29) and averaged for the whole day; in b) and c), temperatures were measured in cores. Level ice samples are (+, x) and ridge samples are (o). The dark gray bars in the salinity plot show the positions of salinity measurements. TS profiles were obtained from a different core than that which was used for uniaxial compression.

6.4% for R2 (May 26) and 10.4% for R3 (June 10). The average normalized compressive strengths were $0.4\sigma_{max}$ for R1 (11 samples on May 29), $0.2\sigma_{max}$ for R2 (6 samples on May 26) and $0.2\sigma_{max}$ for R3 (4 samples on June 13). The strength decreased until the ice temperature approached $-3\text{ }^{\circ}\text{C}$ (Fig. 9). For the ice samples tested on May 26 and June 13, the average temperature increased (from $-5.5\text{ }^{\circ}\text{C}$ to $-2.3\text{ }^{\circ}\text{C}$) and the average brine volume increased (from 4.7% to 10.4%), whereas the average strength decreased (from $0.4\sigma_{max}$ to $0.2\sigma_{max}$).

A similar development in borehole strength was measured by Johnston (2006) who found that the borehole strength continuously

decreased until the ice became isothermal at $-1.8\text{ }^{\circ}\text{C}$. When the ice became isothermal (in July and August), the brine drained and was replaced by air; thus, additional radiation increased the gas pocket volumes and increased the microporosity. The increase in gas volume and microporosity was visually observed in the ice cores. Johnston (2006) further suggests that when the microporosity reaches 15–20%, the strength changes very little with increasing microporosity. Moslet (2007) shows the same pattern for the horizontal level ice uniaxial compressive strength, which is similar to the consolidated layer strength. Høyland (2007) also found uniaxial compressive strength

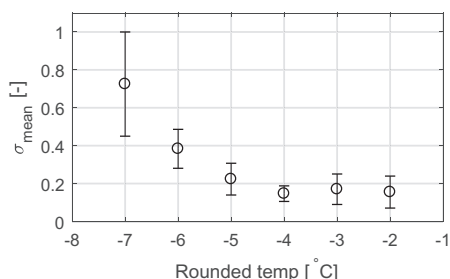


Fig. 9. Mean strength with standard deviation compared to temperature rounded to the closest integer.

values to level out for microporosity values above 15–20%.

The University Center in Svalbard (UNIS) conducted field measurements of decaying ice strength using the same compression machine (KOMPIS) as used for our measurements. From 2004 to 2011, several annual expeditions were performed on the Arctic ice cover offshore of Svalbard. During these expeditions, the small-scale strengths of > 3000 ice samples were measured in the field via uniaxial compression (with KOMPIS). Among these expeditions, one was conducted on decaying ice on June 7–8, 2004 in the Van Mijen Fjord of Svalbard (data from Moslet (2007)). During this expedition, 45 vertical samples of level ice were compressed. The temperature, salinity and density of each sample were also measured. The results from these measurements are shown in Fig. 10. When the ice was at or warmer than -1.8°C , any increases in the brine volume had a negligible effect on the ice strength. The correlation between strength and microporosity was similar to that between strength and brine volume. The gas volume did not change with increasing temperature. Similar to Johnston (2006), Moslet (2007) and Høyland (2007), the sample ice strengths collected from the Van Mijen Fjord rapidly decreased until the ice cover reached an isothermal state, and the brine volume exceeded 15–20%; at this point, the ice strength remained constant and was unaffected by further increases in brine volume. Measuring the strength and physical properties of the decaying ice was difficult because the air temperature exceeded T_f , which enhanced the brine drainage. More data are required to better understand how changes in microporosity affect the strength in decaying ice.

4.3.3. Effective modulus

The effective (elastic) modulus profiles were similar to the compressive strength profiles (Fig. 8), where an increase in temperature resulted in a decrease in effective modulus. Taking the stiffness of the testing machine (KOMPIS) into account produced only a negligible effect (a maximum increase of 5%) on the sample's effective modulus. For vertical level ice samples tested in the field using KOMPIS, Moslet (2007) found that the microporosity had a strong effect on the elastic modulus, and the elastic modulus continuously decreased with increasing microporosity. Although the elastic modulus (Moslet, 2007) is not directly comparable to the effective (secant) modulus (N-ICE2015-data), the effective modulus decreased until the ice reached an

isothermal state, which is similar to the changes in strength. Furthermore, the increased ice temperature induced an increase in brine volume as well as microporosity. However, when the ice temperatures were isothermal, both the strength and effective modulus remained constant and were unaffected by further increases in microporosity.

4.3.4. Observed failure modes

During N-ICE2015, all the compressed samples were ductile except for the two strongest (σ_{max} and $0.6\sigma_{\text{max}}$) and coldest (-6.9°C and -6.2°C) R1 samples. The decaying ice failure mode was also observed via uniaxial compression tests on vertical level ice samples, which were tested in the field in 2004 in the Van Mijen Fjord, and the data are from (Moslet, 2007). According to these measurements, 92% of the level ice samples of decaying ice experienced ductile failure. For samples colder than -1.8°C , only 33% of the samples experienced ductile failure. All level ice samples (sampled in Van Mijen Fjord in 2004 displayed in Fig. 10) with microporosities above 15–20% experienced ductile failure. The correlation between microporosity and failure mode in ice ridge samples was also measured in the field by Høyland (2007), who found that 96% (total 129 samples) experienced ductile failure when the microporosity was above 15–20%. Moreover, Moslet (2007) showed that level ice samples with gas volumes > 7% failed in a ductile manner. However, ductile failure was not observed in the ridge samples tested by Høyland (2007). Moslet (2007) and Høyland (2007) both used the same experimental setup and equipment, which are described in Section 3.3. The averages and standard deviations of the strength, temperature and brine volume of the 2004 data in Fig. 10 were $6 \pm 1 \text{ MPa}$, $-2.1 \pm 0.2^{\circ}\text{C}$ and 0.10 ± 0.01 , respectively, for the brittle samples and $1 \pm 1 \text{ MPa}$, $-1.3 \pm 0.7^{\circ}\text{C}$ and 0.20 ± 0.10 , respectively, for the ductile samples. This finding indicates that the decaying ice was ductile, and the strength changed less with the brine volume (microporosity) than that with the brittle samples (see Fig. 10).

5. Conclusions and recommendations

In this paper, we have presented measurements obtained from drifting ice in the Arctic Ocean in May and June 2015. The changes in rubble macroporosity, ridge drilling resistance and the sail and consolidated layer strengths were investigated. The repeated measurements showed that the rubble macroporosity in the decaying saline first-year ridges decreased and reached a minimum measured rubble macroporosity of 10%. We suggest that the rubble macroporosity in saline ridges continuously decreases over the life of a first-year ridge and that the process accelerates during the decay phase. A decrease in drilling resistance was observed as the in situ ice temperature increased. The ice drilling resistance varied with depth in the ridges during the main phase, whereas the drilling resistance was soft through all ridge depths during the ridge decay phase. Furthermore, the decreasing trend of drilling resistance and measured uniaxial compressive strengths of the sail and consolidated layer were all in agreement. After the ice reached an isothermal state of approximately -1.8°C , the brine volume increased, whereas the ice strength remained constant. This process is not fully understood; however, it may be connected to the ice failure mode. For ductile ice failures at temperatures close to T_f , the strength appears less dependent on changes in microporosity than does

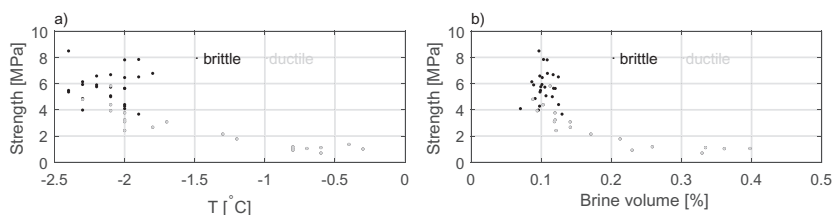


Fig. 10. Vertical uniaxial compressive strength of decaying level ice compared to a) temperature (T) and b) brine volume. Samples were collected and tested in situ in early June 2004 in the Van Mijen Fjord of Svalbard.

The same compression machine (KOMPIS) was used as that used during the N-ICE2015 campaign, results displayed in Figs. 8 and 9.

colder ice, which exhibits brittle failures.

Measuring strength in decaying ice is difficult, and more data are required to fully understand how the strength in decaying ice is affected by brine volume, especially to rule out equipment limitations. To understand the processes inside the rubble that occur without measured temperature gradients, salinities should be continuously measured in future investigations. Furthermore, the currently used technique for obtaining the macroporosity is uncertain due to factors such as drill chips filling the boreholes, drill auger jams, bending of drill augers and subjective observations made by the drill operator. To eliminate these uncertainties, more advanced measurement techniques should be explored.

Acknowledgments

The authors wish to acknowledge the support of the Research Council of Norway through the Centre for Research-based Innovation, SAMCoT (grant no 203471/O30), and the support of the SAMCoT partners. We would like to thank the Norwegian Polar Institute (NPI) for inviting us aboard and the N-ICE2015 campaign, as well as the crew of the RV Lance for their help and good humor. Thanks to all the members of the sea ice groups for their cooperative and productive work. Special thanks are extended to Annu Oikkonen, who provided excellent assistance and a positive mood. The authors wish to acknowledge the economic support of the Research Council of Norway through the project “Field studies and modeling of sea state, drift ice, ice actions and methods of iceberg management on the Arctic Shelf, 2015–2017 (FIMA)”. The logistics department at UNIS is also acknowledged for helping with preparations and packing.

References

- Amundrud, T.L., Melling, M., Ingram, R.G., Allen, S.E., 2006. Effect of structural porosity on the ablation of sea ice ridges. *J. Geophys. Res.* 111, C06004. <http://dx.doi.org/10.1029/2005JC002895>.
- Bonnemaire, B., Høyland, K.V., Liferov, P., Moslet, P.O., 2003. An ice ridge in the Barents Sea, part 1: morphology and physical parameters in-situ. In: Proceedings of the 17th International Conference on Port and Ocean Engineering under Arctic Conditions Trondheim, Norway, pp. 559–568.
- CAN/CSA-S471-92, R2001, 2001. General Requirements, Design Criteria, the Environment, and Loads. Standards Council of Canada.
- Cohen, L., Hudson, S.R., Walden, V.P., Graham, R.M., Granskog, M.A., 2017. Meteorological conditions in a thinner Arctic sea ice regime from winter to summer during the Norwegian Young Sea Ice expedition (N-ICE2015). *J. Geophys. Res.* Atmos. 122 (14), 7235–7259. <http://dx.doi.org/10.1002/2016JD026034>.
- Cox, G.F.N., Weeks, W.F., 1983. Equations for determining the gas and brine volumes in sea-ice samples. *J. Glaciol.* 29 (102), 306–316.
- Ekeberg, O.C., 2015. Studies of Ice Ridge Shape and Geometry from Upward Looking Sonar Data. PhD thesis. NTNU (135pp).
- Granskog, M., Assmy, P., Gerland, S., Spreen, G., Steen, H., Smedsrud, L.H., 2016. Arctic research on thin ice: consequences of Arctic sea ice loss. *EOS Trans. Am. Geophys. Union* 97 (5), 22–26. <http://dx.doi.org/10.1029/2016EO044097>.
- Haapala, J., Oikkonen, A., Gierisch, A., Itkin, P., Nicolaus, M., Spreen, G., Wang, C., Karvonen, J., Lensu, M., 2017. In: N.P. Institute (Ed.), N-ICE2015 Ship Radar Images, <http://dx.doi.org/10.21334/npolar.2017.6441ca81>.
- Hansen, E., Ekeberg, O.C., Gerland, S., Pavlova, O., Spreen, G., Tschudi, M., 2014. Variability in categories of Arctic sea ice in Fram Strait. *J. Geophys. Res.* Oceans 119 (10), 7175–7189.
- Hansen, E., Gerland, S., Høyland, K.V., Pavlova, O., Spreen, G., 2015. Time variability in the annual cycle of sea ice thickness in the Transpolar Drift. *J. Geophys. Res.* Oceans 120 (12), 8135–8150.
- Hopkins, M.A., Tuhkuri, J., Lensu, M., 1999. Rafting and ridging of thin ice sheets. *J. Geophys. Res.* Oceans 104 (C6), 13605–13613.
- Høyland, K.V., 2002. Consolidation of first-year sea ice ridges. *J. Geophys. Res.* Oceans 107 (C6) (15-1-15-16).
- Høyland, K.V., 2007. Morphology and small-scale strength of ridges in the North-western Barents Sea. *Cold Reg. Sci. Technol.* 48 (3), 169–187.
- Høyland, K.V., Liferov, P., 2005. On the initial phase of consolidation. *Cold Reg. Sci. Technol.* 41 (1), 49–59.
- Hudson, S.R., Lana, Cohen, Von, W., 2015. In: N.P. Institute (Ed.), N-ICE2015 Surface Meteorology [Data set], <http://dx.doi.org/10.21334/npolar.2015.056a61d1>.
- ISO/FDIS/19906, 2010. Petroleum and Natural Gas Industries - Arctic Offshore Structures. International Standardization Organization, Geneva, Switzerland.
- Johnston, M., 2006. A comparison of physical properties and strength of day-year ice in the Arctic and sub-Arctic. *Ann. Glaciol.* 44, 13.
- Johnston, M.E., 2017. Seasonal changes in the properties of first-year, second-year and multi-year ice. *Cold Reg. Sci. Technol.* 141, 36–53.
- Kharitonov, V.V., 2008. Internal structure of ice ridges and stamukhas based on thermal drilling data. *Cold Reg. Sci. Technol.* 52 (3), 302–325.
- Kwok, R., Rothrock, D.A., 2009. Decline in Arctic sea ice thickness from submarine and ICESat records: 1958–2008. *Geophys. Res. Lett.* 36 (15).
- Lei, R., Xie, H., Wang, J., Leppäranta, M., Jónsdóttir, I., Zhang, Z., 2015. Changes in sea ice conditions along the Arctic Northeast Passage from 1979 to 2012. *Cold Reg. Sci. Technol.* 119, 132–144.
- Leppäranta, M., Hakala, R., 1992. The structure and strength of first-year ice ridges in the Baltic Sea. *Cold Reg. Sci. Technol.* 20 (3), 295–311.
- Leppäranta, M., Manninen, T., 1988. The Brine and Gas Content of Sea Ice with Attention to Low Salinities and High Temperatures. Finnish Institute of Marine Research, Helsinki, Finland, pp. 15 (Finnish Institute of Marine Research Internal Report, 1988-2).
- Leppäranta, M., Lensu, M., Kosloff, P., Veitch, B., 1995. The life story of a 1st-year sea-ice ridge. *Cold Reg. Sci. Technol.* 23 (3), 279–290.
- Mahoney, A.R., Barry, R.G., Smolyanitsky, V., Fetterer, F., 2008. Observed sea ice extent in the Russian Arctic, 1933–2006. *J. Geophys. Res.* Oceans 113 (C11).
- Maslanik, J., Stroeve, J., Fowler, C., Emery, W., 2011. Distribution and trends in Arctic sea ice age through spring 2011. *Geophys. Res. Lett.* 38 (13).
- McPhee, M.G., 2008. Revisiting Heat and Salt Exchange at the Ice-Ocean Interface: Ocean Flux and Modeling Considerations. Springer, New York.
- Moslet, P.O., 2007. Field testing of uniaxial compression strength of columnar sea ice. *Cold Reg. Sci. Technol.* 48 (1), 1–14.
- Oikkonen, A., Haapala, J., Lensu, M., Karvonen, J., Itkin, P., 2017. Small-scale sea ice deformation during N-ICE2015: from compact pack ice to marginal ice zone. *J. Geophys. Res.* Oceans 122, 5105–5120. <http://dx.doi.org/10.1002/2016JC012387>.
- Peterson, K.A., Fer, I., McPhee, M.G., Randelhoff, A., 2017. Turbulent heat and momentum fluxes in the upper ocean under Arctic sea ice. *J. Geophys. Res.* Oceans 122, 1439–1456. <http://dx.doi.org/10.1002/2016JC012283>.
- Poplin, J.P., Wang, A.T., 1994. Mechanical properties of rafted annual sea ice. *Cold Reg. Sci. Technol.* 23 (1), 41–67.
- Rösel, A., Divine, D., King, J.A., Nicolaus, M., Spreen, G., Itkin, P., Pokashenski, C.M., Liston, G.E., Ervik, Å., Espeseth, M., Gierisch, A., Haapala, J., Maass, N., Oikkonen, A., Orsi, A.J., Shestov, A., Wang, C., Gerland, S., Granskog, M.A., 2016. In: N.P. Institute (Ed.), N-ICE2015 Total (Snow and Ice) Thickness Data from EM31, <http://dx.doi.org/10.21334/npolar.2016.ab29f1e2>.
- Schulson, E.M., Duval, P., 2009. Creep and Fracture in Ice. Cambridge University Press.
- Schwerdtfeger, P., 1962. The thermal properties of sea ice. *J. Glaciol.* 789–807.
- Shafrova, S., Høyland, K.V., 2008. Morphology and 2D spatial strength distribution in two Arctic first-year sea ice ridges. *Cold Reg. Sci. Technol.* 51 (1), 38–55.
- Shestov, A., 2011. Morphology and Physical Properties of Old Sea Ice in the Fram Strait. In: Port and Ocean Engineering under Arctic Conditions, Montréal, Canada, pp. 159–170.
- Shestov, A.S., Marchenko, A.V., 2016a. The consolidation of saline ice blocks in water of varying freezing points: laboratory experiments and computer simulations. *Cold Reg. Sci. Technol.* 122, 71–79.
- Shestov, A.S., Marchenko, A.V., 2016b. Thermodynamic consolidation of ice ridge keels in water at varying freezing points. *Cold Reg. Sci. Technol.* 121, 1–10.
- Shestov, A., Høyland, K.V., Ervik, Å., 2018. Decay phase thermodynamics of ice ridges in the Arctic ocean. *Cold Reg. Sci. Technol.* (under review).
- Sinha, N.K., 1984. Uniaxial compressive strength of first-year and multi-year sea ice. *Can. J. Civ. Eng.* 11 (1), 82–91.
- SNiP2.01.07-85, 1987. Construction Codes and Regulations. Loads and Forces. Technical Standards Used in Russia and Kazakhstan, pp. 34.
- Strub-Klein, L., Sudom, D., 2012. A comprehensive analysis of the morphology of first-year sea ice ridges. *Cold Reg. Sci. Technol.* 82, 94–109.
- Strub-Klein, L., Barrault, S., Goodwin, H., Gerland, S., 2009. Physical properties and comparison of first- and second-year sea ice ridges. In: Port and Ocean Engineering under Arctic Conditions, Luleå, Sweden, pp. 948–958.
- Surkov, G., 2000. Разработка методов расчета нагрузок от торосов на сооружения континентального шельфа. (Ph.D. thesis, St Petersburg).
- Timco, G.W., Burden, R.P., 1997. An analysis of the shapes of sea ice ridges. *Cold Reg. Sci. Technol.* 25 (1), 65–77.
- Timco, G.W., Frederking, R., 1984. A procedure to account for machine stiffness in uniaxial compression tests. In: IAHR Ice Symposium Hamburg, pp. 39–47.
- Timco, G.W., Frederking, R., 1990. Compressive strength of sea ice sheets. *Cold Reg. Sci. Technol.* 17, 227–240.
- Timco, G.W., Weeks, W.F., 2010. A review of the engineering properties of sea ice. *Cold Reg. Sci. Technol.* 60 (2), 107–129.
- Xia, W., Xie, H., Ke, C., 2014. Assessing trend and variation of Arctic sea-ice extent during 1979–2012 from a latitude perspective of ice edge. *Polar Res.* 33.

Appendix 2

Decay phase thermodynamics of ice ridges in the Arctic Ocean

This appendix includes the paper published in the journal Cold Regions Science and Technology (see below).

- Shestov, A., Høyland, K. and Ervik, Å., 2018. Decay phase thermodynamics of ice ridges in the Arctic Ocean. Cold Regions Science and Technology, <https://doi.org/10.1016/j.coldregions.2018.04.005>.



Contents lists available at ScienceDirect

Cold Regions Science and Technology

journal homepage: www.elsevier.com/locate/coldregions

Decay phase thermodynamics of ice ridges in the Arctic Ocean

Aleksy Shestov^{a,b,*}, Knut Høyland^b, Åse Ervik^{a,b}^a The University Centre in Svalbard, Longyearbyen, Norway^b Sustainable Arctic Marine and Coastal Technology (SAMCoT), Centre for Research-based Innovations (CRI), Norwegian University of Science and Technology, Trondheim, Norway

ARTICLE INFO

Keywords:

Ice ridges
Thermodynamics
Consolidation
Decay phase
Melting

ABSTRACT

Four ice ridges (R1, R2, R3, and R4) were studied during the spring of 2015 in the Arctic Ocean. During the Norwegian Young Sea Ice expedition (N-ICE2015) from January 11 to June 23, the R/V Lance was moored at four different ice floes (Floe 1, Floe 2, Floe 3, and Floe 4) and drifted along with them. Ice ridge studies were performed on Floe 3 (R1, R2) and Floe 4 (R3, R4). From May 21 to June 23, all ice ridges were drilled several times for structural measurements and cored for physical property measurements. In addition, ridges R1 and R4 were instrumented with Oceanetic thermistor buoys, model 908-20 (OTB 908-20), which remotely logged the vertical temperature profile through the sail and keel of the ridges from April 29 to June 28. After combining these datasets, we obtained thermodynamic properties and evaluated heat budgets of the ridge keels in R1 and R4. Ridge R1 was measured during the transition from the main phase to the decay phase, and ridge R4 was measured during the decay phase. In R1, a 3–4 W/m² upwards vertical conductive heat flux through the keel was calculated, which caused cooling of the keel and the growth of new ice (i.e., 0.5 m over 22 days from May 5 to May 27, as observed by temperature readings). The total amount of heat extracted from the keel was spent on cooling the keel and growing new ice in fractions of 0.4 and 0.6, respectively. In R4, a downwards vertical conductive heat flux (up to 2 W/m²) transported energy into the keel through the top surface of the keel, while the bottom of the keel melted (i.e., 1.6 m over 12 days from June 12 to June 24) due to the oceanic heat flux.

1. Introduction

Ice ridges are key ice features in both an engineering and a geophysical context. They provide quasi-static design forces on marine structures when icebergs are not a threat and constitute a significant portion of the ice volume (Hansen et al. (2013)). The role of ice ridges in the global heat and mass balance has not been studied extensively; particularly, their role in thinning Arctic sea ice cover (Kwok et al., 2009) needs to be better quantified. As more of the Arctic sea ice becomes first-year ice (Maslanik et al., 2011), a larger fraction of the total volume will become first-year ridges. An essential difference between first-year ridges and old ridges is that the former melt more easily; therefore, the Arctic ice cover as a whole has become more sensitive to global warming.

Three essential properties concerning the consolidation and melting of first-year ice ridges are the thickness of the consolidated layer, the keel depth (and keel volume) and the rubble macro-porosity (i.e., the macro-porosity of the unconsolidated layer). All of these vary through the life of a first-year ice ridge, and three state phases can be identified: a) an initial phase, b) a main phase and c) a decay phase. The initial

phase is characterized by the presence of reserved cold energy in the ice blocks in the rubble, which is extracted into the surrounding sea waters and spent on forming freeze bonds between ice blocks. Parallel atmospheric cooling causes the spreading of the freezing front from the sea surface downwards. Thus, a portion of the upper part of the keel may have a typical linear temperature profile, but the temperature profile in the keel is mainly inconsistent in the spatial dimension and irregular through its depth. The initial phase lasts until all reserved cold energy is extracted, and the temperature profile becomes isothermal (despite the upper portion of the linear profile).

Subsequently, the main phase starts and the cold air aloft cools the ridge from above. During both the initial and main phases, oceanic turbulent heat fluxes are low. This results in a growing consolidated layer, and the erosion of water exposed portions of the bottom of the keel. During the main phase, most of the consolidated layer is being developed.

In the decay phase, the ridge is heated both from above and below. A practical definition of the beginning of the decay phase is when the air temperature exceeds 0 °C. It takes some time before the entire ridge becomes isothermal (depending on the snow insulation, the sail

* Corresponding author at: UNIS, Pb. 156, 9171 Longyearbyen, Norway.
E-mail address: aleksy.shestov@unis.no (A. Shestov).

thickness, and the thickness of the consolidated layer), and the consolidated layer will continue to grow as long as the temperature gradient is positive close to its bottom. Below the ridge, temperature in the upper ocean layers usually exceeds the freezing point so that melting accelerates. Surface melting produces fresh water drizzling down into the keel. By the end of this phase, it is the end of summer; the ridge has either completely melted/disintegrated or has transformed into a second-year ridge. The processes during late spring and summer (i.e., the decay phase) that transform the first-year ridge into a second-year ridge are not completely understood but include both mechanical erosion and thermal effects that are accompanied by a keel collapse. Additionally, Shestov and Marchenko (2016a) and Shestov and Marchenko (2016b) performed laboratory and numerical calculations and demonstrated two macro-porosity reducing effects without a vertical negative temperature gradient in the consolidated layer. First, they showed how the strongly nonlinear specific heat capacity (Schwerdtfeger, 1963) causes a transformation from macro- to micro-porosity of the keel under heating (i.e., the penetration of fresher and warmer water into keel cavities). Second, they demonstrated how a cyclic change in different salinities of water in these cavities sucks the energy out of the ridge and contributes to further consolidation and reduction in macro-porosity.

Two studies from Strub-Klein and Sudom (2012) and Timco and Burden (1997) resulted in comprehensive literature reviews on ridges starting in 1976. Very few ridge studies investigated the seasonal development of ridges; the exceptions are, to the authors' knowledge, Leppäranta et al. (1995), Blanchet (1998), Høyland (2002) and Strub-Klein and Høyland (2011). The three latter papers mostly addressed the consolidated layer, whereas Leppäranta et al. (1995) measured seasonal ridge development that extended into the decay phase (e.g., the consolidated layer, temperature profiles, keel depth, volume and the macro-porosities of ridge and rubble).

N-ICE2015 (Granskog et al., 2016) was a multidisciplinary expedition that had the primary objectives to understand the effects of the new, thinner and first year sea ice regime in the Arctic on energy fluxes, ice dynamics and the associated ice ecosystem. The expedition was conducted at four different drifting stations (i.e., Floe 1–Floe 4) in the period from January 11 to June 23 in the pack ice north of Svalbard (Fig. 1). The research vessel *Lance* was moored to the ice and drifted along with it. Such a research platform provided an excellent opportunity to gain a better understanding of morphological and thermodynamic changes occurring during the ice ridge summer transformation process. Through collaboration with the Centre for Research-based Innovations' "Sustainable Arctic Marine and Coastal Technology" (SAMCoT), a systematic study of the seasonal development of first-year ice ridge properties in the late main phase and the early decay phase was conducted. This paper mainly provides insights into how

thermodynamic processes affect the growth of the consolidated layer and the melting of the keel during the transition from the main phase to the decay phase. A companion paper (Ervik et al., 2018) presented measurements on the development of rubble macro-porosity and the strength of the consolidated layer and sail.

2. Expedition and data collection techniques

An overview of the N-ICE2015 is given by Granskog et al. (2016), and the work and data collection on the ice ridges presented in this paper were conducted on Floe 3 and Floe 4 from April 29 to June 5 and from June 9 to June 28, respectively (Fig. 1a). Floe 3 was several kilometers in size; the distance to the ice edge was approximately 200 km on April 26 and 40 km on June 5. Floe 4 was smaller than Floe 3 and was closer to the ice edge; the distance to the ice edge was approximately 70 km on June 9 and 15 km on June 17 (Oikkonen et al., 2017). During the period of active sampling and cross-sectional drilling, both Floe 3 and Floe 4 experienced a similar drift through the marginal zone into open water (Fig. 1b). However, the air temperatures were different, and Floe 3 thermodynamically transitioned from the main phase to the decay phase when the air temperature changed from values near -15°C to values close to 0°C . In turn, Floe 4 was observed during its decay phase with air temperature values near 0°C during the entire period (Fig. 2). An overview of the collected ridge data and a preliminary presentation of results and analysis are given in the following three papers: (Ervik and Shestov, 2016a), (Shestov and Ervik, 2016) and (Ervik and Shestov, 2016b).

We investigated four ice ridges: R1 and R2 on Floe 3, and R3 and R4 on Floe 4. Two Oceanetic thermistor buoys, model 908-20 (OTB 908-20) (Oceanetic, 2014) were installed: one in R1 and one in R4. Instruments logged the vertical temperature profile through these ridges from April 29 to June 1 and from June 12 to June 28, respectively. The OTB 908-20 is an autonomous ice tracking buoy that is equipped with a thermistor string. The installation of the buoy itself requires drilling two boreholes (one hole 15 cm in diameter and one hole 5.1 cm in diameter) so that the buoy and support mast can be fixed on the sail surface, respectively (Fig. 3). The string fits into an additional 5.1 cm diameter borehole and has 35 sensors spaced 30 cm from each other. The buoy logs the GPS position and the thermistor string readings every hour and transmits data once a day via an Iridium modem. Data from all buoys that were deployed during the entire N-ICE2015 expedition were collected in the dataset, archived and made available to use for other analyses (Itkin et al. 2015). In this dataset, the OTB 908-20 buoys deployed on ridges R1 and R4, corresponded to buoys RIDGE_2015a (IMEI 300234061879260) and RIDGE_2015b (IMEI 300234061874260), respectively.

Cross-sectional drilling, which was used to measure keel geometry

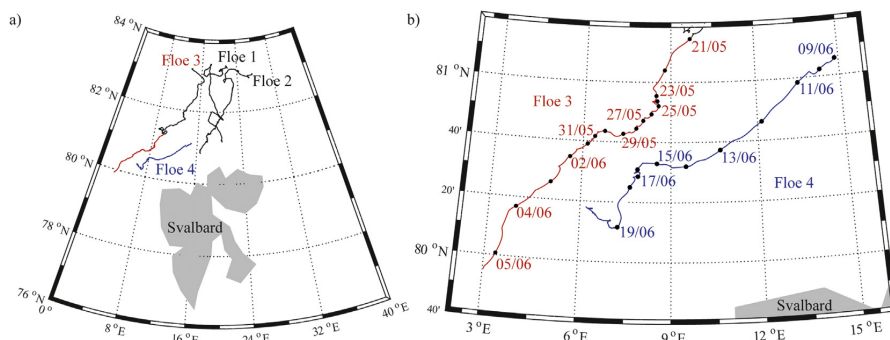


Fig. 1. Drift trajectories of all drifting stations (Floe 1–Floe 4) from the N-ICE2015 expedition (a), and drift trajectories for Floe 3 and Floe 4 during the period of active sampling and morphology drilling (b), from May 21 to June 5 and from June 9 to June 22, respectively. Note that station Floe 3 drifted south from approximately 83°N to 80°N , while ridge studies were carried out between 81°N and 80°N .

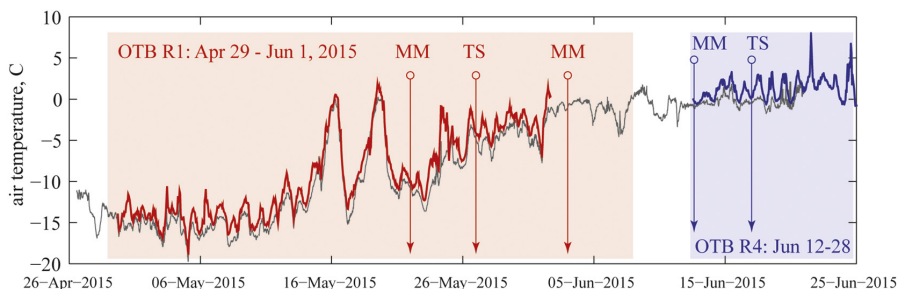


Fig. 2. Air temperature records from OTB 908-20 buoys for ridges R1 (red) and R4 (blue) from April 29 to June 1 and from June 12 to June 28, respectively. The gray line shows air temperature records from the R/V Lance meteorological station. Drilling and sampling activities on ridges are denoted by MM (morphology mapping) and TS (temperature and salinity profiles). (For interpretation of the references to colour in this figure legend, the reader is referred to the web version of this article.)

and macro-porosity, of all four ridges was performed with a series of 5.1 cm diameter augers; each were 1 m in length and were driven by a combustion powered engine. The rubble macro-porosity was calculated by dividing the total length of the voids inside the rubble by the length of the borehole inside the rubble. Temperature, salinity, density and uniaxial compressive strength were measured in the ice cores extracted from the ridges using a 7.2 cm diameter core auger, which was driven by a combustion powered engine. Once a new section of the core was extracted, single point temperature measurements along the core were performed using a core thermometer (Ebro, 2016). Based on the time and equipment availability, density profiles were performed only on ridges R2 and R3. In the case of R2, a separate core was extracted for density measurements and transported to the laboratory, where a hydrostatic weighing volume estimation method (see Pustogvar and Kulyakhtin (2016)) was used to calculate the density. In this method, the sample was weighed in air and paraffin, consequently, where the density of paraffin was measured with an aerometer (Stecloprigor, 1983). In the case of R3, density measurements were carried in situ on the same core by using a geometry-based volume estimation method. The core was cut into samples, where sizes and masses were registered using a caliper and electronic scales (Kern, 2016), respectively. Finally, the samples were placed inside sealed boxes, melted onboard the vessel and the salinity of solution was measured using a conductivity meter (Mettler, 2014).

As a result, ridges R1 and R4 had temperature profile records in time from the buoys, and several single-time temperature and salinity profiles of the sail and keel were measured in situ from the cores. For ridges R2 and R3, we do not have temperature records in time, but we have several single-time temperature, salinity, and density profiles (the R2 density profile was performed in the lab afterwards; see above) that were measured in situ. Therefore, in this paper we focused on the thermodynamics of ridges R1 and R4 by utilizing results of the density measurements from ridges R2 and R3. Authors find such an approach applicable for further analysis because for both Floe 3 and Floe 4, ridges R1 and R2 and R3 and R4 were in the direct vicinity of each other, respectively. This allows for a detailed analysis of ridge thermodynamic properties and heat budget calculations. Measurements on macro-porosity and details on the geometrical profiles and cores for all four ridges are presented in an accompanying paper (Ervik et al., 2018).

3. Governing equations

Using physical properties of ice obtained in the field, we calculated thermal properties of the ridge keel. Temperature $T_{si}(z)$, salinity $S_{si}(z)$, and density $\rho_{si}(z)$ were obtained from the extracted cores. The sea ice gas volume content was calculated using the results of Cox and Weeks (1983).

$$v_{gas}(z) = v_{gas}(T_{si}(z), S_{si}(z), \rho_{si}(z)). \tag{1}$$

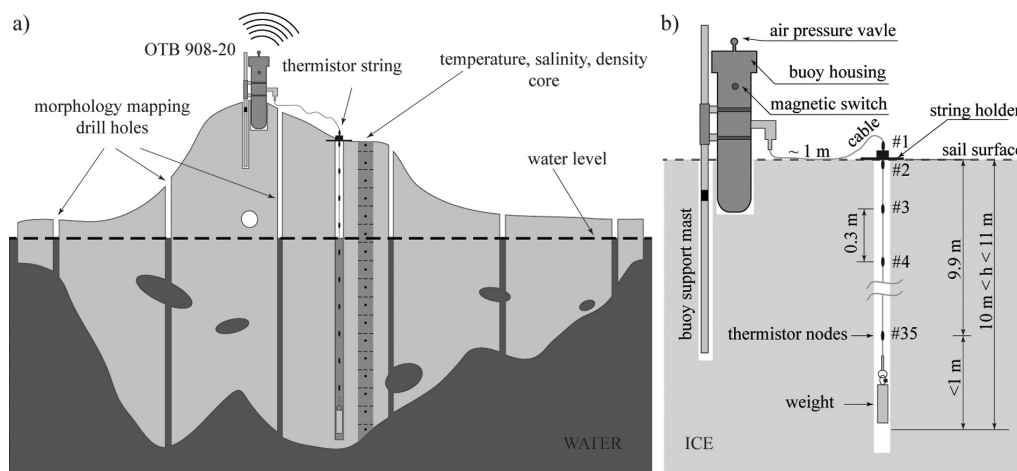


Fig. 3. Principal scheme of the ice ridge investigation (a) and a detailed scheme of the OTB 908-20 installation (b). Note that the borehole for the thermistor string had to be approximately 11 m long to place all thermistor nodes inside the keel. If the keel was shorter, then some of the nodes would have been placed below the keel in the water.

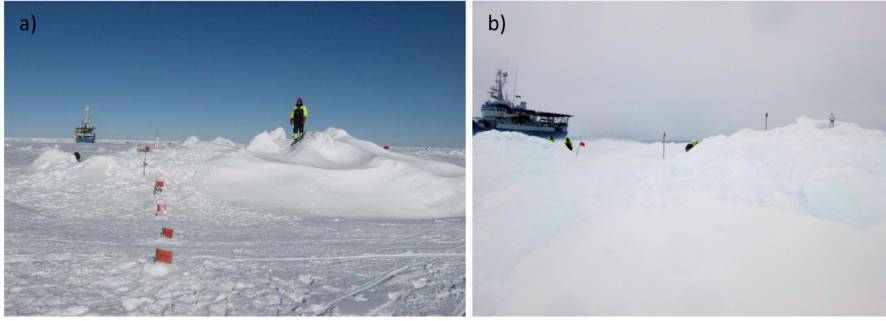


Fig. 4. Ice ridge sails with marked points for morphology drilling at R1 (a) and R4 (b).

Additionally, temperature profiles $\theta_{si}(z, t)$ were registered by OTB 908-20 buoys. Based on these data, the specific heat capacity and thermal conductivity were calculated using a model from Schwerdtfeger (1963).

$$c_{si}(z, t) = c_{si}(\theta_{si}(z, t), S_{si}(z)), \quad (2)$$

$$k_{si}(z, t) = k_{si}(\theta_{si}(z, t), S_{si}(z), \nu_{gas}(z)). \quad (3)$$

Using the calculated thermal conductivity profiles and the measured temperature profiles, we obtained a vertical heat flux in the solid part (i.e., the consolidated layer) of the keel due to conduction for both ridges (R1 and R4)

$$J_z(z, t) = -k_{si}(z) \frac{\partial \theta(z, t)}{\partial z}, \quad (4)$$

where $k_{si}(z)$ is the thermal conductivity and $\frac{\partial \theta(z, t)}{\partial z}$ is calculated between each of the two closest thermistor nodes. In such notations (i.e., the upwards positive direction of z-axis, which we use in our calculations), the positive conductive heat flux is defined as transporting energy upwards, and the negative heat flux transports energy downwards.

The heat budget of the consolidated layer is based on conductive heat fluxes entering and leaving the layer through its boundaries through the internal energy change inside the layer. Since in each ridge we had only one linear vertical profile of temperature measurements, it was assumed that the thickness of the ridge had a reasonably uniform distribution both along the length and width of the ridge. Then, we may approximate our computational domain of the consolidated layer (CL) with a 1-D vertical column of unit cross-sectional area that is limited by two horizontal planes: $z = z_{bottom}$ at the bottom and $z = z_{top}$ at the top of consolidated layer. We defined the top of the consolidated layer as the waterline, and the bottom position changed as the consolidated layer grew. Denoting vertical heat fluxes through the bottom surface and the top surface as $J_z(z_{bottom}, t)$ and $J_z(z_{top}, t)$, respectively, the net vertical heat flux into the CL is expressed as:

$$J_{CL}(t) = J_z(z_{bottom}, t) - J_z(z_{top}, t). \quad (5)$$

If $J_{CL}(t) > 0$, the consolidated layer, in bulk, is being heated, if $J_{CL}(t) < 0$, it is being cooled. The total net transfer of heat into the CL domain is expressed as follows:

$$Q_{CL}(t) = \int_{t_0}^t J_{CL}(t) dt, \quad (6)$$

where t_0 is an arbitrary initial time moment. By analogy with Eq. (6), the amount of heat transferred through the top surface and the bottom surface of the consolidated layer can be defined as

$$Q_{top}(t) = \int_{t_0}^t J_z(z_{top}, t) dt \quad (7)$$

and

$$Q_{bottom}(t) = \int_{t_0}^t J_z(z_{bottom}, t) dt. \quad (8)$$

The heat flux through the bottom of the consolidated layer is caused by the temperature gradient that is formed due to atmospheric cooling; as a result, the consolidated layer must be supplied by the latent heat of fusion released from the ice formation under the consolidated layer. Thus, the amount of heat transferred through the bottom surface of the consolidated layer is identical to the amount of heat spent on phase change (i.e., the growth of new ice) below the consolidated layer:

$$Q_{bottom}(t) = Q_F(t) = \int_{t_0}^t L_i \rho_i \eta (1 - \eta_b) \frac{\partial h_{CL}}{\partial t} dt, \quad (9)$$

where L_i and ρ_i are the latent heat of fusion and the density of fresh ice, respectively; η is the macro-porosity of ice rubble below the consolidated layer, η_b is the brine fraction of ice, and h_{CL} is the thickness of the consolidated layer.

Since the phase change inside the domain is captured by the effective specific heat capacity, the total change in energy inside the domain is expressed as:

$$E_{CL}(t) = \int_{t_0}^t \int_{z_{bottom}}^{z_{top}} \rho_{si}(z) c_{si}(z, t) \frac{\partial \theta(z, t)}{\partial t} dz dt, \quad (10)$$

where ρ_{si} and c_{si} are density and the specific heat capacity of sea ice, respectively.

The total net heat transfer into the domain (Eq. (6)) is spent on changing the internal energy inside the domain (Eq. (10)) (i.e., on the changing temperature profile under a given specific heat capacity profile); therefore, the following should be true:

$$Q_{CL}(t) = E_{CL}(t). \quad (11)$$

4. Results

Both ridges R1 and R4 were covered with snow (up to 1 m thick) and had sails of comparable size (Figs. 4, 5). The R1 keel was bigger than the R4 keel. The vertical lines (Fig. 5) represent boreholes; the dark gray represents cavities, and the light gray represents ice with different resistances to drilling. The unconsolidated rubble macro-porosity in R1 was 11% (measured May 22) and 10% (measured June 3–4), whereas in R4 it was 27% (measured June 12). More details and analysis of the hardness, as well as the porosity, were presented in a companion paper by Ervik et al. (2018).

A substantial amount of snow led to the formation of snow-ice (Provost et al., 2016), which contributed to between 17% and 28% of the total ice thickness level throughout the whole season. The role of snow on top of ice ridge in the insulating consolidated layer, versus the

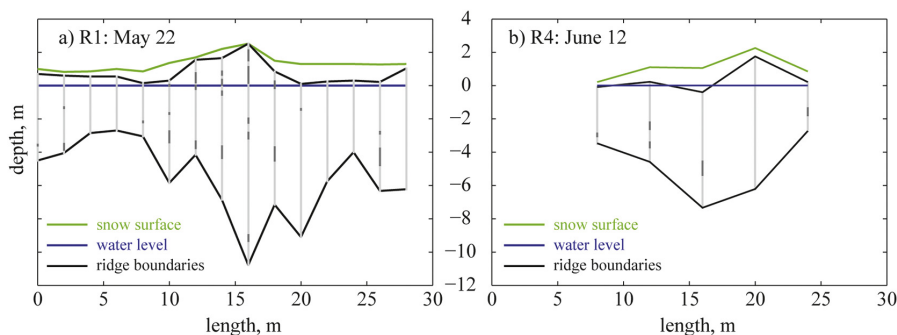


Fig. 5. Cross-sectional drilling of ridges R1 (a) and R4 (b). The vertical lines show drill holes and their morphology (different types of ice are shown in light gray, and gaps of non-ice are shown in dark gray).

role of snow in changing hydrostatic equilibrium and causing the consolidated layer to be submerged – is important. Authors admit that both of mentioned above processes took place in studied ridges and affected the thermodynamics and morphology structure of their consolidated layer. From one hand snow insulation reduces the ability of consolidated layer to grow at its bottom, but from another hand submerging part of sail underwater leads to consolidated layer growing from above. A more detailed discussion could have been brought if snow accumulation and air temperature regime in time were known from the beginning of ridge lifetime. Further, all calculated heat budgets of consolidated layers during observation period are given for particular snow and air temperature conditions ridges experienced. Whatever amount of snow was on top of ridge sail it was automatically taken into account by measuring vertical temperature profiles directly in the consolidated layer.

Temperature and salinity profiles obtained in situ from ice cores are shown together with temperature profiles registered by the OTB 980-20 for respective dates for R1 and R4 (Fig. 6). Temperature and salinity profiles are shown over negative and positive ranges along the horizontal axis, respectively. The horizontal black lines near the top, 0 m, and near the bottom of the plot represent the sail top surface, freeboard, and keel bottom surface, respectively. In R1, data are missing because the core barrel became stuck in the ridge. In R4, data are missing due to very loose snow ice along the surface of the sail, which was not possible to keep intact when coring for salinity measurements. Density and gas volume content profiles of sea ice are shown together, as they are dependent on one another (Fig. 7). The sea ice gas volume content will be

used further in calculations of thermal conductivity (Eq. (3)). Due to time and equipment constraints, density was only measured in ridges R2 (Floe 3) and R3 (Floe 4), which are neighbor ridges to R1 (Floe 3) and R4 (Floe 4), respectively. Therefore, we assume that the gas volume content profiles in R2 and R3 are consistent with those in R1 and R4, respectively.

OTB 980-20 buoy temperature readings in R1 and R4 are shown two different ways: a 1-D plot of all temperature profiles in temperature - height space (Fig. 8a, b), and a 2-D contour plot of temperature shown in colour in time - height space (Fig. 8c, d). Note that the keel of R1 extends beyond the length of the thermistor string, while in the case of R4, the thermistor string extends through the ridge and hangs below the keel into the water (Figs. 3, 5). This causes differences in the interpretation of observed information. For R1 (Fig. 8c), we can track the development of the consolidated layer by the breaking point of the temperature profile (i.e., the temperature gradient); the melting of the keel most likely occurs too, but this is beyond the range of our observations. However, for R4 (Fig. 8d), we observe melting of the keel from the bottom.

It is known from the model presented in Schwerdtfeger (1963) that specific heat capacity profiles are mainly determined by sea ice salinity, while thermal conductivity profiles are mainly determined by the sea ice gas volume content. Temporal changes in the temperature profile at a certain depth showed no considerable effect on either the specific heat capacity or the thermal conductivity (Fig. 9a, b, c, d), except for the specific heat capacity at the top layer of the keel in R4 (Fig. 9c). The thermal conductivity did not vary much with regards to spatial

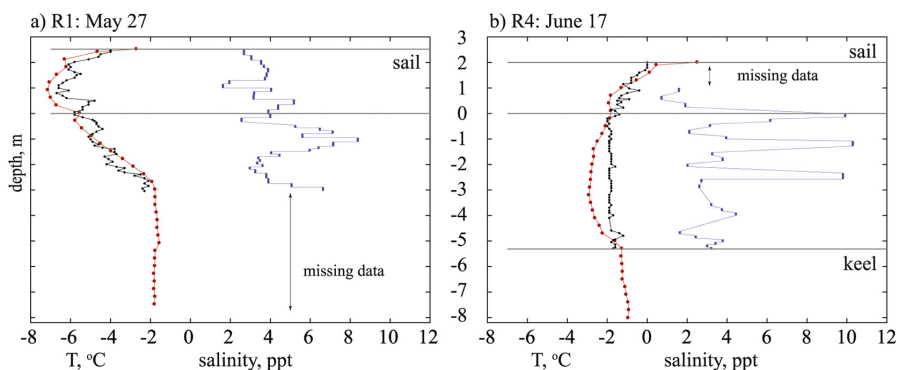


Fig. 6. Vertical profiles of temperature and salinity in ridges R1 (a) and R4 (b). Temperature (measured in the core – black; obtained by the OTB – red) and salinity (measured from the core – blue) profiles are shown along negative and positive ranges on the horizontal axis, respectively. Missing data are due to technical problems and snow ice at the top surface of the sail (see description in the text). (For interpretation of the references to colour in this figure legend, the reader is referred to the web version of this article.)

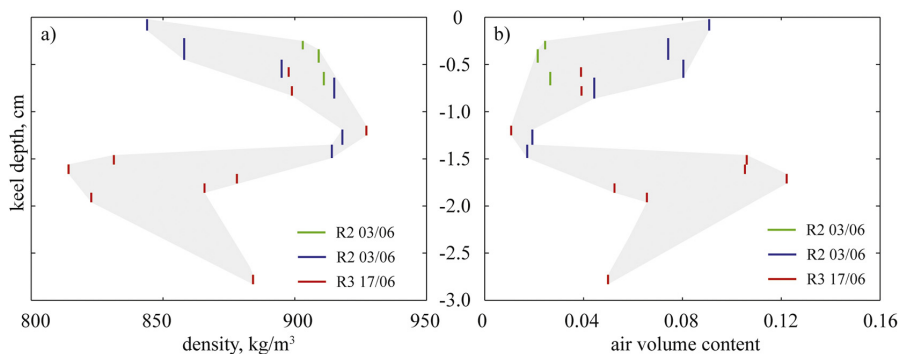


Fig. 7. Ice ridge keel density profile (a) and corresponding gas volume content of ice (b) calculated for corresponding temperatures at which density measurements were conducted. Densities of the R3 samples were obtained in situ at -2°C using a geometrical volume estimation method. Samples from R2 were transported to the lab, where the hydrostatic weighting method for volume estimation was implemented at -15°C . Note that the density profiles were only available for ridges R2 and R3, while the OTB 908-20 buoys were installed in ridges R1 and R4. However, authors found density and gas volume content profiles that were representative and applicable for further analysis of ridges R1 and R4, since both Floe 3 and Floe 4 had ridges R1 and R2 and R3 and R4, respectively, in the direct vicinity of each other.

temperature differences. However, the spatial difference in temperature as a function of depth strongly affects the specific heat capacity of the keel. The temperature difference along the depth profiles in R1 and R4 is reflected in the shapes of the specific heat capacities subsequently. In R1, the warmer bottom part of keel has a higher specific heat capacity (Figs. 6a and 9a). In R4, the temperature profile is close to the isotherm (near -1.8°C), with a slightly warmer top layer of the keel and a salinity profile that varies from 2 to 4 ppt, with peaks up to 10 ppt at depths of 0 m, -1 m, and -2 m (Fig. 6b). The shape of the specific

heat capacity profile for R4 (Fig. 9c) is defined by the two profiles mentioned above. The shape of the thermal conductivity profiles for the R1 and R4 keels (Fig. 9b, d) follows the mirror-shape of the gas volume content profile (Fig. 7b), as explained in the beginning of this paragraph.

The vertical profile of the vertical heat flux (Eq. (4)) in ridges R1 and R4 are shown with 2-D contour plots in the time–depth space (Fig. 10a, b). Discrepancy between the two methods to define the bottom of the consolidated layer and the bottom of the keel (white lines

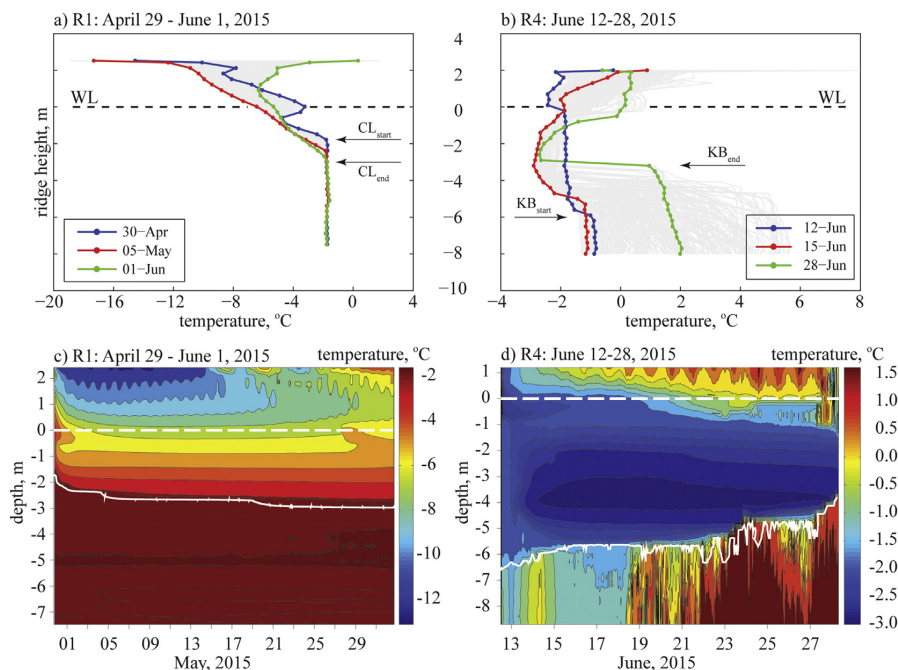


Fig. 8. Temperature readings from OTB 908-20 buoys in ridge R1 (a, c) and R4 (b, d). Vertical 1-D temperature profiles (a, b) are plotted in temperature - height space (blue corresponds to the moment when the thermistor strings were installed, red indicates the coldest profiles, green corresponds to the end of observations and gray shows all the data; WL – water level, CL – consolidated layer, and KB – keel bottom). The 2-D contour plots of temperature (c, d) are plotted in time - height space (the horizontal white dashed line at the zero level indicates the water level and the white solid line shows growth of the consolidated layer in R1 (c) and the melting of R4 in the ridge keel (d)). Note that the R4 keel first registered as deep as 6.2 m; thus, values below that (b) correspond to sea water temperatures. (For interpretation of the references to colour in this figure legend, the reader is referred to the web version of this article.)

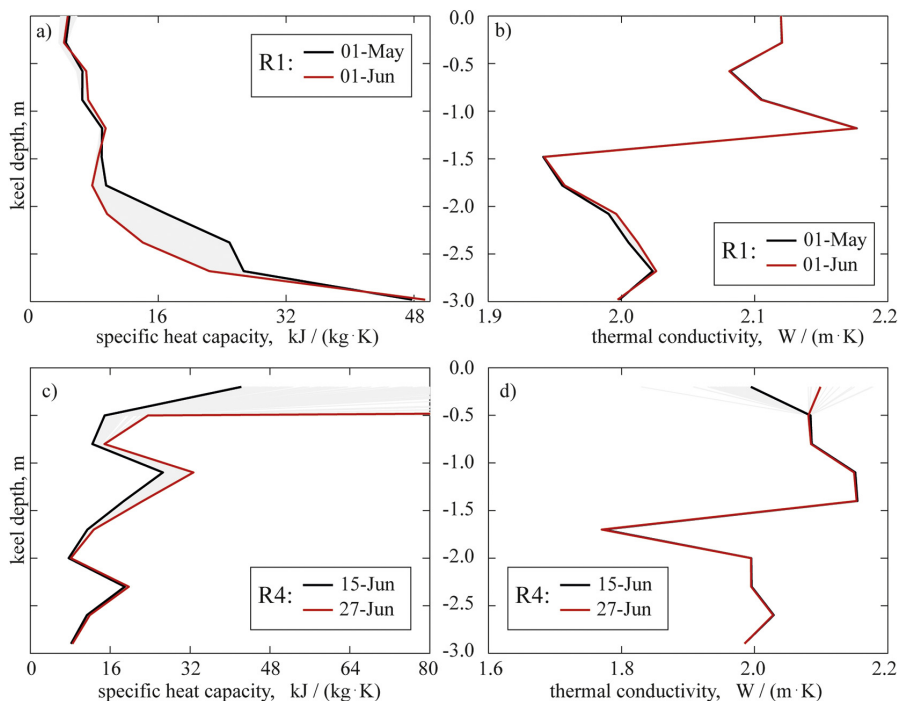


Fig. 9. Specific heat capacity (a, c) and thermal conductivity (b, d) of the consolidated layer for the ice ridge keel from R1 (a, b) and R4 (c, d). Black and red profiles correspond to the beginning and the end of observation, respectively (for dates, see the legend on each plot). Gray profiles show all profiles plotted within a 1-hour interval. (For interpretation of the references to colour in this figure legend, the reader is referred to the web version of this article.)

in R1 (Fig. 8c and Fig. 10a) and R4 (Fig. 8d and Fig. 10b), respectively) will be addressed later in the discussion of the paper. In the case of R1, we observe an upwards heat flux of $3\text{--}4\text{ W/m}^2$ throughout the consolidated layer of the keel. This heat flux is caused by atmospheric cooling, which lasts until May 27 (Fig. 10a). Below the consolidated layer (i.e., inside the unconsolidated rubble) we observe an isothermal vertical temperature profile (Fig. 8a, c). As a result, the vertical heat flux calculated using Eq. (4) is equal to zero in the unconsolidated rubble (Fig. 10a). It should be understood that Eq. (4) is valid for solid mediums and conduction only; we can expect turbulent heat fluxes in the cavities inside the unconsolidated rubble below the consolidated layer. At the same time, assuming that some of the cavities are closed and all of them are at a temperature near the freezing point, we expect turbulent heat flux to be low and negligible. The length of the

thermistor string in R1 was not long enough to measure the water temperature below the keel. However, at the bottom of the keel, we can expect a considerable oceanic heat flux, which, if present, would cause the melting of ice rubble at the bottom of the keel. This provides thermal insulation for the upper unconsolidated rubble and the consolidated layer from oceanic heat flux. Both the positive upwards heat flux in the consolidated layer and the low (or zero) heat flux just below it cause freezing of the unconsolidated rubble below the consolidated layer. This explains why we can observe melting of the keel at the bottom simultaneously with the growth of the consolidated layer. The rate of the consolidated layer growth can be estimated from the uppermost vertical position, where the vertical heat flux is equal to zero, as a function of time (Fig. 10a). According to this, the consolidated layer develops from -2.3 m to -2.8 m depth, or 0.5 m total.

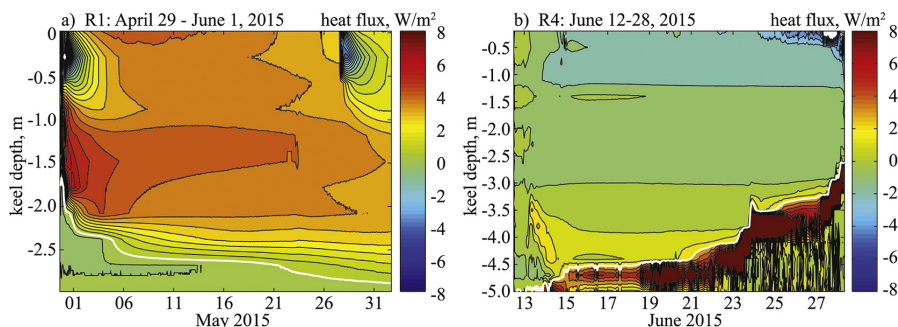


Fig. 10. Vertical conductive heat fluxes in the consolidated layer for ridges R1 (a) and R4 (b) shown in time-depth space as 2-D contour plots. The positive heat flux is defined as transporting energy upwards, and negative heat flux is defined as transporting energy downwards.

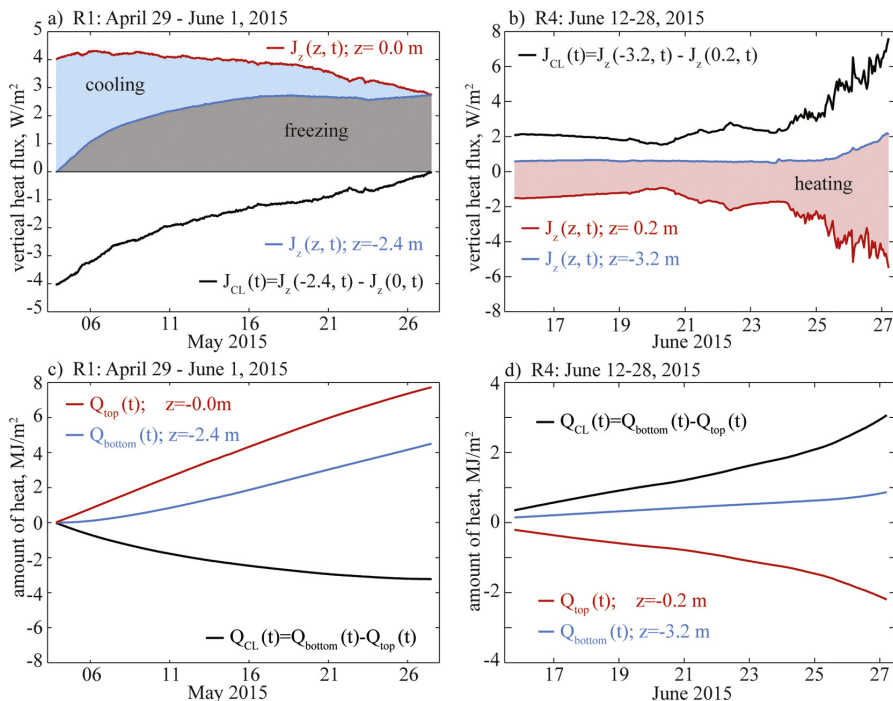


Fig. 11. Vertical conductive heat fluxes (Eqs. (4)–(5)) through the top and bottom surface of the consolidated layer and the net vertical heat flux into the consolidated layer for R1 (a) and R4 (b) (see the legends for corresponding surface levels). Areas shown by different colors (a, b) correspond to the amount of heat related to the process (i.e., cooling, freezing, heating) that each area is correspondingly labeled. The net amount of heat (integrals (Eqs. (6)–(8)) of the corresponding fluxes in (a) and (b)) transferred throughout the top and bottom surfaces of the consolidated layer and accumulated in the consolidated layer for R1 (c) and R4 (d). The rapid increase of the net heat flux into the CL (b) is most likely related to the moment when the chosen upper level of the consolidated layer started to melt. The positive heat flux is defined as transporting energy upwards and negative heat flux is defined as transporting energy downwards. The positive heat flux into the consolidated layer indicates that it is being heated, and the negative heat flux indicates that it is being cooled.

In R4, we did not observe heat fluxes throughout the consolidated layer; however, a strong oceanic heat flux caused rapid melting of the ridge keel from below. During a minor storm event from June 11 to June 13, when R4 was instrumented, the oceanic turbulent heat flux reached values up to 300–400 W/m^2 ; after the storm ceased, the heat flux stayed in the range of 10–30 W/m^2 until measurements were stopped on June 19 (Peterson et al., 2016). During that period, ridge R4 lost more than 1 m in keel (which coincides with consolidated layer in the case of R4) depth per 10 days (Fig. 10b); it should be noted that melting due to the oceanic heat flux started before atmospheric heating from above the ridge reached the consolidated layer.

Vertical heat fluxes (Eq. (4)) through the top $J_z(z_{top}, t)$ and the bottom $J_z(z_{bottom}, t)$ of consolidated layer and the total net heat flux (Eq. (5)) into consolidated layer $J_{CL}(t)$ are shown as 1-D plots in the heat flux–time space (Fig. 11a, b). By integrating the abovementioned heat fluxes, we obtained corresponding net amounts of heat transferred in time. The net amounts of heat transferred into the consolidated layer $Q_{CL}(t)$ (Eq. (6)) through the top surface $Q_{top}(t)$ (Eq. (7)) of the consolidated layer and the bottom surface $Q_{bottom}(t)$ (Eq. (8)) of the consolidated layer are shown as 1-D plots in the heat–time space (Fig. 11c, d).

The consolidated layer of R1 was cooling during the time of observation (Fig. 11a) and, as a result, the total net amount of heat transferred into the consolidated layer from May 5 to May 27 was $Q_{CL, R1} = -3.22 MJ/m^2$ (Fig. 11c). The total net amount of heat transferred through the top and bottom of the consolidated layer in R1 was $Q_{top, R1} = 7.73 MJ/m^2$ and $Q_{bottom, R1} = 4.51 MJ/m^2$, respectively (Fig. 11c).

Heat transferred through the bottom of the keel upwards was supplied by the latent heat of fusion released when ice formed below the consolidated layer $Q_{bottom, R1} = Q_{F, R1}$ (Eq. (9)).

In contrast, the consolidated layer in R4 was heating (Fig. 11b) from June 15 to June 24, and the total net amount of heat transferred into the consolidated layer during this period was $Q_{CL, R4} = 2.09 MJ/m^2$ (Fig. 11d). Mainly, this amount of heat was provided through the top surface of the consolidated layer $Q_{top, R1} = -1.44 MJ/m^2$, while the high ocean turbulent heat flux from below was consumed by the process of ice melting due to the latent heat of fusion. Therefore, we observed a low net amount of heat transferred through the bottom surface $Q_{bottom, R4} = 0.63 MJ/m^2$ for the same time period (Fig. 11d). Note that the rapid increase in net heat flux into the consolidated layer after June 24 (Fig. 11b) was most likely artificial and related to the moment when the chosen for calculations the top surface level ($z = -0.2$ m, Fig. 11b, d) of the consolidated layer started to melt. All numbers provided above were calculated until the mentioned moment (i.e., when such melting occurred).

5. Discussion

Shestov and Marchenko (2016b) explain a new hypothesis on possible spring-summer transformation mechanisms due to the freshening of sea water. They show the potential for the thermodynamic consolidation of ice rubble in keels in water at varying freezing points towards the end of the winter season. Thus, the authors found it very beneficial to collect data on ice ridges during the summer season to fill

the gap in observational data. This is of particular interest regarding processes during the decay phase that transform the first-year ridge into a second-year ridge. Such processes remain not completely understood. Thus, all four ice ridges studied during the N-ICE2015 expedition will add to the knowledge of ice ridge studies. In particular, ridges R1 and R4 give a good description of thermal properties and the heat budget for ice ridges during decay phase. By size, these ridges could be classified as medium- to small-size ice ridges. The morphology mapping results (Fig. 5) show the presence of voids in the ridge keels. Salinity profiles (Fig. 6) show values up to 5 ppt that are higher at some levels. Both the presence of voids inside the rubble and relatively high values of salinity indicate that ridges R1 and R4 are most likely both first-year ridges that are transitioning into second-year ridges.

Ridges R1 and R4 were observed subsequently in the season and, as a result, experienced different air temperature regimes. Ridge R1 went through a transition from winter (the main phase) to summer (the decay phase), with air temperatures changing from near -15°C to close to 0°C . Ridge R4 was observed during the summer (the decay phase) and experienced air temperature values close to 0°C during the entire observation period (Fig. 2). In the case of R1, temperatures inside the ridge ranged from -12°C to -2°C (Fig. 8a, c), while in the case of R4, temperatures ranged from -3°C to 0°C (Fig. 8b, d). Due to the presence of atmospheric cooling for R1, the sail and consolidated layer showed a linear temperature profile a majority of the time (Fig. 8a), while the unconsolidated rubble below showed an isothermal vertical temperature profile. When the air temperature increased, the sail and upper part of the consolidated layer warmed up, and the unconsolidated rubble kept an isothermal vertical profile at about -1.8°C . In turn, R4 had a C-shape temperature profile at its coldest temperature, with the lowest value occurring near -3°C at a 4 m keel depth on June 15 (Fig. 8b). When air and water temperatures increased, the sail and the upper part of the keel warmed up, while the bottom part of the keel melted.

Although there were no continuous data logged that showed the transition from a linear temperature profile into a C-shape profile, this transition can be seen partly in the two temperature record datasets in ridges R1 and R4. Before temperature logging stopped on June 1 in R1, the sail and consolidated layer were warming, creating the upper part of the C-shape profile in the sail (Fig. 8a, green profile). Meanwhile, at the beginning of the R4 observations, it is seen that the upper curve of the C-shape profile moved down into the consolidated layer, and the lower curve of it formed as well (Fig. 8b, red profile). The time gap between the two data sets was from June 1 to June 12. The OTB 908-20 in R1 stopped logging on June 1 either due to battery limitations or a polar bear attack on May 31. Ridge R1 was still intact on June 5 when the vessel disconnected and sailed north. In the end, the OTB 908-20 in R1 worked for 33 days, and the one in R4 worked for 16 days. The R4 OTB 908-20 most likely stopped working when the ridge reached the ice edge, and the buoy flooded and finally sank. Under such circumstances, we cannot give a confident estimate on the battery life of the OTB 908-20 in Arctic summer conditions, but we found it convenient to install and operate. However, there are two points that should be considered. First, during the installation of the OTB 908-20 thermistor string, it had to be stretched to ensure the position of the thermistor nodes relative to the ice ridge. Second, once the thermistor string was installed, the part that falls below the water level (i.e., in the keel) will be mostly frozen in the ice (with the exception of voids, if any), while the part above the water level (i.e., in the sail) will be in the open borehole filled with air and some ice pieces (Fig. 3a). Due to this, the results focused on the keel part only, as temperature readings and density measurements were of better quality compared to the sail part.

Measuring density in samples collected from the sail was difficult due to high micro-porosity and instability, which often led to samples splitting into several pieces. Thus, only data obtained from the keel cores were used. Furthermore, a number of assumptions were made in the calculations presented in the results. Density profile measurements

were performed only on ridges R2 and R3 (Fig. 7a). Combining these measurements, a common gas content profile was constructed (Fig. 7b). Ridges R2 and R3 were in the vicinity of ridges R1 and R4, respectively. Assuming that the density profiles of neighboring ridges were similar, we had to accept the gas content profile constructed in such a way (Fig. 7b) for further calculations for ridges R1 and R4. Due to the limited number of salinity and density profiles, we had to assume that brine pockets and gas pockets stayed closed and, as a result, the salinity and gas volume content profiles were constant over time during the period of observation. This was not necessarily true, but it had to be assumed in order to perform the heat budget analysis. Density mostly governed the thermal conductivity and, as Fig. 9 shows, this property varied less than 10% and did not have a large effect on the overall consolidation and melting processes.

According to Schwerdtfeger (1963) (Eqs. (2) and (3)), the specific heat capacity is governed by temperature and salinity, while the thermal conductivity is mainly governed by the gas volume content and is less dependent on temperature and salinity. Due to the differences in salinity and temperature profiles from ridges R1 and R4, the specific heat capacity also differs. In the case of R1 (Fig. 9a), the specific heat capacity is $8\text{--}10\text{ kJ}/(\text{kg K})$ in the upper part of the consolidated layer (0 to -2 m) and is $48\text{ kJ}/(\text{kg K})$ in the bottom part of consolidated layer. In the case of R4 (Fig. 9c), the upper part of the consolidated layer (0 to -1 m) shows higher values of the specific heat capacity ($40\text{--}80\text{ kJ}/(\text{kg K})$), whereas in the bottom part of the consolidated layer, values were lower ($10\text{--}30\text{ kJ}/(\text{kg K})$). Specific heat capacity has a different effect on freezing during winter than on heating during spring. During winter, the specific heat capacity slows the freezing of new ice, and during spring, it slows the heating of the ice ridge deeper inside the consolidated layer as higher values of the specific heat capacity require more energy per unit mass to be removed or added, respectively. Thermal conductivity profiles in the consolidated layer in both ridges range from 2.0 to $2.2\text{ W}/(\text{m K})$, with higher values in the upper part of the layer.

Analysis of the heat budget for the two ice ridge keels showed two different thermodynamic states due to seasonal variations in air temperature. Ridge R1 was subjected to atmospheric cooling and maintained a conductive heat flux upwards through the consolidated layer of $3\text{--}4\text{ W}/\text{m}^2$ (Fig. 10a) during the time of observation (from May 5 to May 27). Below the consolidated layer (in the rubble), there was no heat flux to provide the possible formation of new ice (Eq. (9)). The ocean turbulent heat flux in May, when R1 was observed, was in the range of $5\text{--}10\text{ W}/\text{m}^2$ (Peterson et al., 2016); however, when the heat flux reached the bottom of the keel, it was spent on melting the bottom of the keel. Thus, we had an insulation mechanism, which prevented the consolidated layer from being heated and allowed it to continue consolidating during the main phase and even into the beginning of the decay phase. This was not the case for level ice, which meant that the ratio of the consolidated layer thickness to the thickness of the level ice increased into the first part of the decay phase. Both methods of estimating consolidated layer growth, i.e., measured temperature data (Fig. 8a, c) and calculated conductive heat flux data (Fig. 10a), showed growth in the consolidated layer thickness from 2.3 m to 2.8 m .

In ridge R4 (Fig. 10b), there was a low vertical conductive heat flux downwards between $0\text{ W}/\text{m}^2$ and $-1\text{ W}/\text{m}^2$ throughout the whole keel, which was consolidated to a high degree (i.e., the keel macroporosity was 8%) (Ervik et al., 2018). The high values below the keel (Fig. 10b) corresponded to temperature differences in the water, but not to the conductive heat flux in a solid medium. Real oceanic heat flux, including convection, may be substantially higher. For measurements in ridge R4, ocean heat fluxes peaked at $400\text{ W}/\text{m}^2$ (Peterson et al., 2016) cause fast melting of the keel. Defined using temperature readings and calculated vertical heat flux, the keel melted by 2 m (from 5.9 m to 3.9 m) (Fig. 8b, d) and by 1.6 m (from 5.0 m to 3.5 m) (Fig. 10b), respectively. Since direct drillings during cross-sectional mapping of R4 (Fig. 5b) showed a keel depth of 6.2 m , the authors were inclined to

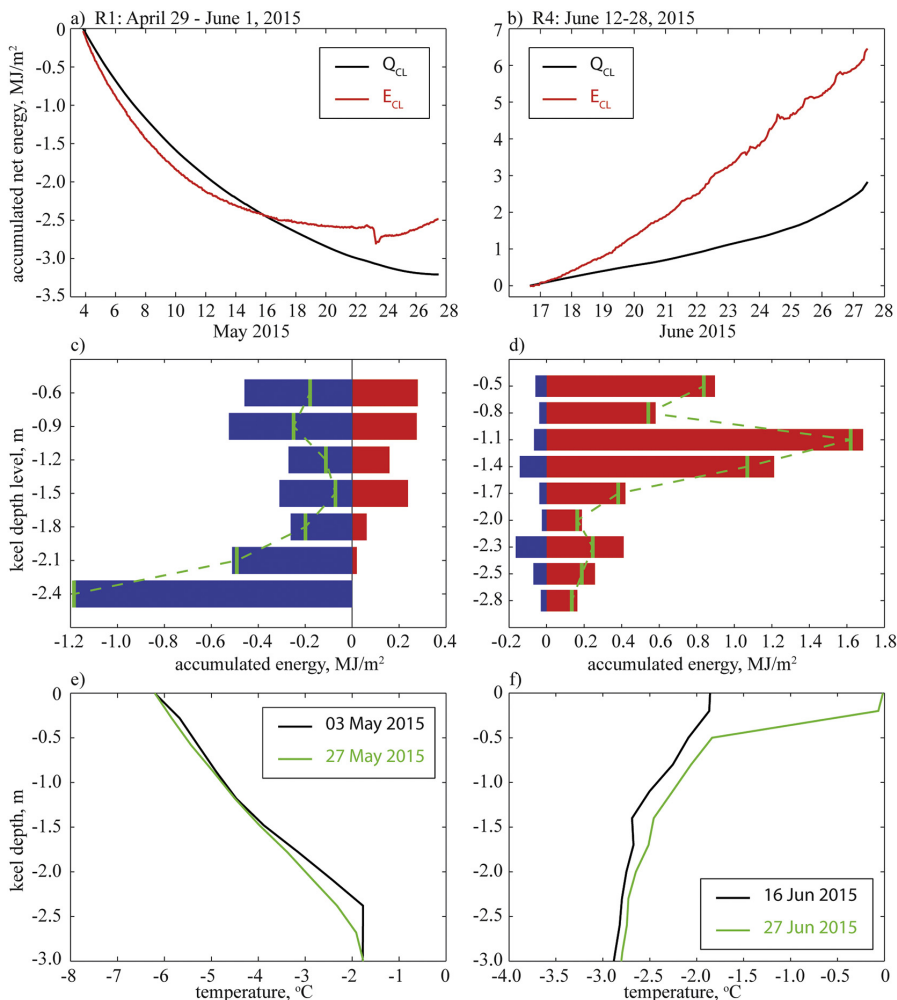


Fig. 12. The net heat budget of ice ridges R1 (a) and R4 (b) calculated based on conductive heat fluxes and the change in internal energy. The distribution of internal energy changes based on depth for R1 (c) and R4 (d) (blue – cooling, red – heating, and green – net final). The temperature profile change in the consolidated layer for R1 (e) and R4 (f) are also shown. (For interpretation of the references to literature in this figure legend, the reader is referred to the web version of this article.)

consider the first option as the correct value. The reason for the difference can be caused by a borehole that was never fully refrozen at the bottom of the R4 keel due to the installation of the OTB 908-20 thermistor buoy (on June 12), which coincided with drastically increased ocean turbulent heat fluxes (300–400 W/m² from June 11 to 13) (Peterson et al., 2016).

As long as atmospheric cooling was sufficiently high ($J_z(z_{top}, t) > J_z(z_{bottom}, t)$), cooling caused enough heat loss to provide both cooling of the consolidated layer and formation of new ice below it (Fig. 11a). As soon as atmospheric cooling weakened to the level where $J_z(z_{top}, t) = J_z(z_{bottom}, t)$, there was no change in the total energy inside the consolidated layer domain ($E_{CL}(t) = 0$). However, there was still non-zero vertical conductive heat flux throughout the bottom of the consolidated layer and, as a result, the development of the consolidated layer continued. The observation period for the R1 ridge stopped on June 1 at the moment described above ($J_z(z_{top}, t) = J_z(z_{bottom}, t)$); this means that the consolidated layer for R1, as a whole, was continuously cooled during the observation period. Further reductions in

atmospheric cooling ($J_z(z_{top}, t) < J_z(z_{bottom}, t)$) would cause heating of the consolidated layer domain, but the growth of ice below it would continue until the temperature gradient became zero.

The numbers reported in the result section (Fig. 11c) show that from May 5 to May 27, the amount of heat transferred through the top surface of the consolidated layer in R1 was $Q_{top, R1} = 7.73 \text{ MJ/m}^2$; 42% of it was spent on cooling the consolidated layer, while 58% was spent on growing new ice at the bottom of consolidated layer. The macro-porosity (η) of the rubble in R1 was found to be 0.10 (Ervik et al., 2018) during the observation period; thus, using Eq. (9), we can estimate growth in the consolidated layer as follows:

$$\Delta h_{CL} = \frac{Q_{bottom, R1}}{L_i \rho_i \eta (1 - \eta_b)} \approx 0.20 \text{ m}, \tag{12}$$

which is less than the 0.5 m value found from both measurements (Fig. 8c and Fig. 10a). To get the level of measured growth for the consolidated layer, the macro-porosity (η) of the rubble in R1 was required to be 0.04 (Eq. (12)). Since temperature measurements were

performed at one point only, local macro-porosity is important and can differ due to its uneven spatial distribution. Hoyland (2007) showed that macro-porosity of ice rubble was lower just below the consolidated layer as opposed to further down. There are two more reasons why the consolidated layer grew more than the calculated value according to Eq. (12): frazil ice filled the boreholes during drilling, and there was a high fraction of brine (up to 0.18) in the newly formed ice at warm temperatures (approximately -1.8°C , Fig. 8a). Both of these factors reduced the effective rubble macro-porosity and also reduced the amount of ice required formed to consider the rubble fully consolidated.

In the case of ridge R4, its consolidated layer, as a whole, was continuously heated (Fig. 11b) during the observation period and consumed $Q_{CL, R4} = 1.83 \text{ MJ/m}^2$ of heat (Fig. 11d). Mainly, the entire amount of heat was supplied through the top surface of the consolidated layer, while at the bottom surface, ice rapidly melted and consumed ocean turbulent heat flux. As a result, melting provided thermal insulation for the consolidated layer domain from the ocean. The macro-porosity (η) of rubble in R4 was found to be 0.27 (Ervik et al., 2018). Implementing Eq. (9) for melting, we may estimate the average ocean turbulent heat flux required to maintain the observed melting rate (0.13 m/day):

$$\langle J_{\text{ocean}, R4} \rangle = (1 - \eta)(1 - \eta_b)\rho_i L_i \frac{\Delta h_{\text{keel}}}{\Delta t} \approx 298 \text{ W/m}^2. \quad (13)$$

The calculated ocean heat flux value (298 W/m^2) was close to the range of the observed peaked values ($300\text{--}400 \text{ W/m}^2$) during the minor storm event from June 11 to June 13 (Peterson et al., 2016), though there were no ocean heat flux measurements after June 19 when the melting of the R4 occurred. However, we assumed that after June 19, heat flux values were also comparable to the peak values.

There are few factors that can accelerate the keel deterioration compare to the one-dimensional melting model in Eq. (13). First, currents can wash away some loose blocks in the unconsolidated rubble part of the keel. Second, under the buoyancy, the keel may collapse, or more gradually creep and with this reduce the macro-porosity without any heat transfer at all. Authors believe that when the macro-porosity of first-year ridges reduces to approximately zero over the summer (and they become second-year ridges), this mechanism occurs. Third, keels, compared to the level ice, both have a larger exposed area to sea waters due to its deeper penetration into the water column and higher permeability of unconsolidated rubble. Thus, the observed effective melting rate can be reached even under the influence of a lower ocean turbulent heat flux than the one calculated according to Eq. (13).

The net heat balance of ice ridges is shown in Fig. 12. According to Eq. (11), the total net heat transfer into the consolidated layer domain was equal to the change in internal energy, which appeared to be accurate for R1 (Fig. 12a) and less accurate for R4 (Fig. 12b). For R4, it can be a consequence of affected temperature readings due to the started melting process that caused an imperfect contact between the sensors and the ice. The change in internal energy (the right term in Eq. (11)) was not evenly distributed across the depths in R1 and R4 (Fig. 12c and d). When R1 was cooling, the highest change in internal energy was at the bottom part of the consolidated layer (Fig. 12c). When R4 was heating, most of the internal energy was accumulated at the top of the consolidated layer (Fig. 12d). The difference between R1 and R4 was due to different temperature profiles (Fig. 12e and f), which defined the effective specific heat capacity of the sea ice (Fig. 9a and c). During active atmospheric cooling for R1, the warmest part of the consolidated layer was at the bottom. For R4, heat was transferred into the consolidated layer from the top surface, and the warmest part was at the top of the consolidated layer. As a result, the effective specific heat capacity of the consolidated layer in R1 was higher at the bottom of the layer (Fig. 9a), while for R4, it was higher at the top of the layer (Fig. 9c). Such layers of high specific heat capacity values act as insulators. During atmospheric cooling, these layers slow down the

formation of new ice below the consolidated layer; during heating from above, these layers slow down heating of the consolidated layer further inside the layer, below its upper layers. Slower processes are meant in comparison to fresh ice, which has a much lower specific heat capacity and is nearly independent of temperature.

6. Conclusion

The thermodynamics of two first-year ice ridges, R1 and R4, drifting in the Arctic Ocean were studied during the transition from the main phase to the decay phase of the ridge lifecycle (May and June 2015). Ridges were equipped with thermistor strings, morphologically mapped by drilling, and cored for physical property evaluation. The ridge R1 was observed at the end of the main phase, and we found the conductive heat flux through the keel to be $3\text{--}4 \text{ W/m}^2$ (Fig. 10a). Heat budget calculations showed that for 22 days (from May 5 to May 27), the keel transferred 7.73 MJ/m^2 of energy upwards due to atmospheric cooling (Fig. 11c). From that energy, 40% was spent on cooling the keel and 60% was spent on growing new ice that extended the consolidated layer (Fig. 11a). As observed from temperature readings and vertical heat flux calculations, the consolidated layer grew by 0.5 m (Figs. 8c and 10a). The ridge R4 was studied during the decay phase, and its consolidated layer consumed 1.83 MJ/m^2 of energy for 12 days (from June 12 to June 24) (Fig. 11d). Mainly, heat was transferred through the top surface of the keel, with heat flux values of up to 2 W/m^2 (Fig. 10b). During this period consolidated layer (which, in the case of ridge R4, coincides with keel) melted by approximately 1.5 m. The calculated average ocean heat flux needed to provide the observed melting rate of consolidated layer (0.13 m/day) was 298 W/m^2 . This number is close to the observed range from Peterson et al. (2016) at that time (from June 12 to June 19), which has peak values of ocean turbulent heat flux from 300 to 400 W/m^2 .

The amount of energy needed to grow new ice (increase the thickness of consolidated layer) was comparable to the amount of energy required to cool down the consolidated layer (which changed the temperature profile accordingly); this was due to the high specific heat capacity of saline ice, especially in warm temperatures. In saline ice, any changes in temperature require a phase change in brine pockets to fulfill the thermodynamic equilibrium condition. In relation to this, we shown that energy in the consolidated layer was consumed non-uniformly; more energy accumulated in the regions of the consolidated layer that had higher temperatures. During the main phase, this occurred at the bottom part of the consolidated layer, and it slowed the growth of ice; in the decay phase, this occurred at the top part of the consolidated layer, and it insulated the deeper portion of the consolidated layer and kept it colder for a longer time.

Acknowledgements

The authors wish to acknowledge the support of the Research Council of Norway through the Centre for Research-based Innovation SAMCoT (project number 203471), as well as the support of all the SAMCoT partners. This work was supported by the Norwegian Polar Institute's Centre for Ice, Climate and Ecosystems (ICE) through the N-ICE project. We are very thankful to all of the scientific crew of the N-ICE2015 expedition for their cooperation and good atmosphere on-board, as well as to the crew members of the R/V Lance for their hospitality and fast and professional reactions when needed. Special thanks to the logistics department of UNIS for always fulfilling our last-minute needs for equipment transportation and storage space. The author wishes to acknowledge the Research Council of Norway for providing thermistor buoys through the project "Field studies and modeling of sea state, drift ice, ice actions and methods of icebergs management on the Arctic shelf, 2015-2017 (FIMA 243930/H30)". Special thanks to Polona Itkin for deploying our buoy in the R1 ridge almost a month before we started direct measurements on it.

References

- Blanchet, D., 1998. Ice loads from first-year ice ridges and rubble fields. *Can. J. Civ. Eng.* 25 (2), 206–219.
- Cox, G.F.N., Weeks, W.F., 1983. Equations for determining the gas and brine volumes in sea-ice samples. *J. Glaciol.* 306–316.
- Ebro, E., 2016. TFX 410-1 Precision Core Thermometer. <http://shop.ebro.com/tfx-410-1.html>.
- Ervik, Å., Shestov, A., Hoyland, K.V., Nord, T.S., 2018. On the decay of first-year ice ridges: measurements and evolution in rubble macro-porosity, ridge drilling resistance and consolidated layer strength. *Cold Reg. Sci. Technol.* <http://dx.doi.org/10.1016/j.coldregions.2018.03.024>. (In Press).
- Ervik, Å., Shestov, A.S., 2016a. Studies of Drifting Ice Ridges in the Arctic Ocean During May–June 2015. Part I. An Overview of all Measurements. Proceedings of 23rd IAHR International Symposium on ICE 2016, Ann Arbor, Michigan, USA.
- Ervik, Å., Shestov, A.S., 2016b. Studies of Drifting Ice Ridges in the Arctic Ocean during May–June 2015. Part III. Evolution in Geometry and Small-Scale Strength. Proceedings of 23rd IAHR International Symposium on ICE 2016, Ann Arbor, Michigan, USA.
- Granskog, M.A., Assmy, P., Gerland, S., Spreen, G., Steen, H., Smedsrud, L.H., 2016. Arctic research on thin ice: consequences of Arctic sea ice loss. *Eos* 97.
- Hansen, E., Gerland, S., Granskog, M.A., Pavlova, O., Renner, A.H.H., Haapala, J., Løyning, T.B., Tschudi, M., 2013. Thinning of Arctic sea ice observed in Fram Strait: 1990–2011. *Journal of Geophysical Research: Oceans* 118 (10), 5202–5221.
- Høyland, K.V., 2002. Consolidation of first-year sea ice ridges. *Journal of Geophysical Research: Oceans* 107 (C6), 15–1–15–16.
- Høyland, K.V., 2007. Morphology and small-scale strength of ridges in the north-western Barents Sea. *Cold Reg. Sci. Technol.* 48 (3), 169–187.
- Itkin, P., Spreen, G., Hudson, S.R., Cheng, B., 2015. N-ICE2015 Basic Buoy Data (In: N. Norwegian Polar Institute (Editor)). <https://data.npolar.no/dataset/6ed9a8ca-95b0-43be-bedf-8176bf56da80>.
- Kern, K., 2016. Precision balance KB 2000-NM. <https://www.kern-sohn.com/shop/en/laboratory-balances/precision-balances/KB/>.
- Kwok, R., Cunningham, G.F., Wensnahan, M., Rigor, I., Zwally, H.J., Yi, D., 2009. Thinning and volume loss of the Arctic Ocean sea ice cover: 2003–2008. *Journal of Geophysical Research: Oceans* 114 (C7) (n/a–n/a).
- Leppäranta, M., Lensu, M., Kosloff, P., Veitch, B., 1995. The life story of a first-year sea ice ridge. *Cold Reg. Sci. Technol.* 23 (3), 279–290.
- Maslanik, J., Stroeve, J., Fowler, C., Emery, W., 2011. Distribution and trends in Arctic sea ice age through spring 2011. *Geophys. Res. Lett.* 38 (13) (n/a–n/a).
- Mettler, T., 2014. SG3-FK2 - SevenGo™ Conductivity (2m; Field Kit). http://www.mt.com/us/en/home/phased_out_products/PhaseOut_Ana/SG3_FK2_conductivity_US_eStore.html.
- Oceanetic, M., 2014. Oceanetic Model 908-20 Thermistor Buoy. <http://www.oceanetic.com/products.html>.
- Oikkonen, A., Haapala, J., Lensu, M., Karvonen, J., Itkin, P., 2017. Small-scale sea ice deformation during N-ICE2015: from compact pack ice to marginal ice zone. *Journal of Geophysical Research: Oceans* 122 (6), 5105–5120.
- Peterson, A.K., Fer, I., McPhee, M.G., Randelhoff, A., 2016. Turbulent Heat and Momentum Fluxes in the Upper Ocean Under Arctic Sea Ice. (Submitted to JOURNAL OF GEOPHYSICAL RESEARCH).
- Provost, C., Sennéchaël, N., Miguet, J., Itkin, P., Rösel, A., Koenig, Z., Villacieros, N., Granskog, M.A., 2016. Observations of Snow-ice Formation in a Thinner Arctic Sea ICE Regime During the N-ICE2015 campaign: Influence of Basal ICE Melt and Storms. (Submitted Journal of Geophysical Research).
- Pustogvar, A., Kulyakhtin, A., 2016. Sea ice density measurements. Methods and uncertainties. *Cold Reg. Sci. Technol.* 131, 46–52.
- Schwerdtfeger, P., 1963. The thermal properties of sea ice. *J. Glaciol.* 4, 789–807.
- Shestov, A., Ervik, Å., 2016. Studies of Drifting Ice Ridges in the Arctic Ocean during May–June 2015. Part II. Thermodynamic Properties and Melting Rate. Proceedings of 23rd IAHR International Symposium on ICE 2016, Ann Arbor, Michigan, USA.
- Shestov, A.S., Marchenko, A.V., 2016a. The consolidation of saline ice blocks in water of varying freezing points: laboratory experiments and computer simulations. *Cold Reg. Sci. Technol.* 122, 71–79.
- Shestov, A.S., Marchenko, A.V., 2016b. Thermodynamic consolidation of ice ridge keels in water at varying freezing points. *Cold Reg. Sci. Technol.* 121, 1–10.
- Steclopribor, P., 1983. Aerometers for Oil Products AN. <http://www.steclopribor.com/areometri-dlya-nefteproduktov-an-areometri-dlya-nefteproduktov-s-termometrom> (In Russian).
- Strub-Klein, L., Høyland, K.V., 2011. One Season of a 1st Year Sea Ice Ridge Investigation - Winter 2009. Proceedings of 21th International Conference on Port and Ocean under Arctic Conditions (POAC) Montreal, Canada.
- Strub-Klein, L., Sudom, D., 2012. A comprehensive analysis of the morphology of first-year sea ice ridges. *Cold Reg. Sci. Technol.* 82 (0), 94–109.
- Timco, G.W., Burden, R.P., 1997. An analysis of the shapes of sea ice ridges. *Cold Reg. Sci. Technol.* 25 (1), 65–77.

Appendix 3

Full-scale actions from first-year ridge interactions with fixed structures

This appendix includes the conference paper presented at the 23rd International Conference on Port and Ocean Engineering under Arctic Conditions (see below).

- Ervik, Å., 2015. Full-scale actions from first-year ridge interactions with fixed structures. Proceedings of the 23rd International Conference on Port and Ocean Engineering under Arctic Conditions (POAC), Trondheim, Norway, Paper no. 129.



FULL SCALE ACTIONS FROM FIRST YEAR RIDGE INTERACTIONS WITH FIXED STRUCTURES

Åse Ervik¹

¹Centre for Sustainable Arctic Marine and Coastal Technology, Norwegian University of Science and Technology, Trondheim, Norway

ABSTRACT

The objective of this paper was to study full scale actions from first year ice ridges on fixed structures. The first part is a review of reported full scale global loads and associated failure modes from ice ridges compared to level ice, on three fixed structures. The instrumented structures are the Molikpaq, the piers of the Confederation Bridge and Nordstromgrund lighthouse. The highest ridge loads on Nordstromgrund lighthouse and the piers of the Confederation Bridge were associated with crushing and combined crushing/bending respectively. On Molikpaq crushing of first year ridges was not reported. In the second part of this paper data is analyzed. A limit force analysis was performed to estimate a critical ice ridge length of approximately 9km for crushing to occur on the Molikpaq compared to 20m on Nordstromgrund lighthouse. Accordingly some Nordstromgrund data were analyzed to compare global loads derived from load panels and tilt. A ratio between panel load and tilt was found for a quasi-static 5m deep ridge interaction with the instrumented side of the lighthouse. For the ridge a ratio of 8.2 kN/ μ radians was derived, compared to 12kN/ μ radians for level ice both ratios without uncertainties. The different ratio indicates that load panels underestimate ridge keel loads. The analysis also showed that it is not possible to obtain a unique ratio between global load and tilt for ridges, due to the stiff bottom foundation that makes the tilt sensitive to changes in point of action i.e. ridge keel depth.

INTRODUCTION

Actions from ice ridges are assumed to establish dimensioning loads on infrastructure and offshore installations in ice-infested areas, when icebergs are not present. In the past decades great effort has been put into predicting ice ridge loads. A study by Timco and Croasdale (2006) shows that ice ridge loads on a vertical structure predicted by twenty-one ice experts ranged with a factor of five. The study shows that research on ice ridge structure interactions is still needed. This paper begins with a review of full scale first year ice ridge loads on three instrumented fixed structures. The structures are the Molikpaq (CAN), the piers of the Confederation Bridge (CAN) and the Nordstromgrund Lighthouse (SWE). The purpose is to investigate ice ridge load levels and associated failure modes compared to level ice, measured on fixed structures.

The second part of this paper is an analysis of some ridge interaction data. Global loads derived from load panels and tilt are compared, for this analysis data from Nordstromgrund lighthouse are used. Finally, a limit force analysis is performed to compare the minimum ice ridge length for crushing to occur on the three structures.

Structure geometry, instrumentation and location

Ice actions depend on the type of interaction. In the following the three structure geometries, instrumentations and locations are presented. Nordströmgrund lighthouse is a vertical structure and Molikpaq is close to vertical. The piers of the Confederation Bridge on the other hand are conical which favors breaking of ice in bending. Both Nordströmgrund lighthouse and the Confederation Bridge piers are narrow structures while the Molikpaq is a wide structure (Table 1). All the structures are fixed to the sea bed in the bottom foundation, but free to rotate and deflect in all other parts limited by the structure stiffness.

Table 1. Some key structure and location parameters

	Molikpaq	Confederation Bridge	Nordströmgrund Lighthouse
Structure width (MWL) [m]	90	14.2	7.6
Inclination (MWL) [°]	82	52	90
Dominant ice drift dir.	NE	NW (SE tides)	NE

*MWL mean water level

Full scale data is obtained by instrumenting the structures with load panels, accelerometers, tiltmeters, optic sensors (laser, EM, ULS) and video coverage. In addition weather data and dairies are documented. Global loads on the Molikpaq and Nordströmgrund lighthouse were found by load panels (Timco et al., 2000),(Bjerkås, 2006) , tiltmeters were used to find global loads on the Confederation bridge piers after 2003 when load panels broke (Brown, 2007).

In addition to measuring load and responses some ice parameters were measured. At Molikpaq ice velocities and ice ridge sails were estimated from videos. At Nordströmgrund ice velocities and direction were estimated form videos, wind speed/directions and air temperatures by a weather station. Ice thickness above water was found with laser, below water an electro-magnetic device (EM) was used. For ridge keels EM footprint data is too coarse, an upward looking sonar (ULS) gives more precise ridge profiles. At Nordströmgrund a ULS was installed in 2000 but broke early in 2001. Based on linear regression between available ULS and EM data at Nordströmgrund; maximum keel depths from ULS was approximately 3 times the EM maximum (Bjerkås, 2006). At the Confederation bridge a weather station records wind speed/direction and air temperatures. Since the Confederation Bridge is 13km long; wind loads must be subtracted from tilt measurements to find ice loads. Ice drift speeds were measured by an acoustic doppler current profiler and ice thickness is measured with ULS.

Molikpaq was (1984-1986) located in the Beaufort Sea, experiencing heavy ice conditions including old ice features. The Confederation Bridge crosses the Northumberland Strait in Canada and the Nordströmgrund lighthouse is located outside Luleå in Sweden, both are located in temperate areas only experiencing first-year ice features. Based on this; loads from first-year ice ridges were expected to be dimensioning, at least for the temperate structures. Location of the structures are shown in Figure 1.

Classification of ice features

In this paper actions from ice ridges and level ice are compared. WMO (1970) classify ice as either deformed or undeformed, where undeformed ice is level ice while deformed ice is

Table 2. Instrumentation and monitoring, Molikpaq; Timco et al. (2000) and Timco et al. (2005), Confederation Bridge; Brown et al. (2009), Brown (2001), Nordströmgrund lighthouse; Bjerkås (2006) and Schwarz and Jochmann (2001)

	Molikpaq	Confederation Bridge	Nordströmgrund Lighthouse
Load panels	yes (1984-86)	yes (1997-2003)	yes (1987-1989) (1998-2003)
Location panels	SE, E, NE, N	NW	NE, E
Max panel depth [m]	3/6m	2m	1.5m
Response measurements	4 16 (12th April 1986) Extensometer and 10 strain gauges (1984-86)	Tiltmeters, accelerometers	Tiltmeters (1986) (2003), accelerometers (1973-1989) (2001-2003)
Video	yes (1984-86)	yes (1997-)	yes (1979) (2001-2003)
Other instruments	-	upward looking sonar (ULS) (1997-), Acoustic Doppler Current Profiler (1999-2000)	Laser, electromagnetic device (EM) (2001-2003), ULS (2000-2001)

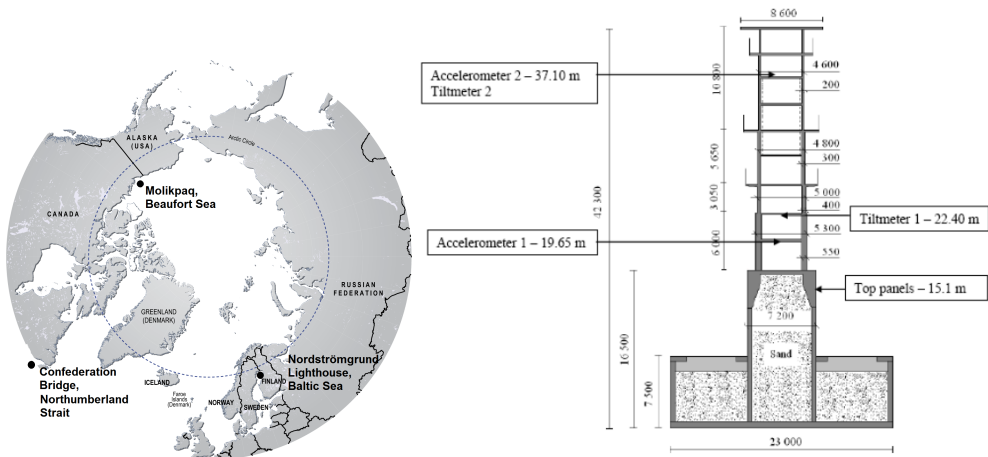


Figure 1. To the left: Map showing the location of the Molikpaq, the Confederation Bridge and the Nordströmgrund lighthouse (Ahlenius, 2005). To the right: Nordströmgrund lighthouse (1998-2003) Bjerkås et al. (2013).

both rafter and ridged ice. Level ice is thermally grown ice. When visually studying ice it

is seldom possible to distinguish level ice from rafted ice, therefore ice thickness should be measured manually and compared to thermodynamic estimates in order to distinguish between undeformed and deformed ice.

Limit scenarios and failure modes

It is important to distinguish between load limiting mechanisms and failure modes. There are three recognized load limiting mechanisms. They are limit stress, limit force and limit momentum. Ice load is limited by stress when ice fails directly against the structure (in crushing, bending, buckling, creep or shear), this requires sufficient driving forces. If the driving forces from the wind and current are insufficient to fail the ice or if inhomogeneities in ice sheet causes the ice to fail adjacent to the structure surface; driving forces limits the ice load i.e. a limit force mechanism. If the momentum of the ice is insufficient the ice will come to halt and the ice load is limited by momentum or energy.

The mode of which the ice fails against the structure controls the load level. Recognized failure modes are crushing, bending, creep, buckling, splitting and spalling (ISO19906, 2010). For ridges other failure modes are also reported such as ridge spine failure, failure behind the ridge (Timco et al., 2000) and dodging (Kärna and Jochmann, 2004). The dodging failure was described for a ridge with a sail height of 2m on the 1st of April 2002 (Kärna and Jochmann, 2004): "Instead of a ridge penetration, the drift direction changed for a while. Then the structure found the boundary between the level ice and the rafted ice.". Timco et al. (2000) and Bjerkås (2006) also differ between local and global failures. Where local failures occur continuously over the whole structure width while global failures occur on a concentrated part of the structure. The failure mode that produces the highest load is crushing since the crushing strength is generally the highest strength in sea ice.

REVIEW OF GLOBAL LOADS AND FAILURE MODES

Failure modes and global loads both dependent on structure geometry and ice parameters; when designing the Confederation bridge between 20 and 25 parameters were used to find design ice loads (Brown et al., 2009). Table 3 gives a summary of maximum loads and failure modes of ridges compared to level ice.

The maximum reported first year ridge load on Molikpaq was 89MN associated with a global failure behind the ice ridge. On Molikpaq crushing of first year ridges was not observed. For level ice the maximum global load found was 131MN. The level ice failure mode was unknown, but the second largest level ice load (110MN) was caused by crushing of level ice with a thickness of 1.2m (Timco and Johnston, 2004). Molikpaq, being in the Arctic, encountered old ice features in addition to first year ice, crushing of level old ice produced the overall highest loads up to 466MN. Wright (1986) reports that strong dynamic vibrations were sometime associated with crushing of old ice features.

Some of the Nordstömgrund data are not yet analyzed, but the highest ridge load reported until today is 3MN occurred during crushing of a ridge of 9m depth. During the interaction the ice velocity decreased to zero and dynamic accelerations up to 1m/s^2 were registered. The largest quasi-static ridge load reported is 1.3MN for crushing of a ridge keel of 6m (Bjerkås, 2006). The highest level ice load reported to this date is 3.5MN measured during crushing of level ice with dynamic accelerations up to 2m/s^2 (Bjerkås et al., 2013). For large ice ridges dodging was sometimes reported at Nordströmgrund lighthouse. In Figure 2 the full time series

from 30th of March is shown, a dodging event is seen from 18.00-19.30. For large ice ridges limiting mechanisms seems to be important, it is stressed that a comprehensive study of all Nordströmgrund data is not yet done, and should be carried out to validate what caused extreme loads.

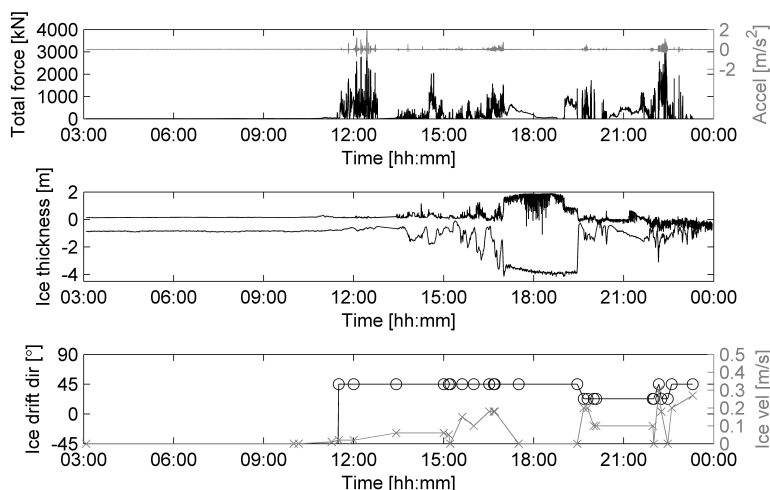


Figure 2. Extreme events from the 30th of March including dodging of and ice ridge. In the bottom plot x marks ice drift velocity and o marks ice drift direction.

Brown et al. (2009) reported the highest ice loads and associated failure modes measured until 2009 on the two center piers of the 13km long Confederation Bridge. The highest ridge load measured was 8.3MN associated with a continuous failure. The failure seemed to be a combination of crushing and bending. The highest level ice load was 8.9MN also associated with a combination of bending and crushing failure.

ANALYSIS AND DISCUSSION

In the second part of this paper some data are analyzed, first an attempt is made to compare panel loads to tilt measured at Nordströmgrund for a quasi-static ice ridge event. This is done in an attempt to investigate if tilt can be used to obtain global ice ridge loads. Accordingly limit ridge building forces are applied to estimate the critical ridge lengths for limit stress to occur on the three structures.

Analyses of tilt and panel loads on Nordströmgrund lighthouse

Global loads on Nordströmgrund lighthouse were originally derived from load panels. Loads from level ice heading from east would be captured by load panels fixed on the N-SE of the lighthouse reaching 1.5m below mean water level (MWL). However, load panels are not capable of obtaining total loads from ridges which reach deeper than 1.5m below MWL.

Frederking (2005) calibrated tilt data from a quasi-static level ice event with heading from the east, he found a ratio between global load and tilt of $12\text{kN}/\mu\text{radians}$. Arguing that once

Table 3. Full-scale actions from first year ice features. Highest load reported from first year ice ridge (F_{MaxR}) compared to highest overall load reported from first year ice (F_E).

Maximum ice ridge event	Molikpaq (Timco et al., 2000)	Confederation Bridge (Brown et al., 2009)	Nordströmgrund (STRICE data 2002, Bjerkås (2006))
Date/time [dd.mm.yyyy/hr.min]	NA	29.02.2008/09.29	30.03.2003/22.15
Failure mode	Failure behind/spine	crushing and bending	crushing
h_i [m]	0.8	0.6	0.75
h_k [m]	NA, h_s ca. 1.0	6.6	9*
F_{MaxR} [MN]	89	8.3	3.0
Ice drift [m/s]	0.10	0.00	0.18
Drift direction [°]			23
Maximum level ice event	Molikpaq (Timco and Johnston, 2004)	Confederation Bridge (Brown et al., 2009)	Nordströmgrund (STRICE data, Frederking (2005))
Date/time [dd.mm.yyyy/hr.min]	NA	04.04.2003/07.02	30.03.2003/12.27
Failure mode	NA	crushing and bending	crushing
Mean h_i [m]	2.0	0.58	0.75
F_E [MN]	131	8.9	3.5
Ice drift [m/s]	0.01	1.31	0.02
Drift direction [°]			0
Ratio $\frac{F_{MaxR}}{F_E}$	0.68	0.93	0.86

*approximate keel depth from EM-data times 3, a relation found by linear regression between ULS and EM (Bjerkås, 2006)

calibrated; tilt could be used to find total global loads regardless of the ice drift direction. He assumed that the foundation and lighthouse stiffness was omni directional and that wind loads were negligible. The data was filtered with a 3sec moving average. In the following an attempt is made to compare this ratio to a ratio for an ice ridge.

Based on the calibration done by Frederking (2005), eight quasi-static ice ridge events from the 2003 STRICE- data were analyzed. The maximal ratio between global panel load and tilt was found for an approximately 5m deep ridge. The ratio was $8.2\text{kN}/\mu\text{radians}$, this value is lower than the value for level ice, suggesting that the total ridge load is not captured.

The ratio above is based on loads measured at MWL, however the actual load point of action for a ridge depends on the ridge depth. In the following estimate the ridge load is approximated by a linearly distributed load with a resultant force F acting at a water depth of $1/3h_k$ (Figure 3). If the lighthouse is approximately a cantilever beam with varying cross section (see Figure 1 and Figure 3) the tilt is given by the equation of rotation of an elastic cantilever beam with

two cross sections 1 and 2 in Equation 1.

$$\theta = \frac{F[(l_2 + l_1)^2 - l_1^2]}{2EI_2} + \frac{Fl_1^2}{2EI_1} \quad (1)$$

where F is the resultant ice load, $l_2 = 7.5m$ is the length of the bottom foundation, l_1 is the distance from the bottom foundation to the load F ($l_1RI \approx 1/3h_k$, $l_1LI \approx MWL$), E is the elastic modulus of the lighthouse. The second area moment is $I = d^4/64$, where d is the diameter, $d_2 = 23m$ and $d_1 = 7.5m$. Now by changing l_1LI to l_1RI according to Figure 3 tilt from the same load for a 5m deep ridge and level ice is compared.

By applying Equation 1 tilt is reduced by approximately 40% for the ridge compared to level ice, due to the change in point of action and the large bottom foundation. As a result the ratio between global panel load and tilt for a 5m deep quasi static ridge should be approximately $20kN/\mu$ radians. This estimate needs validation by more advanced numerical tools. Further this analysis shows that it is not possible to find a unique ratio between global load and tilt for ridges.

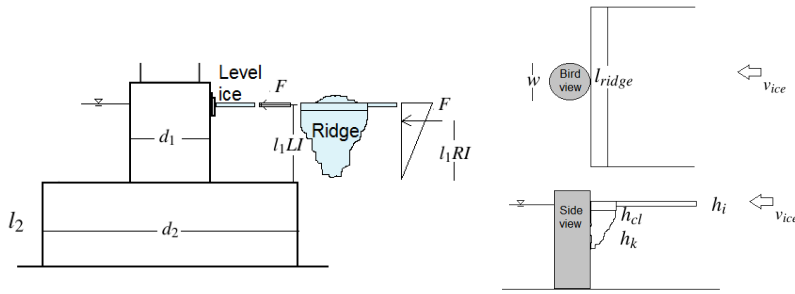


Figure 3. To the left; Simplified level ice and ridge interaction with Nordströmgrund lighthouse. To the right; a ridge interaction seen from above and the side. To illustrate ridge limit ridge building force.

Limit force estimate of critical ridge length

Limit stress is typically applied to estimate dimensioning extreme quasi-static ice loads. In the following a limit stress analysis is applied to estimate minimum ice ridge lengths for crushing to occur on the three structures review in the beginning of this paper. Limit stress requires that the global load from an ice ridge acting on a structure, is lower than the global ridge building force action on the parent ice sheet, illustrated in Figure 3. This is expressed in Equation 2 and 3. It is assumed that the driving forces from the drag and wind are small compared to the ridge building force (Croasdale, 2009).

$$F_i > F_{cl} + F_k + F_s \quad (2)$$

F_i is the ridge building force, F_{cl} is the force from the consolidated layer, F_k is the keel load and F_s is the sail load. Sail loads are assumed to be negligible and are left out of this analysis, this gives Equation 3

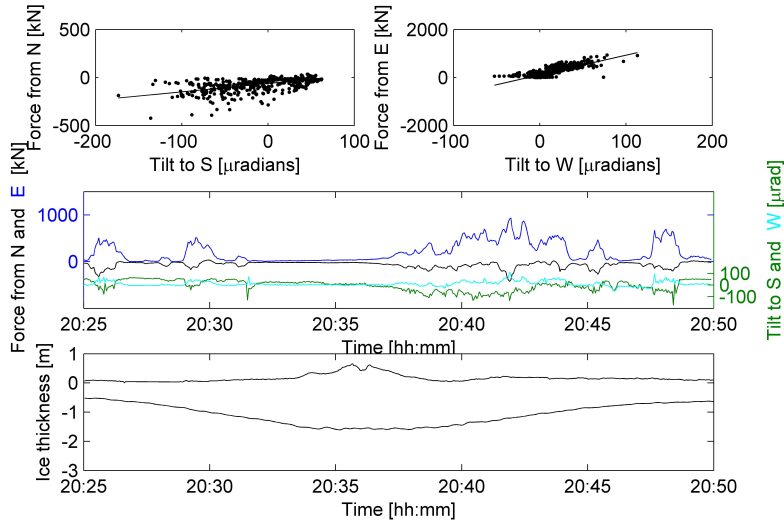


Figure 4. Tilt vs force on the 19th of March 2002 from an ice ridge event, thickness was measured with EM. N (North), S (South), E (East) and W (West).

$$p_i l_{ridge} > p_{cl} w h_{cl} + p_k w h_k \quad (3)$$

p_i is the ridge building force per unit ridge length, l_{ridge} is the length of the ridge, p_{cl} is the ice crushing pressure of the consolidated layer, w is the structure width, h_{cl} is the consolidated layer thickness, p_k is the pressure from the ridge keel and h_k is the keel depth. Ice crushing occur when the ridge length is above a critical length given by Equation 4.

$$l_{ridge} > \frac{p_{cl} h_{cl}}{p_i} w + \frac{p_k h_k}{p_i} w \quad (4)$$

In ISO19906 (2010) the crushing pressure of consolidated layer p_{cl} is given according to Equation 5.

$$p_{cl} = C_R \left(\frac{h_{cl}}{h_{ref}} \right)^n \left(\frac{w}{h_{cl}} \right)^m \quad (5)$$

C_R is a reference strength depending on the area (Beaufort Sea $C_R = 2.8$, Temperature areas $C_R = 1.8$), m is a constant, n is a constant depending on the ice thickness and h_{ref} is 1m. I believe m is a constant used to describe non simultaneous failure over the consolidated layer similar to the Equation ($p_{cl} = A_k D^m h^n$) by Bjerckås (2004), he suggests $-0.3 < m < -0.1$ in ISO19906 (2010) $m = -0.16$.

The reference crushing strength (C_R) in ISO19906 (2010) is 2.8MPa for the Beaufort sea. This value was based on first year and old ice data (ISO19906, 2010). Timco and Johnston (2004) measured ice pressured from first year ice on structures in the Beaufort sea and found that "the maximum Global Pressure measured for all types of ice loading events never exceeded 2 MN/m²". Based on this; I have changed C_R to 2 for the estimation of critical first year ice ridge length in the Beaufort Sea (Table 5).

In ISO19906 (2010) the rubble keel pressure (Equation 6) is estimated by a passive failure Mohr Coulomb model based on Dolgopolov et al. (1975). In the model the rubble fails simultaneously on shear plans inside the rubble. The original model of (Dolgopolov et al., 1975) was based on observations from model scale tests on ice rubble and the last group in Equation 6 was replaced by $1 + 2h_k/3w$. The rubble keel pressure p_k is given by Equation 6.

$$p_k = \mu \left(\frac{h_k \gamma_e \mu}{2} + 2c \right) \left(1 + \frac{h_k}{6w} \right) \quad (6)$$

$$\mu = \tan \left(45 + \frac{\phi}{2} \right) \quad (7)$$

$$\gamma_e = (1 - \eta)(\rho_w - \rho_i)g \quad (8)$$

where μ is the passive pressure coefficient, ϕ is the internal angle of friction at failure, c is the average keel cohesion, w is the structure width and γ_e is the effective buoyancy. Typical values for these ridge parameters are presented in Table 4 based on ISO19906 (2010).

For conical structures a load reduction due to bending failure is expected. ISO19906 (2010) only consider bending of level ice, in the absence of such formulas crushing is considered also for the conical piers of the Confederation bridge.

The ridge building force per unit ridge length is expressed by Equation 9 which is an empirical formula from ISO19906 (2010). The value of R depends on the ice thickness, in ISO19906 (2010) the expression for $Rh_i^{1.25}$ is equal 2, obtained by curve fitting data of 1m thick ice for structure widths greater than 100m. I have used $2 = A = Rh_i^{1.25}$, Equation 9.

$$p_i = Rh_i^{1.25} l_{ridge}^{-0.54} = Al_{ridge}^{-0.54} \quad (9)$$

Finally; the critical ridge length for limit stress is estimated by Equation 10 and presented in Table 5. Ridge parameters are taken from Table 3 and 4. For Nordströmgrund parameters were based on the ridge that caused the largest quasi-static load of 1.3MN. h_{cl} was never measured and is therefor estimated by $h_{cl} = 1.8h_i$ based on measurements by Høyland (2000). For Mo-likpaq h_k was neither measured, it is estimated by $h_k = 4.5h_s$ based on Timco et al. (2000).

Table 4. Ice ridge parameters used in this estimation (ISO19906, 2010).

Parameter	ϕ [°]	c [kPa]	ρ_w [kg/m ³]	ρ_i [kg/m ³]	η [-]
	30	7	1025	920	0.3

$$l_{ridge}^{0.46} > \left(p_{cl}h_{cl} + p_k h_k \right) \frac{w}{A} \quad (10)$$

The ridge loads calculated from the analytical models in Table 5 are between 1.5 and 6 times the measured loads.

Table 5. Table over critical length l_{ridge} together with ridge loads F_{cl} , F_k and $F_{tot} = F_{cl} + F_k$. Ridge sizes are taken from Table 3. h_{cl} was not measured for any of the structures and for Molikpaq h_k was also not measured, these values are estimated.

	Molikpaq	Confederation Bridge	Nordströmgrund lighthouse
w [m]	90	14.3	7.6
h_i [m]	0.8	0.6	0.3
h_{cl} [m]	1.44	1.08	0.54
h_k [m]	4.5	6.6	6.1
n	-0.34	-0.38	-0.44
C_R MPa	2*	1.8	1.8
F_{cl} [MN]	118	18	6
F_k [MN]	12	3	2
F_{tot} [MN]	130	21	8
l_{ridge} [m]	9000	200	20

*Adjusted down to 2 from 2.8 to only account for first year ice ridges.

CONCLUSIONS

In this paper actions from first year ice ridges on fixed structures has been studied. The first part of this paper was a review on full scale global loads and associated failure modes on three fixed structures, actions from first year ridges and level ice were compared. The three instrumented structures was the Molikpaq, the piers of the Confederation Bridge and Nordströmgrund lighthouse. In the second part of this paper some ice ridge structure interaction data were analyzed. Data from Nordströmgrund lighthouse were used to obtain a ratio between global panel loads and tilt for ridges compared to level ice. Finally a limit force analysis was performed to estimate minimum ice ridge lengths for crushing to occur on the three fixed structures.

From this work the following conclusions were made:

- The highest ridge loads on Nordströmgrund lighthouse and the piers of the confederation bridge were associated with crushing and combined crushing/bending respectively, while

on Molikpaq crushing of ice ridges did not occur. Measured full scale global ice ridge loads were in the same order as loads from level ice for all three structures.

- From a limit force analysis it was estimated that the critical ridge length to produce local crushing was 9km on Molikpaq compared to 20m for Nordströmgrund lighthouse and 200m on the piers of the confederation bridge.
- From full scale data of a quasi-static 5m deep ice ridge iteration with the Nordströmgrund lighthouse; a ratio between global panel load and tilt was found. The ridge ratio obtained was 8.2 kN/ μ radians compared to 12kN/ μ radians for level ice derived by Frederking (2005). The low value indicates that load panels underestimate ridge loads. Additionally; an analytical estimate suggest that the same load from a 5m deep ridge would give approximately 40% less tilt than level ice due to the change of point of action and large bottom foundation. As a result a general ratio between global load and tilt cannot be obtain for ice ridges. For ice ridges; advanced numerical tools (FEM,DEM) are needed to obtain global loads from tilt.

ACKNOWLEDGMENTS

The author wishes to acknowledge the support of the Research Council of Norway through the Centre for Research-based Innovation SAMCoT, and the support of all SAMCoT partners. The author also acknowledges professor Knut V. Høyland for valuable discussions.

REFERENCES

- Ahlenius (2005). Arctic map, political, <http://www.grida.no/>. 2005.
- Bjerkås (2004). Global design ice loads' dependence of failure mode. *International Journal of Offshore and Polar Engineering*, (Vol. 3 No. 3).
- Bjerkås (2006). Ice actions on offshore structures, with applications of continuous wavelet transform on ice load signals. *Doctoral thesis for the degree of philopphiae doctor, NTNU*.
- Bjerkås and Bonnemaire (2004). Ice ridge-structure interaction, Part II: Loads from ice ridges and their surrounding ice sheets. *Proceedings of the 17th International Symposium on Ice*. pp122-129.
- Bjerkås, Meese, and Alsos (2013). Ice induced vibrations - observations of a full scale lock-in event. *Proceedings 23rd International Offshore and Polar Engineering Anchorage*. pp1272-1279.
- Bonnemaire and Bjerkås (2004). Ice ridge-structure interaction, Part I: Geometry and failure modes of ice ridges. *Proceedings of the 17th International Symposium on Ice*. pp114-122.
- Brown (2001). Four years of ice force observations on the Confederation Bridge. *Proceedings of the 16th International Conference on Port and Ocean engineering under Arctic Conditions (POAC)*. pp285-299.
- Brown (2006). Confederation bridge - an innovative approach to ice force. *Proceedings of the 2006 Annual Conference of the Transportation Association of Canada*.
- Brown (2007). Analysis of ice event loads derived from structural response. *Cold Regions Science and Technology*, (47). pp224-232.

- Brown, Tibbo, Tripathi, Obert, and Shrestha (2009). Extreme ice load events on the Confederation Bridge. *Cold Regions Science and Technology*. 14p.
- Croasdale (2009). Limit force ice loads-an update. *Proceedings of the 20th International Conference on Port and Ocean engineering under Arctic Conditions (POAC)*, (30).
- Dolgoplov, Afanasiev, Korenkov, and Panfilov (1975). Effect of hummocked ice on piers of marine hydraulic structures. *Third International Symposium on Ice Problems, IAHR*, (Vol. 3 No. 3).
- Frederking (2005). Tiltmeter application at Nordströmgrund lighthouse - STRICE project. *Proceedings of the 18th international conference on Port and Ocean engineering under Arctic Conditions*, (Vol 1). pp399-408.
- Høyland (2000). Consolidation of first-year sea ice ridges. *Journal of geophysical research*, (Vol. 107, NO C6, 3062).
- ISO19906 (2010). Petroleum and natural gas industries - arctic offshore structures. 412p.
- Kärna and Jochmann (2004). Field observations on ice failure modes. *Proceedings of the 17th International Symposium on Ice*.
- Schwarz and Jochmann (2001). Four years of ice force observations on the Confederation Bridge. *Proceedings of the 16th International Conference on Port and Ocean engineering under Arctic Conditions (POAC)*. pp669-683.
- Tibbo, Obert, Shrestha, Tripathi, Mayne, and Brown (2009). Year twelve of the Confederation Bridge ice monitoring program. *Proceedings of the 20th International Conference on Port and Ocean engineering in Arctic Conditions (POAC)*. pp47-57.
- Timco and Croasdale (2006). How well can we predict ice loads? *Proceedings of the 18th IAHR International Symposium on Ice*. pp167-174.
- Timco, Croasdale, and Wright (2000). An overview of first-year sea ice ridges. *Canadian Hydraulic Centre - technical report*, (5-112). p157.
- Timco and Johnston (2004). Ice loads on the caisson structures in the Canadian Beaufort Sea. *Cold regions science and technology*, (No 38). pp185-209.
- Timco, Johnston, and Wright (2005). Multi-year ice loads on the Molikpaq: May 12,1986 event. *Proceedings of the 18th International Conference on Port and Ocean engineering under Arctic Conditions (POAC)*, (pp453-462).
- Timco, Wright, Johnston, and Frederking (1999). First-year ice ridge loads on Molikpaq. *Proceedings of the 4th International Conference on Development of the Russian Arctic Offshore*. pp172-179.
- WMO (1970). WMO sea ice nomenclature. *World Meteorological Organization*, (Tech rep NO 259.TP.145). pp1272-1279.
- Wright (1986). Winter ice interactions with an arctic offshore structure. *IAHR International Symposium on Ice Problems 1986*, (Vol. 3 pp49-73).

Appendix 4

Ice-ridge interactions with the Norströmsgrund lighthouse: global forces and interaction modes

This appendix includes the paper published in the journal Cold Regions Science and Technology (see below).

- Ervik, Å., Nord, T.S., Høyland, K. V., Samardzija, Li, H.. Ice-ridge interactions with the Norströmsgrund lighthouse: global forces and interaction modes. Cold Regions Science and Technology, 158: 195-220
<https://doi.org/10.1016/j.coldregions.2018.08.020>



Contents lists available at ScienceDirect

Cold Regions Science and Technology

journal homepage: www.elsevier.com/locate/coldregions

Ice-ridge interactions with the Norströmsgrund lighthouse: Global forces and interaction modes

Åse Ervik^{a,b,*}, Torodd S. Nord^{a,b}, Knut V. Høyland^a, Ilija Samardžija^a, Hongtao Li^a^a Sustainable Arctic Marine and Coastal Technology (SAMCoT), Centre for Research-based Innovation (CRI), Norwegian University of Science and Technology, Trondheim, Norway^b The University Centre in Svalbard (UNIS), Longyearbyen, Spitsbergen

ARTICLE INFO

Keywords:

Full-scale ice ridge-structure interactions
Global forces
Classification of interaction modes
Instrumentation

ABSTRACT

The signatures in force and response time series from ice-ridge interactions on vertically sided structures are not described in standards and are among the least understood types of ice-structure interactions. In this paper, we identified 35 high global-force ridge events at the Norströmsgrund lighthouse in the winters of 1999/2000 to 2002/2003. During these events, load panels rendered global forces in excess of 3 MN, where the highest global force measured was approximately 6 MN. The type of ice-ridge interaction mode was further classified based on the signatures in force and the response time series as well as video records. The classified ice-ridge interactions included 1) limit-force stalling, 2) limit-stress ductile failure and 3) limit-stress brittle failure. Based on the suggested format of classification, recommendations for future instrumentation are proposed.

1. Introduction

First-year ice ridges are accounted for in the design of marine structures in Arctic, subarctic or temperate areas such as the Baltic Sea and ice ridge interactions may establish the ultimate limit state for a structure. Ice ridges are typical features in the Baltic Sea and account for, on average, one-third of the total ice mass (Leppäranta and Hakala, 1992). The fraction is lower than the total ice mass in the Arctic Ocean (66% in the Fram Strait) (Hansen et al., 2014). The first offshore wind farm with ten gravity-based turbines designed for ice conditions is under construction (as of 2017) in the southern part of the Gulf of Bothnia (N61°62.9' E21° 35.34'), 10 km east of Pori in Finland (4COffshore, 2017; Eranti, 2017). Ice forces measured on lighthouses can provide guidance for the design of wind turbine foundations, bridge piers and other vertically sided structures. In this paper, we focus on ice-ridge forces measured at the Norströmsgrund lighthouse, particularly high global forces measured from the consolidated layer.

During the low level ice forces project (LOLEIF) and structures in ice project (STRICE) (winters 1999/2000–2002/2003), ice forces were measured at the Norströmsgrund lighthouse located in the Gulf of Bothnia (N65°6.6' E22° 19.3'), 60 km southeast of Luleå in Sweden.

Since 1971, year-around navigation has been maintained in the Gulf of Bothnia, and ice-breaking activities have increased the movability of the ice in the area around the Norströmsgrund lighthouse (Engelbrektsen, 1987). Consequently, the lighthouse is often located in the transition zone between land-fast ice and dynamic-drift ice. The ice drift is wind-driven and predominantly along the coast in the south-westerly and northeasterly directions (Engelbrektsen, 1987). Typical level-ice conditions are 40–60 cm, but the thickness of rafted ice may exceed 1 m, and ridges are frequent. The Norströmsgrund lighthouse is a gravity-based concrete structure (displayed in Fig. 1) with a diameter of 7.5 m at mean water level (MWL) and 23 m at the underwater caisson at +7.5 m elevation from the seabed (Bjerkås and Nord, 2016). The estimated MWL was +14.5 m elevation from the seabed (Jochmann and Schwarz, 2000). The lighthouse was instrumented to measure ice forces at MWL, structural responses (accelerations and tilt), ice thickness, meteorological data and videos. A detailed description of the instrumentation is available in Bjerkås (2006), Haas (2000) and Jochmann and Schwarz (2000).

The ice forces measured at the lighthouse have been presented in several conference papers (Bjerkås and Bonnemaire, 2004; Bonnemaire and Bjerkås, 2004; Frederking, 2005; Haas and Jochmann, 2003; Li

Abbreviations: EM, electromagnetic ground conductivity geophysical instrument; FDD, freezing degree days; FMI, Finnish Meteorological Institute; HSE, health, safety and environment; JOIA, Japan Ocean Industries Association project; LOLEIF, low level ice forces project; MWL, mean water level; STRICE, structures in ice project; SMHI, Swedish Meteorological Institute; ULS, upwards looking sonar

* Corresponding author at: Sustainable Arctic Marine and Coastal Technology (SAMCoT), Centre for Research-based Innovation (CRI), Norwegian University of Science and Technology, Trondheim, Norway.

E-mail address: ase.ervik@ntnu.no (Å. Ervik).

<https://doi.org/10.1016/j.coldregions.2018.08.020>

Received 1 February 2018; Received in revised form 13 August 2018; Accepted 22 August 2018

Available online 24 August 2018

0165-232X/© 2018 The Authors. Published by Elsevier B.V. This is an open access article under the CC BY license

(<http://creativecommons.org/licenses/by/4.0/>).

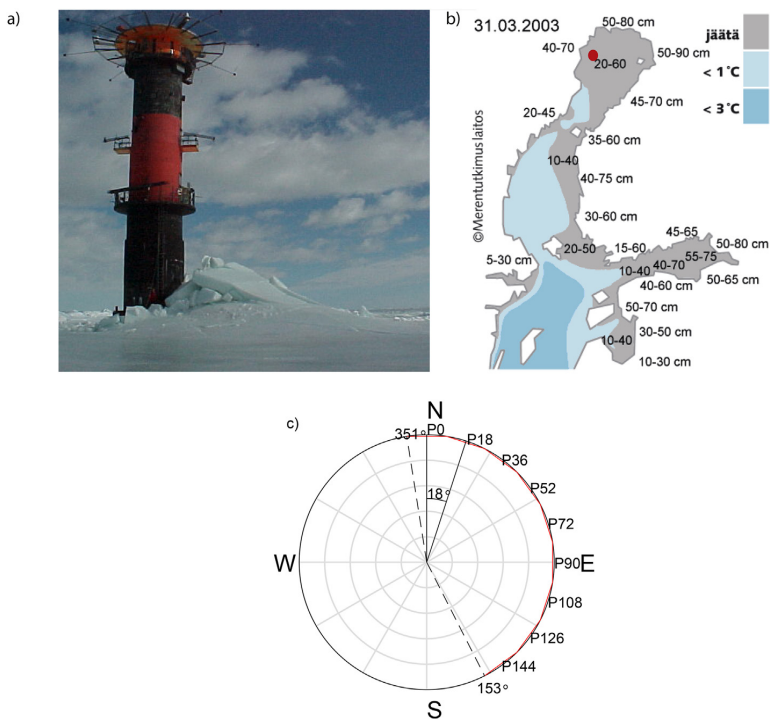


Fig. 1. a) The Norströmsgrund lighthouse (Photo: Basile Bonnemaire, 2003 March 27); b) the Gulf of Bothnia with the position of the lighthouse marked with a red dot and ice-covered areas shaded in gray, the light blue and blue areas represents water at temperatures colder than +1 °C and + 3 °C, respectively (2003 March 31, FMI); c) load panel orientation. (For interpretation of the references to colour in this figure legend, the reader is referred to the web version of this article.)

et al., 2016; Poirier, 2014; Sudom and Frederking, 2014), reports (Franson and Bergdahl, 2009; Haas, 2000; Heinonen et al., 2004; Jochmann and Schwarz, 2000; Kärrnä and Yan, 2009) and a few journal papers (Bjerkås, 2004; Nord et al., 2016).

Time series of forces and responses are crucial when observations of processes at the ice-structure interface are attributed to the different modes of ice-structure interaction, e.g., ductile or brittle failure. The signatures of these different interaction modes when level ice interacts with a structure are well-established (Jordaan, 2001; Sodhi and Haehnel, 2003). Interaction mode classification was important to narrow the scope of experimental campaigns and the development of phenomenological models in the “ice-induced vibrations” community. For ice-ridge interactions, very little has been reported on the signatures in force and response, and only Bjerkås (2006), Brown et al. (2010), Ervik (2015) and Poirier (2014) have presented time series of force signatures in ridge interactions and identified ridge failure modes. However, to our knowledge, the identified signatures in forces and responses have never been systematically associated with the type of ice ridge-structure interaction mode. High global force ridge events were chosen for this study because they are likely to establish events that will govern the quasi-static ultimate limit state design and the high global force ridge events are required when probabilistic design methods are applied.

This paper is the first to 1) identify a significant number of high global-force ridge events measured at the Norströmsgrund lighthouse and 2) classify ice-ridge-interaction modes based on the signatures of the force and response time series. In the discussion, the interaction classification for ice ridges is compared to the classification for level ice (Sodhi and Haehnel, 2003). Based on the suggested format of classification and lessons learned from LOLEIF and STRICE, recommendations for future instrumentation are proposed. Classifying ice ridge interactions into different modes based on forces and responses may improve the design of structures if certain interaction modes can be avoided or if

the driving forces exclude certain interaction modes.

2. Background

2.1. Limiting mechanism

Load-limiting mechanisms include limit stress, limit momentum/energy and limit force (Croasdale, 1984; Croasdale, 2009; Timco et al., 2017). Ice forces are limited by stress when the ice fails directly against the structure (e.g., crushing, bending, buckling and splitting), and thus sufficient driving forces are available. If the momentum of the ice floe is insufficient, the ice will come to a halt, and the forces are limited by momentum or energy. This is particularly important for icebergs and other massive features. The limit force occurs when ice forces are limited by the driving forces such that the wind and current forces are insufficient to cause the ice to fail at the structure surface. The limit-force mechanism also includes limit pack-ice forces, which occur when the ice fails elsewhere in the ice pack due to, e.g., ridge building, buckling against thicker ice or level-ice failure against rubble piles. Because of the complex dynamics of the ridge-building process, the range of pack-ice driving forces is still unknown (Timco et al., 2017). For a single ridge embedded in level ice, the ridge length/structure width may give the condition for the limit stress/limit ridge-building force. For the Norströmsgrund lighthouse (7.5 m wide), the critical ridge-building length is approximately 20 m, whereas for Molikpaq (~90 m wide), the critical ridge length is several kilometers (Croasdale, 2009; Ervik, 2015). Unfortunately, the video coverage at the Norströmsgrund lighthouse was insufficient to observe far-field ice deformation, which makes classification of the limiting mechanisms other than limit stress difficult.

2.2. Interaction modes

Bonnemaire and Bjerckås (2004) identified four types of failure modes during ice-ridge interactions with the Norströmsgrund lighthouse, including crushing, splitting, bending and failure on a wedge in front of the structure. These types of failure modes were classified based on visual observations of the ice failure from videos. Among the failure modes, the crushing failure mode produced the highest global forces. When level-ice fails against compliant vertically sided structures the combined observations of crushing and structural response are classified as one of the following four interaction modes: 1) ductile failure (also referred to as creep deformation in Sodhi et al., 1998), 2) intermittent crushing, 3) frequency lock-in crushing, or 4) continuous brittle crushing, arranged by increasing indentation speed (ISO19906, 2010; Sodhi and Haehnel, 2003). The classification of interaction modes by means of measured quantities requires time series of force and response, preferably alongside video footage of the ice failure. At the ice-structure interface, damage processes in the ice adjacent to the indenter differ depending on the confinement (Jordaan, 2001; Wells et al., 2011), which is important for the appearance and failure of high-pressure zones (O'Rourke et al., 2016a; O'Rourke et al., 2016b). Sodhi et al. (1998) showed that the highest level-ice forces on a medium-scale stiff structure were caused by low-velocity ductile failure with high contact area. In this paper, modes of ice ridge interactions are classified and compared to the four modes identified for level ice.

3. Method

In the following, we present how events are identified and the methods used to obtain the 1) global ice force, 2) acceleration, 3) tilt, 4) ice thickness and type of ice feature, and 5) ice speed. Finally, a few simplistic signal-processing tools are presented.

3.1. Event identification

All data files recorded during LOLEIF and STRICE were considered in this study. A program in MATLAB 2017a (The MathWorks, Inc., Natick, Massachusetts, United States) was developed to search through all data files and filter out data files based on requirements (e.g., ranges in ice thickness, acceleration and/or global panel force). The individual data file records contained time series of various length, sampling frequency and interaction modes. First, data files with a global force in excess of 3MN was filtered out. Then the ridge events were selected manually, based on a combination of global force, acceleration, ice thickness and video footage, to capture different interaction modes in which the maximum global force exceeded 3 MN. The 3 MN global force limit was applied to obtain a manageable amount of high global force data files for detailed analysis, the limit was approximately 50% of the maximum global force (~6 MN). Unfortunately, a quantifiable criteria to define event time intervals was not found, due to different sampling frequencies between measurements within the same data file (ice thickness, drift speed, global force/acceleration were sampled with different frequencies). Small variations in the position of the event time interval may affect the mean values and standard deviations of forces and accelerations, however the maximum global forces and the identified interaction modes and thus the main results are unaffected. A data file record is shown in Fig. 2 with 5 identified ridge events with a global force above 3 MN. The red and blue vertical lines represent the beginning and end of an event, respectively, and the horizontal red dashed line is the global force limit (3 MN). In some cases, two data files were combined to obtain one event.

3.2. Panel forces

The lighthouse was instrumented with 9 load panels (P0-P144 in Fig. 1c) covering 162° of the lighthouse circumference from the north

(351°) to southeast (153°). The width and height of the load panels were 1.2 m and 1.6 m, respectively. One load panel (facing 90°, P90 in Fig. 1c) was segmented, and local forces were measured in eight segments (approximately 0.6 m wide and 0.4 m high). The panel force was calculated as the sum of the local forces on each segment. The other load panels each measured a single normal force. The global force on the lighthouse was the vector sum of the panel forces (see Appendix A.1). The load panels were incapable of measuring shear forces, and the load panel measurement range was 2 MN + 50% overload. The sampling frequency was manually set to 1–100 Hz, and the vertical position of the load panels was from +13.4 m to +15 m elevation (from the seabed). The water level in the Baltic Sea is affected by the air pressure; deep low-pressure passages over the Bothnian Bay combined with high pressures over the southern Baltic can create sea level fluctuations up to ± 2 m, although tides are not present (SMHI, 2014a). The water level elevation at the position of the Norströmsgrund lighthouse was generated using E.U. Copernicus Marine Service Information with a root-mean-square-error of 0.09 m (Axell et al., 2017; Copernicus, 2017). The water level was used both to evaluate the load panel vertical coverage and to quantify the distribution of the local forces.

3.3. Tilt

Frederking (2005) showed that tilt (inclination) measurements could be used to calculate the global static or slow-varying level ice forces on the lighthouse in 2002 after it was installed, zeroed and calibrated (February 27). Two biaxial inclinometers were installed at +22.8 m and +37.1 m elevation. Unfortunately, for both events in 2003 and ridge interactions, tilt could not be reliably used to obtain global forces because of signal drift and the inelasticity of the lighthouse foundation (Frederking, 2005; Sudom and Frederking, 2014).

3.4. Acceleration

Two accelerometers were installed at +16.5 m, close to the ice action point, and two were installed close to the top of the lighthouse at +37.1 m elevation. Nord et al. (2016) showed that global dynamic forces on the lighthouse could be identified by employing the joint input-state estimation algorithm in conjunction with a limited number of accelerometer measurements and a modally reduced order model. In this study, the acceleration measurements were mainly used for ice-structure interaction mode classification. Only acceleration measurements with 10 Hz sampling frequency or higher were considered.

3.5. Ice thickness

The ice thickness at the Norströmsgrund lighthouse was measured with both a upwards looking sonar (ULS) and an electromagnetic ground conductivity geophysical instrument (EM) sensor (Haas and Jochmann, 2003). The ULS was mounted on the lighthouse underwater caisson (+7.5 m elevation), approximately 5 m southeast of the lighthouse, and the EM sensor was mounted on a hanging frame 10 m east of the lighthouse at approximately 2 m above MWL. The ULS always identified the deepest point of the ice but was operational only in 2000 and 2001. The EM averaged the ice thickness over an area of approximately 6 m in diameter (the footprint). For ice ridges, the EM sensor underestimated the maximum keel depth but measured the approximate thickness of the consolidated layer and some part of the rubble, depending on the conductivity (Haas, 2017). The conductivity is affected by salinity and macroporosity. Therefore, calculating ice thickness from EM measurements requires inverse modeling because salinity and macroporosity are unknowns (Haas, 2000; Haas, 2017). Both Bjerckås (2006) and Haas and Jochmann (2003) showed that the maximum keel depth from the ULS was approximately 3 times the EM thickness.

The type of ice feature (level, rafted or ridged ice) was determined

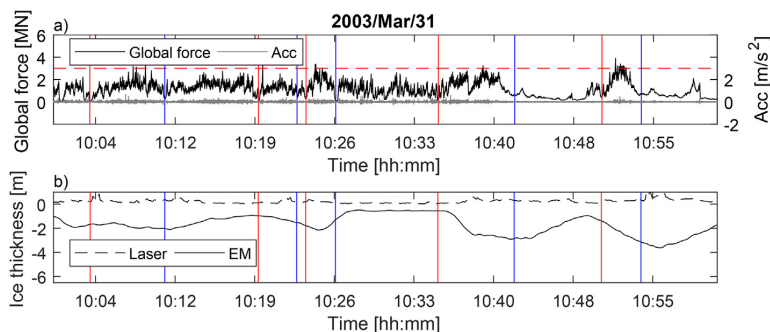


Fig. 2. Example of a data file record with 5 events. The vertical red and blue lines represent the beginning and end of an event, respectively: a) global force and acceleration (Acc at +16.5 m) and b) ice thickness. (For interpretation of the references to colour in this figure legend, the reader is referred to the web version of this article.)

Table 1
Description of the winters of 1999/2000–2002/2003 and corresponding ice conditions.

Winter	1999/2000	2000/2001	2001/2002	2002/2003
Max ice extent [km ²]	96,000	129,000	102,000	233,000
Date of max ice extent	02/24	03/26	02/01	03/05
Max. fast ice thickness [cm]	50–85	50–60	55–80	70–90
Classification of the winter	Mild	Mild and short	Mild	Average

based on a combination of ice thickness measurements, video records, and the level-ice thickness calculated from the number of freezing degree days (FDDs) according to the empirical expression proposed by Zubov (1945). Air temperature measurements at the Rødkallen meteorological station located 23.6 km north-northeast of Norströmsgrund were used to obtain the FDDs. Daily mean temperatures were calculated by the Ekholm-Modén model, which uses weighted averages of the minimum and maximum temperatures as well as the temperatures at 7 am, 1 pm and 7 pm (SMHI, 2014b).

3.6. Ice speed

The ice speed was sporadically estimated from visual observations by personnel stationed at the lighthouse and stored in a logbook. Continuous ice speed was additionally estimated by using videos from one video camera fixed to the southeast side of the lighthouse at +31.5 m elevation. An automated algorithm based on cross correlation between pairs of images was used to estimate the ice speed (Samaradzija, 2018). The algorithm could not be used in cases of poor and unequal lighting during the night, if the ice was uniform without any distinct features or if ice cracks formed. In those cases, the ice-drift estimate was performed manually from video recordings.

3.7. Signal processing

To classify the type of ice interaction mode, both force-time series and acceleration-time series were investigated qualitatively, similar to that described by Sodhi and Haehnel (2003) for level ice and adopted by ISO19906 (2010). Additionally, we tested some simplistic signal-processing tools to 1) quantify the global dynamic force and 2) quantify the stationarity in force-time series for the different interaction modes. A stationary time series has constant mean and variance over time. To quantify the dynamic global force, the time series was filtered with a Butterworth high-pass filter with a cutoff frequency of 0.3 Hz. The cutoff frequency was chosen such that it both removed as much as practically possible of the slow-varying drift in the global force signals, and that the filter worked for a range of sampling frequencies. For the acceleration-time series, the standard deviation was calculated. To

quantify the signal stationarity, the global force-time series was filtered by averaging the global force within 7-s intervals (μ_{F7s}) each 7 s (not a 7-s moving average), calculating the standard deviation of the interval means ($\sigma_{\mu F7s}$), and calculating the autocorrelation.

4. Results

4.1. Met-ocean conditions

The ice cover in the Gulf of Bothnia is low salinity (approximately 0.7‰), first-year ice. A typical ice season extends from February to April. The ice conditions for the winters of 1999/2000 to 2002/2003, including the maximum ice extent, the maximum fast ice thickness and a general classification of the winter based on the seasonal FDDs (FMI, 2016), are summarized in Table 1. The average seasonal FDDs (dashed line in Fig. 3a) from 1953 to 2015 was 994, compared to 654 in 1999/2000, 862 in 2000/2001, 806 in 2001/2002 and 1069 in 2002/2003. In Fig. 3b the time development of FDD for each of the four winters is displayed, the circles mark dates with high global force ridge events.

The mean wind and ice-drift direction were predominantly from the northeast for the identified high-force ridge events, as shown in Fig. 4. This may not represent the dominant wind direction, as only events in which the load panel coverage was high are included. The ice drift was

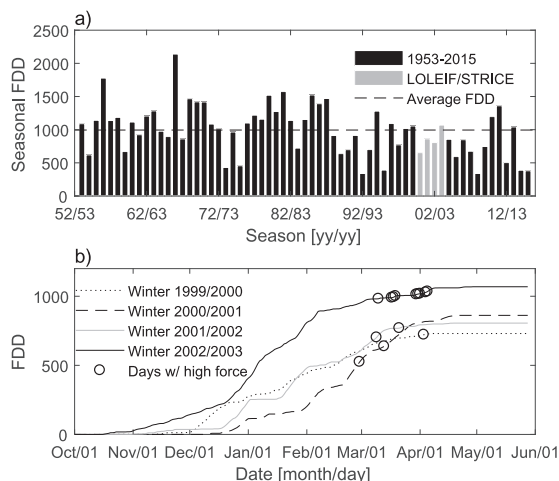


Fig. 3. FDDs measured at the Rødkallen meteorological station located 23.6 km north-northeast of the Norströmsgrund lighthouse, a) seasonal FDDs from 1952/1953 to 2014/2015 and b) time development in FDD for winters 1999/2000 to 2002/2003, where circles display days with high global force ridge events.

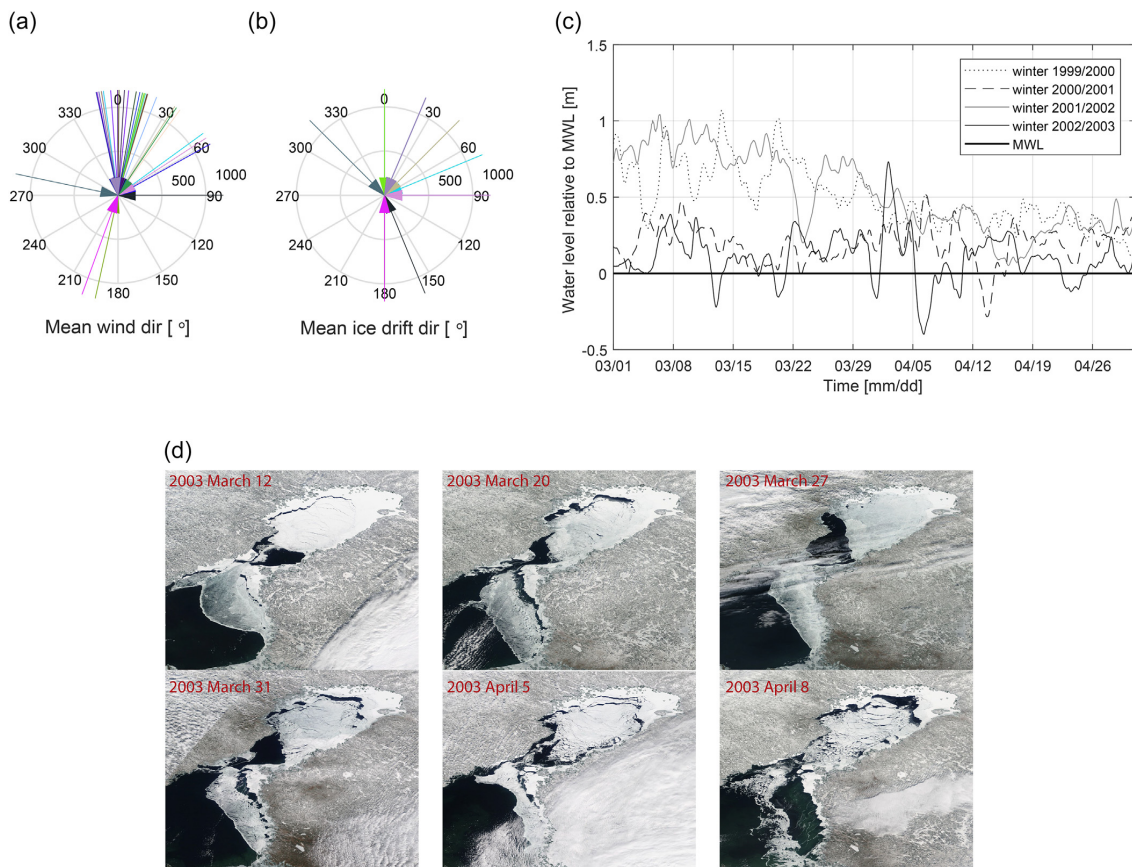


Fig. 4. Wind and ice-drift directions, water level and ice maps. a) Mean wind direction in the 35 ridge events that were identified; b) mean ice-drift direction for the 35 identified ridge events; c) water level relative to the MWL, data from the Copernicus data base (Copernicus, 2017) for the winter seasons of 1999/2000–2002/2003; d) optical satellite images top row from left; March 12, March 20, March 27 and bottom row from left; March 31, April 5 and April 8 (NASA, 2018).

from 20° counter-clockwise to 67.5° clockwise of the wind direction. Eighty percent of the events were caused by ice drift from counter-clockwise, and the wind and ice-drift directions were never identical. The fluctuation in water level at the location of the Norströmsgrund lighthouse is shown in Fig. 4c, which is based on data gathered from Copernicus (2017). During LOLEIF/STRICE, the maximum and minimum water level elevations (from MWL) were +1.1 and −0.4 m, respectively, and the results were used to study the local forces in section 4.3.2. The dynamic movement of the ice sheet in March and April 2003 in the Gulf of Bothnia is displayed in Fig. 4d, images are from an optical satellite (NASA, 2018).

4.2. Events and interaction modes

During LOLEIF and STRICE, ice interacted with the Norströmsgrund lighthouse on 162 days, where 519 data files were recorded. In total, 35 ridge events with a maximum global force above 3 MN were identified. These events occurred in March and April on 14 different days (see Table A.1 in Appendix A.2). We identified the following three ice-ridge interaction modes:

- Limit-force stalling (stalling in short);
- Limit-stress ductile failure (ductile in short); and
- Limit-stress brittle failure (brittle in short).

The type of ice-ridge interaction mode was stalling in 4 events (on 4 days), ductile in 2 events (on 2 days) and brittle in 29 events (on 7 days). No intermittent or frequency lock-in ice ridge events were identified among the high global force events. The different interaction modes are described in the following text, and signatures of time series are displayed in Fig. 5 (stalling event), Fig. 6-1 and 2 (ductile event, second highest force measured), Fig. 7 (brittle event, highest force measured) and Fig. 8 (brittle event, third highest force measured). Figs. 5–8a) display time series of the global force (black line), including a seven-second average (red line) and accelerations measured at +16.5 m (light gray line) and +37.1 m elevation (dark gray line). Figs. 5–8b) display the average panel force, including a blue arrow marking the wind direction, on the left and the panel force distribution at the time of maximum global force, including a red arrow marking the ice-drift direction, on the right. Figs. 5–8c) display time series of EM (black line) and laser (gray line) ice thickness. Figs. 5–8d) display the average segment force on the left and the segment force at the time of maximum global force on the right. The water level is marked with red arrows and the text WL. Figs. 5–8e) display time series of ice speed from image processing and a table with ice speed for the logbook and met-ocean data. Figs. 5–8f) display time series of panel forces, with legend numbers indicating load panel numbers (Fig. 1c). The time series were not resampled and were measured with a sampling frequency in the range of 1–100 Hz, as noted in the figure captions. The force dropped at

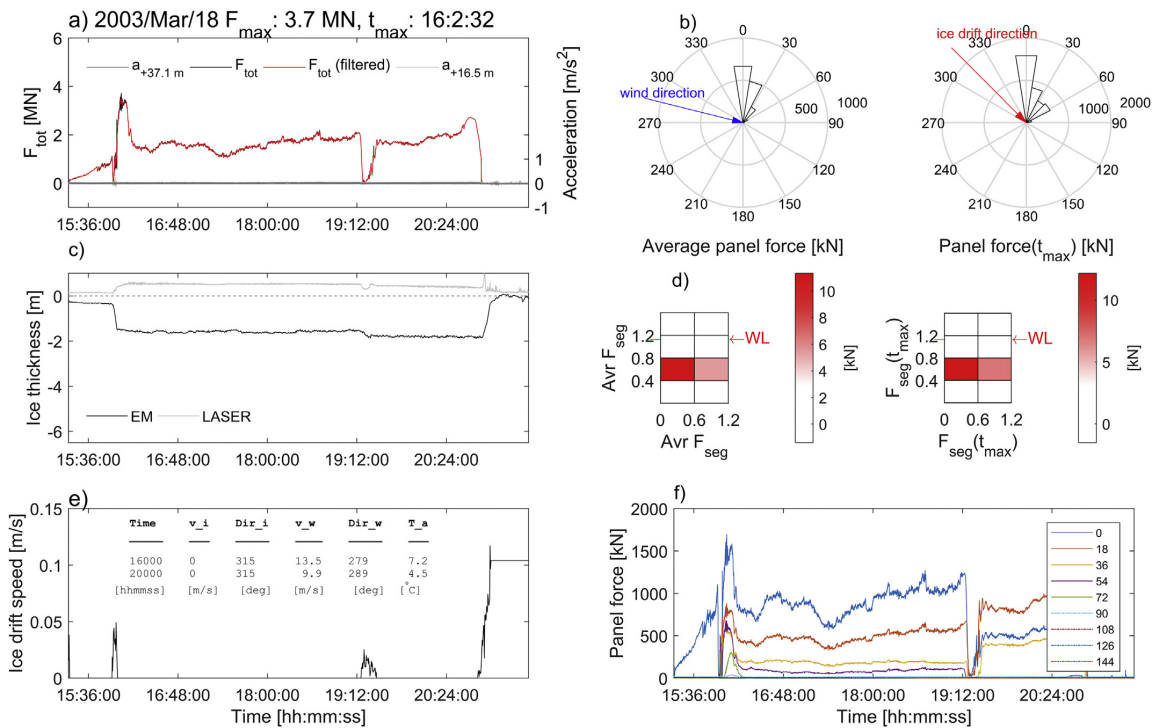


Fig. 5. Event no. 16, stalling event with a sampling frequency of 1 Hz. Fig. 5–8 a) time series of the global force (black line) including a seven-second average (red line) and accelerations measured at +16.5 m (light gray line) and +37.1 m elevation (dark gray line); b) at left, the average panel force, including a blue arrow marking the wind direction; at right, the panel force distribution at the time of maximum global force, including a red arrow marking the ice-drift direction; c) time series of EM (black line) and laser (gray line) ice thickness; d) at left, the average segment force; at right, the segment force at the time of maximum global force. The water level is marked with red arrows and the text WL; e) time series of ice speed from image processing and a table with ice speed for the logbook and met-ocean data; f) time series of panel forces. Legend numbers indicate load panel orientations from north 0° to southeast 144°. (For interpretation of the references to colour in this figure legend, the reader is referred to the web version of this article.)

the end of the events due to a change in interaction mode from failure at the lighthouse or stalling to shearing, bending, splitting, change in ice-drift direction or the ridge passing the lighthouse. In Fig. 8e, the ice speed drops to zero because of global ridge shear failure.

Table 2 provides a summary, for the different interaction modes, of the standard deviations of the range of acceleration (σ_{Acc}), dynamic global force ($\sigma_{F_{dyn}}$), and average global force in 7-s intervals ($\sigma_{\mu F_{7s}}$) over the time interval delineated by the red and blue lines for each event. Table 2 also displays the maximum divided by the mean global force, ice speed at the time of the maximum global force ($v(t_{max})$), mean air temperature (μ_{TA}) and mean wind speed (μ_W) for the different interaction modes.

The dynamic force had low amplitudes during all stalling events, with $\sigma_{F_{dyn}}$ in range 3–14 kN. The acceleration measured at +16.5 m elevation with a sampling frequency of 10 Hz was low ($\sigma_{Acc} = 0.007 \text{ m/s}^2$) and on the order of the magnitude of the acceleration measured during open-water interactions sampled at 84 Hz. The ice speed was equal to zero most of the time duration in stalling events, and the duration of these events was between 5 min and 6 h. The peak global force measured during stalling events was recorded either just before the ice sheet started moving or the moment the ice sheet came to a halt. However, for the second type of stalling events (where the global force peaked the moment the ice sheet came to a halt) the force development was not always captured by the load panels because the ice sheet rotated such that the ice interacted with parts of the lighthouse not instrumented. During stalling events, the ice sheet could be stalled against

the lighthouse for several hours attaining a high global force. The stalled events ended when either the ice-drift direction changed, allowing the thick ice feature to avoid the lighthouse, or a global failure occurred, e.g., cracks and splitting. During limit-force stalling events, the wind speed was 7–14 m/s, the mean air temperature was -1.2°C (minimum of -3.8°C and maximum of $+5.2^\circ\text{C}$), and the ice drift was from 23° , 157° , 180° or 315° .

The dynamic force had low amplitudes during all ductile events, with $\sigma_{F_{dyn}}$ in range 8–27 kN. The acceleration measured at +16.5 m elevation with a sampling frequency of 10 Hz was $\sigma_{Acc} = 0.008 \text{ m/s}^2$, approximately the same as the acceleration for stalling events. The ice speed was 0.005–0.02 m/s, lower than for the brittle events, and the duration of these events was between 5 min and 2 h. The wind velocity under these conditions was 7–8 m/s, the mean air temperature was $+0.8^\circ\text{C}$ (minimum of -2.7°C and maximum of $+4.4^\circ\text{C}$), and the ice drift was from 72° or 90° .

During brittle events, the signature of the force-time series was dynamic ($\sigma_{F_{dyn}}$ 83–203 kN). The structure acceleration was larger than the structure acceleration for both ductile and stalling events, and the standard deviation of the acceleration ranged from 0.02 to 0.11 m/s^2 . The ice speed was 0.1–0.4 m/s, higher than for any other interaction mode. The ice drift was mostly from 23° , but a few events were from 0° , 45° , and 90° , and one was from 180° . The duration of these events was 1 min to 1 h. The wind speed was 7–14 m/s and the mean air temperature was -6.6°C (minimum of -14.4°C and maximum of -0.8°C).

The standard deviation of the acceleration for the events with a sampling frequency equal to or > 10 Hz is displayed in Fig. 9. Events with a sampling frequency (f_s) > 10 Hz were resampled to 10 Hz. Different failure modes are indicated by different symbols.

4.3. Forces and pressures

4.3.1. Global force and pressure

The largest global forces were caused by the ice ridges with the largest EM ice thickness (Fig. 10a), but the global pressure decreased with increasing ice thickness (Fig. 10b) and was independent of ice speed (Fig. 10c). Fig. 10a shows the maximum global force compared to EM ice thickness. The gray and black markers represent all data points and events with ice drift from northeast (45°) to east (90°), respectively. In Fig. 10b, the global pressure is compared to the EM ice thickness. The solid lines and dashed lines represent, respectively, the global pressure equation (A.8–21) in ISO19906 (2010) and the suggested enhancement by Määttänen and Kärnä (2011). We expect that global pressures for ridges (data points displayed in Fig. 10a–b) lie underneath the lines displaying equation A.8–21 in ISO19906 (2010) and the enhancement by Määttänen and Kärnä (2011), which represents a 10^{-2} annual probability of exceedance for competent level ice. The EM ice thickness displayed in Fig. 10a–b) overestimates the consolidated layer thickness and the C_R value is expected to be lower for the consolidated layer than for level ice. The maximum global pressure is compared to drift speed in Fig. 10c. Note that the maximum panel vertical length was 1.6 m, the water level varied, and thus local forces from thicker ice might be missing.

4.3.2. Local forces

The high global-force ridge events were associated with high panel forces simultaneously across the lighthouse, and there was no correlation between the type of interaction mode and the number of load panels with high local forces. Fig. 11a displays the maximum force

compared to the number of load panels with a panel force above 0.5 MN. Fig. 11b shows results from the segmented panel and displays the elevation (from the seabed) of the segment with the highest local force compared to the water level. For events with ice drift of 45°–90°, the local segment forces at the time of maximum global force (t_{max}) are shown in Fig. 12. The title for each subplot represents the type of failure mode, EM ice thickness and the event No., and WL denotes the water level (cf., Fig. 4c). In most events, independent of ice thickness, there was one vertical layer of segments with high local forces.

5. Discussion

5.1. The effect of met-ocean conditions on high global force ridge events

For the identified ridge events, both the wind and ice-drift directions were mostly from the northeast. However, events from the southwest would not be detected by the load panels, and in 2003, the predominant wind direction was from the southwest (Li et al., 2016). Differences in direction between wind and ice drift are important for the design of wind turbine foundations because ice-induced vibrations may be damped when the ice and wind come from the same direction (Hendrikse, 2017). The wind direction measurements had greater accuracy than the measurements of ice-drift direction. Wind was measured in a meteorological tower, whereas ice drift was determined from visual observations by personnel stationed at the lighthouse. The mean difference between the wind and ice-drift directions was 22°; the difference was > 10° for all but 7 events, and in 80% of the events, the ice drift was shifted clockwise of the wind direction. The ice drift in the Baltic is generally shifted 20°–30° clockwise of the wind direction (Leppäranta and Myrberg, 2009).

All the 35 identified high global force ridge events occurred in March and April and among the 35 events, 77% occurred in winter of 2002/2003. This may have several reasons, and probably a combination of the ice movement, ice temperature and growth of the

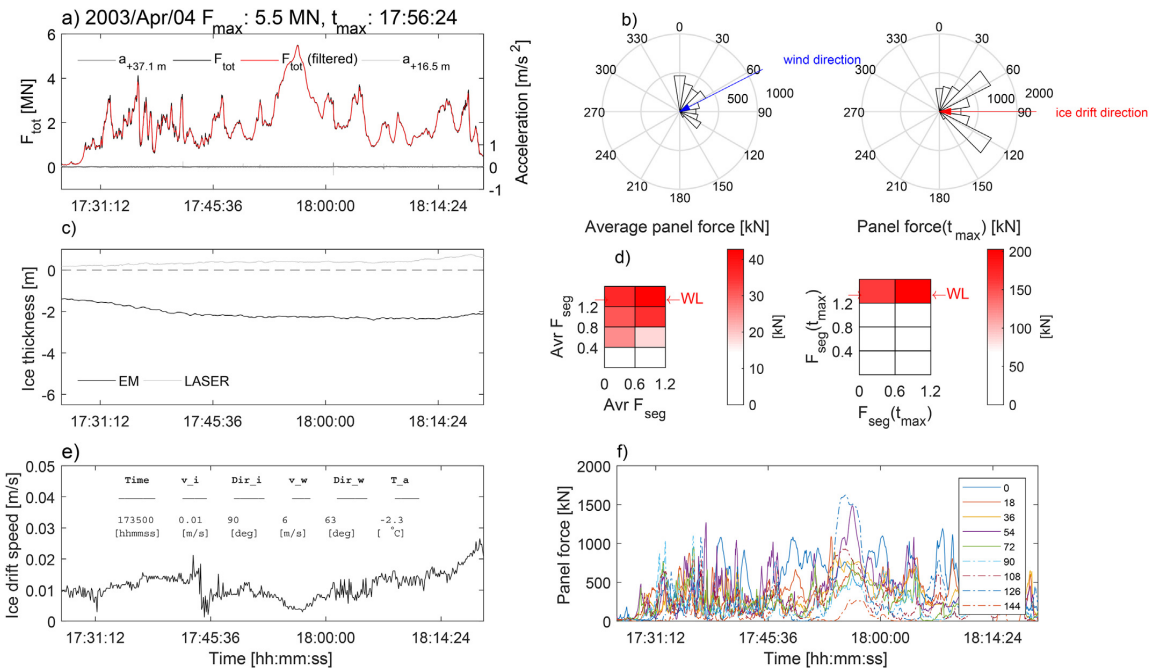


Fig. 6. 1 (top) Event no. 10, ductile event, second highest force recorded (sampling frequency of 10 Hz). 2 (bottom) Event no. 10, ductile event, second highest force recorded (sampling frequency of 10 Hz), displays a zoom around the peak force.

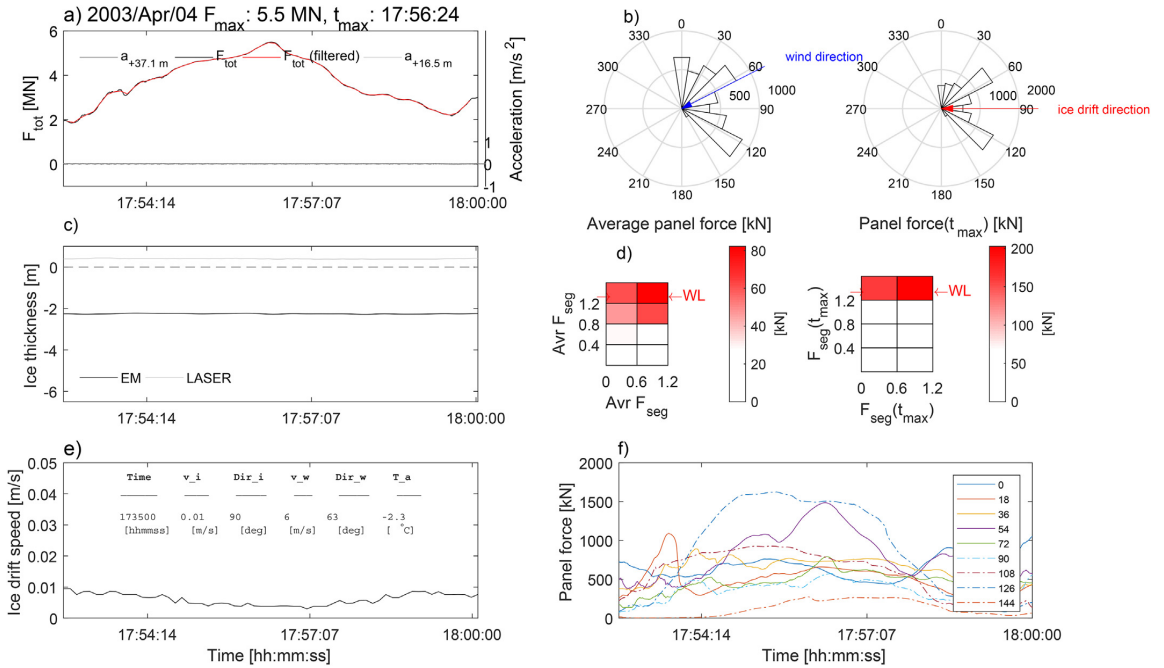


Fig. 6. (continued)

consolidated layer thickness. The frequency (in per cent) of both high ice concentration (> 90%) and ice ridges in the Bay of Bothnia were typically at maximum in March and April based on data from 1965 to 1985 (Engelbrekton, 1987). In 2003 February 14, a global crack

formed north in the Bay of Bothnia resulting in a global movement of the Baltic ice sheet of approximately 15 km until March 31 displayed in Fig. 4d. Assuming ice drift from the north only (and no rafting or ridge formation), Bjerkås et al. (2012) found that the daily drift past

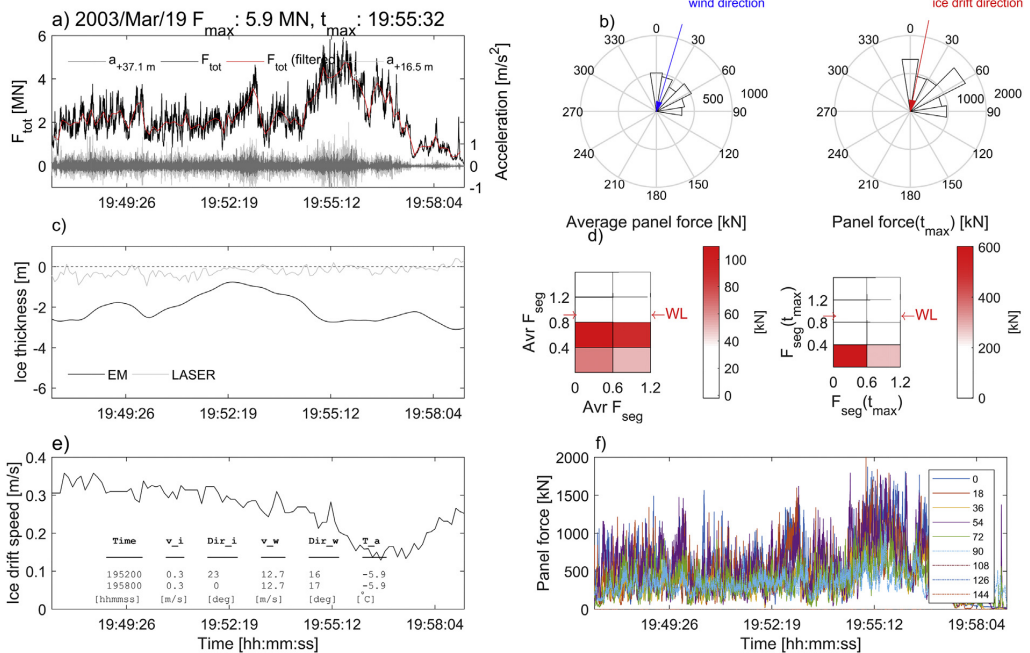


Fig. 7. Event no. 19, brittle event, highest force recorded (sampling frequency of 30 Hz).

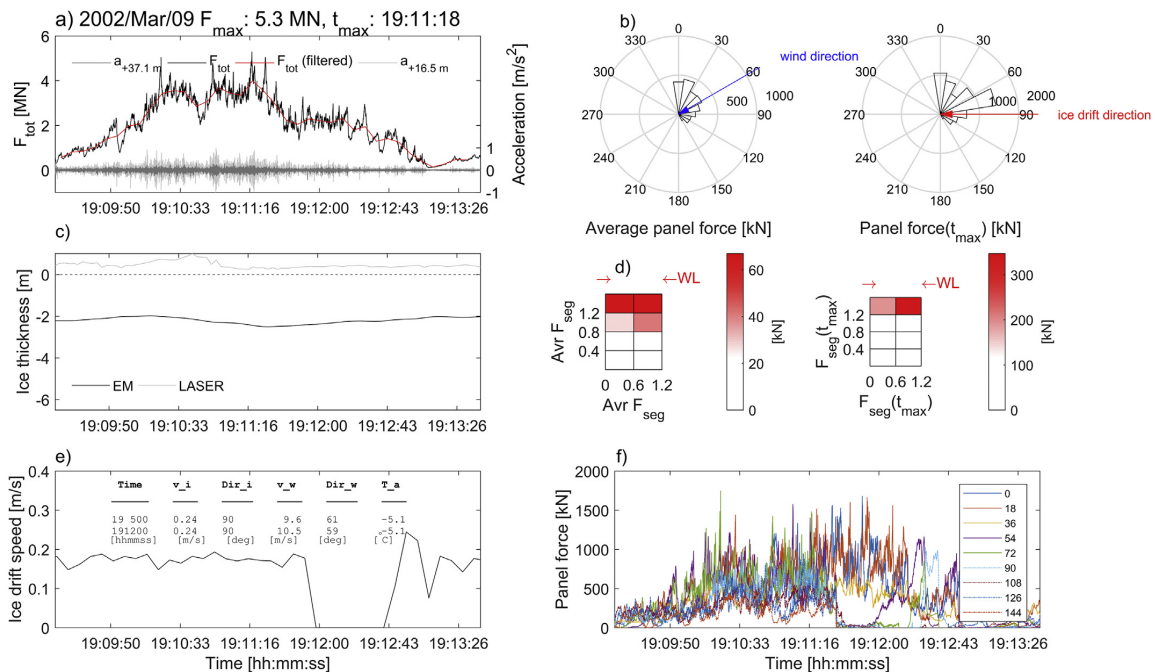


Fig. 8. Event no. 7, brittle event, third highest force measured (sampling frequency of 30 Hz).

Table 2
Summary of the parameters identified for the different interaction modes.

Interaction mode	Stalled	Ductile	Brittle
σ_{Acc} [m/s ²]	0.007	0.008	0.02–0.11
$\sigma_{F_{dyn}}$ [kN]	3–14	8–27	83–203
$\sigma_{F_{r7s}}$ [kN]	441–855	460–1040	279–1117
F_{max}/F_{mean} [–]	3.2–4.2	1.6–2.8	1.8–5.5
$v(t_{max})$ [m/s]	–0	0.005–0.02	0.1–0.4
μ_{rA} [°C]	–1.2	+0.8	–6.6
μ_w [m/s]	10.7	7.6	10.1

Norströmsgrund was approximately 300–350 m. However, the ice drift between February 14 and March 31 changed directions several times, such that the ice drift past Norströmsgrund was probably considerably higher and from both a northerly and southerly direction. This would partly explain the frequent occurrence of high global force ridge events in March and April 2003. According to the FDD data presented in Fig. 3b and ice temperatures presented by Bjerkås et al. (2012), high global force ridge events occurred when the ice growth had slowed down, i.e. consolidated layer thicknesses were at maximum, and ice temperatures were increasing towards the melting point. The high number of FDD in 2003 also fits with the frequent occurrence of high global force ridge events.

The air temperature was generally higher on days with ductile events (–2.7 °C, +4.4 °C) than on days with brittle events (–14.4 °C, –0.8 °C). It takes time for ice to heat up, and the average number of FDDs one week before the ductile and brittle events was 12.4 and 34.3, respectively. Therefore, the ice was, on average, warmer in ductile interactions than in brittle interactions.

5.2. Interaction modes and forces

The identified ice ridge-structure interaction modes include 1) limit-force stalling, 2) limit-stress ductile failure, and 3) limit-stress brittle

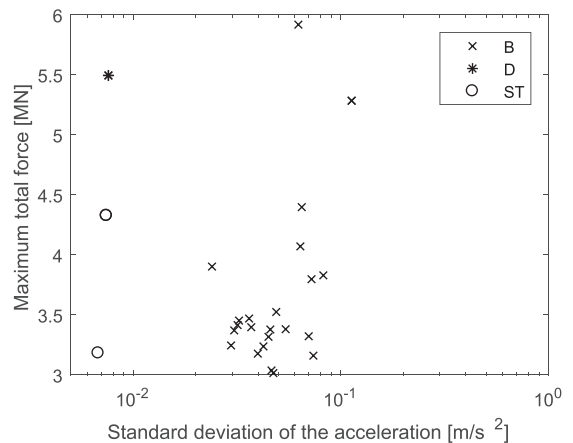


Fig. 9. Standard deviation of the acceleration resampled to 10 Hz. B = brittle, D = ductile, ST = stalling events.

failure. In addition to 35 ridge events 7 level and rafted ice events were identified with a global panel force above 3 MN, where ice ridge events governed the highest global forces measured (see Tabel A.1 in Appendix A.2).

5.2.1. Limit-force stalling

When the global force was limited by the driving- or pack-ice driving forces, the ice sheet came to a halt, and the events were classified as stalled. During stalling events, the signature of the global-force time series either increased (events no. 1 and 11), decreased (event no. 15), remained constant (event no. 16) or slowly oscillated, for which

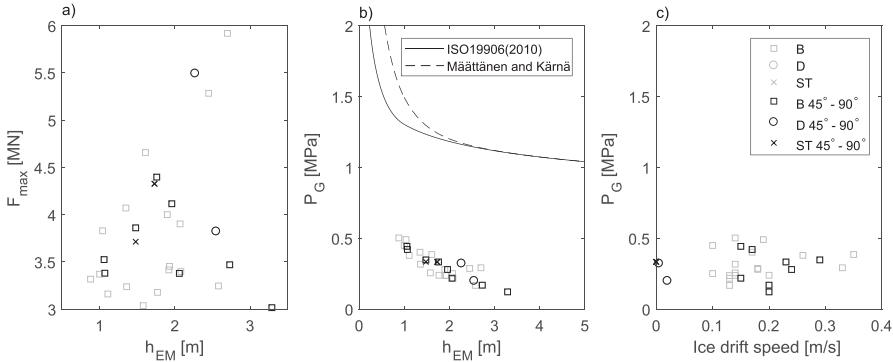


Fig. 10. Global force and pressure compared to EM ice thickness and drift speed. a) Maximum force compared to ice thickness, b) global pressure compared to ice thickness, and c) global pressure compared to ice speed. B = brittle, D = ductile and ST = stalling event, 45°-90° represents events with ice drift from north to northeast.

the tilt also oscillated (event no. 14, Fig. 13). The accuracy of the ice-drift measurements was insufficient to quantify ice speeds on the order of mm/s at which ice creeps (Michel and Toussaint, 1977; Sodhi and Haehnel, 2003). Among the identified high-force events, the ice interacted with the lighthouse only in stalling events from the southeast to the northwest 157.4°-315° (Fig. 4) outside the load panel coverage (351°-153°). For the stalling event in Fig. 5, the ice-structure interface was to the northwest (315°), and thus only a fraction (3.7 MN) of the global force was measured. In Section 5.2.5, the missing panel forces are estimated with a mirroring technique. In the event in Fig. 1a (2003 March 26–27), a large ice ridge came to a halt and was grounded on the underwater caisson (~7 m below MWL) (Bjerkås et al., 2003). Because the ice interacted with the south-southwest interface of the lighthouse (with no load panels), the event was not identified as a high-force event. The tilts measured at +22.8 m were compared between the maximum global force event no. 19 (Fig. 7), the stalling event no. 16 (Fig. 5) and the grounding event on 2003 March 26–27 (Fig. 1), and the absolute maximum values were, respectively, 1.33 mrad, 1.31 mrad and 1.41 mrad. Because the events occurred within approximately one week in 2003, we assume that the measurement signal drift was negligible, and therefore it is likely that the event on March 26–27 was also a high-force event. Applying the relation between global force and tilt proposed by Frederking (2005) the tilt values 1.33 mrad, 1.31 mrad and

1.44 mrad would correspond to a global force equal to 16.0 MN, 15.7 MN and 17.3 MN, respectively. These global force values are on the limit of the lighthouse design capacity, and because of reported issues with the tilt signals in 2003 (Frederking, 2005; Sudom and Frederking, 2014), these global forces are likely severely overestimated. Due to the combination of varying water level and nonlinearities in the lighthouse foundation we also believe that simply assuming a linear relation between tilt and global force is too simplistic.

5.2.2. Limit-stress ductile and brittle failure

Level-ice ductile failure occurs at low indentation speeds, and the force signature gradually increases, reaches a peak value and decreases to a steady state value of approximately 50% of the peak force without structural vibrations (Michel and Toussaint, 1977; Sodhi and Haehnel, 2003). This classification agrees with the classification identified for ridge interactions, with the exception of the steady state force. The force signature for the ductile ridge interaction (identified in this paper) increased, attained a peak and decreased but never reached a steady state value, perhaps because of heterogeneities in the ice ridge, variations in ice drift speed or the formation of cracks. During ductile events, both the dynamic force (σ_{Fdyn} 8–27 kN) and structural acceleration (σ_{Acc} ~0.008 m/s²) were low, and the interactions were thus quasi-static. The type of ice-ridge interaction was related to ice speed, where interactions

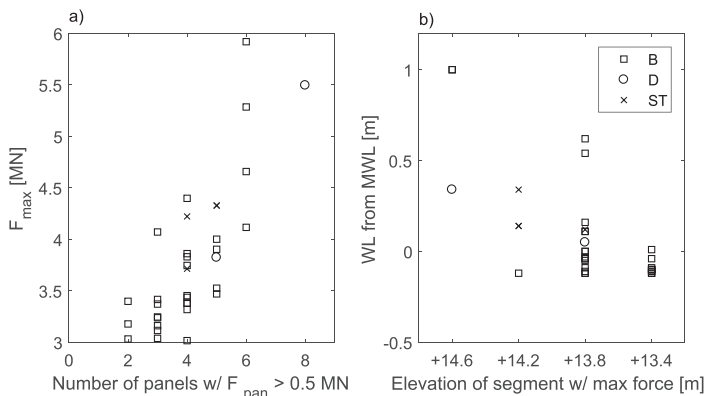


Fig. 11. Horizontal and vertical force distribution for the 35 ridge events. a) Maximum global force compared to the number of load panels with a panel force above 0.5 MN; b) the position of the WL relative to MWL compared to the elevation (from the seabed) of the segment with the maximum local force. MWL is marked by 0 m.

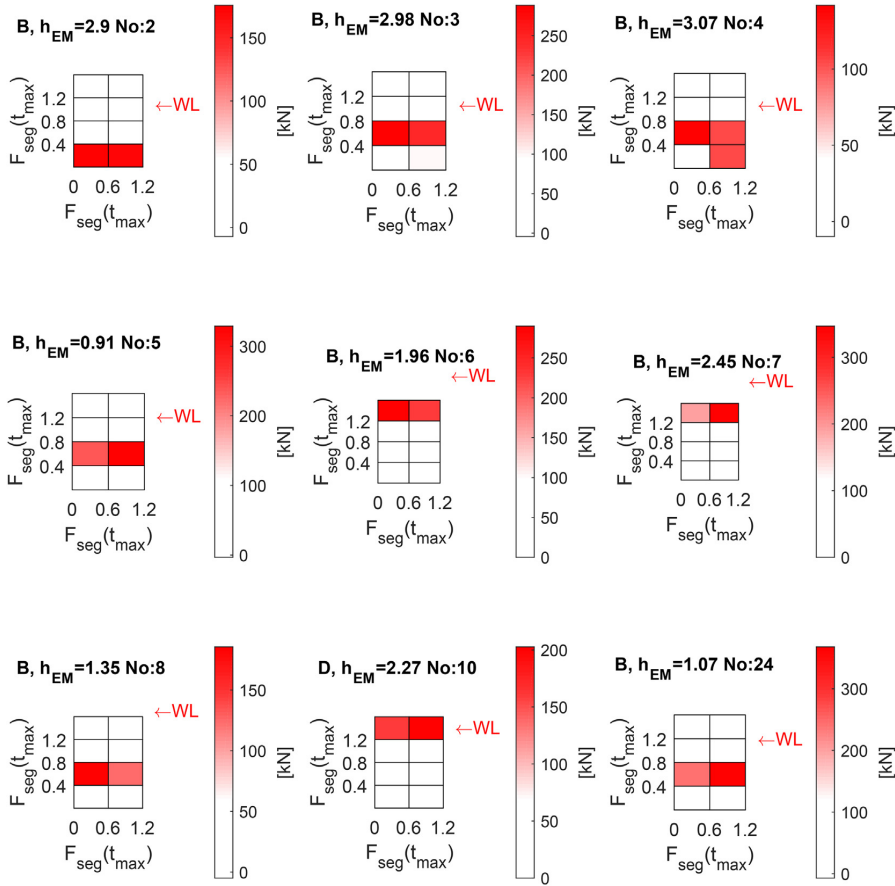


Fig. 12. Local segment forces on the load panel oriented to the east (90°) for events with ice drift of 45°–90°. B = brittle and D = ductile. t_{max} is the time of the maximum global force, and h_{EM} is EM thickness at t_{max} .

with low ice speed (0.005–0.02 m/s) were ductile, whereas interactions with high ice speed (0.1–0.4 m/s) were brittle. In the Japan Ocean Industries Association project (JOIA), ductile level-ice interactions (thickness of ~0.2 m) against a vertically sided flat indenter (1.5 m wide) were observed at an indentation speed of 0.0003 m/s, whereas brittle interactions were observed at indentation speeds of 0.003–0.03 m/s (Sodhi et al., 1998). Both JOIA and LOLEIF/STRICE data qualitatively show that ductile interactions occur at lower ice speeds than brittle interactions, although the transition indentation speeds are quantitatively different. The increased transitional ice speed for the identified ridge interactions can be explained by the increased vertical confinement compared to level ice (Schulson and Buck, 1995; Schulson and Nickolayev, 1995).

During level-ice brittle failures, the interaction force attains a steady state mean value with random variations above and below the average force level (Sodhi and Haehnel, 2003). This classification of the force signature is qualitatively different from the classification presently identified for ice ridge-structure interactions. The force-time series appeared non-stationary for ridged ice, as shown in Figs. 5–8, but stationary for the rafted-ice event shown in Fig. 14. The mean force measured during ridge interactions varied throughout the event. An attempt was made to quantify the stationarity of the force-time signature by calculating the standard deviation of the mean (σ_{UF7s}) of the global force in 7-s intervals each 7-s (Table 2 and Appendix A.2). The

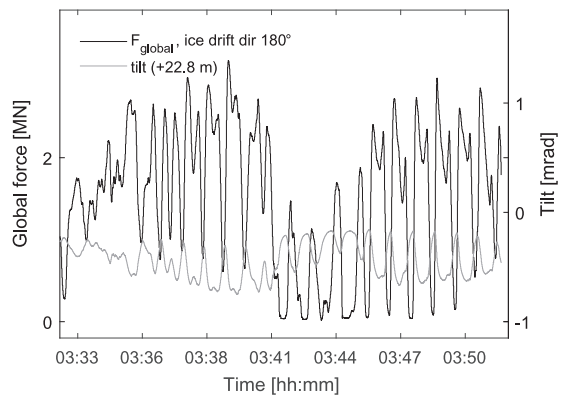


Fig. 13. Tilt and global force for stalling event no. 14 (2003 March 10).

ridge events in Fig. 5–8 were less stationary, with σ_{UF7s} 626–1117 kN, compared to a value of 324 kN for the rafted event in Fig. 14. The standard deviation of event no. 3 (Fig. 15) had the lowest σ_{UF7s} value (276 kN), but the stationarity in the time series in event no. 3

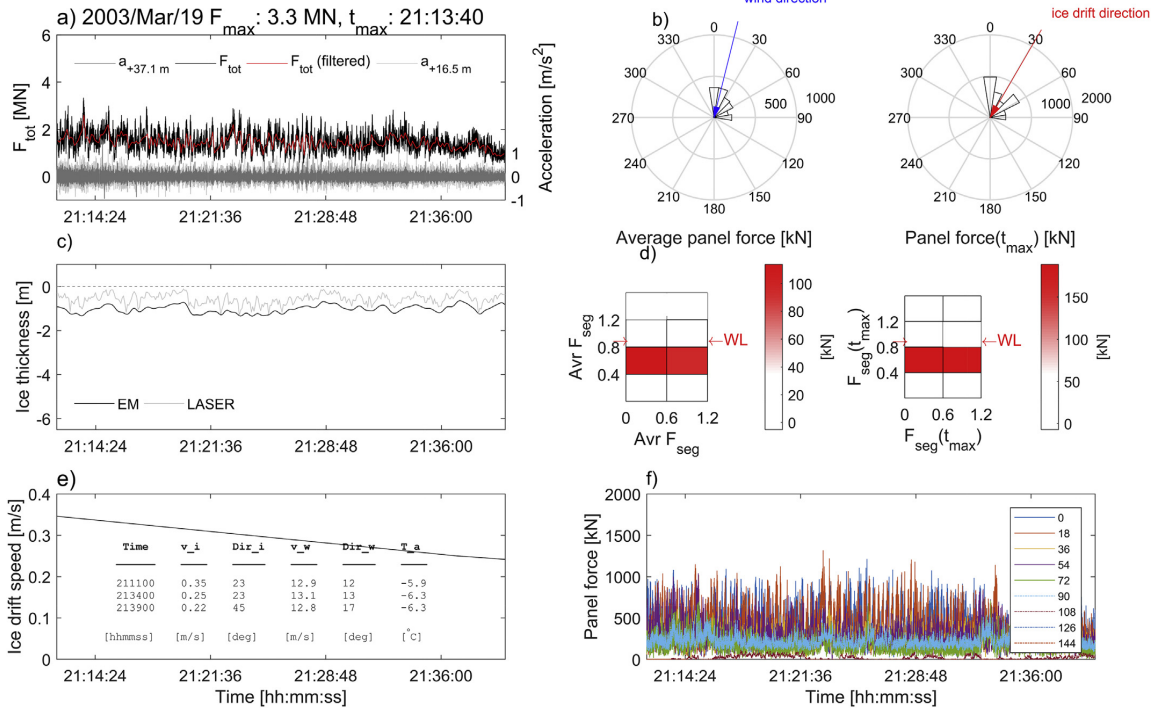


Fig. 14. Event no 22, rafted ice brittle event. Sampling frequency 30 Hz. (The figure setup is the same as that in Fig. 5–8).

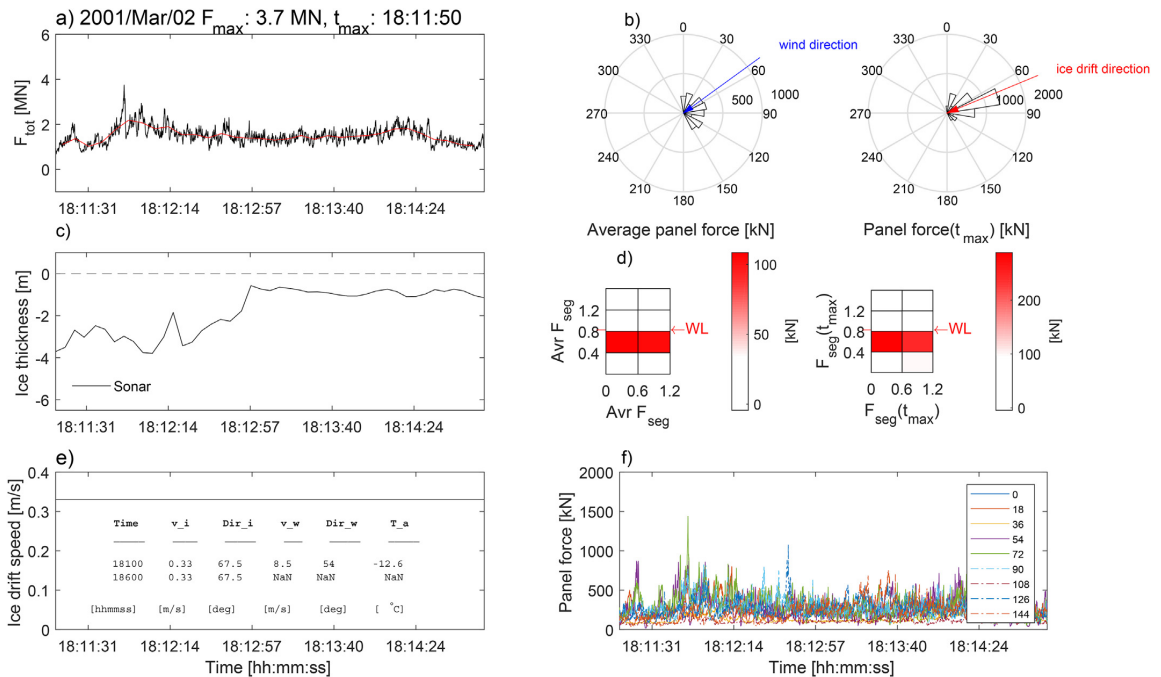


Fig. 15. Event no 3, ice ridge brittle event. Note that EM, laser thickness and acceleration data were unavailable in 2001. Sampling frequency 30 Hz. (The figure setup is the same as that in Fig. 5–8).

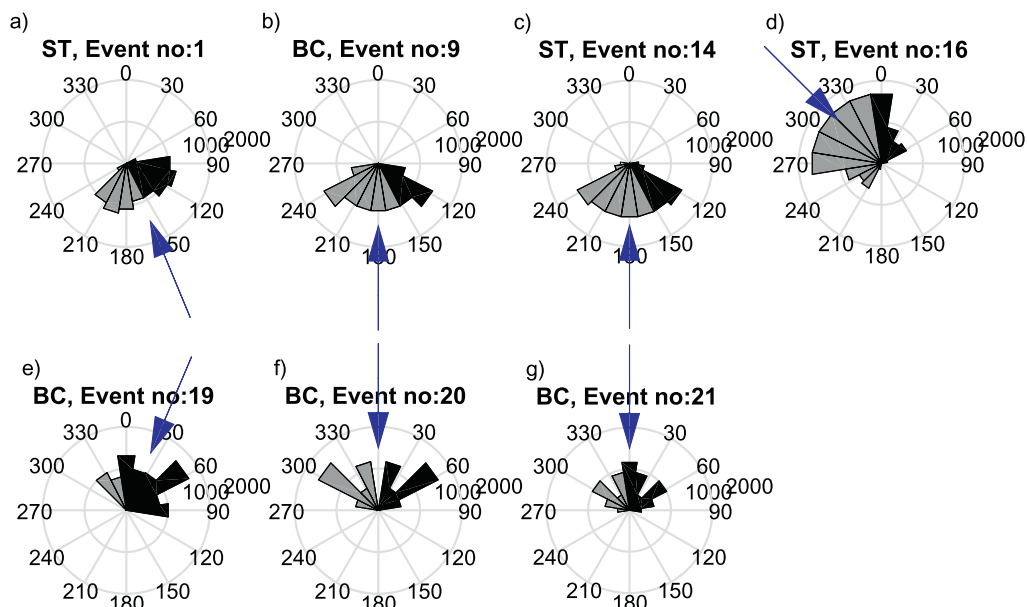


Fig. 16. Force distribution with the mirroring technique. The blue arrows mark the direction of the ice drift. The black panel forces show the measurements on actual load panels, and the gray panel forces are estimated on fictive panels. ST = stalled, B = brittle events. (For interpretation of the references to colour in this figure legend, the reader is referred to the web version of this article.)

qualitatively appeared similar to that in event no. 22 (Fig. 14). An attempt was also made to calculate the autocorrelation of the force-time signals resampled to 1 Hz. However, it was difficult to identify a consistent time lag to evaluate the autocorrelation. Because of variations in ice speed, sampling frequency and event lengths, the most appropriate means of quantifying stationarity requires further research and preferably more data and is outside the scope of this paper. The standard deviations of the dynamic force σ_{dyn} and acceleration σ_{acc} were 83–203 kN and 0.02–0.11 m/s², respectively, for brittle ridge events and 126–140 kN and 0.04–0.07 m/s², respectively, for level- or rafted-ice events. There was generally a larger spread in measured quantities for brittle-ridge events than level- or rafted-ice events, noting that there was also a greater number of high-force ridge events than level- or rafted-ice events.

5.2.3. Intermittent crushing and frequency lock-in failures

At the Norströmsgrund lighthouse, intermittent crushing events were not observed in either the ice ridge interactions presented here or in level-ice interactions (Kärnä and Yan, 2009). The stiffness of the Norströmsgrund lighthouse at the MWL is approximately 1.7 GN/m (Heinonen et al., 2004). For a global force equal to 5.5 MN (the maximum measured global ductile force, event no. 10), applying the static stiffness, the estimated displacement of the structure at MWL was approximately only 3 mm. For this event, the failure mode did not alternate to brittle failure at a lighthouse displacement of 3 mm.

For the considered high-force ridge interactions, frequency lock-in vibrations were not observed. Due to the uneven ice thickness, heterogeneities in ice ridges, and damping from the rubble, frequency lock-in vibrations are perhaps less likely to occur for ridged ice.

5.2.4. Local forces

Local forces at t_{max} for events with ice drift of 45°–90° are displayed in Fig. 12. Because of the relatively large segments (0.4 × 0.6 m²), detailed pressure distributions were unavailable. However, for the brittle interactions and one ductile, the vertical force distribution was

independent of the EM thickness and limited to one segment height. Note that the water level was sometimes located outside the load panel coverage. Line-like contact was observed in full-scale ice-ship brittle crushing interactions (Riska et al., 1990) and laboratory crushing tests (Franson et al., 1991; Joensuu and Riska, 1989). Line-like contact also explains why the global pressure decreases with increasing ice thickness (in Fig. 12). However, the maximum local force measured in one of the segments during an event was generally higher for ridges than for rafted or level ice, perhaps due to higher confinement. The thickness of the consolidated layer was measured only approximately based on the EM thickness (Haas, 2017). The position of the water level was compared to the position of the segment with the maximum local force in Figs. 11 and 12. Ervik et al. (2018) showed that the strongest part of the consolidated layer measured in-situ was the coldest part, which was probably located close to the relatively cold air surface. Therefore, we may expect the highest local forces from the top of the consolidated layer, however because of the unknown sail height it is unclear where the top of the consolidated layer is located relative to the water level. The results in Fig. 12 (no. 2–4) display the same water level but varying position of the segment with maximum local force. The interpretation of the water level with respect to the position of the consolidated layer is however questionable. Further, Fig. 12 indicate that local forces were missed by limited load panel coverage at least in event no. 6 and 7. Due to the limited vertical panel coverage (1.6 m), it is unlikely that rubble forces were measured. Kulyakhtin (2017) determined based on basin model tests and a continuum model for ice rubble that the rubble force was governed by the rubble accumulation. Brown et al. (2010) concluded that the rubble forces on the conical Confederation Bridge piers were insignificant and over-estimated during the design process. For the Norströmsgrund lighthouse, rubble forces were probably missed by the load panels, and thus quantifying rubble forces is outside the scope of this paper.

5.2.5. Missing forces and probability of exceedance

For each of the four winter seasons (1999/2000–2002/2003), there

was at least one annual event with a global (panel) force above 3 MN. The overall maximum global force was approximately 6 MN with limited panel coverage. In 7 events, the ice drift was from a direction only partly covered with load panels. For these events, panel forces were mirrored with respect to the ice-drift direction on fictive load panels at the ice-structure interface. In cases where the ice came from a direction with no panel coverage (in Fig. 16b–d), the force on the panel closest to the ice-drift direction was extrapolated to the ice-drift direction and mirrored accordingly. With this technique, the maximum global force was estimated as ~9 MN for the stalling event in Fig. 5. Panel force distributions are displayed in Fig. 16a–g, where the black and gray panel forces represent measurements and mirroring estimates, respectively, and the blue arrows display ice-drift directions. The challenge when mirroring forces is the assumption of simultaneous failures and synchronization of panel forces. Furthermore, two of the load panels (36° and 108°) had problems with water filling and freezing inside, and thus force components may have been missing (Kärnä and Yan, 2009). Friction forces were quantified with the method described by Nord et al. (2016) with a friction coefficient $\mu = 0.15$ (Frederking and Barker, 2001). The friction force depends on both the ice-drift direction and the relative velocity between the structure and the ice and was calculated for a few of the events. These calculations revealed that the friction force had a small effect on the maximum global force (~5–8% increase), similar to observations by Nord et al. (2016). Therefore, the global forces presented throughout this paper were calculated as the vector sum of normal panel forces excluding friction forces.

The probability of exceedance is displayed in Fig. 17 ($i/(n + 1)$, where i is the rank of the global force and n is the number of events). Fig. 17a) displays the 42 identified events (including the level and rafted ice events) with a global panel force above 3 MN. Although this study focuses on ridge events, all event with a global forces in excess of 3 MN were initially identified and are included in Appendix A.2. The level and rafted ice events rendered lower global forces compared to ridge events, where the maximum level ice global force was 4.3 MN measured in a frequency lock-in event (no. 28). In Fig. 17b), the global force was recalculated for the 7 events displayed in Fig. 16, and one can see that the maximum force increased to 9.4 MN. The global forces measured at the vertically sided lighthouse were significantly higher than those measured at the conical piers of the Confederation Bridge, with similar structural width and ice conditions. For the Confederation

Bridge, the force level with a probability of exceedance of 0.1 was approximately 2 MN based on twenty years of measurements (Brown et al., 2010; Shrestha and Brown, 2018), compared to approximately 4.5 MN from four years of measurements at the Norströmsgrund lighthouse (Fig. 17a). The number of events recorded at the Confederation Bridge was approximately 16,000/9000 on the two piers.

5.3. Instrumentation

The goal in instrumenting a structure subjected to ice is to understand more about the modes of ice interactions, particularly ice-ridge interactions, which often govern the quasi-static design forces. Increasing this knowledge will eventually help designers of experiments and models to study certain interaction modes by controlling, e.g., ice speed, concentration or ice floe sizes. There are many concerns to consider, such as cost, accuracy, robustness, health, safety and environment (HSE) and instrument calibrations. We suggest that necessary instrumentation include accelerometers and inclinometers or strain gauges. For accurate tilt and acceleration measurements, instruments need repeated zeroing and calibration (Bruce and Brown, 2001; Frederking, 2005). The sampling frequency should be constant for all measurements and sufficient to capture dynamic modes of interaction. Acceleration and tilt or strain measurements, when repeatedly calibrated, are sufficient to determine both global forces and responses and to classify the type of interaction mode. Load panels are expensive, have limited coverage, only measure normal forces, and can break (Brown et al., 2010; Kärnä and Yan, 2009). However, if local forces and pressures are of interest, load panels are useful when positioned at the interface coinciding with the predominant ice-drift direction. In addition to measuring forces and responses, ice thickness, ice speed and ice concentration should be measured. To measure level-ice thickness and the deepest part of ridge keels, a combination of laser and ULS is suitable. However, ULS instruments are difficult to deploy and can break (Haas, 2000; Haas, 2017) at shallow water depth. For ridges, an EM sensor overestimates the thickness of the consolidated layer and underestimates the keel depth. An EM sensor is easier to deploy and less likely to break than ULS. However, further research is required to understand how the EM measurements are affected by macro-porosity and generally develop accurate methods to measure the consolidated layer thickness. To calculate ice speed and the ice floe concentration and size

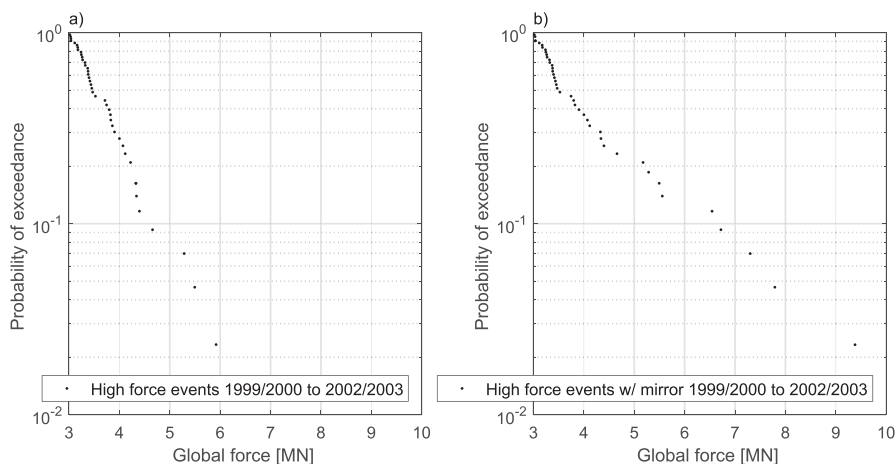


Fig. 17. Probability of exceedance for events above 3 MN from four years of measurements: a) global force from instrumented panels; b) global force including fictive panel forces.

and to quantify pack-ice driving forces, a combination of video, radar and satellite images is useful (Karvonen, 2016; Oikkonen et al., 2017). Finally, both met-ocean data (air temperature, wind speed/direction and water level) and ice properties (salinity, density, strength, and micro-structure) are important parameters.

6. Conclusions and recommendations

All data files from LOLEIF and STRICE were analyzed, and 35 ridge events with a global panel force above 3 MN were identified. In addition to 35 ridge events 7 level and rafted ice events were identified with a global panel force above 3 MN, where ice ridge events governed the highest global forces measured. For the identified ridge events, the type of interaction mode was classified based on the signatures in the force and response time series as well as footage of the ice failure. The following conclusions were drawn:

- The overall maximum global force was ~6 MN, but because of instrumentation limitations, the global forces were under-predicted.
- Three types of ice-ridge interaction modes were identified ordered by increasing ice speed: 1) limit-force stalling events, 2) limit-stress ductile events, and 3) limit-stress brittle events. All of these interaction modes potentially give a high global force.
- For the brittle high force events (and one ductile event) local forces acted on one vertical row of segments independent of ice thickness.

Appendix A. Appendices

A.1. Global panel force

$$F_{NS} = P0 + P18 \cdot \cos(18^\circ) + P36 \cdot \cos(36^\circ) + P54 \cdot \cos(54^\circ) + P72 \cdot \cos(72^\circ) - P108 \cdot \cos(72^\circ) - P126 \cdot \cos(54^\circ) - P144 \cdot \cos(36^\circ)$$

$$F_{EW} = P18 \cdot \sin(18^\circ) + P36 \cdot \sin(36^\circ) + P54 \cdot \sin(54^\circ) + P72 \cdot \sin(72^\circ) + P90 + P108 \cdot \sin(72^\circ) + P126 \cdot \sin(54^\circ) + P144 \cdot \sin(36^\circ)$$

$$F_G = \sqrt{F_{NS}^2 + F_{EW}^2}$$

A.2. Table with results for all events

Table A.1

Summary of measured quantities for each event, where events displayed in Fig. 5–8,14 and 15 are marked with bold letters.

Event No.	Date yy.mm.dd	FM	F_{max} [MN]	F_{max}/F_{mean} [MN]	$\sigma_{F_{dyn}}$ [kN]	σ_{Acc} [m/s ²]	σ_{MF7s} [kN]	$v(t_{max})$ [m/s]	μ_W [m/s]	$v-dir$ [°]	$w-dir$ [°]	Ice type	$h_{EM}(t_{max})$ [m]
1	00.04.03	ST	4.2	2.6	NaN	NaN	855	~0	6.9	158	90	RI	0.72 ¹
2	01.03.02	B	3.0	2.2	131	NaN	419	0.25	10.1	68	NaN	RI	2.90 ¹
3	01.03.02	B	3.7	2.5	152	NaN	279	0.33 ²	8.5	68	54	RI	2.98 ¹
4	01.03.02	B	3.4	2.0	142	NaN	548	0.33	8.5	68	54	RI	3.07 ¹
5	01.03.13	B	3.1	2.2	104	NaN	467	0.10	8.8	90	36	RI	0.91
6	02.03.09	B	4.1	3.2	109	0.078	899	0.24	10.2	90	61	RI	1.96
7	02.03.09	B	5.3	2.5	153	0.113	1117	0.18 ²	10.5	90	61	RI	2.45
8	02.03.21	B	4.1	2.2	120	0.064	728	0.17	7.6	45	16	RI	1.35
9	03.04.01	B	3.2	1.9	149	0.074	434	0.26	14.3	180	193	RI	1.11
10	03.04.04	D	5.5	2.8	8	0.008	1040	0.005	7.1	90	57	RI	2.27
11	03.04.05	ST	4.3	2.3	14	0.007	441	~0	11.1	23	14	RI	1.73
12	03.04.05	B	3.0	1.9	136	0.069	439	0.24	11.6	23	12	LI	0.72
13	03.04.05	B	3.2	5.5	101	0.040	397	0.2	10.8	23	14	RI	1.77
14	03.03.10	ST	3.2	2.2	NaN	0.007	831	~0	11.1	180	200	RI	1.73
15	03.03.17	D	3.8	1.6	27	NaN	460	0.02	8.0	NaN	22	RI	2.55
16	03.03.18	ST	3.7	2.4	3	NaN	626	~0	13.7	315	282	RI	1.48

(continued on next page)

- Based on the suggested format of classification, recommendations for future instrumentation include 1) repeated calibrated and zeroed acceleration, tilt or strain gauge measurements, 2) video, radar and satellite images (for ice thickness, drift speed, ice concentration and floe size measurements), and 3) met-ocean data (including air temperature, water level, wind speed and direction measurements).

Acknowledgments

The authors wish to acknowledge the support of The Research Council of Norway through the Centre of Research based Innovation; Sustainable Arctic Marine and Coastal Technology (SAMCoT) (grant no 203471/O30), and the support of the SAMCoT partners. This study was conducted using E.U. Copernicus Marine Service Information, which was very useful. We are also very grateful to the numerous volunteers from the LOLEIF and STRICE projects for running the lighthouse and maintaining the measurements continuously for several weeks during the four field seasons. We are also thankful to Prof. Dr. Christian Haas for answering emails and clarifying the limitations of the ice thickness instrumentation. Finally, we thank Dr. Kari Kolari and Dr. Lennart Fransson for sharing data and reports. We acknowledge the use of imagery from the NASA Worldview application (<https://worldview.earthdata.nasa.gov/>) operated by the NASA/Goddard Space Flight Center Earth Science Data and Information System (ESDIS) project.

Table A.1 (continued)

Event No.	Date yy.mm.dd	FM	F_{max} [MN]	F_{max}/F_{mean} [MN]	$\sigma_{F_{dyn}}$ [kN]	σ_{Acc} [m/s ²]	$\sigma_{\mu F7s}$ [kN]	$v(t_{max})$ [m/s]	μ_W [m/s]	$v-dir$ [°]	$w-dir$ [°]	Ice type	$h_{EM}(t_{max})$ [m]
17	03.03.19	B	4.0	2.1	198	NaN	699	0.18 ²	13.1	23	15	RI	1.90
18	03.03.19	B	4.7	2.6	185	0.067	442	0.35 ²	13.9	23	15	RI	1.61
19	03.03.19	B	5.9	2.5	203	0.062	890	0.33²	13.5	23	16	RI	2.70
20	03.03.19	B	3.8	2.2	158	0.082	448	0.19 ²	13.9	0	15	RI	1.04
21	03.03.19	B	3.9	2.2	166	0.090	469	0.29 ²	14.1	0	14	RI	1.48
22	03.03.19	B	3.3	2.3	NaN	0.070	324	0.25²	13.1	23	12	RA	1.25
23	03.03.19	B	3.8	2.8	NaN	0.072	545	0.24 ²	13.3	23	10	RA	0.94
24	03.03.30	B	3.4	2.0	NaN	0.054	431	0.17 ²	13.2	45	33	RI	1.07
25	03.03.30	B	4.4	2.2	NaN	0.065	772	0.23 ²	13.0	23	34	RI	1.76
26	03.03.30	FLI	3.2	2.5	187	0.213	544	0.04	5.4	45	51	RA	0.80
27	03.03.30	FLI	3.3	2.4	128	0.169	448	0.04	6.3	45	59	LI	0.75
28	03.03.30	FLI	4.3	2.6	288	0.313	819	0.04	6.2	45	59	LI	0.64
29	03.03.31	B	3.0	2.2	94	0.047	567	0.20	8.7	23	12	RI	3.29
30	03.03.31	B	3.5	2.7	83	0.036	871	0.20	9.6	23	10	RI	2.73
31	03.03.31	B	3.4	2.0	129	0.046	473	0.15	8.6	23	6	RI	2.06
32	03.03.31	B	3.5	2.6	120	0.049	710	0.15	8.4	23	4	RI	1.06
33	03.03.31	B	3.0	1.8	129	0.046	354	0.14	8.3	23	356	RI	1.58
34	03.03.31	B	3.2	2.0	129	0.042	407	0.14 ²	7.8	23	81	RI	1.36
35	03.03.31	B	3.3	2.3	140	0.042	754	0.14 ²	7.8	23	2	LI	0.50
36	03.03.31	B	3.5	2.7	93	0.032	729	0.14 ²	7.3	23	90	RI	1.93
37	03.03.31	B	3.3	1.9	133	0.045	469	0.14 ²	7.8	23	351	RI	0.88
38	03.03.31	B	3.4	2.5	97	0.032	462	0.13	7.8	23	352	RI	1.92
39	03.03.31	B	3.4	2.6	99	0.031	337	0.10	8.0	23	349	RI	1.00
40	03.03.31	B	3.4	2.0	122	0.037	603	0.13	7.8	23	350	RI	2.08
41	03.03.31	B	3.2	1.9	95	0.030	567	0.13	6.9	23	348	RI	2.58
42	03.03.31	B	3.9	2.0	84	0.024	777	0.10	8.1	23	351	RI	2.07

FM = failure mode, ST = stalled ice sheet, B = brittle failure, D = ductile failure and FLI = frequency lock-in event. F_{max} is the maximum global force; F_{mean} is the mean global force, $\sigma_{F_{dyn}}$ is the standard deviation of the dynamic global force, σ_{Acc} is the standard deviation of the acceleration with a sampling frequency of 10 Hz; $\sigma_{\mu F7s}$ is the standard deviation of the global force in seven-second intervals; $v(t_{max})$ is the ice speed at the time of the maximum global force; μ_W is the mean wind speed; and $v-dir$ and $w-dir$ are the directions of the ice drift and wind, respectively. RI = ridged ice, LI = level ice, and RA = rafted ice. $h_{EM}(t_{max})$ is the EM ice thickness at the time of the maximum global force.

¹ Indicates ice thickness measured with sonar instead of EM.

² Indicated ice velocities that were estimated manually.

A.3. Event description

Event no. 1 (sonar ice thickness, no acceleration data) – stalled

Start 16:02:00 ice sheet comes to halt which defines the beginning of a stalled event.

End 21:48:52 ice sheet starts moving and failing in a brittle manner, ice drift direction from the south. The force drops and the ice sheet has turned 90° since it stopped.

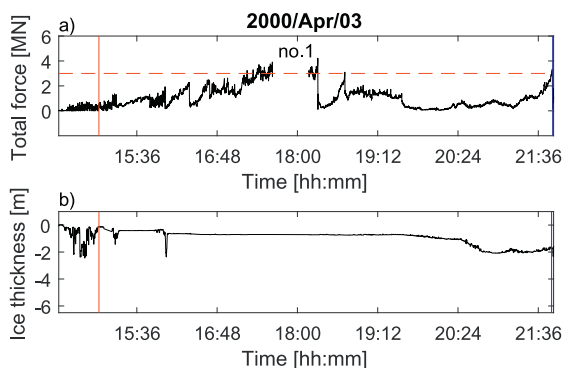


Fig. A.1. a) Global force and b) sonar ice thickness for event 1. The vertical red line represents the beginning of the event, and the blue vertical line represents the end of the event. (For interpretation of the references to colour in this figure legend, the reader is referred to the web version of this article.)

Event no. 2 (sonar ice thickness, no acceleration data) – brittle failure

Start 15:36:31 increase in ice thickness results in increase in force level, brittle failure mode.

End 15:47:54 global ice ridge bending failure, force drop.

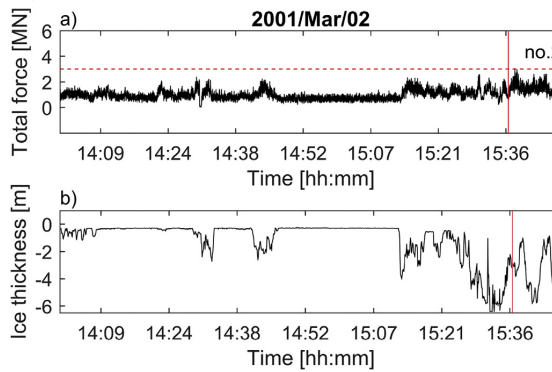


Fig. A.2. a) Global force and b) sonar ice thickness for event 2. The vertical red line represents the beginning of the event, and the blue vertical line represents the end of the event. (For interpretation of the references to colour in this figure legend, the reader is referred to the web version of this article.)

Event no. 3 (sonar ice thickness, no acceleration data)-brittle failure

Start 18:11:14 increase in ice thickness and force, brittle failure.

End 18:15:00 ridge sail interacts with lighthouse and force decreases due to discontinuities and small cracks.

Event no. 4 (sonar ice thickness, no acceleration data)-brittle failure

Start 18:28:33 brittle failure, force increase due to thickness increase.

End 18:31:22 ridge sail interacts with lighthouse and force decreases due to discontinuities and small cracks.

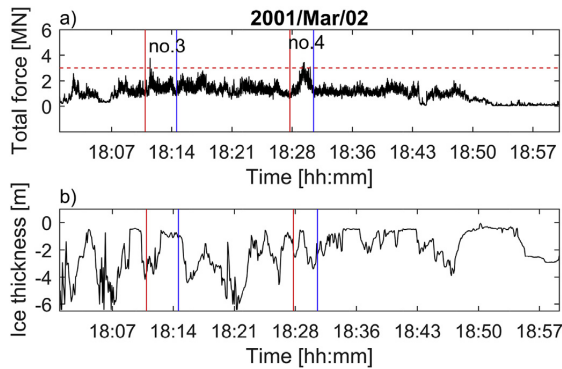


Fig. A.3. a) Global force and b) sonar ice thickness for event 3 and 4. Vertical red lines represents the beginning of an event, and blue vertical lines represents the end of an event. (For interpretation of the references to colour in this figure legend, the reader is referred to the web version of this article.)

Event no. 5-brittle failure

Start 20:05:47 no video in the beginning of the event, video starts 20:15.

End 20:22:54 end of ice sheet and the event, radial cracks and splitting, force drops.

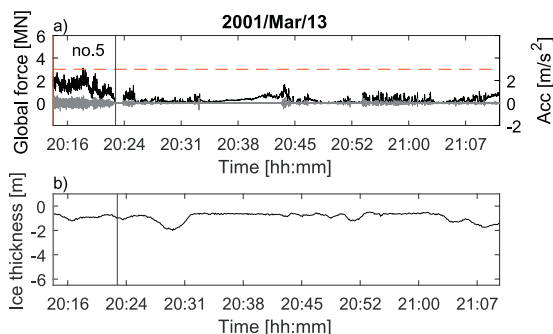


Fig. A.4. a) Global force and acceleration b) EM ice thickness for event 5. The vertical red line represents the beginning of the event, and the blue vertical line represents the end of the event. (For interpretation of the references to colour in this figure legend, the reader is referred to the web version of this article.)

Event no. 6 – brittle failure

Start 19:06:03 increase in ice thickness and force, brittle failure.
 End 19:07:40 radial cracks form, force drops.

Event no. 7 – brittle failure

Start 19:09:16 increase in ice thickness and force, brittle failure.
 End 19:13:40 radial cracks form, force drops.

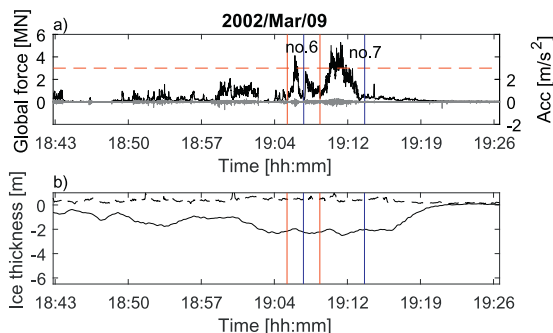


Fig. A.5. a) Global force and acceleration b) EM ice thickness for event 6 and 7. Vertical red lines represents the beginning of an event, and blue vertical lines represents the end of an event. (For interpretation of the references to colour in this figure legend, the reader is referred to the web version of this article.)

Event no. 8-brittle failure

Start 20:38:00 contact between ridged ice sheet and lighthouse after circumferential crack.
 End 20:43:50 end of ice sheet, radial cracks and force drops.

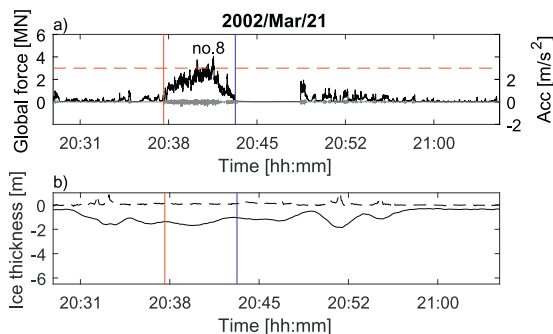


Fig. A.6. a) Global force and acceleration b) EM ice thickness for event 8. The vertical red line represents the beginning of the event, and the blue vertical line represents the end of the event. (For interpretation of the references to colour in this figure legend, the reader is referred to the web version of this article.)

Event no. 9-brittle failure

Start 18:00:00 increase in ice thickness and force, brittle failure.
 End 18:05:00 circumferential crack, force drops.

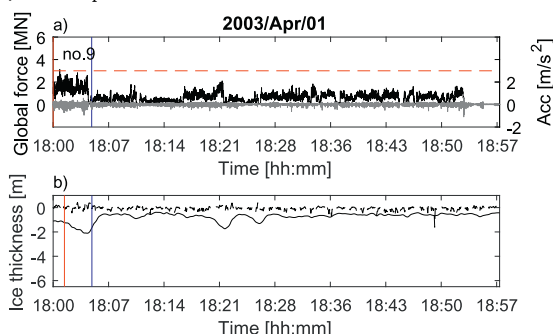


Fig. A.7. a) Global force and acceleration b) EM ice thickness for event 9. The vertical red line represents the beginning of the event, and the blue vertical line represents the end of the event. (For interpretation of the references to colour in this figure legend, the reader is referred to the web version of this article.)

Event no. 10-ductile failure

Start 17:26:13 ridged ice sheet, full contact after circumferential crack, ductile failure and low ice speed.
 End 18:20:10 ice ridge sail splitting and force drops.

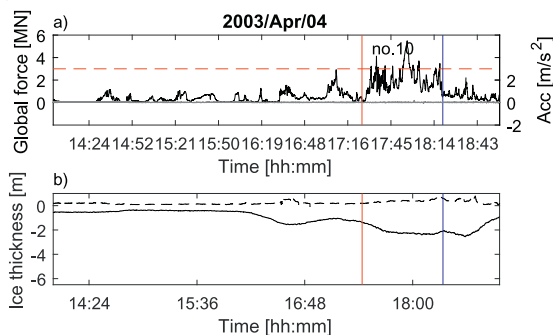


Fig. A.8. a) Global force and acceleration b) EM ice thickness for event 10. The vertical red line represents the beginning of the event, and the blue vertical line represents the end of the event. (For interpretation of the references to colour in this figure legend, the reader is referred to the web version of this article.)

Event no. 11-stalled

Start 08:02:00 ridged ice sheet comes to halt, defines the beginning of a stalled event, force increases. Force drop in the middle of the event appears to be due to instrument error.
 End 08:06:30 ice sheet splits and starts moving again, force drops.

Event no. 12-brittle failure

Start 08:27:53 ridged new ice sheet, full contact between ice sheet and lighthouse, brittle failure.
 End 08:37:00 radial crack, ice sheet splits, force drops.

Event no. 13-brittle failure

Start 09:47:00 ridged ice sheet edge comes in full contact with lighthouse after crack, brittle failure.
 End 09:49:42 the edge of the ice sheet loses contact with lighthouse, force drops.

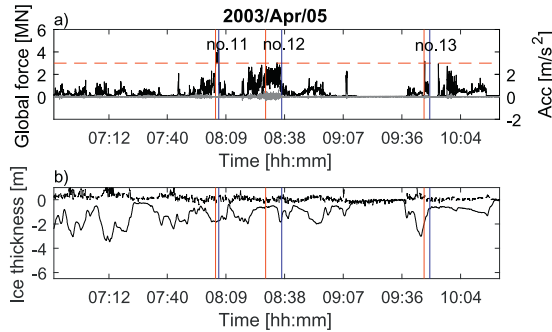


Fig. A.9. a) Global force and acceleration b) EM ice thickness for event 11–13. Vertical red lines represents the beginning of an event, and blue vertical lines represents the end of an event. (For interpretation of the references to colour in this figure legend, the reader is referred to the web version of this article.)

Event no. 14-stalled

Start 03:32:00 ridged ice sheet comes to halt, defines beginning of a stationary event, both force and tilt oscillates. Cause of oscillations unknown. End 03:52:30 ice sheet starts moving force decreases.

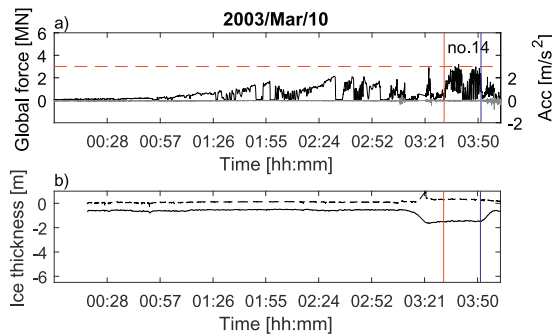


Fig. A.10. a) Global force and acceleration b) EM ice thickness for event 14. The vertical red line represents the beginning of the event, and the blue vertical line represents the end of the event. (For interpretation of the references to colour in this figure legend, the reader is referred to the web version of this article.)

Event no. 15-ductile failure

Start 15:06 ice sheet slows down from to 0.1 m/s, force increases and acceleration decreases.

End 15:12:30 end of ductile event defined when the ice sheet comes to halt, after which the force decreases because the ice sheet turns away from the instrumented side of the lighthouse, tilt increases while force decrease, ice sheet starts drifting in the opposite direction (ice drift has changed 180°) 21:30.

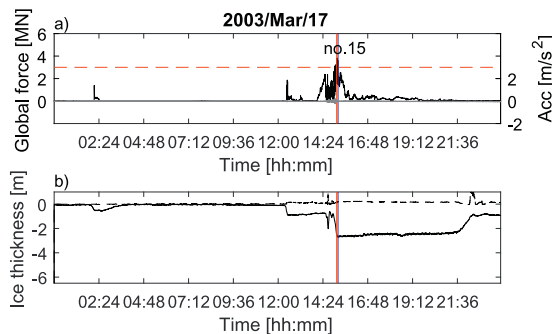


Fig. A.11. a) Global force and acceleration b) EM ice thickness for event 15. The vertical red line represents the beginning of the event, and the blue vertical line represents the end of the event. (For interpretation of the references to colour in this figure legend, the reader is referred to the web version of this article.)

Event no. 16-stalled

Start 15:20:00 ridged ice sheet, comes to a halt, (19:15 ice cracks leads to ice movement and force drop, comes to a halt again at 19:28 force increases).

End 20:55:00 ice sheet moves away from the lighthouse in the opposite direction (ice drift has changed 180°).

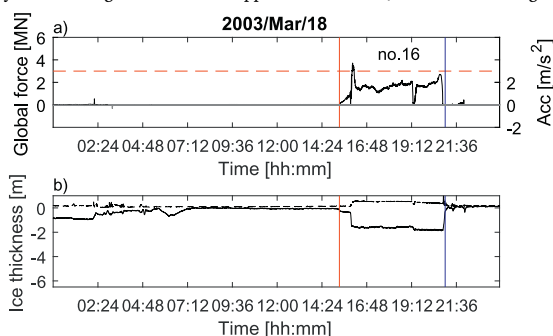


Fig. A.12. a) Global force and acceleration b) EM ice thickness for event 16. The vertical red line represents the beginning of the event, and the blue vertical line represents the end of the event. (For interpretation of the references to colour in this figure legend, the reader is referred to the web version of this article.)

Event no. 17-brittle failure

Start 19:18:00 contact between ice sheet and lighthouse after circumferential crack, brittle failure.

End 19:23:22 cracks form because end of the ice sheet approaches and the force drops.

Event no. 18-brittle failure

Start 19:32:00 new ridged ice sheet and full contact, brittle failure.

End 19:47:16 force decreases due to discontinuity in the ice sheet (ice ridge sail) and small cracks.

Event no. 19-brittle failure

Start 19:47:20 force increases continuous brittle failure after ridge sail has passed.

End 19:58:56 cracks for as the end of ice sheet approaches and the force drops.

Event no. 20-brittle failure

Start 20:00:00 contact between ice sheet and lighthouse, brittle failure.

End 20:12:00 force decrease due to discontinuity in the ice sheet (ice ridge sail) and small cracks.

Event no. 21-brittle failure

Start 20:12:00 force increases brittle failure.

End 20:17:40 radial cracks form as the end of ice sheet approaches and the force drops.

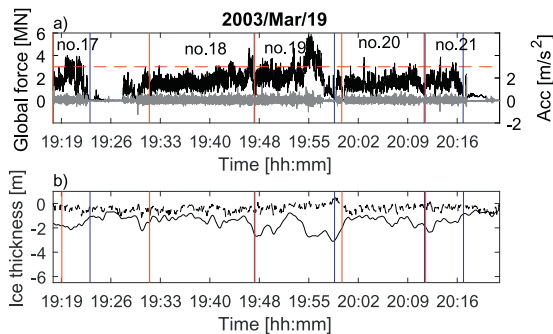


Fig. A.13. a) Global force and acceleration b) EM ice thickness for event 17–21. Vertical red lines represents the beginning of an event, and blue vertical lines represents the end of an event. (For interpretation of the references to colour in this figure legend, the reader is referred to the web version of this article.)

Event no. 22-brittle failure

Start 21:10:00 level/rafted ice sheet full contact with lighthouse, brittle failure.
 End 22:11:10 radial cracks and splitting because the ice sheet comes to the end, force drops.

Event no. 23-brittle failure

Start 22:24:00 contact between the end of a level/rafted ice sheet, failure/splitting of the ice sheet edge, peak force measured 22:25:29 when ice sheet comes to a halt.

End 22:26:00 the force drops after the ice sheet has stopped, slits and gradually drifts away.

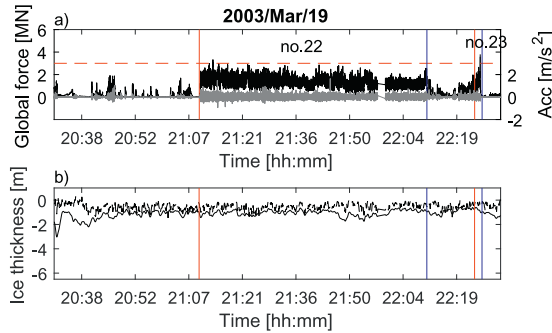


Fig. A.14. a) Global force and acceleration b) EM ice thickness for event 22 and 23. Vertical red lines represents the beginning of an event, and blue vertical lines represents the end of an event. (For interpretation of the references to colour in this figure legend, the reader is referred to the web version of this article.)

Event no. 24-brittle failure

Start 22:08:04 ridged ice sheet starts interacting with lighthouse, brittle failure.
 End 22:20:25 circumferential crack forms and the force drops.

Event no. 25-brittle failure

Start 22:21:37 contact after circumferential crack, brittle failure.
 End 22:27:07 circumferential crack forms and the force drops.

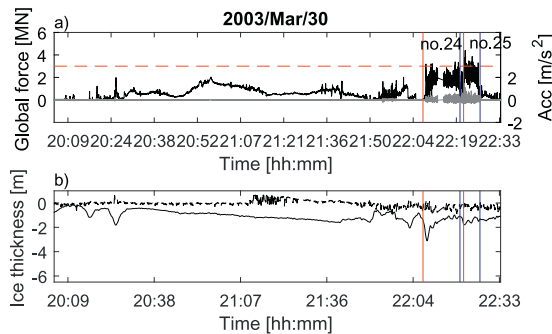


Fig. A.15. a) Global force and acceleration b) EM ice thickness for event 24 and 25. Vertical red lines represents the beginning of an event, and blue vertical lines represents the end of an event. (For interpretation of the references to colour in this figure legend, the reader is referred to the web version of this article.)

Event no. 26-frequency lock-in vibrations

Start 12:04:51 full contact between level ice sheet and lighthouse after circumferential crack, frequency lock-in vibrations.
 End 12:06:21 circumferential crack forms.

Event no. 27- frequency lock-in vibrations

Start 12:14:00 full contact between level ice sheet and lighthouse after circumferential crack, frequency lock-in vibrations.
 End 12:15:24 circumferential crack forms.

Event no. 28- frequency lock-in vibrations

Start 12:25:22 full contact between level ice sheet and lighthouse after circumferential crack, frequency lock-in vibrations.

End 12:27:50 circumferential crack forms.

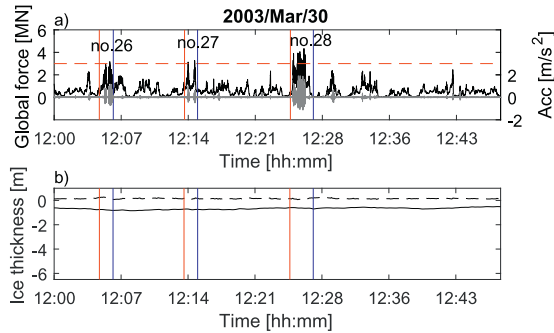


Fig. A.16. a) Global force and acceleration b) EM ice thickness for event 26–28. Vertical red lines represents the beginning of an event, and blue vertical lines represents the end of an event. (For interpretation of the references to colour in this figure legend, the reader is referred to the web version of this article.)

Event no. 29-brittle failure

Start 07:17:20 contact between ridged ice sheet and lighthouse after circumferential crack, brittle failure.
End 07:20:00 ice ridge plug/bending failure forms and the force drops.

Event no. 30-brittle failure

Start 07:21:23 full contact between deformed ice sheet and lighthouse, brittle failure.
End 07:21:53 circumferential crack, force drop.

Event no. 31-brittle failure

Start 07:30:43 full contact between deformed ice sheet and lighthouse, brittle failure
End 07:51:08 circumferential crack, force drop.

Event no. 32-brittle failure

Start 07:51:36 full contact between deformed ice sheet and lighthouse, brittle failure.
End 07:53:49 circumferential crack, force drop.

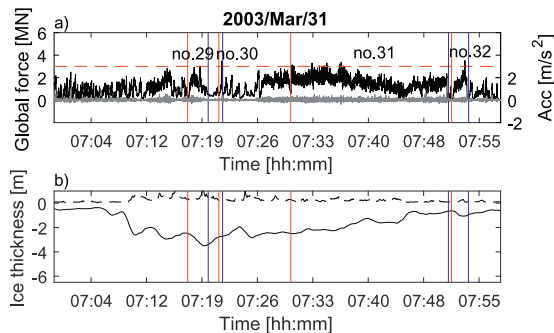


Fig. A.17. a) Global force and acceleration b) EM ice thickness for event 29–32. Vertical red lines represents the beginning of an event, and blue vertical lines represents the end of an event. (For interpretation of the references to colour in this figure legend, the reader is referred to the web version of this article.)

Event no. 33-brittle failure

Start 08:02:11 ice ridge brittle failure, force increase because of thickness increase.
End 08:18:06 circumferential crack, force drop.

Event no. 34-brittle failure

Start 08:21:25 ice ridge brittle failure, force increase because of thickness increase.
End 08:34:50 circumferential crack, force drop.

Event no. 35-brittle failure

Start 08:34:50 full contact between deformed ice sheet and lighthouse after circumferential crack, brittle failure (one circumferential crack 08:36:40).

End 08:37:56 circumferential crack, force drop.

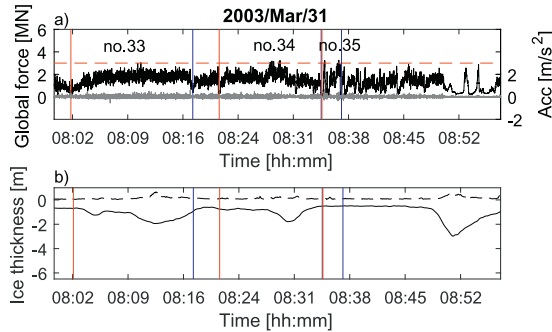


Fig. A.18. a) Global force and acceleration b) EM ice thickness for event 33–35. Vertical red lines represents the beginning of an event, and blue vertical lines represents the end of an event. (For interpretation of the references to colour in this figure legend, the reader is referred to the web version of this article.)

Event no. 36-brittle failure

Start 09:27:27 full contact between ridges ice sheet and lighthouse after circumferential crack, brittle failure.

End 09:31:18 circumferential crack and force drop.

Event no. 37-brittle failure

Start 09:47:00 full contact after crack with ridges ice sheet, – brittle failure.

End 09:53:13 plug/bending failure, force drop.

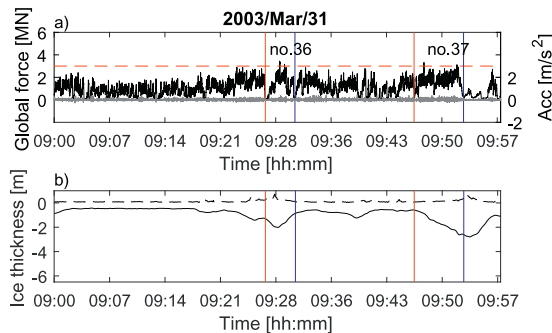


Fig. A.19. a) Global force and acceleration b) EM ice thickness for event 36 and 37. Vertical red lines represents the beginning of an event, and blue vertical lines represents the end of an event. (For interpretation of the references to colour in this figure legend, the reader is referred to the web version of this article.)

Event no. 38-brittle failure

Start 10:04:17 contact between lighthouse and ridged ice sheet after crack, brittle failure.

End 10:11:03 splitting of ridge, force drop.

Event no. 39-brittle failure

Start 10:19:31 contact after circumferential crack between deformed ice sheet and lighthouse, brittle failure.

End 10:23:45 force decreases at the sail due to discontinuities, no visual cracks.

Event no. 40-brittle failure

Start 10:23:49 force increases when the ridge sail passes, brittle failure.

End 10:26:30 circumferential crack forms and the force decreases.

Event no. 41-brittle failure

Start 10:35:46 force increases due to ice thickness increase, brittle failure.
End 10:42:40 ice ridge plug/bending failure and the force drops.

Event no. 42-brittle failure

Start 10:50:33 ice force increases due to ice thickness increase, brittle failure.
End 10:54:06 ice ridge plug/bending failure and the force drops.

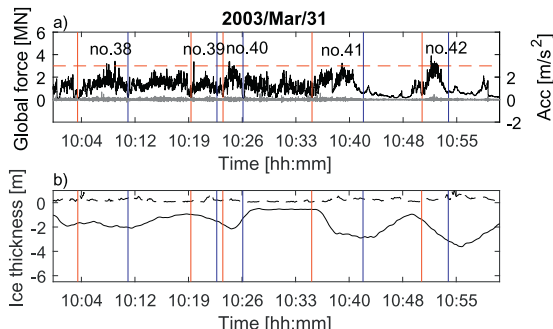


Fig. A.20. a) Global force and acceleration b) EM ice thickness for event 38–42. Vertical red lines represents the beginning of an event, and blue vertical lines represents the end of an event. (For interpretation of the references to colour in this figure legend, the reader is referred to the web version of this article.)

References

4COffshore, 2017. Tahkoluoto Offshore Wind Power Project Offshore Wind Farm. [http://www.4coffshore.com/windfarms/tahkoluodon-merituulipuiston-\(pori-2\)-finland-f03.html](http://www.4coffshore.com/windfarms/tahkoluodon-merituulipuiston-(pori-2)-finland-f03.html), Accessed date: 3 January 2018.

Axell, L., Golbeck, L., Jandt, S., Izotova, J., 2017. Copernicus Report: Balticea reanalysis_phys_003_008.

Bjerkås, M., 2004. Global Design Ice Loads' Dependence of failure mode. *Int. J. Offshore Polar Eng.* 14 (3), 6.

Bjerkås, M., 2006. Ice Action on Offshore Structures. NTNU.

Bjerkås, M., Bonnemaire, B., 2004. Ice ridge-structure interaction Part II: Loads from first-year ice ridges and their surrounding ice sheets. In: *Proceedings of IAHR Symposium on Ice*, St. Petersburg, Russia.

Bjerkås, M., Nord, T.S., 2016. Ice Action on Swedish Lighthouses Revisited, *Proceedings of the 23rd IAHR International Symposium on Ice*. Michigan USA, Ann Arbor.

Bjerkås, M., Bonnemaire, B., Sodhi, D.S., Gerisch, S., Jochmann, P., 2003. STRICE Report: Extended Observations of Ice-Structure Interactions at the Lighthouse Norströmsgrund Winter 2003. Report N. D-3.1.

Bjerkås, M., Loney, C. and Gürtner, A., 2012. Seasonal Variations in the Occurrence of Ice Induced Vibration of a Bottom Fixed Structure, the Twenty-second International Offshore and Polar Engineering Conference. *International Society of Offshore and Polar Engineers*, Rhodes, Greece.

Bonnamaire, B., Bjerkås, M., 2004. Ice ridge-structure interaction, part I: Geometry and failure mode of ice ridges. In: *International Symposium on Ice International Association of Hydraulic Engineering and Research (IAHR)*, St. Petersburg, Russia.

Brown, T.G., Tibbo, J.S., Tripathi, D., Obert, K., Shrestha, N., 2010. Extreme ice load events on the Confederation Bridge. *Cold Reg. Sci. Technol.* 60 (1), 1–14.

Bruce, J.R., Brown, T.G., 2001. Operating an ice force monitoring system on the confederation bridge. In: *Proceedings of the 16th International Conference on Port and Ocean Polar Engineering under Arctic Conditions*, Ottawa, Ontario, Canada, pp. 299–308.

Copernicus, 2017. Copernicus Marine Environment Monitoring Service: Sea Level in the Baltic Sea. <http://marine.copernicus.eu/documents/QUID/CMEMS-BAL-QUID-003-008.pdf>.

Croasdale, K.R., 1984. The Limiting Driving Force Approach to Ice Loads. *Offshore Technology Conference*.

Croasdale, K.R., 2009. Limit Force Ice Loads - an Update, *Proceeding of the 20th International Conference on Port and Ocean Engineering under Arctic Conditions*, Luleå, Sweden.

Engelbrekton, A., 1987. Analysis of Field Observations from Norströmsgrund Lighthouse During the Period 1979–1985. A Study project Ice Forces Against Offshore Structures. VBB Project M7334. Report, No 2. Jan 15. VBB; 1987.

Eranti, E., 2017. Pilot Wind Turbine Project. <http://www.erantiengineering.fi/pilot-wind-turbine.htm>, Accessed date: 3 January 2018.

Ervik, Å., 2015. Full scale actions from first-year ridge interactions with fixed structures. In: *Proceedings of the 23rd International Conference on Port and Ocean Engineering under Arctic Conditions* Trondheim, Norway, pp. 129–140.

Ervik, Å., Høyland, K.V., Shestov, A., Nord, T.S., 2018. On the decay of first-year ice ridges: measurements and evolution of rubble macroporosity, ridge drilling resistance and consolidated layer strength. *Cold Reg. Sci. Technol.* 151, 196–207. <https://doi.org/10.1016/j.coldregions.2018.03.024>.

FMI, 2016. Ice Winters in the Baltic Sea. <http://en.ilmatieteennlaitos.fi/baltic-sea-ice-winters>, Accessed date: 25 May 2017.

Franson, L., Bergdahl, L., 2009. Recommendations for Design of Offshore Foundations Exposed to Ice Loads. Vol. 09, pp. 55.

Franson, L., Olofsson, T., Sandkvist, J., 1991. Observations of the Failure Process in Ice Blocks Crushed by a Flat Indentor. In: *S.J.S. Proc. of the POAC '91*, Canada. Vol.1, pp. 501–514.

Frederking, R., 2005. Tiltmeter application at Norströmsgrund lighthouse-STRICE project. In: *Proceedings of the 18th International Conference on Port and Ocean Engineering under Arctic Conditions (POAC)* Potsdam, USA.

Frederking, R., Barker, A., 2001. Friction of Sea Ice on Various Construction Materials, *Technical Report National Research Council Canada NRC*. <https://doi.org/10.4224/12328729>.

Haas, C., 2000. LOLEIF Report: EM Ice Thickness Measurements at the Lighthouse Norströmsgrund, Luleå, Sweden, within the LOLEIF Project. Part 1: System Installation, Modelling and Calibration.

Haas, C., 2017. EM Thickness and the Consolidated Layer. (personal communication).

Haas, C., Jochmann, P., 2003. Continuous EM and ULS thickness profiling in support of force measurements. In: *Proceedings of the 17th International Conference on Port and Ocean Engineering under Arctic Conditions (POAC)*, Trondheim, Norway.

Hansen, E., Ekeberg, O.C., Gerland, S., Pavlova, O., Spreen, G., Tschudi, M., 2014. Variability in categories of Arctic Sea ice in Fram Strait. *J. Geophys. Res. Oceans* 119 (10), 7175–7189.

Heinonen, J., Kärnä, T., Luo, C., 2004. Strice Report: Dynamic Behaviour of the Norströmsgrund Lighthouse. VTT Technocal Research Center of Finland, Luleå University of Technology.

Hendriks, H., 2017. Ice-induced Vibrations of Vertically Sided Offshore Structures. *Delft University of Technology*<https://doi.org/10.4233/uuid:325ebcfb-f920-400c-8ef6-21b2305b6920>.

ISO19906, 2010. Petroleum and Natural Gas Industries - Arctic Offshore Structures. *International Standardization organization*, Geneva, Switzerland.

Jochmann, P., Schwarz, J., 2000. LOLEIF-report: Ice Force Measurements at Lighthouse Norströmsgrund - Winter 1999. Rep no 5.

Joensuu, A., Riska, K., 1989. Ice and Structure Interaction (Finnish). Helsinki University of Technology, Ship Laboratory, Report M-88, Espoo, Finland (57 p).

Jordaán, L.J., 2001. Mechanics of ice–structure interaction. *Eng. Fract. Mech.* 68 (17), 1923–1960.

Kärnä, T., Yan, Q., 2009. Analysis of the Size Effect in Ice crushing- Edition 2, *Technical Report No. RTEU50-IR-6/2005*. VTT.

Karvonen, J., 2016. Virtual radar ice buoy – a method for measuring fine-scale sea ice drift. *Cryosphere* 10 (1), 29–42.

Kulyakhtin, S., 2017. Unconsolidated Ice Rubble Modelling With Continuum Approach. PhD thesis. Norwegian University of Science and Technology, NTNU. <http://hdl.handle.net/11250/2448966>.

Leppäranta, M., Hakala, R., 1992. The structure and strength of first-year ice ridges in the Baltic Sea. *Cold Reg. Sci. Technol.* 20 (3), 295–311.

Leppäranta, M., Myrberg, K., 2009. *Physical Oceanography of the Baltic*. Springer (ISBN: 978-3-540-79702-9).

Li, H., Bjerkås, M., Høyland, K.V., Nord, T.S., 2016. Panel loads and weather conditions at Norströmsgrund lighthouse 2000–2003. In: *Proceedings of the 23rd IAHR International Symposium on Ice*. Michigan USA, Ann Arbor.

- Määttänen, M., Kärnä, T., 2011. ISO 19906 ice crushing load design extension for narrow structures. In: *Proceeding of the 21st International Conference on Port and Ocean Engineering under Arctic Conditions*, Montreal, Canada.
- MATLAB and Statistics Toolbox Release, 2017a. The MathWorks, Inc. Natick, Massachusetts, United States.
- Michel, B., Toussaint, N., 1977. Mechanisms and Theory of Indentation of Ice Plates. *J. Glaciol.* 19 (81), 285–300.
- NASA, E., 2018. <https://worldview.earthdata.nasa.gov/>.
- Nord, T.S., Øiseth, O., Lourens, E.-M., 2016. Ice force indentification on the Norstrømsgrund lighthouse. *Comput. Struct.* 169, 24–39.
- Oikkonen, A., Haapala, J., Lensu, M., Karvonen, J., Itkin, P., 2017. Small-scale sea ice deformation during N-ICE2015: From compact pack ice to marginal ice zone. *J. Geophys. Res.* 122, 5105–5120. <https://doi.org/10.1002/2016JG012387>.
- O'Rourke, B.J., Jordaan, I.J., Taylor, R.S., Gürtner, A., 2016a. Experimental investigation of oscillation of loads in ice high-pressure zones, part 1: single indenter system. *Cold Reg. Sci. Technol.* 124, 25–39.
- O'Rourke, B.J., Jordaan, I.J., Taylor, R.S., Gürtner, A., 2016b. Experimental investigation of oscillation of loads in ice high-pressure zones, part 2: double indenter system — coupling and synchronization of high-pressure zones. *Cold Reg. Sci. Technol.* 124, 11–24.
- Poirier, L., 2014. Detailed ice ridge loading events on Norstrømsgrund lighthouse. In: *International Conference and Exhibition of Performance of Ships and Structures on Ice (ICETECH)*, Banff, Alberta.
- Riska, K., Rantala, H., Joensuu, A., 1990. Full Scale Observations of Ship-Ice Contact, Helsinki University of Technology, Ship Laboratory, Report M-97 Espoo. (54 p).
- Samaradzija, I., 2018. Two Applications of a Cross-correlation Based Ice Drift Tracking Algorithm; Ship-based Marine Radar Images and Camera Images From a Fixed Structure. *International Symposium on Ice International Association of Hydraulic Engineering and Research (IAHR)*, Vladivostok, Russia.
- Schulson, E.M., Buck, S.E., 1995. The ductile-to-brittle transition and ductile failure envelopes of orthotropic ice under biaxial compression. *Acta Metall. Mater.* 43 (10), 3661–3668.
- Schulson, E.M., Nickolayev, O.Y., 1995. Failure of columnar saline ice under biaxial compression: failure envelopes and the brittle-to-ductile transition. *J. Geophys. Res.* 100 (B11), 22383–22400.
- Shrestha, N., Brown, T.G., 2018. 20 years of monitoring of ice action on the Confederation Bridge piers. *Cold Reg. Sci. Technol.* 151, 208–236.
- SMHI, 2014a. Air pressure and sea level. Swedish Meteorological Institute. <http://www.smhi.se/en/theme/air-pressure-and-sea-level-1.12266>, Accessed date: 16 May 2017.
- SMHI, 2014b. Hur Beraknas Medeltemperatur (How are Mean Temperature Calculated). Swedish Meteorological and Hydrological Institute (SMHI). <http://www.smhi.se/kunskapsbanken/meteorologi/hur-beraknas-medeltemperatur-1.3923>, Accessed date: 15 May 2017.
- Sodhi, D.S., Haehnel, R.S., 2003. Crushing ice forces on structures. *J. Cold Reg. Eng.* 17 (4).
- Sodhi, D.S., Takeuchi, T., Nakazawa, N., Akagawa, S., Saeki, H., 1998. Medium-scale indentation tests on sea ice at various speeds. *Cold Reg. Sci. Technol.* 28 (3), 161–182.
- Sudom, D., Frederking, R., 2014. First-Year Ice Ridge Loads on Norstrømsgrund Lighthouse in 2002 and. *International Conference and Exhibition on Performance of Ships and Structures in Ice (ICETECH)*, Banff, Alberta, Canada, pp. 2003.
- Timco, G.W., Sudom, D., Frederking, R., Barker, A., Wright, B.D., 2017. A critical review of Arctic pack ice driving forces: New sources of data. *Cold Reg. Sci. Technol.* 138, 1–17.
- Wells, J., Jordaan, I., Derradji-Aouat, A., Taylor, R., 2011. Small-scale laboratory experiments on the indentation failure of polycrystalline ice in compression: main results and pressure distribution. *Cold Reg. Sci. Technol.* 65 (3), 314–325.
- Zubov, N., 1945. *Ldy Aztkiki (Arctic Ice)*. Glavsevmorputi Press, Moscow, Russia.

Appendix 5

A Continuum Model of Large Deformation Continuous Ductile Ice Crushing

This appendix includes the conference paper presented at the 24th International Conference on Port and Ocean Engineering under Arctic Conditions (see below).

- Ervik, Å., Høyland, K.V, Grimstad, G., Nord, T.S. A Continuum Model of Large Deformation Continuous Ductile Ice Crushing. Proceedings of the 24th International Conference on Port and Ocean Engineering under Arctic Conditions (POAC), Busan, Korea, Paper no. 104.



A continuum model of large deformation continuous ductile ice crushing

Åse Ervik^{1,2,3}, Knut Vilhelm Høyland^{1,2}, Gustav Grimstad^{1,2}, Torodd Skjerve Nord^{1,2,3}
¹Sustainable Arctic Marine and Coastal Technology (NTNU, Trondheim, Norway)
²Department of Civil and Environmental Engineering (NTNU, Trondheim, Norway) ³UNIS
(Longyearbyen, Norway)

ABSTRACT

This paper presents numerical modelling techniques for modelling of large deformation continuous ductile ice crushing. Two continuum formulations, the Coupled Eulerian Lagrangian (CEL) method and Smoothed Particle Hydrodynamics (SPH) method available in ABAQUS/Explicit 6-13 are used in combination with a modified version of a constitutive model originally developed for concrete. First, an analytical small strain problem is modelled in order to compare the accuracy of the two continuum formulations. With the CEL method the problem was solved exactly, while the SPH method produced an error of 42%. Finally, a medium-scale continuous ductile ice crushing indentation experiment conducted in the Van Mijen fjord in Spitsbergen 2003 is modelled with the CEL formulation. Required parameters like the initial uniaxial compressive strength and the elastic modulus was measured during the experiment, other required material parameters are estimated. The calculated global load on the cylindrical indenter was in good agreement with the load measured during the experiment.

KEY WORDS: CEL; SPH; Large deformations; Ductile ice crushing; Consolidated layer

INTRODUCTION

Ice ridges are accounted for in quasi-static design of structures in ice-infested waters. The combined force from the consolidated layer and the force from the ice rubble give the ice ridge design force. A relatively inexpensive means to assess ice ridge forces is by numerical modelling. In order to model the continuous failure of the consolidated layer and rubble accumulation, a suitable model must handle large deformations. This article focuses on crushing of the consolidated layer. First, two continuum formulations that allow for large deformations are presented: the Coupled Eulerian Lagrangian (CEL) method and the Smoothed Particle Hydrodynamics (SPH) method. Then a constitutive model for continuous ductile crushing of the consolidated layer is proposed. An analytical small strain problem is used to test the accuracy of the two continuum formulations. The medium-scale large deformation

The type of ice failure is determined by the ice velocity, temperature and the structure shape and observed time histories of the measured forces and responses. In the modelled medium-scale indentation experiment, an ice sheet was towed against a vertical fixed cylindrical indenter with an average indentation speed of 3.5mm/s. According to Moslet et al. (2004) the ice failure mode was ductile crushing (see Figure 2a). However, because of the low stiffness of the system (indenter, steel wires etc.), the indentation speed was highly non-linear, resulting in cycles of ductile crushing. During force build up, elastic energy was stored in the system, and when the ice reached the failure limit, the elastic energy was released resulting in a high indentation speed. The cycles of ductile crushing lasted for approximately 50 s with an approximate indentation speed of 1 mm/s. According to Sodhi et al. (1998) this indentation speed is associated with ductile crushing. In the analysis, presented here, the experiment is simplified by assuming that the ice indentation speed is constant and that the cylindrical indenter is rigid. The purpose of this model is to predict the development in the peak force and therefore, the sudden force drops observed in the experiment force time history (Figure 2a) is outside the scope of this study.

Several constitutive models have been used to simulate ice crushing. E.g. the crushable foam model (Hallquist, 1998) was used by Gagnon (2011) to simulate brittle ice crushing including spalling. One problem with this model is the lack of physical explanation. Another model widely used to simulate brittle crushing during high velocity iceberg-ship interactions (Kirkegaard, 1993; Løset and Kvamsdal, 1994; Riska and Frederking, 1987), is the pressure dependent elliptical yield surface presented by Derradji-Aouat (2003). Liu et al. (2011) used this constitutive model to simulate a high velocity iceberg-ship impact and used element erosion to delete elements that exceeded an effective strain limit. For the current application (ductile crushing), element erosion as a failure criterion is not suited. Obtaining a physical consistent criterion for when to delete elements is difficult and additionally the energy balance is not satisfied when mass is removed from the analysis. In the end of the next section, we develop phenomenologically a constitutive model that captures the important physical behavior of ductile failure of ice in the consolidated layer.

BACKGROUND

From FEM to CEL

In the finite element (FE) Lagrangian formulation, expressed in the equations below, the material is fixed to the mesh, while in the CEL formulation the material moves independently of the mesh.

The concept of the FE method can be explained through kinematic-, constitutive- and equilibrium equations. First, the displacement vector $\mathbf{u}(x)$ is approximated by a linear combination of shape functions collected in a matrix $\mathbf{N}(x)$. Each shape function is associated with an unknown nodal displacement collected in a column vector \mathbf{d} , Equation 1.

$$\mathbf{u}(x) \approx \mathbf{N}(x) \cdot \mathbf{d} \quad (1)$$

The kinematic equation is expressed in Equation 2, where ∂ is the Cartesian differential operator (with respect to the material configuration) and $\boldsymbol{\varepsilon}$ is the column strain vector.

$$\boldsymbol{\varepsilon}(x) \approx \partial \mathbf{N}(x) \cdot \mathbf{d} = \mathbf{B}(x) \cdot \mathbf{d} \quad (2)$$

The principal of virtual work in the weak form of the equilibrium equation, Equation 3-4, is used to derive the stiffness matrix \mathbf{K}_e . Where $\delta \mathbf{u}$ and $\delta \boldsymbol{\varepsilon}$ are arbitrary virtual displacements and strain fields, respectively.

$$\int_V \boldsymbol{\sigma}^T \delta \boldsymbol{\varepsilon} dV = \int_V \mathbf{b}^T \delta \mathbf{u} dV + \int_S \mathbf{t}^T \delta \mathbf{u} dS \quad (3)$$

$$\int_V \boldsymbol{\sigma}^T \mathbf{B}(x) \delta \mathbf{d} dV = \int_V \mathbf{b}^T \mathbf{N}(x) \delta \mathbf{d} dV + \int_S \mathbf{t}^T \mathbf{N}(x) \delta \mathbf{d} dS \quad (4)$$

For a linearly elastic material the stress ($\boldsymbol{\sigma}$) is expressed through the constitutive equation: $\boldsymbol{\sigma} \approx \mathbf{D}_e(x) \mathbf{B}(x) \mathbf{d}$, where $\mathbf{D}_e(x)$ is the elasticity matrix. For a linearly elastic material the element stiffness matrix (Equation 5) is used to evaluate the unknown displacement vector \mathbf{d} .

$$\mathbf{K}_e \mathbf{d} = \mathbf{f}_{ext} \quad (5)$$

$$\mathbf{K}_e = \int_V \mathbf{B}^T(x) \mathbf{D}_e(x) \mathbf{B}(x) dV$$

For non-linear materials (plasticity), the stress is a function of the $\mathbf{B}(x)$ matrix and x such that \mathbf{K}_e becomes a nonlinear integral, which is evaluated through a numerical quadrature.

In ABAQUS, the CEL method is implemented through a Lagrangian-plus-remap algorithm, which consists of two steps for each explicit time increment. First, in a conventional Lagrangian increment, deformations, strains and stresses are computed. Second, in an advection remap increment, the material advection is computed and the mesh is brought back to its initial configuration.

SPH

The smoothed particle hydrodynamics (SPH) method is a mesh free Lagrangian formulation, first developed for astrophysical problems involving extreme deformations by Lucy (1977) and Gingold and Monaghan (1977) later extended to strength of materials by Libersky and Petschek (1991). There are four key ideas behind the SPH method. The material domain is discretized into a finite number of disengaged particles. Field functions (density, velocity, energy) are approximated by integral representations:

$$f(x) = \int_{\Omega} f(\tilde{x}) \delta(x - \tilde{x}) d\tilde{x}, \quad \delta \begin{cases} 1 & x = \tilde{x} \\ 0 & x \neq \tilde{x} \end{cases} \quad (6)$$

Where, $f(x)$ is a field function of the three dimensional position vector x , Ω is the volume of the support domain over which $f(x)$ is integrated, and δ is the Dirac delta function. The Dirac delta function is approximated by a smoothing kernel function W defined over a smoothing length h . The smoothing function should be a positive, even function, with compact support, and satisfy the Dirac delta function when the smoothing length approaches zero and unity over its support domain. The field function with the smoothing approximation accordingly reads:

$$\langle f(x) \rangle = \int_{\Omega} f(\tilde{x}) W(x - \tilde{x}, h) d\tilde{x} \quad (7)$$

$\langle \rangle$ is the kernel approximation operator. Finally, through a particle approximation the integral in Equation 2, is discretized by summation over all particles within the support domain:

$$\langle f(x_i) \rangle = \sum_{j=1}^N \frac{m_j}{\rho_j} f(x_j) W(x_i - x_j, h) \quad (8)$$

Where, $d\tilde{x}$ is the volume of the support domain at the location of particle j that is replaced by a finite volume of the particle m_j/ρ_j .

Constitutive model

The constitutive model presented in the following, will be used to simulate experiment no 2 presented in Moslet et al. (2004), material parameters and test setup is presented in the next section. The initial uniaxial compressive strength and the elastic modulus were measured during the experiment, other material parameters required for the model are estimated. The model was initially developed for modelling failure in concrete by Lubliner et al. (1989).

The elastic behavior of the consolidated layer is described though two isotropic elastic parameters, the elastic modulus and Poisson's ratio. Compared to orthotropic S2 level ice, the texture of the consolidated layer is isotropic (see e.g. Kankaanpää (1997)). Furthermore, Høyland (2007) and Poplin and Wang (1994) found little difference between the horizontal and vertical uniaxial compressive strength of ice from the consolidated layer. Therefore, the constitutive model of the consolidated layer is assumed isotropic.

The yield surface is pressure-dependent, and allow different strengths in compression and tension, expressed as follows:

$$F(\boldsymbol{\sigma}, \boldsymbol{\kappa}) = \frac{1}{1-\alpha} \left[\sqrt{3J_2} + \alpha I_1 + \beta(\boldsymbol{\kappa}) \langle \sigma_{max} \rangle \right] - \sigma_c(\boldsymbol{\kappa}) \quad (9)$$

$$\alpha = \frac{\sigma_b - \sigma_c}{2\sigma_b - \sigma_c}$$

$$\beta = \frac{\sigma_c(\boldsymbol{\kappa})}{\sigma_t(\boldsymbol{\kappa})} (1-\alpha) - (1-\alpha)$$

where J_2 is the second deviatoric invariant, I_1 is the first principal invariant, σ_{max} is the maximum principal stress, the Macauley bracket $\langle x \rangle = 0.5 \cdot (x + |x|)$, $\boldsymbol{\kappa}$ is the hardening vector, σ_c is the uniaxial compressive strength, σ_t is the uniaxial tensile strength and σ_b is the biaxial compressive strength (tension is positive).

The initial ice strength depends on the state of the ice (temperature, strain rate, confinement) and the type of the ice (grain size and micro-porosity). Generally, the uniaxial compressive strength of an ice sample is approximately an order of magnitude greater than the uniaxial tensile strength of the same sample (Schulson and Duval, 2009). The tensile strength was not measured during the experiment (Moslet et al., 2004), we therefore assume that the uniaxial compressive strength was ten times that of the uniaxial tensile strength. Biaxial strength was neither measured and we assume that $\sigma_b = 1.2 \cdot \sigma_c$, which is in line with measurements of the

biaxial strength of granular/discontinuous- columnar sea ice presented by Timco and Frederking (1984)

The main differences between the elliptical (Derradji-Aouat, 2003) failure surface and the present yield surface, is that the former is intended for brittle failure (without plasticity) while the latter is intended for ductile failure including plasticity. Additionally, the elliptical failure surface constrains the hydrostatic pressure. This implies that, upon a certain limit, increasing the hydrostatic pressure (confinement) results in a decrease in deviatoric strength. However, the data (Gagnon and Gammon, 1995; Gratz and Schulson, 1994; Jones, 1982; Rist and Murrell, 1994) used by Derradji-Aouat (2003), shows no decrease in deviatoric stress with increasing confinement. For polycrystalline ice at -11°C , Jones (1982) measured increasing deviatoric strength for hydrostatic pressures 0-20MPa and strain rates 10^{-6} - 10^{-2} . In the problem of interest the confinement and the hydrostatic pressure is expected to be lower than 20MPa such that the shape of the failure surface at high confinement is irrelevant.

The non-associated flow rule is:

$$d\boldsymbol{\varepsilon}^p = d\lambda \frac{\partial Q}{\partial \boldsymbol{\sigma}} \quad (10)$$

$$Q = \sqrt{(\sigma_{t0} \tan \psi)^2 + 3J_2} + \frac{I_1}{3} \tan \psi$$

Where, $d\boldsymbol{\varepsilon}^p$ is the plastic flow increment vector, $d\lambda$ is the plastic multiplier, G is plastic potential, σ_{t0} is the initial uniaxial tensile strength, ψ is the dilatancy angle.

Frictional materials, such as ice, concrete or rock, may contract or dilate during shearing, such that the plastic flow disobeys the normality condition. To the authors knowledge, there are no experiments which provide measurements of the dilatancy of isotropic ice. However, for concrete, rock and soils, the dilatancy angle was measured in the range 0° - 20° , with decreasing values for increasing confinement (for loose soils negative dilatancy angles can occur). In test 2 (next section) a dilatancy of 15° was used.

The hardening/softening of the yield surface (expressed through $d\boldsymbol{\kappa}$) is generalized though the development of uniaxial strengths ($\boldsymbol{\kappa} = [\kappa_t \kappa_c]^T$). In a uniaxial test, a brittle failure is defined as a sharp drop in the stress- strain curve after the peak stress, whereas a ductile failure is defined as a continuous development in the stress-strain curve after the peak stress. The intention here is to model a ductile crushing failure and to study the effect of localized failure. Høyland et al. (2000) found that the residual uniaxial compressive strength of ice samples from the consolidated layer, tested at -10°C and at nominal strain of 10% was 25-50% of the peak stress. In the next section we will test the effect of a softening behavior compared to a perfectly plastic behavior. The expression for the hardening/softening is:

$$d\boldsymbol{\kappa} = \mathbf{h}(\boldsymbol{\sigma}, \boldsymbol{\kappa}) d\hat{\boldsymbol{\varepsilon}}^p \quad (11)$$

$$\mathbf{h}(\boldsymbol{\sigma}, \boldsymbol{\kappa}) = \begin{pmatrix} r(\boldsymbol{\sigma}) & 0 & 0 \\ 0 & 0 & (1-r(\boldsymbol{\sigma})) \end{pmatrix}$$

$$r(\boldsymbol{\sigma}) = \frac{\sum_{i=1}^3 \langle \sigma_i \rangle}{\sum_{i=1}^3 |\sigma_i|}$$

Where σ_i are the principal stress components. The plastic strain increments in the modified vector $d\hat{\boldsymbol{\varepsilon}}^p$ are ordered from largest to smallest.

TEST SETUP

Small strain test

The first test is a small deformation ($u \ll L$) and small strain ($<1\%$) analytical problem. A linearly elastic cube ($1 \times 1 \times 1 \text{ m}^3$) of material is tested in uniaxial compression. The cube is compressed 0.01m, against a frictionless rigid plate. The material parameters and the analytical force is given in Table 1. The cube is discretized by 10 elements/particles per 1m. For the CEL analysis, void elements are placed around the cube (Figure 1b). Since boundary conditions cannot be applied directly to particles in the SPH simulation (Dassault-Systèmes, 2013), a frictionless and rigid top plate is used to apply the displacement to the cube (Figure 1c). In the SPH simulation a cubic spline smoothing function is used (Equation 7). By default in the SPH formulation the smoothing length is computed in the beginning of the analysis containing on average 30-50 particles.

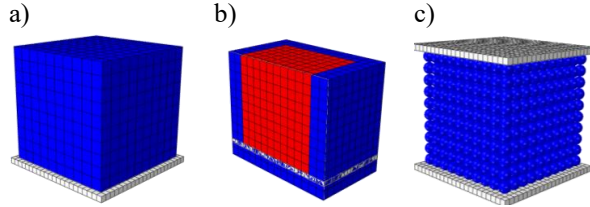


Figure 1. Uniaxial compression: the white plate is fixed and rigid a) FEM setup, blue is deformable cube b) CEL setup, red is the material and blue is the void elements c) SPH setup, particles with diameter of the parent element size additional top plate

Medium scale ice-structure indentation test

In this test, we are modelling experiment number 2 described in Moslet et al. (2004). In the experiment, an ice sheet ($0.16-0.26 \times 7 \times 8 \text{ m}^3$) was towed against a fixed cylindrical indenter ($\text{Ø}0.665 \text{ m}$) in the Van Mijen fjord on Spitsbergen 2003. The setup is shown in Figure 2c. During the experiment the measured maximum ice force measured, was 161kN, the force time history is shown in Figure 2a. The predominant ice crystal structure was granular/isotropic (Moslet et al., 2004). The numerical setup is displayed in Figure 2b. Here, the cylindrical indenter is modelled as rigid and the ice sheet is fixed at the top surface and buoyancy is applied as an upward acceleration (g_B in Equation 12), according to this assumption the ice will

accumulate below the ice sheet. This is done due to instabilities encountered when applying both buoyancy and gravity boundary conditions. Furthermore, the symmetry of the experiment is exploited by modeling only half of the cylinder, the ice sheet size is adjusted to $0.2 \times 2 \times 2 \text{ m}^3$. The material model, summarized above, is rate independent and therefore the velocity in the simulation is increased to 100 mm/s to save computational time. Furthermore, the simulation is run until full contact between the ice sheet and the cylinder is reached. The simulations are carried out using the CEL formulation with the constitutive model described above, material parameters are summarized in Table 1. Two hardening/softening behaviors are tested, first, a perfectly plastic behavior and second a 50% reduction of κ_t and κ_c at 10% equivalent plastic strain (Table 1).

$$g_B = \frac{\rho_w - \rho_{ice}}{\rho_{ice}} g \quad (12)$$

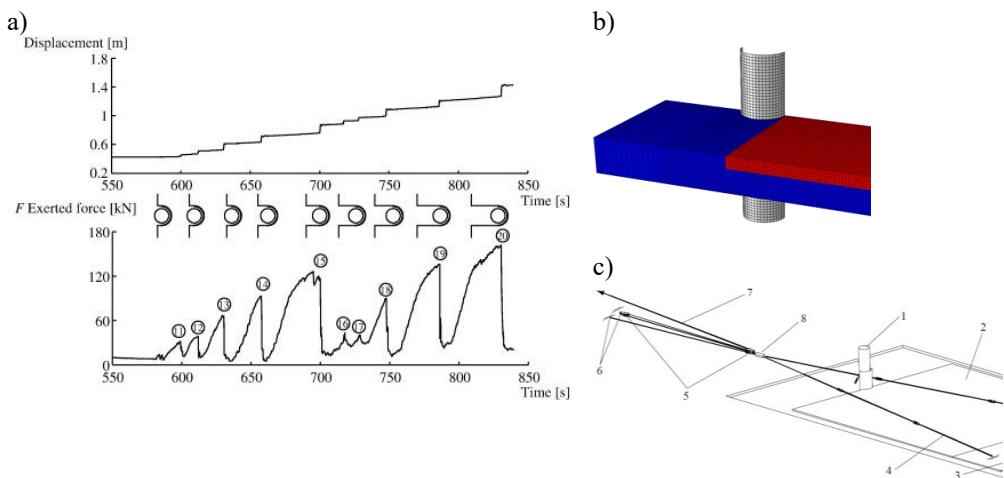


Figure 2. a) Force and displacement time histories (Moslet, 2008) b) CEL setup, the red shaped area is initially filled with material, the blue shaded area is void elements and the rigid cylinder is colored white c) Overview of the experiment setup. The arrow gives the pulling direction of the winch. 1. Cylinder structure, 2. Ice floe, 3. Parent ice piece used as towing floe, 4. Steel bars $\text{Ø}35 \text{ mm}$, 5. Pulleys, 6. Ice anchors, 7. Chains connected to winch, 8. Load cell. (Moslet et al., 2004)

Table 1. Material properties, boundary conditions and test results

Material parameter	Test 1	Test 2 (perfectly plastic)	Test 2 (softening)
Ice density	900 kgm ⁻³	900 kgm ⁻³	900 kgm ⁻³
Water density	-	1000 kgm ⁻³	1000 kgm ⁻³
Ice elastic modulus	5 GPa	2.6 GPa	2.6 GPa
Poisson's ratio	0.3	0.3	0.3
Mean ice temperature	-	-4°C	-4°C
Uniaxial compressive strength	-	1.8 MPa	1.8 MPa (0.9 MPa ε^p_c 10%)
Uniaxial tensile strength	-	0.18 MPa	0.18 MPa (0.09 MPa ε^p_t 10%)
Biaxial compressive strength	-	2.4 MPa	2.4 MPa
Dilatancy	-	15°	15°
F _{max}	50 MN	161 kN	161 kN

RESULTS AND DISCUSSIONS

Small strain test

The rigid plate force is plotted in Figure 3 and the force at the end of the simulation is given in Table 2. The penalty contact stiffness was adjusted such that the contact penalty work was less than 1% of the external energy for all the formulations. The energy balance was checked and is summarized in Table 2. Ae is the artificial strain energy, Vd is viscous energy, Pw is penalty contact work, Wk is the external work and Ie is the internal energy. In an attempt to improve the results of the SPH simulation, the number of particles was doubled. This however had no effect on the results except increasing the computational time and causing instabilities that led to particles escaping the problem domain.

Table 2. Comparison of results

	CEL	FEM	SPH
$Ae / Ie \cdot 100\%$	2	0	0
$Vd / Ie \cdot 100\%$	0	0	0
$Pw / Wk \cdot 100\%$	1	0	-1
$Wk / Ie \cdot 100\%$	99	100	102
F _{end} [MN]	50	50	29

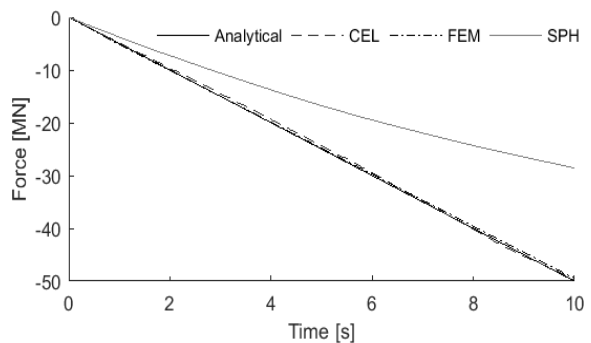


Figure 3. Forces on the bottom plate

With the element based methods (CEL, FEM) the problem was solved exact while the SPH formulation produced an error of 42%. In addition to the inaccuracy of the SPH formulation (in ABAQUS), it has several limitations. First, boundary conditions cannot be applied directly

to particles. Second, different materials modelled with SPH particles do not interact with each other or Eulerian bodies (Dassault-Systèmes, 2013), such that the consolidated layer and the ice rubble modelled with SPH particles would not interact. Third, a positive (tensile) stress corresponds to a purely attractive potential in the SPH formulation, which leads to particle clumping together (tensile instability) (Liu and Liu, 2003).

Medium scale ice-structure indentation test

The result of the simulations are given in Figure 4a, where the total force on the indenter versus the ice sheet displacement is plotted. The grey line is the total force from the ice with a perfectly plastic behavior and the black line is the total force from the ice with softening behavior. The dashed line is the maximum total force measured during the experiment. Figure 4b and c shows the ice accumulation for the ice with the perfectly plastic behavior and the softening behavior, respectively. The energy balance was checked, and the contact energy diffusion was less than 4% and 8% of the external work for the perfectly plastic and softening case respectively. The viscous dissipation and artificial strain energy was less than 1% of the internal energy in both cases and the total energy was close to zero. The highest hydrostatic pressures reached during the simulations was 2MPa and 6 MPa for the perfectly plastic and the softening model respectively.

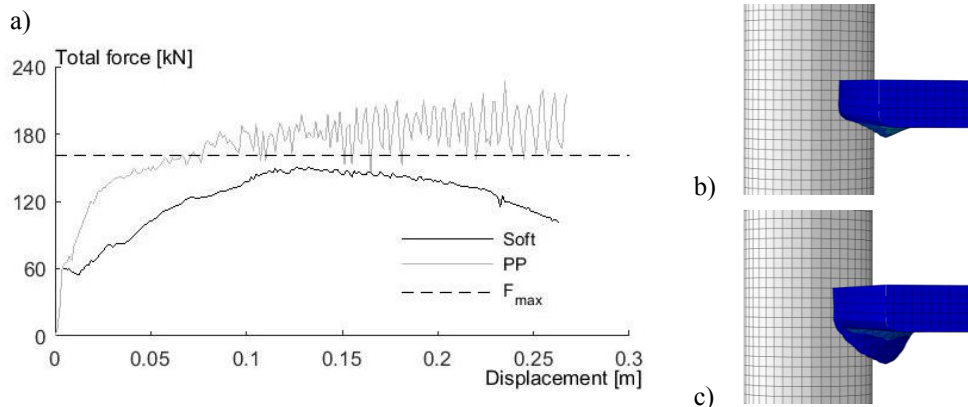


Figure 4. a) Total force on the indenter vs displacement of the ice sheet, the grey line shows the perfectly plastic behavior, the black line shows the softening (soft) behavior and the dashed line is the maximum force measured during the experiment b) is the ice accumulation with the perfectly plastic (PP) material behavior and c) is the ice accumulation with the softening behavior.

The simulation results show good agreement with the experimental measurements. The different hardening behaviors had a clear effect on the simulation results. The softening caused localized failure which increased the amount of local ice accumulation onto the structure. Furthermore, with the strength softening the total forces decreased as the plastic strain of the ice at the structure interface increased and the yield strength decreased. Therefore, the ice force

decreased although the contact area increased. However, the peaks that occurred during the experiment increased in value as the ice contact area increased. Therefore, the development in the force record was best captured with the perfectly plastic behavior. The maximum force obtained during the simulation was 140% and 93% of the measured maximum force for the perfectly plastic and softening case respectively. The maximum hydrostatic pressure reached during the simulation was low (2-6MPa). Therefore, the shape of the yield surface at high hydrostatic pressures is irrelevant, as previously discussed in the section concerning the constitutive model.

To improve the results of the simulations the hardening behavior should be adjusted to the measured development in uniaxial strength, which was unfortunately not available in this study. Furthermore, for better results the system (chains, wires etc.) should be included in the simulations to study the effect of the elastic energy stored in the system. Alternatively, other data which is velocity controlled should be investigated, such as the Joia data presented in e.g. Sodhi et al. (1998).

CONCLUSIONS

The accuracy of two continuum formulations, the CEL and SPH methods, in ABAQUS/Explicit 6-13 was tested by modelling an analytical small strain problem. According to this test, the CEL method produced the highest accuracy between the two formulations. The CEL formulation and a concrete constitutive model was used to model a large deformation medium-scale indentation experiment conducted in the Van Mijen fjord in Spitsbergen in 2003. The elastic modulus and the initial uniaxial compressive strength was measured during the experiment, whereas the other material parameters were estimated. Two different hardening behaviours were tested in the material formulation. The perfectly plastic material model captured the development in the measured total force better than the softening model, whereas the softening model produced the maximum total force closest to the measured value. In future work the parameter sensitivity should be studied. Most of the parameters are uncertain and may vary significantly in nature. The influence of the variation in parameters on the response of the model is unknown and should be investigated further. Additionally, other data sets can be modelled to evaluate the applicability of the model, such as the JOIA experiments (Sodhi et al., 1998) or forces on the Nordstrømsgrund lighthouse (Sudom and Frederking, 2014).

ACKNOWLEDGEMENTS

The authors wish to acknowledge the support of the Research Council of Norway through the Centre of Research-based Innovation, SAMCoT, and the support of the SAMCoT partners.

REFERENCES

- Dassault-Systèmes, 2013. Abaqus 6.13 User's manual
- Derradji-Aouat, A., 2003. Multi-surface failure criterion for saline ice in the brittle regime. *Cold Regions Science and Technology*, 36(1–3): 47-70.
- Gagnon, R.E., 2011. A numerical model of ice crushing using a foam analogue. *Cold Regions Science and Technology*, 65(3): 335-350.

- Gagnon, R.E. and Gammon, P.H., 1995. Triaxial experiments on iceberg and glacier ice. *Journal of Glaciology*, 41(139): 528-540.
- Gingold, R.A. and Monaghan, J.J., 1977. Smoothed particle hydrodynamics: theory and application to non-spherical stars. *Monthly Notices of the Royal Astronomical Society*, 181(3): 375-389.
- Gratz, E. and Schulson, E., 1994. Preliminary observations of brittle compressive failure of columnar saline ice under triaxial loading. *Annals of Glaciology*(19): 33-38.
- Høyland, K.V., 2007. Morphology and small-scale strength of ridges in the North-western Barents Sea. *Cold Regions Science and Technology*, 48(3): 169-187.
- Høyland, K.V., Kjestveit, G., Heinonen, J. and Määttänen, M., 2000. LOLEIF ridge experiments at Marjaniemi; the size and strength of the consolidated layer., 15th International Symposium on Ice Gdansk, Polen, pp. 45-52.
- Jones, J.S., 1982. The Confined Compressive Strength of Polycrystalline Ice. *Journal of Glaciology*, 28(98): 171-178.
- Kankaanpää, P., 1997. Distribution, morphology and structure of sea ice pressure ridges in the Baltic Sea, Helsinki.
- Kirkegaard, H., 1993. Ship Collisions with Icebergs. Doctoral thesis Thesis, Denmark Technology University, 149 pp.
- Libersky, L.D. and Petschek, A.G., 1991. Smooth particle hydrodynamics with strength of materials. In: H.E. Trease, M.F. Fritts and W.P. Crowley (Editors). Springer Berlin Heidelberg, Berlin, Heidelberg, pp. 248-257.
- Liu, G.R. and Liu, M.B., 2003. Smoothed Particle Hydrodynamics a meshfree particle method. World Scientific Publishing Co., 449 pp.
- Liu, Z., Amdahl, J. and Løset, S., 2011. Plasticity based material modelling of ice and its application to ship-iceberg impacts. *Cold Regions Science and Technology*, 65(3): 326-334.
- Lublinter, J., Oliver, J., Oller, S. and Oñate, E., 1989. A plastic-damage model for concrete. *International Journal of Solids and Structures*, 25(3): 299-326.
- Lucy, L.B., 1977. Numerical approach to testing the fission hypothesis. *Astronomical Journal*(82): 1013-1024.
- Løset, S. and Kvamsdal, T., 1994. Iceberg/structure interaction-effects of ice temperature on the impact force, Proceedings of the IAHR Ice symposium, Trondheim, Norway, pp. 205-218.
- Moslet, P.O., 2008. Medium scale ice-structure interaction. *Cold Regions Science and Technology*, 54(2): 143-152.
- Moslet, P.O., Bonnemaire, B., Valkonen, J., Høyland, K.V., Bjerås, M., Dybdahl, J. and Løset, S., 2005. Sea ice- vertical pile interaction experiment, part 3: test results 2004, 18th International Conference on Port and Ocean Engineering Under Arctic Conditions, Portsdam, USA, pp. 471-480.
- Moslet, P.O., Lifero, P., Nilsen, R., Høyland, K.V., Bjerås, M., Bonnemaire, B., Dybdahl, J. and Løset, S., 2004. Sea ice- vertical pile interaction experiment, part 1: test set-up and ice properties, 17th International Symposium on Ice IAHR, St. Petersburg, pp. 11-16.
- Poplin, J.P. and Wang, A.T., 1994. Mechanical properties of rafted annual sea ice. *Cold Regions Science and Technology*, 23(1): 41-67.
- Riska, K. and Frederking, R., 1987. Ice load penetration modelling, Proceedings of the Port and Ocean Under Arctic Conditions Conference Fairbanks, Alaska, USA, pp. 317-327.

- Rist, M.A. and Murrell, S.A.F., 1994. Ice triaxial deformation and fracture. *Journal of Glaciology*, 40(135): 305-318.
- Schulson, E.M. and Duval, P., 2009. *Creep and Fracture in Ice* Cambridge University Press.
- Sodhi, D.S., Takeuchi, T., Nakazawa, N., Akagawa, S. and Saeki, H., 1998. Medium-scale indentation tests on sea ice at various speeds. *Cold Regions Science and Technology*, 28(3): 161-182.
- Sudom, D. and Frederking, R., 2014. First-year ice ridge loads on Norstrømsgrund lighthouse in 2002 and 2003, ICETECH 14.
- Timco, G.W. and Frederking, R.M.W., 1984. An investigation of the failure envelope of granular/discontinuous-columnar sea ice. *Cold Regions Science and Technology*, 9(1): 17-27.

Appendix 6

On FEM ductile ice-structure simulations: the significance of material properties, aspect ratio, structure shape and ice strength heterogeneities

This appendix includes the paper submitted to the journal Cold Regions Science and Technology (see below).

- Ervik, Å., Høyland, K.V, Kim, E. and Nord, T.S. On FEM ductile ice-structure simulations: the significance of material properties, aspect ratio, structure shape and ice strength heterogeneities. Submitted to Cold Regions Science and Technology, under revision.

On FEM ductile ice-structure simulations: the significance of material properties, aspect ratio, structure shape and ice strength heterogeneities

Åse Ervik^{1,2,3}, Knut V. Høyland¹, Ekaterina Kim^{1,4}, Torodd S. Nord^{1,3}

¹ *Sustainable Arctic Marine and Coastal Technology (SAMCoT), Centre for Research-based Innovation (CRI), Norwegian University of Science and Technology, Trondheim, Norway*

² *Multiconsult, Tromsø, Norway*

³ *The University Centre in Svalbard (UNIS), Longyearbyen, Spitsbergen*

⁴ *Center for Autonomous Marine Operations and Systems (AMOS), Norwegian University of Science and Technology, Trondheim, Norway*

Abstract

In this paper we study ductile ice-structure interactions by means of an elastic-plastic finite element model. The model is applied in conjunction with two level factorial design of experiments to identify the statistical significance of material properties to the global ductile ice force transmitted to a structure. The isotropic yield function is pressure dependent and the flow rule is non-associated. The model is applied in simulations of ductile ice failures at two vertically sided structures, a flat indenter in the JOIA experiment and the cylindrical Norströmsgrund lighthouse. In both cases, the simulated global forces are compared to measured forces. Ductile failures established the maximum quasi-static global forces at the flat indenter in the JOIA experiment and the cylindrical Norströmsgrund lighthouse. These events occurred without any significant structural vibrations, so the purpose of the proposed model is to predict quasi-static design forces in cases for which the dynamic response of the structure is not of interest. The model was further used to show that the stress state and thus effective pressure was affected by aspect ratio, structural shape and strength heterogeneities. Low aspect ratios and flat prismatic indenters caused higher lateral ice stresses and thus higher effective pressures than high aspect ratios and cylindrical indenters.

Keywords Finite element model, Statistical significance of material properties, aspect ratio and shape effects, strength heterogeneities

¹ Corresponding author

E-mail address: ase.ervik@ntnu.no (Åse Ervik)

Abbreviations and nomenclature

DOE

design of experiments

FDD

freezing degree days

JOIA

Japan Ocean Industries Association

MWL

mean water level

$\boldsymbol{\varepsilon}, \boldsymbol{\sigma}$

strain, stress

$$\hat{\boldsymbol{\varepsilon}} = \hat{\varepsilon}_1 \geq \hat{\varepsilon}_2 \geq \hat{\varepsilon}_3, \hat{\boldsymbol{\sigma}} = \hat{\sigma}_1 \geq \hat{\sigma}_2 \geq \hat{\sigma}_3$$

3×1 principal strain and stress vector, respectively

$$\boldsymbol{\varepsilon}_{eq}^p = \sqrt{\frac{2}{3}(\boldsymbol{\varepsilon}^p : \boldsymbol{\varepsilon}^p)}$$

equivalent plastic strain

$\mathbf{D}, \mathbf{D}^{ep}$

6×6 elastic and elastic-plastic stiffness matrix, respectively

F

yield function

Q

plastic flow potential

$$I_1 = (\sigma_{11} + \sigma_{22} + \sigma_{33})$$

first stress invariant, the trace of the 3×3 stress tensor, where σ_{11} , σ_{22} and σ_{33} are the diagonal elements

$$J_2 = \frac{1}{6} [(\sigma_{11} - \sigma_{22})^2 + (\sigma_{11} - \sigma_{33})^2 + (\sigma_{22} - \sigma_{33})^2] + (\sigma_{12}^2 + \sigma_{23}^2 + \sigma_{13}^2)$$

second deviatoric stress invariant

$$p = \frac{1}{3} I_1$$

hydrostatic pressure

P_{eff}

effective pressure on structure

E

Elastic modulus

Q

shear modulus

ν

Poisson's ratio

ψ

dilatancy angle

σ_t, σ_c

uniaxial tensile and compressive strength

σ_b

biaxial compressive strength

ρ_i, ρ_w

ice density, water density

1 Introduction

Various types of bottom-founded structures are located in ice-infested waters, including lighthouses, wind turbine foundations, quay structures, platforms, caisson-retained islands and bridges. In spring and summer the global ice movement often accelerates, and although warm ice is known to be weaker than cold ice some of the most severe ice loading events have occurred in spring (Blenkarn, 1970; Engelbrekton, 1987; Ervik et al., 2018b; Neill, 1976). Among these events, high forces at Cook Inlet platforms and at Baltic lighthouses were caused by ductile interactions (Blenkarn, 1970; Ervik et al., 2018b; Neill, 1976). In the medium-scale indentation tests under the sponsorship of the Japan Ocean Industries Association (JOIA), the highest global forces occurred during ductile failures (Saeki et al., 1997; Sodhi et al., 1998).

When level ice fails against compliant vertically sided structures, the combined observation of ice crushing and structural responses are used to classify the interaction mode as one of four: 1) ductile failure (also referred to as creep deformation in (Sodhi and Haehnel, 2003)), 2) intermittent crushing, 3) frequency lock-in crushing and 4) continuous brittle crushing, arranged by increasing indentation speed (ISO19906, 2010; Sodhi and Haehnel, 2003). The corresponding global ice forces are typically estimated using an empirical pressure area relationship.

In ice ridge interactions, considering the global ice forces from the consolidated layer, the situation is similar to the above. Despite frequent measurement of ice properties (e.g., uniaxial compressive strength), there is little explicit use of these properties in the current design formulations. Improving the understanding of how and why parameters of the ice – structure system (aspect ratio, structural shape, heterogeneities, etc.) affect the global ice force, may also improve the current designs formulations.

A numerical model is considered as a supplement to field experiments where parameters in of the ice-structure system can be controlled. The application of numerical models also allows for studying global and local forces as well as responses, without issues related to instrumentation. In numerical models, the ice properties and boundary conditions can be controlled and thus effects of aspect ratio, structural shape and strength heterogeneities can be studied.

In this paper, ductile ice failure is simulated with an elastic-plastic FEM. The elastic-plastic constitutive model applied in the FEM, is relatively simple however the model allows for a more realistic representation of the ice by introducing strength heterogeneities. The model is formulated based on relatively few parameters, and as will be shown in this paper the most significant material properties to the global force are documented in the literature and easy to measure (Timco and Weeks, 2010). The statistical significance of material properties to the global force, is quantified by simulations in conjunction with two level factorial design of experiments. The model is further applied in simulations of ductile ice failure at two vertically sided structures, where the simulated global forces are compared to measured forces. The two structures are the medium-scale structure with flat indenter in the JOIA experiment and the full-scale cylindrical Norströmsgrund lighthouse. Results from simulations are used to explain observed effects of aspect ratio, structure shape and

strength heterogeneities on the global force, results which may improve current design formulations.

2 Background

2.1 A review of ice strength in modelling context

In the 80s and 90s, several studies were initiated to investigate the multiaxial yield and failure surfaces in both polycrystalline/granular (isotropic) and columnar (S3 anisotropic and S2 orthotropic) ice. The studies were motivated by separate objectives, and so differences exist in strain rate, temperature, porosity, loading history, sample preparation, crystal size and orientation.

Triaxial compression data in isotropic iceberg (Gagnon and Gammon (1995), Rist and Murrell (1994)), polycrystalline ice (Jones, 1982) and multiyear sea ice (Riska and Frederking, 1987), all showed that for temperatures lower than approximately -10°C and strain rates higher than approximately 10^{-4} s^{-1} , the deviatoric strength

$$\left(\sqrt{3J_2} = \sqrt{0.5(\sigma_{11} - \sigma_{22})^2 + (\sigma_{11} - \sigma_{33})^2 + (\sigma_{22} - \sigma_{33})^2 + 3(\sigma_{12}^2 + \sigma_{23}^2 + \sigma_{13}^2)} \right) \quad \text{significantly}$$

increased by increasing the pressure ($I_1 = \sigma_{11} + \sigma_{22} + \sigma_{33} = 3p$), at least for I_1 up to approximately 10 MPa, see Fig. 1. Biaxial compressive strength tested in cubic isotropic ice samples loaded in two principal directions is displayed in Fig. 2. The data in Fig. 2 displays ductile tests only (ductile failure was defined by a continuous decrease in the stress/strain curve upon peak stress), where the data was mirrored with respect to the diagonal $\hat{\sigma}_1 = \hat{\sigma}_2$. The data displayed in Fig. 2 shows the difference between the uniaxial and biaxial compressive strength, although the true biaxial compressive strength ($\sigma_b = \hat{\sigma}_1 = \hat{\sigma}_2$) was not measured. The data indicate that there was large variations in the ratio between biaxial and uniaxial compressive strength ($\sigma_b / \sigma_c \approx 1-3$).

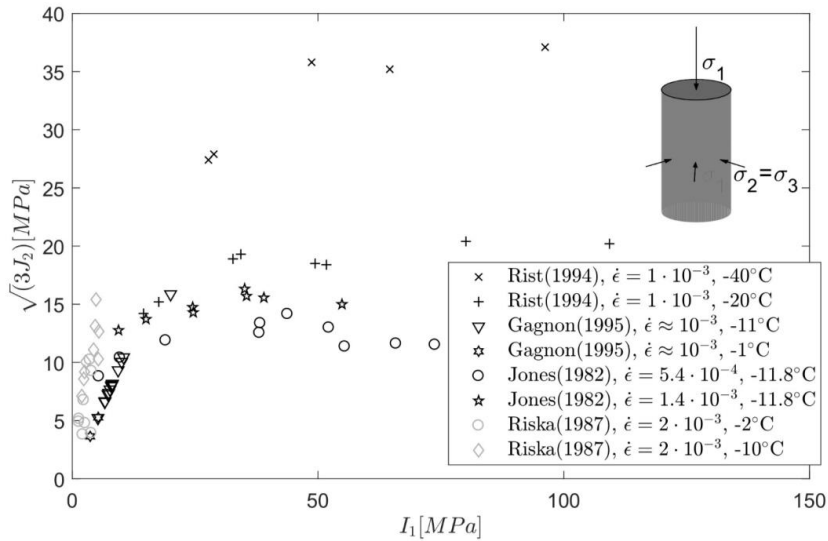


Fig. 1 Multi-axial compression data, strain rate $\sim 10^{-3} \text{ s}^{-1}$. In polycrystalline ice (Jones, 1982; Rist and Murrell, 1994) and iceberg ice (Gagnon and Gammon, 1995). The references (Rist and Murrell, 1994) and (Gagnon and Gammon, 1995) was shorted to respectively Rist (1994) and Gagnon (1995).

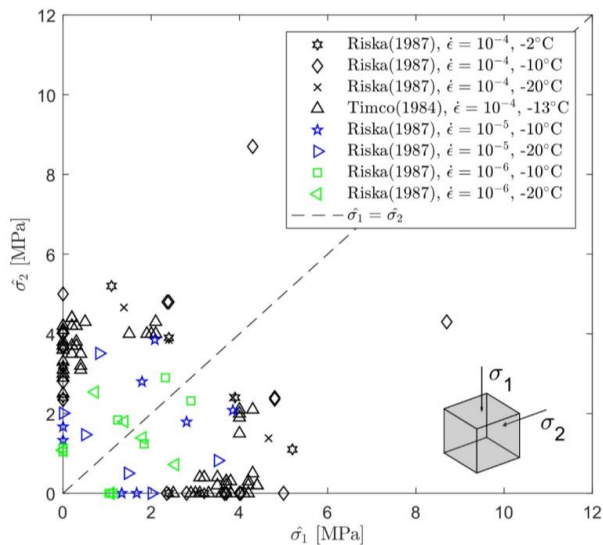


Fig. 2 Ductile biaxial compression data, where data points were mirrored with respect to the line $\hat{\sigma}_1 = \hat{\sigma}_2$. Timco (1984) is short for Timco and Frederking (1984), and Riska (1987) is short for Riska and Frederking (1987). The Timco (1984) data was obtained by digitalization of images.

2.2 Material models

Based on some of the aforementioned studies, an analogy was drawn between ice and materials such as rock, soil and concrete. Ralston (1980) applied two anisotropic pressure dependent yield functions including the model presented by Pariseau (1968) and Smith (1974). The Pariseau (1968) yield function was an anisotropic version of the Drucker Prager yield function. The Smith (1974) yield function was an extension of the Pariseau (1968) yield function that upon a given pressure (I_1) included decreasing deviatoric strength to the pressure melting point. Nadreau and Michel (1986) presented the teardrop model, which like the model in Smith (1974) included decreasing deviatoric strength to the pressure melting point. The teardrop yield function was limited to the compression-compression-compression plane, as the equation highly overestimated the tensile strength. Generally the abovementioned yield functions did not capture the behavior of the ice under tensile stresses. The anisotropic Pariseau (1968), Smith (1974) and teardrop yield functions require a large number of independent strength properties (9, 12 and 15, respectively), whereas the numbers of independent strength properties are significantly reduced in case of isotropy (to 2, 3 and 3, respectively).

In addition to the yield function, the flow potential is also required to formulate the elastic-plastic stiffness matrix. According to the normality condition, the plastic flow is normal to the yield surface, and the flow potential is associated i.e. identical to the yield function. Pressure dependent materials such as rock/soil/concrete dilate i.e. they disobey the normality condition. Measurements presenting dilatancy (volumetric expansion) or generally triaxial strain measurements in ice are rare, however Dorris (1991) presents both stress and strain measured in multiyear Arctic sea ice, and showed that the ice dilated, where the dilatancy increased with increasing strain rate and decreasing pressure (I_1). The dilatancy is described via a parameter called the dilatancy angle. The dilatancy angle is the ratio between the volumetric and deviatoric strain. For rocks and concrete, the dilatancy angle (ψ) is typically in the range 10° to 20° at low to moderate pressure (I_1), depending on strain rate and temperature, (Alejano and Alonso, 2005; Vakili, 2016; Vermeer, 1998).

The Tsai and Wu (1972) model was proposed as a failure function (not yield function), applied in high-velocity brittle iceberg-ship impacts by Liu et al. (2011) and Kim (2014).

The aforementioned anisotropic yield functions require a large number of independent strength properties (9-15), a significantly larger number than commonly measured in field experiments. In addition, for a generally anisotropic material there are 81 independent elastic constants, whereas for an isotropic material there are only two independent elastic constants. We will therefore assume material isotropy. In addition, we expect the first principal invariant (I_1) in the considered ice interaction events (section 2.2 and 2.3) to be less than approximately 10 MPa (this is confirmed in the result section 6.2), and so to further reduce the number of required strength properties we will neglect the pressure decrease at high I_1 . In field indentation experiments the ice may experience stress states that are combinations of tensile and compressive stresses. This requires that the model

fits both the tensile and compressive ice strength. In this paper we will apply the pressure dependent yield function presented by Lubliner et al. (1989), available in ABAQUS 6.13, which is similar to the Pariseau (1968) yield function, but is extended to also fit the tensile strength, and is given in Eq. (1).

$$F(\boldsymbol{\sigma}) = \frac{1}{1-\alpha} \left(\sqrt{3J_2} - \alpha \cdot I_1 + \beta \cdot \langle -\hat{\sigma}_{\min} \rangle \right) - \sigma_c \quad (1)$$

, where $\alpha = \frac{\sigma_b - \sigma_c}{2\sigma_b - \sigma_c}$, $\beta = \frac{\sigma_c}{\sigma_t} \cdot (1-\alpha) - (1+\alpha)$ and the operator $\langle -\hat{\sigma}_{\min} \rangle$ is defined as

$$\langle -\hat{\sigma}_{\min} \rangle = \frac{1}{2} (\hat{\sigma}_{\min} - \text{abs}(\hat{\sigma}_{\min})), \text{ which is non-zero in the tensile part of the yield function only.}$$

Moreover, because measurements suggests that ice dilate (Dorris, 1991), we are interested in studying whether the dilatancy in ice, though the dilatancy angle, significantly influences the global force in ice-structure interactions. We therefore apply a non-associated flow rule with flow potential given in Eq. (2) that is expressed though the dilatancy angle ψ , available in ABAQUS 6.13. The dilatancy angle will be varied within the range (10°-20°), and the significance is quantified by means of two level factorial design of experiments (in section 3).

$$Q(\boldsymbol{\sigma}) = \sqrt{(\sigma_t \tan \psi)^2 + 3J_2} - \frac{I_1}{3} \tan \psi \quad (2)$$

2.3 Data from the JOIA indentation experiment

In the JOIA experiment a stiff flat indenter was pushed against first-year level sea ice in Lake Notoro in Sea of Okhotsk, Japan. The indenter was operated by a servo-jack with a capacity of 0.98 MN which could move the indenter at a constant speed. The indenter was instrumented to measure both local and global forces, for details about the instrumentation please refer to Sodhi et al. (1998), Saeki et al. (1997) and Sakai et al. (1998).

The considered events were measured in 1998 and 1999. The mean salinity was 5.5‰ in 1998 (from 139 samples) (Ushikoshi et al., 2001). The level ice was composed of an almost even layer of granular snow-ice and columnar sea ice and the ice was thus more isotropic than columnar level ice (Ushikoshi et al., 2001). This observation supports the use of an isotopic model.

Peak global forces, indentation speeds, uniaxial compressive strengths, ice thicknesses and indenter widths are given in Table 1. Tensile strength was measured in splitting tests and the average ratio between tensile and compressive strength was $\sigma_t / \sigma_c = 0.16$. The compressive and tensile strength was measured in cylindrical samples loaded in the horizontal direction of the ice sheet (Kamio et al., 2000; Matsushita et al., 1999).

Table 1 Measured quantities in 1998 and 1999.

	Indentation speed [ms ⁻¹]	Peak global force [kN]	Uniaxial compressive strength [MPa]	Ice density [kgm ⁻³]	Ice thickness [cm]	Indenter width [m]
JOIA98	0.0003	170-490 (340)*	0.27-1.73 (1.04)*	888	18.6-28.9 (24.5)*	1.5
JOIA99	0.0003	280-380 (360)*	0.57-3.27 (1.60)*	875	35.0-37.3 (35.7)*	0.6

*minimum-maximum (mean)

2.4 The Norströmsgrund lighthouse data

During the winters 1999/2000-2002/2003, ice forces were measured at the Norströmsgrund lighthouse located in the Gulf of Bothnia, 60 km southeast of Luleå in Sweden. Typical level-ice thicknesses in the Baltic are 40-60 cm, but the thickness of rafted ice may exceed 1 m, and ridges are frequent. The Norströmsgrund lighthouse is a gravity-based concrete structure with a diameter of 7.2 m at mean water level (MWL), +14.5 m elevation from the seabed (Bjerkås and Nord, 2016). The lighthouse was instrumented with 9 load panels covering 162° of the lighthouse circumference from the north (351°) to southeast (153°). The width and height of the load panels were 1.2 m and 1.6 m, respectively. A detailed description of the instrumentation is available in Ervik et al. (2018b), Bjerkås (2006), Haas (2000) and Jochmann and Schwarz (2000).

During the winter of 1999/2000-2002/2003, 77% of all global force events with high global forces (>3 MN) were measured in ice-ridge interactions in March and April in 2003. In ice-ridge interactions at the Norströmsgrund lighthouse, the force was most probably caused by the consolidated layer in ice ridges (Ervik et al., 2018b). The maximum global force measured at the Norströmsgrund lighthouse was approximately 6 MN, but due to limited load panel coverage the global force might have reached ~9 MN during a stalling event (Ervik et al., 2018b). The maximum level ice thickness in 2003, estimated from the number of freezing degree days (FDD), was 0.71 m (Li et al., 2016). Strub-Klein and Sudom (2012) found that in the Baltic Sea the maximum measured ratio of the consolidated layer to level ice thickness was 1.84. Accordingly, assuming that the level ice thickness was 0.71 m, the maximum consolidated layer thickness is estimated to be 1.3 m, which is a conservative estimate. Ice thickness was measured with an EM antenna at the Norströmsgrund lighthouse, however for ice ridges, the EM antenna underestimated the maximum keel depth and overestimated the consolidated layer thickness (Ervik et al., 2018b; Haas, 2017). The average ice salinity was 0.7‰ in 121 samples collected in the winters of 2000/2001-2002/2003 (Franson and Weiss, 2003; Franson and Weiss, 2004a; Franson and Weiss, 2004b). The consolidated layer consist of solid ice, and the structure and strength of the consolidated layer is more isotropic than level ice (Høyland, 2007).

During high force ice ridge interactions at the Norströmsgrund lighthouse the following interaction modes were identified, arranged by increasing indentation speed: 1) stalling 2) ductile failure and 3) brittle failure. Among the high force ice ridge events, intermittent crushing and frequency lock-in vibrations were absent (Ervik et al., 2018b).

Uniaxial strengths were measured in samples loaded in the horizontal direction of a sea ice sheet, in ice samples collected in an ice floe close to the Norströmsgrund lighthouse in 2003 March 20, and in ice samples from Holfjarden, 20 km west of Norströmsgrund in 2003 April 15. A temperature profile was measured through the level ice cover on March 20, displayed in Fig. 3a, where the average ice temperature was -0.5°C . The development in the number of freezing degree days (FDD) is displayed in Fig. 3b.

The uniaxial compressive strength measured in cylindrical samples at -1°C strain-rate $5 \cdot 10^{-4} \text{ s}^{-1}$ was 2-5 MPa. The horizontal uniaxial tensile strength was measured in direct tension at constant loading rate 0.5 kNs^{-1} and values ranged from 0.59 MPa to 2.23 MPa (Franson and Weiss, 2004b). According to experimental data (Schulson and Duval, 2009) values of the tensile strength loaded in the horizontal direction of a sea ice sheet ranged from 0.2 MPa to 0.8 MPa.

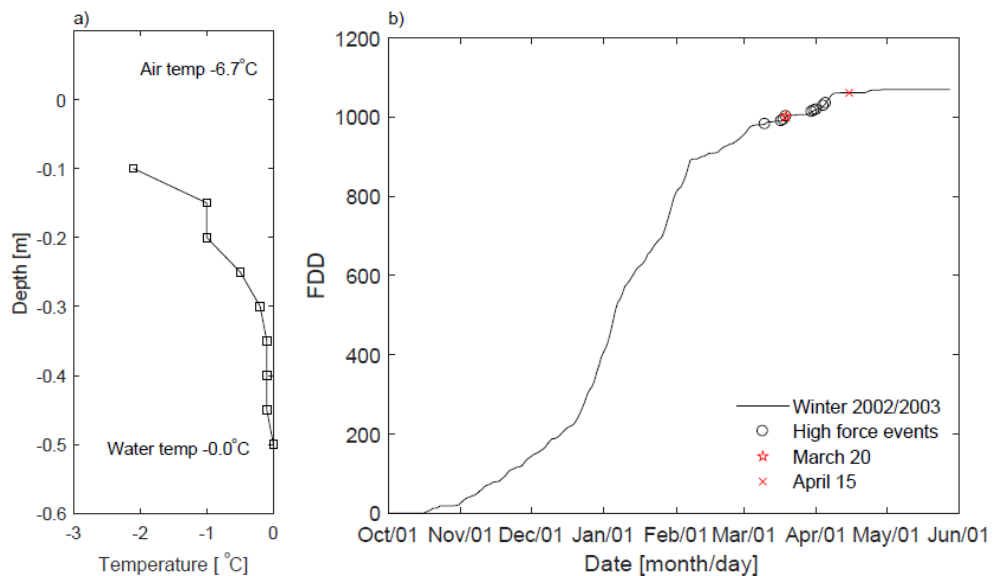


Fig. 3 Ice temperature profile March 20 and FDD development in 2003, days with ice sampling and the dates of high global force events are marked with symbols.

3 Significance of material properties

3.1 Two level factorial design of experiments

In the following we attempt to quantify the significance of the properties in the material model by means of two level factorial design of experiments (2^k factorial DOE). In 2^k factorial DOE, a given set of factors (here material properties) are varied in combination to investigate how the factors affect an output response (here the peak global force). Each factor is given two levels one “low” and one “high” level, then a matrix is made with all combinations of the “low” and “high” values for the different factors. This produces a total of 2^k experiments, where k is the number of factors. The benefit of 2^k factorial compared to one-factor-at-a-time (OFAT) DOE, is that the 2^k factorial DOE considers the interaction between the different factors (Montgomery, 2013).

3.1 Setup for the two level factorial design of experiments

The test chosen for the 2^k factorial DOE was the indentation of 0.3 m thick ice against a vertically sided flat indenter of width 0.6 m. The indenter was modeled as a rigid body which was pushed against a fixed ice sheet and the peak global force on the indenter was used as the output response. The geometry and mesh were modelled with the ABAQUS/CAE 6.13, the model geometry consisted of two solid bodies, the rigid indenter (discretized by the solid element C3D8R) and the deformable ice sheet (discretized by solid Eulerian elements EC3D8R). The choice of the Eulerian elements was made due to the expectation of large deformations. The advantage of the symmetry was exploited and thus only half the indenter and ice sheet was modelled. The ice sheet dimension was $2.25 \cdot 2.25 \cdot 0.3 \text{ m}^3$, and the symmetry plane had $V_y=0 \text{ ms}^{-1}$ boundary condition. The gravity and buoyancy boundary condition was neglected for simplicity, later included in the simulation of the JOIA and Norströmsgrund lighthouse events, the top surface of the ice sheet had $V_z=0 \text{ ms}^{-1}$ boundary condition. The problem geometry and boundary conditions are displayed in Fig. 4.

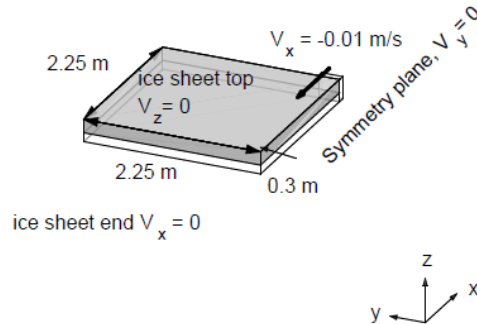


Fig. 4. Sketch of the model geometry and boundary conditions. The gray shaded area display elements filled with material e.g. the ice sheet, whereas the white area displays empty void elements.

Minitab 18.1 was used to produce a matrix for the combination of the “low” and high” value of the 6 factors, which resulted in a total of 64 simulations. Minitab 18.1 was also used to calculate the statistical significance of the factors. The “high” and “low” values for each factor is presented in Table 2. Biaxial compressive strength was expressed as a ratio of the uniaxial compressive strength, which is how the material property is defined in ABAQUS 6.13. The uniaxial tensile strength was also defined as the ratio of the uniaxial compressive strength. Simulations failed if the uniaxial tensile strength was higher than the uniaxial compressive strength, also higher values for tensile than compressive strength are unphysical.

Table 2 Factors in 2^k factorial DOE, low and high value for each factor.

Name	Factor	Low	High
Uniaxial compressive strength	A	1 MPa	10 MPa
Uniaxial tensile/compressive strength	B	0.05	0.15
Biaxial/uniaxial compressive strength	C	1.2	2
Elastic modulus	D	1 GPa	10 GPa
Poisons ratio	E	0.2	0.4
Dilatancy angle	F	10	20

3.2 Results of the two level factorial design of experiments

The normal probability plot (Fig. 5) displays the magnitude, direction, and the significance of the different factors. The effects are t-statistics that test the null hypothesis that the effect is 0, with 95% confidence interval. Positive effects increase the peak global force when the settings change from the low value to the high value of the factor. Negative effects decrease the peak global force when the factor change from the low to the high value. Effects far from 0 on the x-axis have greater magnitude and are more statistically significant. The effects that are not significant are normally distributed, with zero mean and variance (STD^2) and tend to fall along the straight line (red line in Fig. 5). Significant effects have nonzero means and do not lie along the straight line (Montgomery, 2013).

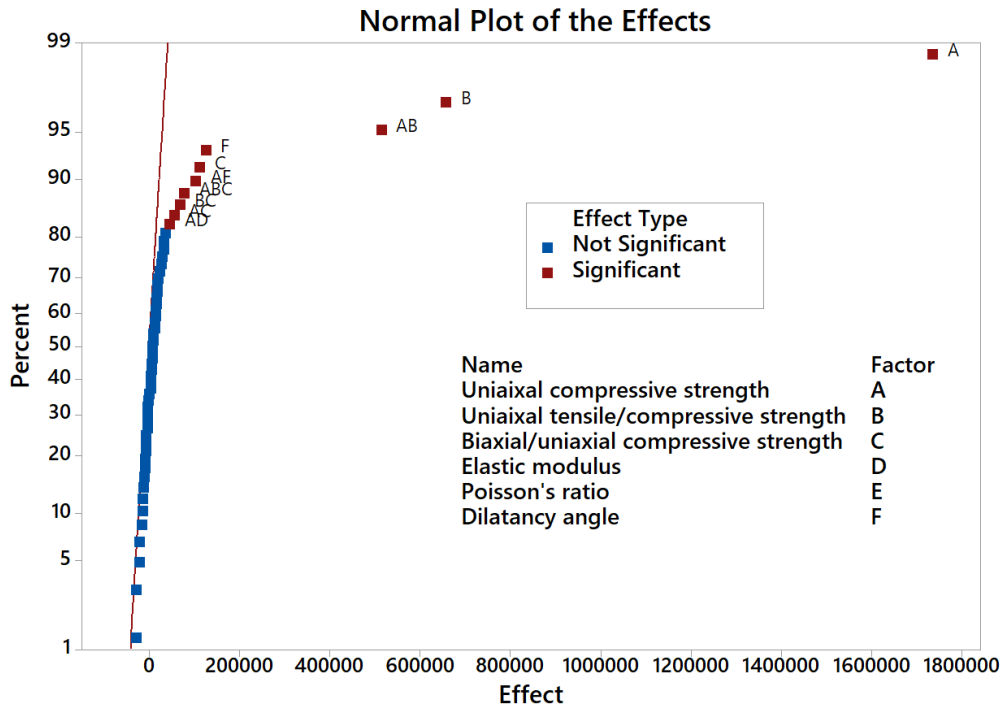


Fig. 5. Normal plot of the effects, the red line shows the effects that are normally distributed with zero mean and variance STD^2 .

Significant factors include A, B, AB, F, C, AF, ABC, BC, AC, AD, where factor names are provided in Fig. 5 and in Table 2. The effect of the main factors (A, B, C, D, E and F) is shown in Fig. 6, where “low” and “high” denotes the low and high value of each factor, respectively. The interaction between main factors is displayed in Fig. 7. The solid and dash lines, respectively, display the change in global force when the value of the second and first effect, respectively, is low and the value of the first and second effect, respectively, is changed from the low to the high setting. Therefore, the lack in parallelism indicates interaction between factors. The three most statistically significant factors and combination of factors were the uniaxial compressive strength (A in Fig. 5), the ratio of the uniaxial compressive/tensile strength (B in Fig. 5) and the combination AB. The absolute effects are provided on the x-axis in Fig. 5. Among the main factors, the poisons ratio (E) and elastic modulus (D) were not significant to the global force, whereas the combination of the uniaxial compressive strength and the elastic modulus (AD) were the least significant factors (among significant factors).

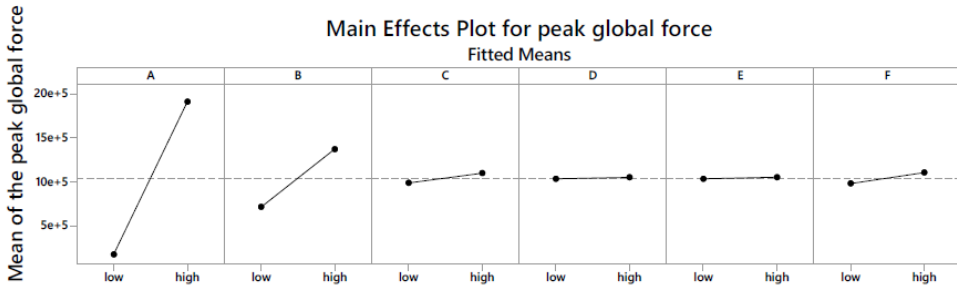


Fig. 6. Main effects plot, where the names for factors A, B, C, D, E and F are given in Table 2. Low and high is the low and high value for each factor, given in Table 2.

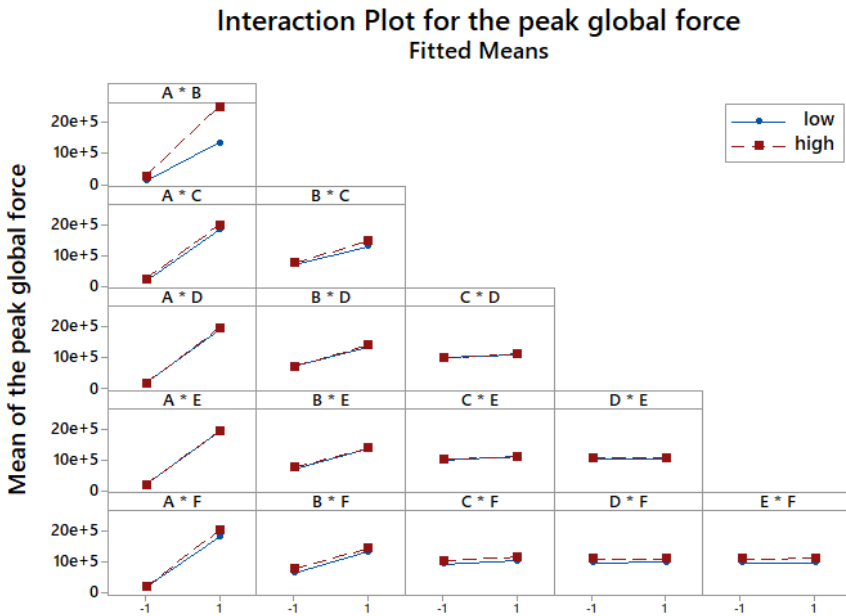


Fig. 7 interactions between factors, the blue lines display the change in mean peak global force when the first effect is low and the second effect is changed from the high to the low value. -1 and 1 on the x-axis denotes low and high, respectively.

4 Ice-structure interaction simulation

The geometries and meshes were modelled with the ABAQUS/CAE 6.13, the model geometries consisted of one solid body (ice sheet) discretized with eight node solid elements with reduced

integration (C3D8R), and the indenter/lighthouse was discretized with four node shell elements with reduced integration (S4R) that were assigned rigid body constraints. In the JOIA simulations the mesh size of the indenter and the ice sheet closest to the indenter was $0.02 \cdot 0.02 \cdot 0.001 \text{ m}^3$ (where 0.001 m was the shell thickness) and $0.02 \cdot 0.02 \cdot 0.02 \text{ m}^3$, respectively. For the Norströmsgrund lighthouse simulations, the mesh size of the lighthouse and the ice sheet in contact with the lighthouse was $2 \cdot 2 \cdot 0.1 \text{ cm}^3$ (where 0.1 cm is the shell thickness) and approximately $0.2 \cdot 0.2 \cdot 0.2 \text{ m}^3$, respectively. Only the part of the lighthouse close to the MWL was modelled. In the JOIA simulations, the advantage of the symmetry of the problem was exploited; thus, only half of the structure and ice sheet was modelled and the side of the ice sheet that represented the symmetry plane, had $V_y=0 \text{ ms}^{-1}$ boundary condition. The ice sheet boundary farthest away from the indenter/lighthouse had $V_x=0 \text{ ms}^{-1}$ boundary condition to prevent the ice sheet from moving away from the indenter/lighthouse. Contact was modelled with the penalty method, where the contact stiffness and friction coefficient were set to 10 GPa and 0.1 , respectively. The contact stiffness was selected to prevent penetration and to ensure that the contact energy was close to zero, whereas the friction coefficient was selected based on typical values for low velocity smooth steel-ice contact (Saeki et al., 1986).

Below the water the sum of the gravity and buoyancy was modelled with a uniform body force $F_b = (\rho_w - \rho_i)g$. The body force was balanced by applying $V_z=0 \text{ ms}^{-1}$ boundary condition at the water level. Ideally the gravity and buoyancy would be applied to the volume above and below the water, respectively. However, when the indenter/lighthouse interacts with the ice sheet, the ice sheet would start oscillating with increasing amplitude. Such oscillations could have been removed by introducing a damping force, however this introduced yet another unknown variable.

Ice properties for the JOIA and Norströmsgrund lighthouse simulations are presented in Table 3. A simulation matrix (Table 4) was made where, among the uncertain properties, the uniaxial compressive and tensile strength was varied, properties that were determined statistically significant, other material properties were kept constant.

Strength heterogeneities were introduced by dividing the ice sheet into approximately 2500 horizontal sections, each containing approximately 100 elements. Each section was randomly assigned a uniaxial compressive strength value in the range provided in Table 4 and the strength was sampled from a uniform distribution

Table 3 Ice properties used in simulation.

Property	E [GPa]	ν [-]	ρ_i [kg/m ³]	ρ_w [kg/m ³]	σ_c [MPa]	σ_t / σ_c	σ_b / σ_c	ψ [°]
JOIA98	2.0	0.3	882	1025	1.04	0.16	1.1	10
JOIA99	2.0	0.3	882	1025	1.60	0.16	1.1	10
NSG	4.8	0.3	894	1005	1-2	0.4-0.59 MPa*	1.1	10

*In the bottom row (NSG) the tensile strength is given in absolute value not as a ratio of the uniaxial compressive strength.

The problem geometry and boundary conditions are displayed in Fig. 8 (JOIA to the left and Norströmsgrund to the right).

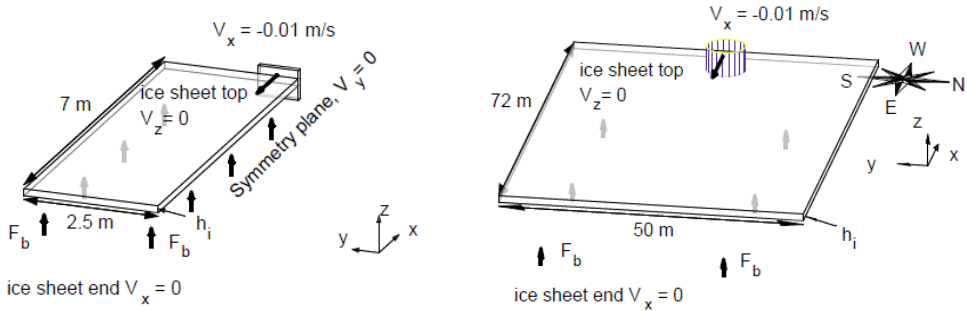


Fig. 8. Outline of the model geometries including boundary conditions, the JOIA setup to the left and the Norströmsgrund lighthouse setup to the right.

Table 4 Simulation matrix, NU=not used, because the model is pressure independent. The spread in uniaxial compressive strength used in heterogeneous simulations is consistent with the measured spread.

Simulation identity	σ_b / σ_c	σ_c [MPa]	Ice thickness [cm]	Indenter width [m]
JOIA98L	1.1	1.04	25.4	1.5
JOIA98H	1.1	1.04(0.27-1.73)*	25.4	1.5
JOIA98VM	NU	1.04	25.4	1.5
JOIA99L	1.1	1.60	35.7	0.6
JOIA99H	1.1	1.60(0.57-3.27)*	35.7	0.6
JOIA99VM	NU	1.60	35.7	0.6
NSGL	1.1	2.0	130	7.2
NSGH	1.1	1.0(0.5-1.6)	130	7.2

*mean value (minimum- maximum)

5 Results

The peak global force in each simulation is provided in Table 5. For the JOIA simulations, the measured global forces and the range of simulated steady state maximum global forces is displayed in Fig. 9. Simulated time series are displayed in separate figures, because the simulation time was significantly shorter than the duration of the measured events. The ice indenter was displaced approximately 1 cm, which was sufficient to reach a steady state global force level. Because of the perfectly plastic material, the relatively high elastic modulus and the constant thickness, a steady state global force was reached.

Table 5. Simulation results, NA= not available. L= homogenous Lubliner, H= heterogeneous Lubliner and VM= von Mises

Simulation identity	Steady state global force [kN]	Effective pressure (P^{eff}) [MPa]	P^{eff}/σ_c [-]	Ice thickness h_i [cm]	Indenter width [m]	Aspect ratio w/h_i [-]
JOIA98L	456	1.20	1.15	25.4	1.5	5.9
JOIA98H	375	0.98	0.94	25.4	1.5	5.9
JOIA98VM	526	1.38	1.32	25.4	1.5	5.9
Measured data 98	340 (170-490)*	0.97 (0.60-1.54)*	NA	25.4 (18.6-28.9)*	1.5	5.9
JOIA99L	555	2.59	1.62	35.7	0.6	1.7
JOIA99H	413	1.93	1.21	35.7	0.6	1.7
JOIA99VM	553	2.58	1.58	35.7	0.6	1.7
Measured data 99	360(280-390)*	1.67(1.38-1.81)*	NA	35.7 (33.9-37.3)*	0.6	1.7
NSGL	25,000	2.67	1.34	1.3	7.2	5.5
NSGH	11,000	1.18	1.18	130	7.2	5.5
Measured data NSG	6,000/9,000	NA	NA	NA	7.2	NA

*mean value (minimum - maximum)

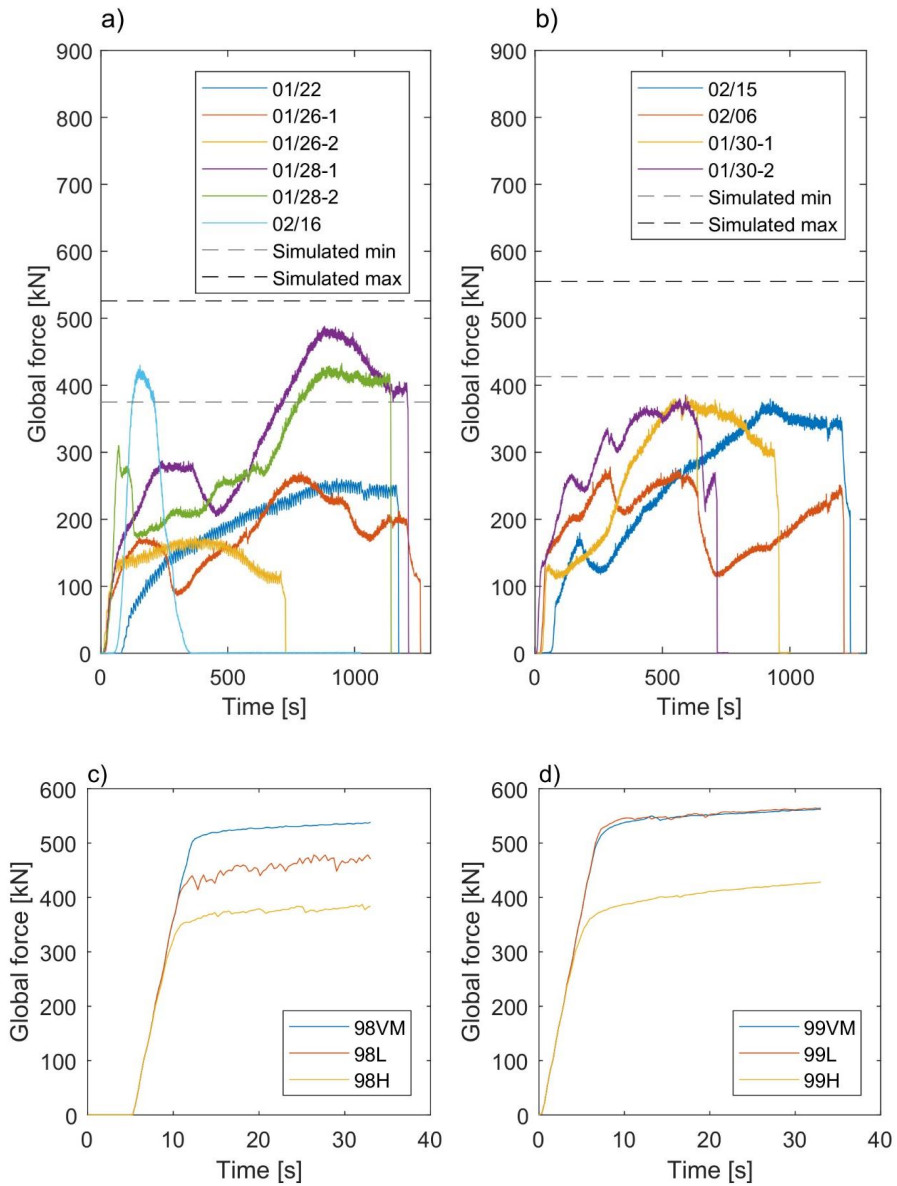


Fig. 9. Global forces time series a) 1998 data including the range in simulated global force and b) 1999 data including the range in simulated global force, c) 98 simulations and d) 99 simulations.

The force distribution across the lighthouse is displayed in Fig. 10, where the red line displays the approximate measured peak global force (Ervik et al., 2018b).

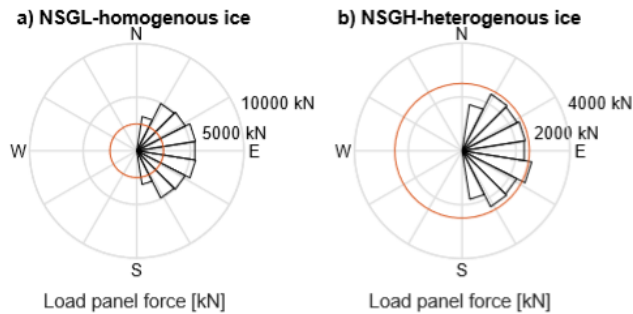


Fig. 10 Force distribution, the title includes the simulation identity. The red circle displays approximately measured peak load panel forces (2500 kN). The ice interacted with the east side of the of the lighthouse. The mean uniaxial compressive strength was 2 MPa in a) and 1 MPa in b).

6 Discussion

Ductile ice deformation was simulated with an elastic-plastic FEM. The model allows for dependency of ice strength on the multiaxial stress state, to model an increase in volume under shear as well as to introduce spatially varying ice strength characteristics.

The statistical significance of material properties to the global force was quantified by simulations in conjunction with two level factorial design of experiments. The model was applied in simulations of ductile ice failure at two vertically sided structures (JOIA – a flat indenter and the Norströmsgrund lighthouse – a cylindrically shaped structure). Furthermore, we will use the simulation results to study the stress state in the ice at different locations at the ice/structure interface, which will further been used to explain how ice thickness, aspect ratio and structure shape as well as strength heterogeneities influence the global ice force.

Here is an overview of topics deliberated in the discussion:

1. The significance of material properties and practical implications.
2. The stress state in the ice and how it can explain observed effects of aspect ratio, structure shape and strength heterogeneities to the global force.
3. How measured global forces are related to simulated forces.

6.1 The significance of material properties

The two level factorial design of experiment (section 3) showed that the strength properties and thereafter the dilatancy angle was most statistically significant to the global force. Among the strength properties, the uniaxial compressive strength and uniaxial tensile strength was most significant. On one hand, this is beneficial because uniaxial strengths are typically measured in field experiments. On the other hand, uniaxial strengths vary significantly both spatially and temporally in naturally grown sea ice. In the 2^k DOE, the uniaxial compressive strength was varied

from 1 MPa to 10 MPa and the uniaxial tensile strength was defined as a ratio of the uniaxial compressive strength. Field uniaxial compressive strength in samples loaded in the horizontal direction varied spatially (both horizontally and vertically) from approximately 1 MPa to 12 MPa, with reducing variability for warmer ice (Shafrova and Moslet, 2006). The range of uniaxial strength depends on the temperature and strain rate, where cold ice loaded at strain rates close to the ductile-brittle transition rate, varies more than warm ice loaded at lower strain rates (Ervik et al., 2018a; Høyland, 2007; Johnston, 2014; Johnston, 2017; Moslet, 2007). Furthermore, the dilatancy angle, which is the ratio between the volumetric and deviatoric strain was also significant to the global force. Few measurements report strains, and thus little is known about the dilatancy in ice. We suggest that the dilatancy should be studied further and that it probably is a function of both temperature, confinement and strain rate as also suggested by Dorris (1991). We expect that the ice dilates more under low degree of confinement, because cracks can form and open freely, whereas under high confinements crack formation and frictional sliding is suppressed.

6.2 The ice stress state

In the following we study the stress state in ice elements and nodes at the ice/structure contact, Fig. 11 displays the node location. Important characteristics of the stress state:

- Stresses are calculated in integration points, one in each element. Nodal stresses are predicted from the element shape functions.
- The global force on the indenter/lighthouse is equal to the normal stress σ_{11} (in the ice) integrated over the contact area. The effective pressure on the indenter/lighthouse is equal to the mean of the normal stress σ_{11} (in the ice) over the contact area.
- In pressure dependent materials, the plastic limit $\sqrt{3J_2}$ depends on I_1 . In the Lubliner model, $\sqrt{3J_2}$ increases with increasing I_1 .
- The magnitude of the normal stress σ_{11} and thus the global force, will increase if lateral σ_{22} or vertical σ_{33} stresses are imposed on the ice.
- The first principal invariant (I_1) was consistently less than 10 MPa in simulations presented in this paper. Multiaxial compression data in Fig. 1 showed that the deviatoric strength increased up to at least 10 MPa, which was a presumption for the selected model.

Stresses in nodes TopSym and TopEnd in simulation JOIA98L, JOIA99L as well as TopSym in NSGL are displayed in Table 6.

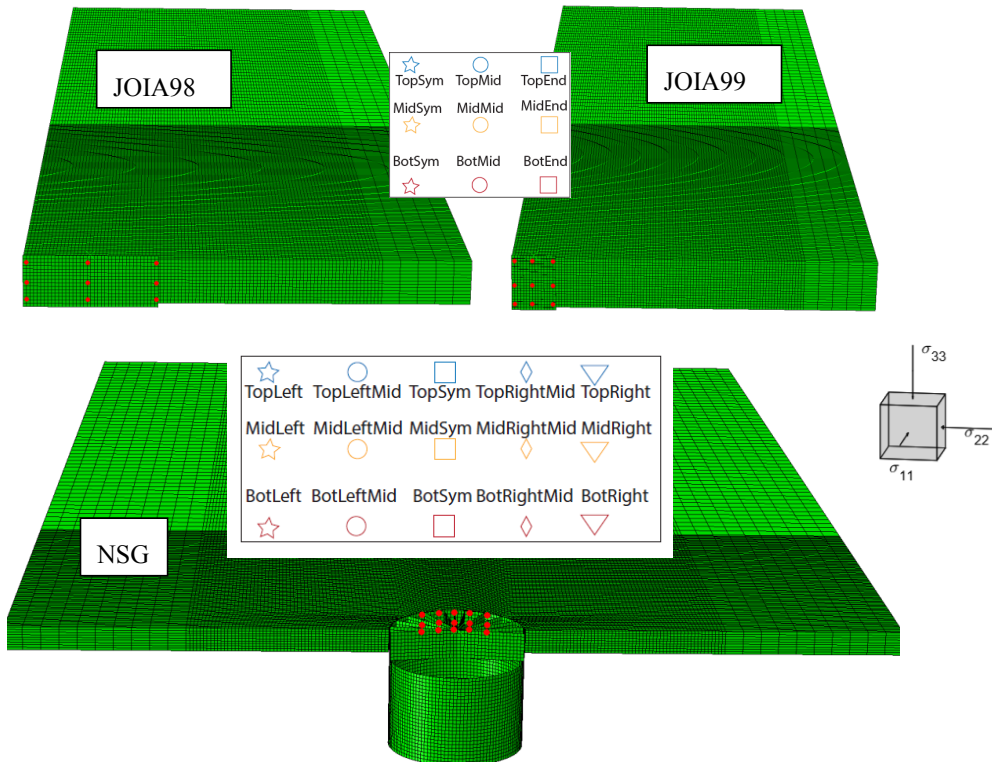
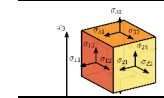


Fig. 11 Nodes in the ice, used to study the ice stress state, top left: JOIA98L, top right: JOIA99L and bottom: NSGL, Red dots display nodes where stresses were studied and the nodal labels and symbols used in Fig. 12, Fig. 15 Table 6 is displayed in the white box.

Table 6 General stress state in nodes at the last simulation step.

	JOIA98L/JOIA98VM		JOIA99L/JOIA99VM		NSGL
	TopSym ☆	TopEnd □	TopSym ☆	TopEnd □	TopSym □
Indenter s_2	Flat		Flat		Cylindrical
Aspect ratio	5.9		1.7		5.5
σ_{11} [MPa]	0.7/0.9	2.2/2.1	2.4/2.3	4.5/4.7	2.9
σ_{22} [MPa]	0.3/0.4	1.1/1.2	1.7/1.9	2.2/2.9	0.9
σ_{33} [MPa]	0.2/0.0	1.4/1.4	0.4/0.6	2.9/2.9	0.6
σ_{12} [MPa]	-0.0/-0.0	0.6/-0.5	-0.0/-0.0	0.3/-0.6	-0.0
σ_{23} [MPa]	-0.0/-0.0	0.0/-0.0	0.0/0.0	0.1/-0.0	-0.0
σ_{13} [MPa]	0.1/-0.0	0.1/-0.0	0.2/-0.0	0.3/0.0	0.1
$\sqrt{3J_2}$ [MPa]	0.5/0.6	1.3/1.0	1.8/1.6	2.3/1.6	2.2
I_1 [MPa]	1.3/1.7	4.8/4.7	4.4/4.8	9.6/11	4.4

6.2.1 The Von Mises yield function

The data displayed in Fig. 1 shows that the plastic limit $\sqrt{3J_2}$ in ice is pressure dependent, which supports the use of the Lubliner yield function. In the von Mises yield function, the plastic limit $\sqrt{3J_2}$ is I_1 -independent and the plastic limit $\sqrt{3J_2}$ is constantly equal to the uniaxial compressive strength. With the pressure dependent Lubliner yield function, and low I_1 , the majority of elements are located under the dashed line (von Mises) in Fig. 12 and the von Mises yield function results in higher forces. Contrarily, when I_1 is high, the majority of elements are located above the dashed line in Fig. 12 and the von Mises yield function results in lower forces. With the von Mises yield function, elements that have reached the plastic limit lie on the pressure independent dashed line in Fig. 12.

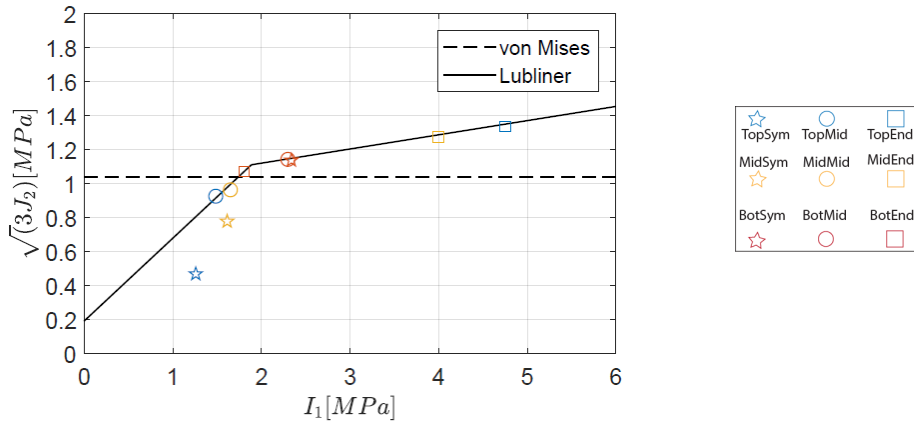


Fig. 12 Deviatoric stress vs. first principal invariant, the markers indicate stresses in nodes from the JOIA98L simulation.

6.2.2 Aspect ratio

The lateral stress σ_{22} increased between JOIA98L and JOIA99L (see Table 6). The lateral stress increased because both the aspect ratio decreased and the ice strength increased. The aspect ratio in the JOIA98L and JOIA99L simulation was 5.9 and 1.7, respectively. An additional simulation was ran with the JOIA98L material model and the JOIA99L aspect ratio. To visualize how the aspect ratio affects the ice stress states, the deviatoric stress is compared to the first principal stress invariant in Fig. 13 (for the nodes in Fig. 11). In addition to the nodal stresses the plastic limits of the von Mises and Lubliner yield functions are displayed. When the aspect ratio decreased from 5.9 to 1.7, with all else being equal, the lateral stress increased as well as $\sqrt{3J_2}$, I_1 and thus the effective pressure. The effective pressure increased from 1.2 MPa to 1.6 MPa, when the aspect ratio decreased from 5.9 to 1.7.

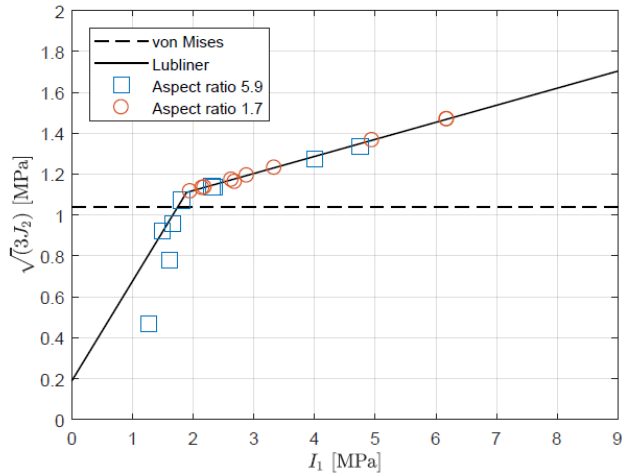


Fig. 13 Aspect ratio effect. von Mises and Lubliner display the plastic limits in the respective material models.

In ISO19906 (2010) the effective pressure is a function of both ice thickness and aspect ratio, whereas the effective pressure equation in API-RP-2N (1995) is independent of both ice thickness and aspect ratio. Määttänen and Kärnä (2011) suggested a modification of ISO19906 (2010) because it was proven unsafe for narrow structures with small aspect ratios (equations for the different standards are presented in Appendix A.1). In Fig. 14 effective pressure is compared to aspect ratio in simulations, measurements and standards. The effective pressure simulated with the Lubliner model captures the aspect ratio effect observed in the JOIA data.

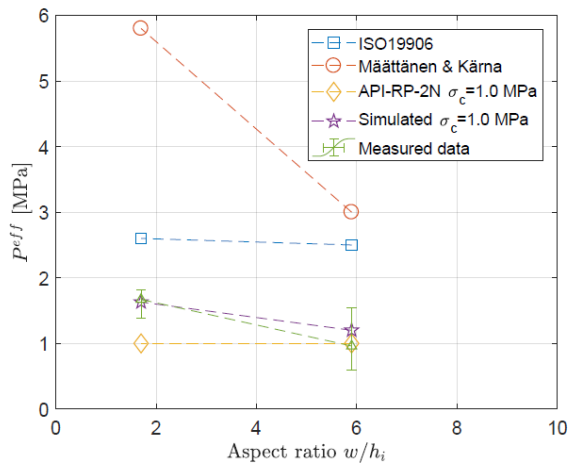


Fig. 14. Aspect ratio and codes. The markers display effective pressure and aspect ratio for JOIA98 (aspect ratio 5.9) and JOIA99 (aspect ratio 1.7) simulation setup.

6.2.3 Structure shape

The structure shape in contact with the ice influences the lateral stress in the ice. With the cylindrical indenter, in the NSGL simulation, the highest stress in the ice was observed on the symmetry line on the ice/structure contact (□ in Fig. 15). Contrary, on the flat indenter the highest stress was observed in the ice in contact with the indenter corners. Tactile sensor data confirm that the pressure was higher on the indenter corners than elsewhere (Sodhi et al., 1998). If the flat indenter (in the JOIA simulations) was replaced with a cylindrical indenter of equal width, the effective pressure would decrease. This is consistent with the observations made by Korzhavin (1962) and adopted by the API-RP-2N (1995). The effect of structural shape is not included in the ISO19906 (2010).

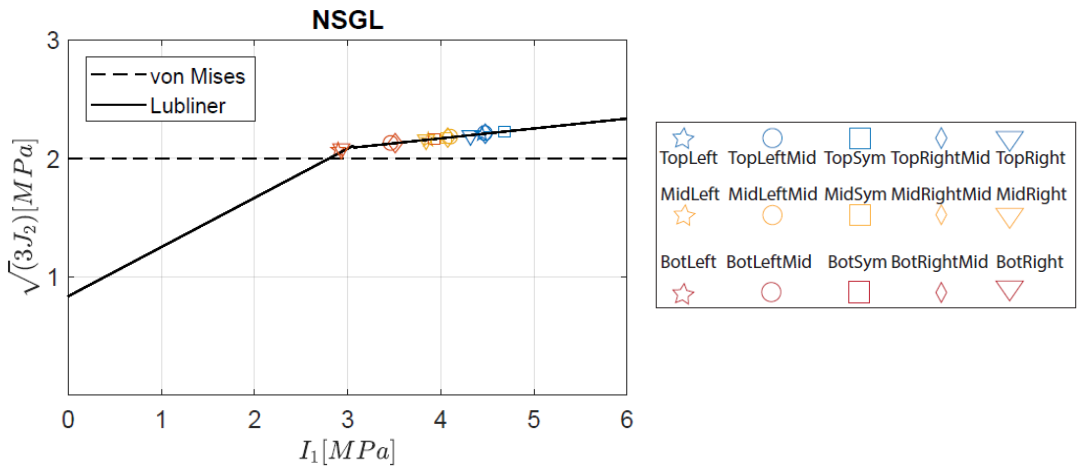


Fig. 15 Deviatoric stress vs. first principal invariant, the markers indicate stresses in nodes from the NSGL simulation.

6.2.4 Ice strength heterogeneities

The JOIA99 simulation was used to study the effect of strength heterogeneities. In Fig. 16 results from homogenous ice simulations are compared with heterogeneous in terms of $\sqrt{3J_2} - \varepsilon_p$ history. The following is noted regarding Fig. 16.

- If the stresses in adjacent elements combined with their shape functions predicts different stress values for their common nodes, stresses are averaged in the node if the nodal stresses are within 75%. If the elements predict nodal stresses that are not within 75% of each other, all stress values are reported.
- Each of the nodes (red dots in Fig. 16a) are surrounded by four elements with one integration point each.

- In the simulation with heterogeneous strength (Fig. 16b) four stress strain curves are displayed for each node because the elements adjacent to the nodes predict stresses that are not within 75% of each other.

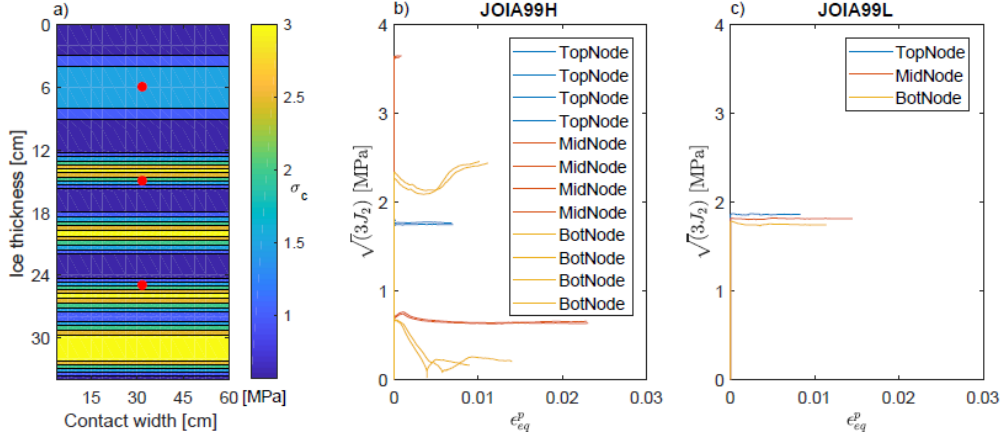


Fig. 16 Heterogeneous vs. homogenous simulations. a) displays the distribution of uniaxial compressive strength in the ice in contact with the indenter b) $\sqrt{3J_2} - \epsilon_p$ history in heterogeneous ice simulation and c) $\sqrt{3J_2} - \epsilon_p$ history in homogenous ice simulation. (Note that in a) the width is 60 cm and the ice thickness/height is 36 cm)

The figure shows that the strain was unevenly distributed across the ice thickness in the heterogeneous strength simulation and that the strain was higher in elements with lower yield strengths. Thus the displacement and strain was carried by elements with lower strength. The mean of the steady state effective pressure and global force was 18-26% lower in simulations with strength heterogeneities compared to simulations with homogenous strength, with equal average strengths and all else being equal (see section 5).

6.3 Measurements compared to simulations

6.3.1 JOIA

In the JOIA events, the range in measured forces was larger in 1998 (170-490 kN) than in 1999 (280-390 kN), perhaps due to larger variation in ice thickness (18.6-28.9 cm) in 1998 than in 1999 (33.9-37.3 cm). The indenter width was 1.5 m and 0.6 m, in the 1998 and 1999 events, respectively. The simulated forces in the JOIA98 and JOIA99 events were 10%-34% and 15%-54% higher than the average measured forces in 1998 and 1999, respectively. The forces in the JOIA98 and JOIA99 simulations were 0.77- 1.07 and 1.06-1.42 times the maximum measured forces in 1998 and 1999, respectively. The uniaxial compressive strength, which is the most statistically significant material property cf. section 6.1, varied more in 1999 than in 1998, and thus the simulated forces were more

uncertain in 1999 than in 1998. We unfortunately have no information about how the uniaxial compressive strength tests were executed, or if the procedures were the same in 1998 and 1999.

Ice interactions with the flat and stiff indenter in the JOIA experiment are considered worst cases in terms of the global force. The intact ice cover and indenter stiffness ensured that the ice failed simultaneously across the full contact area and the ice was grown in a stable environment such that the ice was more homogenous than at the Norströmsgrund lighthouse.

6.3.2 Norströmsgrund lighthouse

The simulated global forces were 1.8 – 4.2 times higher than the maximum measured (6 MN) force, and 1.2- 2.8 times higher than the estimated maximum force (9 MN). The measured data was collected during four mild/average winters (based on FDD from 1952 to 2015), and so the possibility of higher forces should be considered in the design of a similar structure in a location with similar ice conditions. Due to increased global ice transportation in spring and larger contact areas due to weaker and ductile ice, all events with global force > 3 MN measured at the Norströmsgrund lighthouse, occurred in March and April (Bjerkås et al., 2012; Ervik et al., 2018b). The ice temperature increased in March and April towards the freezing point, and the average in-situ ice temperature was -0.5°C 2003 March 20. Ice samples tested in uniaxial compression in the laboratory at strain rate $0.5 \cdot 10^{-3} \text{ s}^{-1}$, were cooled down to -10°C and reheated to -1 °C (Franson and Weiss, 2004b). When the ice is cooled down and reheated the ice strength increases, this was observed in Arctic sea ice (personal communication Høyland, 2018). Thus, the strength of the ice that interacted with Norströmsgrund lighthouse in March and April was probably lower than the laboratory measured 2-5 MPa. The ice thickness used in the simulations (1.3 m) was a conservative estimate using the maximum level ice thickness calculated from FDD and the maximum measured ratio of consolidated layer\level ice thickness.

The ice interactions at the Norströmsgrund lighthouse are not considered worst cases in terms of the global force, because the ice field was broken, measurements were conducted in mild/average winters (based on FDD), conservative ice thickness estimate, the instrumentation was insufficient to measure the total global force and the ice was probably more heterogeneous compared to the JOIA experiment.

Simulations are considered worst cases, in terms of the global force level, because the ice sheet is perfectly level and semi-infinite, the total force is obtained and besides heterogeneities, defects are absent.

7 Conclusions and recommendations

Ductile ice interactions with offshore structures may cause severe actions. In this paper we applied an elastic-plastic FEM in simulations of ductile failure of competent ice in the JOIA experiment and at the Norströmsgrund lighthouse. A non-associated flow rule was included in the applied model in order to study whether the dilatancy in ice was significant to the global force in ductile

ice-structure interactions. Statistical significance of ice properties in the material model was identified by means of two level factorial design of experiments. The stress state in the ice was used to explain how the effective pressure was affected by aspect ratio, structure shape and strength heterogeneities. The following conclusions were made:

- Simulations show that the most statistically significant properties were the strength properties and thereafter the dilatancy angle.
- The pressure dependent model predicts an aspect ratio effect due to changes in lateral stresses.
- The pressure dependent model predicts higher effective pressure with the prismatic indenter than the cylindrical indenter because of increased lateral stresses on the corner of the prismatic indenter.
- The strength in ice is pressure dependent and therefore the pressure independent von Mises yield function should be avoided.

8 Acknowledgments

The authors wish to acknowledge the support of the Research Council of Norway through the Centre of Research-based Innovation SAMCoT (grant no 203471/O30), and the support of the SAMCoT partners. Special thanks are extended to Anna Pustogvar for introducing me to methods in design of experiments. We also acknowledge Dr. Devinder Sodhi for sharing valuable data from the JOIA experiment. Multiconsult AS is acknowledged for the economic support and their patience. The authors also wish to acknowledge the economic support of the Research Council of Norway through the project “Field studies and modeling of sea state, drift ice, ice actions and methods of iceberg management on the Arctic Shelf, 2015-2017 (FIMA)”.

A.1 Appendix - Standards and codes

Table A.1. Empirical equations of effective pressure in standards ISO19906 and API-RP-2N

Effective pressure	Coefficients
API-RP-2N (1995) $\sigma_c \cdot l \cdot f_c$	σ_c uniaxial compressive strength in prismatic ice samples l 1.0 for rectangular and 0.9 for cylindrical structures f_c 0.4-1.0, increasing for decreasing velocity
ISO19906 (2010) $C_R \cdot \left(\frac{h_i}{h_1}\right)^n \cdot \left(\frac{w}{h_i}\right)^{-0.16}$	C_R 1.8 in sub-Arctic/temperate, 2.8 in Arctic h_i ice thickness, $h_1 = 1.0$ m w structural diameter/width $n = -0.5 + h_i / 5$ ($h_i < 1m$) $n = -0.3$ ($h_i \geq 1m$)
Määttänen and Kärnä (2011) $C_R \cdot \left[\left(\frac{h_i}{h_1}\right)^n \cdot \left(\frac{w}{h_i}\right)^{-0.16} + e^{\frac{-w}{3h_i}} \sqrt{1 + 5 \frac{h_i}{w}}\right]$	C_R 1.8 in sub-Arctic/temperate, 2.8 in Arctic h_i ice thickness, h_1 1.0 m w structural diameter/width $n = -0.5 + h_i / 5$ ($h_i < 1m$) $n = -0.3$ ($h_i \geq 1m$)

The API-RP-2N equation was based on the equation developed by Korzhavin (1962). The equation in Määttänen and Kärnä (2011) is an enhancement of the ISO19906 (2010) equation, because the ISO19906 (2010) was proven unsafe for narrow structures. The ISO19906 equations are different from the API-RP-2N equation in that the C_R value is independent of the uniaxial compressive

strength. Moreover, the API-RP-2N equation considers both the effect of structural shape and ice drift speed and thus the type of failure mode, whereas an aspect ratio effect is included in the ISO19906.

References

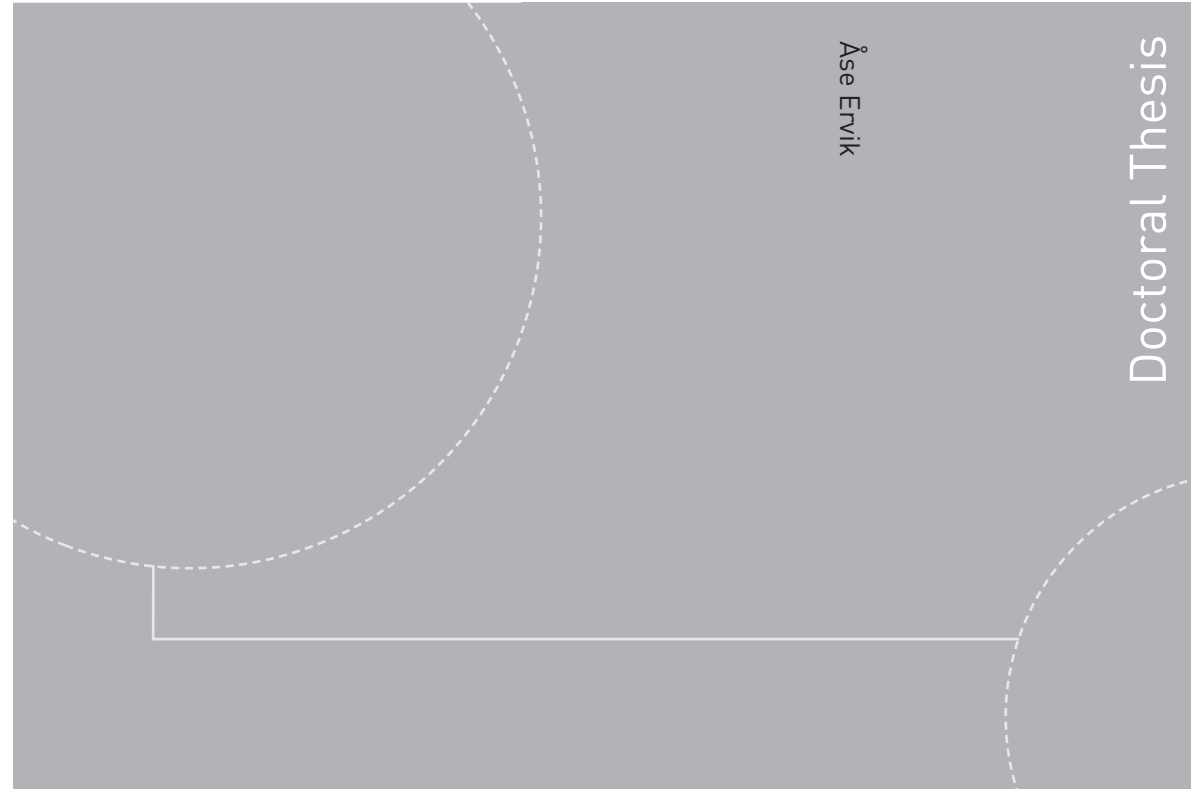
- Alejano, L.R. and Alonso, E., 2005. Considerations of the dilatancy angle in rocks and rock masses. *International Journal of Rock Mechanics and Mining Sciences*, 42(4): 481-507.
- API-RP-2N, 1995. Recommended Practice for Planning, Designing and Constructing Structures and Pipelines for Arctic Conditions American Petroleum Institute, Exploration and Production Department.
- Bjerkås, M., 2006. Ice action on offshore structures, NTNU.
- Bjerkås, M., Lønøy, C. and Gürtner, A., 2012. Seasonal Variations In the Occurrence of Ice Induced Vibration of a Bottom Fixed Structure, The Twenty-second International Offshore and Polar Engineering Conference. International Society of Offshore and Polar Engineers, Rhodes, Greece.
- Bjerkås, M. and Nord, T.S., 2016. Ice action on Swedish lighthouses revisited, Proceedings of the 23rd IAHR International Symposium on Ice, Ann Arbor, Michigan USA.
- Blenkarn, K.A., 1970. Measurements and Analysis of Ice Forces on Cook Inlet Structures. Proceedings of the second annual conference on Offshore Technology Conference, Houston, Texas.
- Dorris, J.F., 1991. A Plasticity Model for the Crushing of Ice. IUTAM-IAHR Symposium St. John's Newfoundland, Canada, Springer-Verlag Berlin Heidelberg.
- Engelbrektsen, A., 1987. Evaluation of Extreme Ice Forces on a Lighthouse in the Botnian Bay, A study of the Björnklack overloading event April 1985. Report No. 1, National Administration of Shipping and Navigation, Sweden, University of Luleå.
- Ervik, Å., Høyland, K.V., Shestov, A. and Nord, T.S., 2018a. On the decay of first-year ice ridges: Measurements and evolution of rubble macroporosity, ridge drilling resistance and consolidated layer strength , <https://doi.org/10.1016/j.coldregions.2018.03.024>. *Cold Regions Science and Technology*, 151: 196-207.
- Ervik, Å., Nord, T.S., Høyland, K.V., Samardzija, I. and Hongtao, L., 2018b. Ice-ridge interactions with the Norströmsgrund lighthouse: global forces and interaction modes. *Cold Regions Science and Technology*, <https://doi.org/10.1016/j.coldregions.2018.08.020>.
- Franson, L. and Weiss, J., 2003. Mechanical properties of ice at Norströmsgrund, Test 2001. STRICE report, No. D-4.3.1.
- Franson, L. and Weiss, J., 2004a. Mechanical properties of ice at Norströmsgrund, Test 2002. STRICE report, No. D-4.3.2.
- Franson, L. and Weiss, J., 2004b. Mechanical properties of ice at Norströmsgrund, Test 2003. STRICE report, No. D-4.3.3.
- Gagnon, R.E. and Gammon, P.H., 1995. Triaxial experiments on iceberg and glacier ice. *Journal of Glaciology*, 41(139): 528-540.

- Haas, C., 2000. LOLEIF report: EM ice thickness measurements at the lighthouse Norstrømsgrund, Luleå, Sweden, within the LOLEIF project. Part 1: system installation, modelling and calibration.
- Haas, C., 2017. EM thickness and the consolidated layer, personal communication
- Høyland, K.V., 2007. Morphology and small-scale strength of ridges in the North-western Barents Sea. *Cold Regions Science and Technology*, 48(3): 169-187.
- Høyland, K.V., 2018. Storage and transportation of ice samples.
- ISO19906, 2010. Petroleum and natural gas industries - Arctic offshore structures. International Standardization organization. , Geneva, Switzerland.
- Jochmann, P. and Schwarz, J., 2000. LOLEIF-report: Ice Force Measurements at Lighthouse Norstrømsgrund - Winter 1999. Rep no 5.
- Johnston, M.E., 2014. A decade of probing the depths of thick multi-year ice to measure its borehole strength. *Cold Regions Science and Technology*, 99: 46-65.
- Johnston, M.E., 2017. Seasonal changes in the properties of first-year, second-year and multi-year ice. *Cold Regions Science and Technology*, 141: 36-53.
- Jones, S.J., 1982. The Confined Compressive Strength of Polycrystalline Ice. *Journal of Glaciology*, 28(98): 171-178.
- Kamio, Z., Takawaki, T., Matsushita, H., Takeuchi, T., Sakai, M., Terashima, T., Akagawa, S., Nakazawa, N. and Saeki, H., 2000. Medium Scale Field Indentation Tests: Physical Characteristics of First-Year Sea Ice at Nototo Lagoon, Hokkaido. Proceedings of the Tenth (2000) International Offshore and Polar Engineering Conference, Seattle, USA, May 28-June 2.
- Kim, E., 2014. Experimental and numerical studies related to the coupled behavior of ice mass and shell structures during accidental collisions, Ph.D thesis NTNU, ISBN 978-82-326-0192-9, Department of Marine Technology, Trondheim.
- Korzhavin, K.N., 1962. Action of Ice on Engineering Structures (English title) IZDATEL 'STVO SIBIRSKOGO OTDELESIYA AKADEMII HAUK SSSR, Publishing House of Siberian Branch of USSR Academy of Sciences, 202p.
- Li, H., Bjerkås, M., Høyland, K.V. and Nord, T.S., 2016. Panel loads and weather conditions at Norstrømsgrund lighthouse 2000-2003, Proceedings of the 23rd IAHR international Symposium on Ice, Ann Arbor, Michigan USA.
- Liu, Z., Amdahl, J. and Løset, S., 2011. Plasticity based material modelling of ice and its application to ship-iceberg impacts. *Cold Regions Science and Technology*, 65(3): 326-334.
- Lubliner, J., Oliver, J., Oller, S. and Oñate, E., 1989. A plastic-damage model for concrete. *International Journal of Solids and Structures*, 25(3): 299-326.
- Matsushita, H., Takawaki, T., Tuboi, T., Takeuchi, T., Sakai, M., Terashima, T. and Saeki, H., 1999. Medium Scale Field Indentation Tests: Strength Characteristics of the Ice Sheet (First-Year Sea Ice), The Ninth International Offshore and Polar Engineering Conference. International Society of Offshore and Polar Engineers, Brest, France.

- Montgomery, D.C., 2013. Design and Analysis of Experiments (8th Edition). John Wiley & Sons. Online version available at: <https://app.knovel.com/hotlink/pdf/id:kt011B0NGM/design-analysis-experiments/strategy-experimentation>. John Wiley & Sons.
- Moslet, P.O., 2007. Field testing of uniaxial compression strength of columnar sea ice. *Cold Regions Science and Technology*, 48(1): 1-14.
- Määttänen, M. and Kärnä, T., 2011. ISO 19906 ice crushing load design extension for narrow structures, Proceeding of the 21st International Conference on Port and Ocean Engineering under Arctic Conditions, Montreal, Canada.
- Nadreau, J.-P. and Michel, B., 1986. Yield and failure envelope for ice under multiaxial compressive stresses. *Cold Regions Science and Technology*, 13(1): 75-82.
- Neill, C.R., 1976. Dynamic ice forces on piers and piles. An assessment of design guidelines in the light of recent research. *Canadian Journal of Civil Engineering*, 3(2): 305-341.
- Pariseau, W.G., 1968. Plasticity theory for anisotropic rocks and soils. In K.E. Gray (ed.), Proc. Tenth Symp. on Rocks Mechanics, pp. 267-295.
- Ralston, T.D., 1980. Yield and plastic deformation in ice crushing failure. In *Sea ice Processes and Models*, R.S. Pritchard (ed.), University of Seattle Press, Seattle, U.S.A.: 234-245.
- Riska, K. and Frederking, R., 1987. Ice load penetration modelling, Proceedings of the Port and Ocean Under Arctic Conditions Conference Fairbanks, Alaska, USA, pp. 317-327.
- Rist, M.A. and Murrell, S.A.F., 1994. Ice triaxial deformation and fracture. *Journal of Glaciology*, 40(135): 305-318.
- Saeki, H., Hiyayama, K.-i., Kawasaki, T., Akagawa, S., Kato, K., Kamesaki, K., Saka, K. and Kurakawa, A., 1997. JOIA Project of Study on Ice Load Proceedings of the Seventh (1997) International Offshore and Polar Engineering Conference, Honolulu, USA, May 25-30, 1997.
- Saeki, H., Ono, T., Nakazawa, N., Sakai, M. and Tanaka, S., 1986. The Coefficient of Friction Between Sea Ice and Various Materials Used in Offshore Structures. *Journal of Energy Resources Technology*, 108(1): 65-71.
- Sakai, M., Aoshima, M. and Saeki, H., 1998. Measurements of Ice Sheet Strain Area During Ice/Vertical Sided Structure Interactions Using Strain Gages In Field Indentation Tests, The Eighth International Offshore and Polar Engineering Conference. International Society of Offshore and Polar Engineers, Montreal, Canada.
- Schulson, E.M. and Duval, P., 2009. *Creep and Fracture in Ice* Cambridge University Press.
- Shafrova, S. and Moslet, P.O., 2006. In-situ uniaxial compression tests of level ice part II: Ice strength spatial distribution. Proceedings of the OMAE2006, 25th International Conference on Offshore Mechanics and Arctic Engineering, June 4-9, Hamburg, Germany.
- Smith, M.B., 1974. A parabolic yield condition for anisotropic rocks and soils, Rice University, PhD thesis, Engineering, mechanical.
- Sodhi, D.S. and Haehnel, R.S., 2003. Crushing Ice Forces on Structures. *Journal of Cold Regions Engineering*, 17(4).

- Sodhi, D.S., Takeuchi, T., Nakazawa, N., Akagawa, S. and Saeki, H., 1998. Medium-scale indentation tests on sea ice at various speeds. *Cold Regions Science and Technology*, 28(3): 161-182.
- Strub-Klein, L. and Sudom, D., 2012. A comprehensive analysis of the morphology of first-year sea ice ridges. *Cold Regions Science and Technology*, 82: 94-109.
- Timco, G.W. and Frederking, R.M.W., 1984. An investigation of the failure envelope of granular/discontinuous-columnar sea ice. *Cold Regions Science and Technology*, 9(1): 17-27.
- Timco, G.W. and Weeks, W.F., 2010. A review of the engineering properties of sea ice. *Cold Regions Science and Technology*, 60(2): 107-129.
- Tsai, S.W. and Wu, E.M., 1972. A general theory of strength for anisotropic materials *Journal of Composite Materials*, vol. 5, pp 58-80.
- Ushikoshi, J., Kamio, Z., Matsushita, H., Sakai, M., Takeuchi, T., Terashima, T., Akagawa, S., Nakazawa, N. and Saeki, H., 2001. Summary of Five Years' Field Test On Mechanical Properties, The Eleventh International Offshore and Polar Engineering Conference. International Society of Offshore and Polar Engineers, Stavanger, Norway.
- Vakili, A., 2016. An improved unified constitutive model for rock material and guidelines for its application in numerical modelling. *Computers and Geotechnics*, 80: 261-282.
- Vermeer, P.A., 1998. Non-Associated Plasticity for Soils, Concrete and Rock. In: H.J. Herrmann, J.P. Hovi and S. Luding (Editors), *Physics of Dry Granular Media*. Springer Netherlands, Dordrecht, pp. 163-196.

ISBN 978-82-326-3980-9 (printed version)
ISBN 978-82-326-3981-6 (electronic version)
ISSN 1503-8181



Åse Ervik

Doctoral Thesis

Doctoral theses at NTNU, 2019:192

Åse Ervik

**Experimental and numerical studies
related to failure of first-year ice
ridges against fixed vertically sided
structures**

Doctoral theses at NTNU, 2019:192

NTNU
Norwegian University of
Science and Technology
Faculty of Engineering
Department of Civil and Environmental Engineering

 **NTNU**
Norwegian University of
Science and Technology

 NTNU

 **NTNU**
Norwegian University of
Science and Technology